

**ANNALS OF THE UNIVERSITY OF CRAIOVA
ANNALES DE L'UNIVERSITÉ DE CRAIOVA**

**ANALELE
UNIVERSITĂȚII
DIN CRAIOVA**

**SERIA: INGINERIE ELECTRICĂ
SERIE: ELECTRICAL ENGINEERING
SÉRIE: INGÉNIERIE ÉLECTRIQUE**

Anul/Year/Année 47

No. 47, Vol. 47, Issue 1, 2023

December 2023

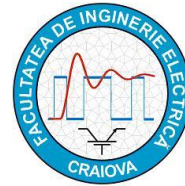
**ISSN 1842-4805 (print)
ISSN 2971-9852 (online)
ISSN-L 1842-4805**

EDITURA UNIVERSITARIA

ANNALS OF THE UNIVERSITY OF CRAIOVA



13, A.I. Cuza Str., CRAIOVA 200585
ROMANIA



**We exchange publications
with similar institutions of country and from abroad**

ANNALES DE L'UNIVERSITÉ DE CRAIOVA

Rue A.I. Cuza, No. 13, CRAIOVA 200585
ROUMANIE

**On fait des échanges des publications
avec les institutions similaires du pays et de l'étranger**

**This journal is published by the Faculty of Electrical Engineering from the University of Craiova.
The authors are fully responsible for the originality of their papers and for accuracy of their notes.**

Editorial board

Prof.dr.ing. Ioan POPA – editor in chief, University of Craiova, Romania
Conf.dr.ing. Mircea DRIGHICIU – editor in chief, University of Craiova, Romania
Prof.dr.ing. Dan MIHAI, University of Craiova, Romania
Prof.dr.ing. Marian CIONTU, University of Craiova, Romania
Prof.dr.ing. Lucian MANDACHE, University of Craiova, Romania
Prof.dr.sc. Ivan YATCHEV, Technical University of Sofia, Bulgaria
Prof.dr.ing. Leszek CZARNECKI, Life Fellow IEEE, Louisiana State University, USA
Prof.dr.ing. Slavoljub ALEKSIC, University of Niš, Serbia
Prof.dr.ing. Mihai IORDACHE, University "Politehnica" of Bucharest, Romania
Prof.dr.ing. Victor ŞONTEA, Technical University of Moldova, Moldova
Prof.dr.ing. Iuliu DELEŞEGA, University "Politehnica" of Timișoara, Romania
Prof.dr.ing. Dumitru-Marcel ISTRATE, "Gh. Asachi" Technical University of Iași, Romania
Prof.dr.ing. Miroslav PRSA, University of Novi Sad, Serbia
Prof.dr.ing. Maria BROJBOIU, University of Craiova, Romania
Prof.dr.ing. Mihai GAVRILAŞ, "Gh. Asachi" Technical University of Iași, Romania
Prof.dr.ing. Daniela DANCIU, University of Craiova, Romania
Prof.dr.ing. Nicolae MUNTEAN, University "Politehnica" of Timișoara, Romania
Prof.dr.ing. Călin MUNTEANU, Technical University of Cluj-Napoca, Romania
Prof.dr.ing. Leonardo-Geo MĂNESCU, University of Craiova, Romania
Prof.dr.ing. Camelia PETRESCU, "Gh. Asachi" Technical University of Iași, Romania
S.I.dr.ing. Ioana Gabriela SÎRBU, University of Craiova, Romania

REVIEWERS COMMITTEE

Lia-Elena ACIU – *Transilvania University of Braşov*, Romania
Maricel ADAM – *"Gh. Asachi" Technical University of Iaşi*, Romania
Mihaela ALBU – *University "Politehnica" of Bucharest*, Romania
Slavoljub ALEKSIC – *University of Niš*, Serbia
Horia BĂLAN – *Technical University of Cluj-Napoca*, Romania
Alexandru BITOLEANU – *University of Craiova*, Romania
Maria BROJBOIU – *University of Craiova*, Romania
Emil CAZACU – *University "Politehnica" of Bucharest*, Romania
Aurel CÂMPEANU – *University of Craiova*, Romania
Mihai CERNAT – *Transilvania University of Braşov*, Romania
Marian CIONTU – *University of Craiova*, Romania
Daniel Cristian CISMARU – *University of Craiova*, Romania
Grigore CIVIDJIAN – *University of Craiova*, Romania
Zlata CVETCOVIC – *University of Niš*, Serbia
Leszek CZARNECKI – *Louisiana State University*, USA
Daniela DANCIU – *University of Craiova*, Romania
Sonia DEGERATU – *University of Craiova*, Romania
Iuliu DELEŞEĞA – *University "Politehnica" of Timişoara*, Romania
Silvia-Maria DIGĂ – *University of Craiova*, Romania
Peter DINEFF – *Technical University of Sofia*, Bulgaria
Radu DOBRESCU – *University "Politehnica" of Bucharest*, Romania
Mircea-Adrian DRIGHICIU – *University of Craiova*, Romania
Laurentiu Marius DUMITRAN – *University "Politehnica" of Bucharest*, Romania
Sorin ENACHE – *University of Craiova*, Romania
Virgiliu FIRETEANU – *University "Politehnica" of Bucharest*, Romania
Dan FLORICĂU – *University "Politehnica" of Bucharest*, Romania
Cristian FOŞALĂU – *"Gh. Asachi" Technical University of Iaşi*, Romania
Teodor Lucian GRIGORIE – *Military Technical Academy "Ferdinand I"*, Romania
Stefan HĂRĂGUŞ – *University "Politehnica" of Timişoara*, Romania
Elena HELEREA – *Transilvania University of Braşov*, Romania
Eugen HNATIUC – *"Gh. Asachi" Technical University of Iaşi*, Romania
Kemal HOT – *Polytechnic of Zagreb*, Croatia
Eugen IANCU – *University of Craiova*, Romania
Nathan IDA – *University of Akron*, USA
Maria IOANNIDES – *National Technical University of Athens*, Greece
Valentin IONIŢĂ – *University "Politehnica" of Bucharest*, Romania
Mihai IORDACHE – *University "Politehnica" of Bucharest*, Romania
Marcel ISTRATE – *"Gh. Asachi" Technical University of Iaşi*, Romania
Wilhelm KAPPEL – *National Research and Development Institute for Electrical Engineering (ICPE – CA) Bucharest*, Romania
Liviu KREINDLER – *University "Politehnica" of Bucharest*, Romania
Gheorghe LIVINŢI – *"Gh. Asachi" Technical University of Iaşi*, Romania
Dumitru Dorin LUCACHE – *"Gh. Asachi" Technical University of Iaşi*, Romania
Lucian MANDACHE – *University of Craiova*, Romania
Gheorghe MANOLEA – *University of Craiova*, Romania
Andrei MARINESCU – *Romanian Academy of Technical Science, Craiova Branch*, Romania
Iliana MARINOVA – *Technical University of Sofia*, Bulgaria
Claudia MARTIŞ – *Technical University of Cluj-Napoca*, Romania
Ernest MATAGNE – *Université Catholique de Louvain*, Belgium

Leonardo-Geo MĂNESCU – *University of Craiova, Romania*
Dan MIHAI – *University of Craiova, Romania*
Alexandru MOREGA – *University "Politehnica" of Bucharest, Romania*
Mihaela MOREGA – *University "Politehnica" of Bucharest, Romania*
Nazih MOUBAYED – *Lebanese University, Lebanon*
Călin MUNTEANU – *Technical University of Cluj-Napoca, Romania*
Florin MUNTEANU – *"Gh. Asachi" Technical University of Iași, Romania*
Valentin NĂVRĂPESCU – *University "Politehnica" of Bucharest, Romania*
Mitică Iustinian NEACĂ – *University of Craiova, Romania*
Petre-Marian NICOLAE – *University of Craiova, Romania*
Dragoș NICULAE – *University "Politehnica" of Bucharest, Romania*
Petru NOTINGHER – *University "Politehnica" of Bucharest, Romania*
Teodor PANĂ – *Technical University of Cluj-Napoca, Romania*
Camelia PETRESCU – *"Gh. Asachi" Technical University of Iași, Romania*
Ioan POPA – *University of Craiova, Romania*
Dan POPESCU – *University of Craiova, Romania*
Daniela POPESCU – *University of Craiova, Romania*
Mihaela POPESCU – *University of Craiova, Romania*
Miroslav PRSA – *University of Novi Sad, Serbia*
Mircea M. RĂDULESCU – *Technical University of Cluj Napoca, Romania*
Victorița RĂDULESCU – *University "Politehnica" of Bucharest, Romania*
Benoit ROBYNS – *Ecole des Hautes Etude d'Ingénieur de Lille, France*
Constantin ROTARU – *Military Technical Academy "Ferdinand I", Romania*
Alexandru SĂLCEANU – *"Gh. Asachi" Technical University of Iași, Romania*
Cristina Gabriela SĂRĂCIN – *University "Politehnica" of Bucharest, Romania*
Constantin SĂRMAȘANU – *"Gh. Asachi" Technical University of Iași, Romania*
Dan SELIȘTEANU – *University of Craiova, Romania*
Victor ȘONTEA – *Technical University of Moldova, Moldova*
Alexandru STANCU – *"A.I. Cuza" University of Iași, Romania*
Ryszard STRZELECKI – *University of Technology Gdansk, Poland*
Flavius-Dan ȘURIANU – *University "Politehnica" of Timișoara, Romania*
Radu-Adrian TÎRNOVAN – *Technical University of Cluj-Napoca, Romania*
Tiberiu TUDORACHE – *University "Politehnica" of Bucharest, Romania*
Raina TZENEVA – *Technical University of Sofia, Bulgaria*
Ioan VADAN – *Technical University of Cluj-Napoca, Romania*
Viorel VARVARA – *"Gh. Asachi" Technical University of Iași, Romania*
Ion VLAD – *University of Craiova, Romania*
Ivan YATCHEV – *Technical University of Sofia, Bulgaria*

CONTENTS

<i>On the Induction Motor Rotor Flux Estimation in the Electric Traction Systems with Rotor Flux-Oriented Control</i> – Mihaela Popescu, Alexandru Bitoleanu, Constantin Vlad Suru, Tudor Mătuşa	1
<i>System for Monitoring Asynchronous Motors Powered at Variable Voltage</i> – Monica-Adela Enache, Ion Vlad, Sorin Enache	8
<i>Influence of Electrical Circuit Parameter Changes on the Local Stability of a Three-Phase Cage Induction Motor Fed with Variable Frequency</i> – Sorin Enache, Ion Vlad, Monica-Adela Enache	14
<i>Installation for Carrying out Thermal Tests on the Current Paths of Electrical Power Equipment</i> – Gheorghe-Eugen Subțirelu, Petre Pistol, Adrian Vintilă, Mihăiță Constantinescu	20
<i>Estimation of the Heating of Crimped Connections Based on Experimental Tests</i> – Alin-Iulian Dolan	28
<i>An Example of Performance Achievement Based on Errors Analysis for Low-Cost Circuits Design</i> – Constantin Daniel Oancea, Daniel Bostan, Viorel Constantin Petre	35
<i>Integrated System for Remote Health Status Monitoring and Analysis</i> – Marian-Ștefan Nicolae, Florentina-Fulgina Bîzîc, Nicolae-Leonide Sîrbu, Iurie Nucă, Raluca-Cristina Presură (Nicolae)	41
<i>Equipment for the Detection of People Falling</i> – Constantin-Daniel Oancea	48
<i>Experimental Study of the Pressure Exerted in the Body of a High-Voltage Fuse and Metal Enclosed Switchgear</i> – Cristian-Eugeniu Sălceanu, Cătălin Dobrea, Daniel Constantin Ocoleanu, Daniela Iovan	54
<i>Comparative Performance Analysis of Photovoltaic Power Plants – a Case Study</i> – Mihaita Linca, Ion Popa, Constantin Vlad Suru, Florin Ravigan	62
<i>Modelling, Simulation and Implementation on dSpace 1103 of the Direct Power Control in a Three-Phase Shunt Active Power Filter System</i> – Mihăiță-Daniel Constantinescu, Mihaela Popescu, Gheorghe-Eugen Subțirelu, Ionuț-Cosmin Toma	69
<i>Data-Driven Control of the Second Order Inertial Systems with Astatism</i> – Irina Cojuhari	76
<i>The Design of a Location Monitoring System for a Fleet of Electric Scooters</i> – Florin Ravigan, Mihăiță Lincă, Laurențiu Alboteanu	82
<i>Configuration of SCADA System Graphical User Interface for Electrical Station</i> – Cosmin-Ionuț Toma, Mihaela Popescu, Mihăiță Daniel Constantinescu, Gabriel Cosmin Buzatu	88
<i>Small Scale Models of Solar Tracking Systems</i> – Ionel Laurentiu Alboteanu, Cristian Bratu, Florin Ravigan	95

On the Induction Motor Rotor Flux Estimation in the Electric Traction Systems with Rotor Flux-Oriented Control

Mihaela Popescu*, Alexandru Bitoleanu*, Constantin Vlad Suru* and Tudor Mătuşa*

* University of Craiova, Faculty of Electrical Engineering, Craiova, Romania, mpopescu@em.ucv.ro

Abstract - Characterized by very good performance in both steady-state and dynamic regimes and also by a relatively simple control structure, the induction motor control with rotor flux orientation is frequently adopted in electric drive systems, especially in electric traction applications. This paper analyses the possibilities of rotor flux estimation in a real Romanian electric traction system of locomotives. Thus, to estimate the magnitude of rotor flux and the angular position of the rotor flux vector, two possibilities are identified and discussed. First, the use of the sensed speed and stator currents is taken into consideration, and then the use of the measured supply voltages and the stator currents is the second alternative. Dedicated algorithms were designed for their related control. Both variants are analyzed through the results of the simulations obtained based on the specific models created in the Matlab/Simulink software. Four values of the imposed speed are taken into account in the performed analysis. It is highlighted that, in real conditions where the drive system is provided with speed sensor and there is no sine filter for the distorted motor supply voltage, the best option to estimate the rotor flux is to use the measured speed and the stator currents.

Cuvinte cheie: motor asincon, control cu orientare după fluxul rotor, estimarea fluxului rotor, tracțiunea electrică a locomotivelor, controlul vitezei.

Keywords: induction motor, rotor flux-oriented control, rotor flux estimation, locomotives electric traction, speed control.

I. INTRODUCTION

The field-oriented control method is one of the most used in the control of induction motors, ever since its proposal in the 1970s [1]. In short, to have good dynamic torque control as in the case of the direct current machine, the field-oriented control refers to the decoupling the torque and flux of the induction motor in a rotating reference frame. Clearly, the field-oriented control has much better performance compared to the classic V/f control [2]. The most common implementations consider the orientation according to the rotor flux. Using the components of the stator current in the rotating coordinates system (d, q) aligned with the rotor flux, the flux control is achieved by the d-axis current, whereas the torque control is achieved by the q-axis current. This control method is used in many applications, such as electric vehicles or traction applications [3]–[8].

To avoid using rotor flux sensors in the control scheme, the indirect control of the rotor flux is most often adopted, which involves the calculation of flux magnitude and its

position starting from the operating equations of the induction motor, through model-based estimators [9]–[12].

There are many flux estimation approaches in the literature, some of which are based on the stator model, while others on the rotor model. For example, the Gopinath observer consists of two open-loop estimators, based on the stator or rotor models, depending on the speed range [13], [14]. An existing alternative in the literature is the use of non-linear observers, especially based on the sliding-mode theory [13], [15], [16]. One of the concerns is increasing the level of robustness in relation to disturbances and variation of the induction motor parameters.

In order to increase the performance of the control system, one of the researchers' concerns is taking into consideration phenomena such as the magnetic saturation, the dependence of motor parameters on temperature and the iron losses [14], [18], [19]. As an adaption method for the estimation of the rotor time constant, the online tuning of this constant is proposed in [18], by using the voltage model of the induction motor, which does not depend on rotor time constant, as the rotor flux reference model. In [19], based on the steady state model of the electrical drive, it is proposed to eliminate the rotor time constant from the control algorithm.

It must be clearly taken into account that the choice of the suitable method for estimating the rotor flux depends on the concrete application of the vector control. Specifically, the requirements regarding the required performance and the existing hardware resources lead to the choice of the appropriate method.

This paper analyses the possible options for estimating the rotor flux in the case of the electric locomotive traction system with induction motor and rotor flux-oriented control, equipped with speed sensor and without sine wave output filter at the inverter output.

This real system belongs to a Romanian company dealing with the modernization of locomotives.

The paper is organized as follows. Section II presents the possibilities of estimating the rotor flux in the physical system taken into consideration. Then, the performance of the rotor flux estimation approaches is analyzed based on modeling and simulation in the Matlab/Simulink environment for different imposed motor speeds. Finally, Section IV concludes this paper.

II. POSSIBILITIES OF ESTIMATING THE ROTOR FLUX

To estimate the rotor flux in the real traction system taken into consideration, two possibilities were identified.

A. Estimation of the Rotor Flux Based on Speed and Stator Currents

When the rotor flux is estimated based on speed and stator currents, the block diagram in Fig. 1 highlights the speed control path followed by the active current (i_{sq}) control path. There is also the rotor flux control path followed by the reactive current (i_{sd}) control path. Each control path contains a controller of proportional-integral (PI) type, which provide the prescribed values of the active current and reactive current respectively.

The gating signals for the power semiconductor devices are provided by a three-phase hysteresis band current controller designed to have a limited switching frequency [4].

Because three coordinate systems are used (three-phase (a, b, c), orthogonal stationary (α, β) and orthogonal rotating (d, q)), the transformation of quantities from one reference frame to another is performed through blocks BT₁, BT₂ and BT₃, that materialize specific transformation expressions [8], [20].

The calculation of the rotor flux magnitude Ψ_r and its angular position (λ) is done in the block C Ψ , which has as inputs the components $i_{s\alpha}$ and $i_{s\beta}$ of the stator current vector and the sensed rotor speed (ω), as shown in Fig. 2. The following equations are involved [4], [8]:

$$\Psi_{r\alpha} = \int \left(-p\omega\Psi_{r\beta} - \frac{R_r}{L_r}\Psi_{r\alpha} + \frac{L_m R_r}{L_r} i_{s\alpha} \right) dt; \quad (1)$$

$$\Psi_{r\beta} = \int \left(p\omega\Psi_{r\alpha} - \frac{R_r}{L_r}\Psi_{r\beta} + \frac{L_m R_r}{L_r} i_{s\beta} \right) dt. \quad (2)$$

$$\Psi_r = \sqrt{\Psi_{r\alpha}^2 + \Psi_{r\beta}^2}. \quad (3)$$

$$\cos\lambda = \frac{\Psi_{r\alpha}}{\Psi_r}, \quad \sin\lambda = \frac{\Psi_{r\beta}}{\Psi_r}. \quad (4)$$

In the above equations, ($\Psi_{r\alpha}$, $\Psi_{r\beta}$) are the components of the rotor flux vector in (α, β) reference frame; L_m is the magnetization inductance; R_r and L_r are the total phase rotor resistance and inductance referred to the stator; ω is the rotor speed; p is the number of pole pairs; λ is the position angle of the rotor flux vector with respect to the α -axis.

As illustrated in Fig. 2, the magnetization inductance is estimated based on magnetization characteristic. Also, the dependence of the rotor resistance as a function of temperature is considered. For this, it is approximated that the temperature of the rotor is equal to that of the stator, which is measured by a temperature sensor.

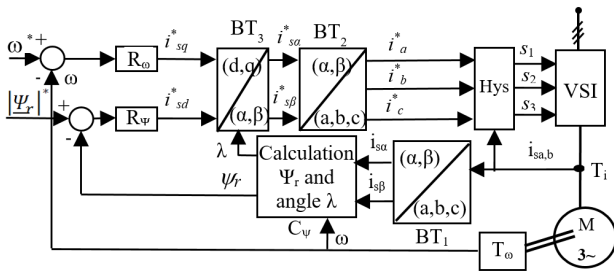


Fig. 1. Control block diagram of the induction motor, when the estimation of rotor flux is based on speed and stator currents.

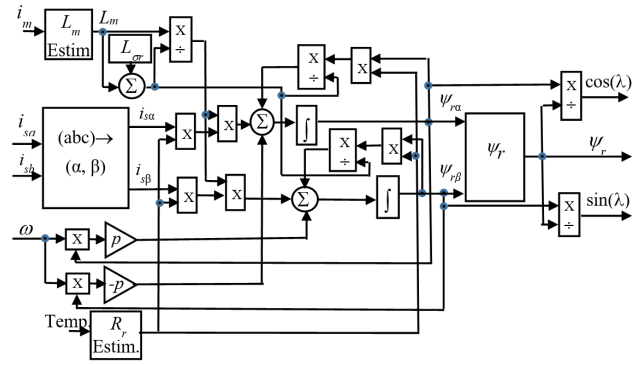


Fig. 2. The calculation of the rotor flux magnitude and its angular position based on speed and stator currents.

B. Estimation of the Rotor Flux Based on Voltages and Stator Currents

The associated control block diagram of the induction motor when the estimation of rotor flux is based on voltages and stator currents is shown in Fig. 3 and the specific structure of rotor flux calculation in Fig. 4 illustrates the following calculation expressions [8]:

$$\Psi_{s\alpha} = \int (v_{s\alpha} - R_s i_{s\alpha}) dt; \quad (5)$$

$$\Psi_{s\beta} = \int \int (v_{s\beta} - R_s i_{s\beta}) dt; \quad (6)$$

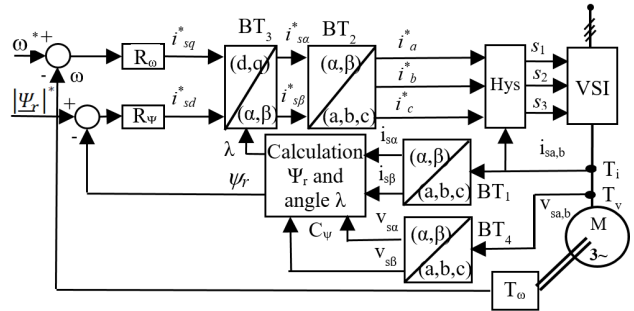


Fig. 3. Control block diagram of the induction motor, when the estimation of rotor flux is based on voltages and stator currents.

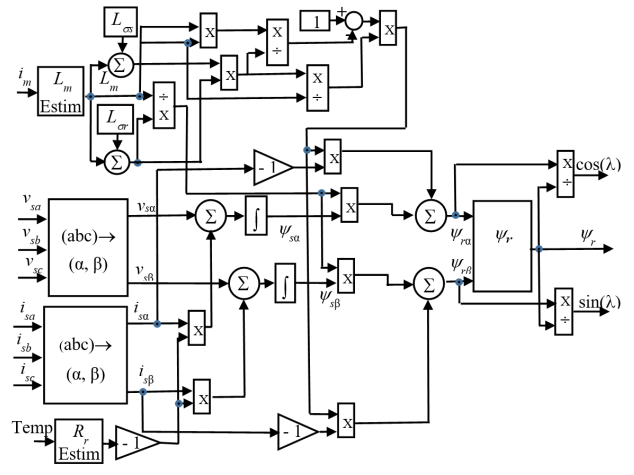


Fig. 4. The calculation of the rotor flux magnitude and its angular position based on voltages and stator currents.

$$\Psi_{r\alpha} = \Psi_{s\alpha} \frac{L_r}{L_m} - i_{s\alpha} \frac{L_s L_r}{L_m} \left(1 - \frac{L_m^2}{L_s L_r}\right); \quad (7)$$

$$\Psi_{r\beta} = \Psi_{s\beta} \frac{L_r}{L_m} - i_{s\beta} \frac{L_s L_r}{L_m} \left(1 - \frac{L_m^2}{L_s L_r}\right). \quad (8)$$

III. PERFORMANCE OF THE ROTOR FLUX ESTIMATION APPROACHES

In order to analyze the performance in the rotor flux-oriented control system applied in the field of electric traction of locomotives for the two flux estimation approaches, specific Simulink models were conceived and the simulation of the system operation at four imposed speeds was carried out. The main parameters of the real induction motor used in Romanian locomotives are summarized in Table I. It is noticed that the load torque taken into consideration has three components: a constant component; a component dependent on the speed; other component dependent on the square of the speed.

A. Case of Rotor Flux Estimation on the Basis of Speed and Stator Currents

1) Prescribed speed is $0.2\omega_N$

In the case of low speed ramp prescription ($0.2\omega_N$), the response of the control system (Fig. 5) shows a very faithful tracking of the prescribed speed by the actual speed. The steady state error is very low (about 0.4%).

The time evolutions of the load and motor torques (Fig. 6) illustrate that, after the end of the transient regime, the motor torque is practically equal to the load torque. Fig. 7 highlights the evolution of the estimated rotor flux and its prescribed value. It can be seen that, in steady state regime, the two values of the flux are practical the same (about 2.488 Wb). The operation of the system with rotor flux orientation is confirmed by the zero value of the q-axis component of the rotor flux.

Also, as shown in Fig. 8, the sinusoidal waveforms of the rotor flux components in the stationary reference frame axes (α and β) confirm the correct operation of the system. The stator current components in the rotating reference frame (d, q) are very close to the prescribed values during the whole operation (Fig. 9).

TABLE I.
MAIN PARAMETERS OF THE INDUCTION MOTOR USED IN ROMANIAN LOCOMOTIVES

U_N (V)	P_N (kW)	f_{1N} (Hz)	p	I_N (A)	n_N (rpm)	T_N (N·m)
1400	1150	62.5	3	576	1237	8877
R_1 (Ω)	$L_{\sigma 1}$ (mH)	R_2 (Ω)	$L_{\sigma 2}$ (mH)	R_m (Ω)	L_{mN} (mH)	
0.021	0.288	0.012	0.275	89.38	9.46	

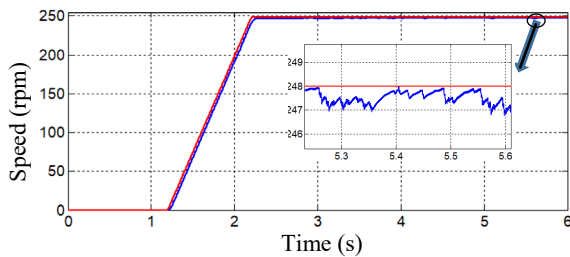


Fig. 5. Real speed (in blue) and prescribed speed (in red) in case of rotor flux estimation based on speed and stator currents, when $0.2\omega_N$ is prescribed.

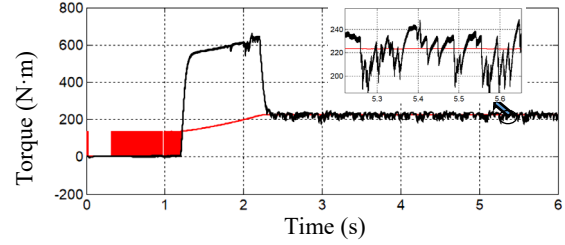


Fig. 6. Load torque (in red) and motor torque (in black) in case of rotor flux estimation based on speed and stator currents, when $0.2\omega_N$ is prescribed.

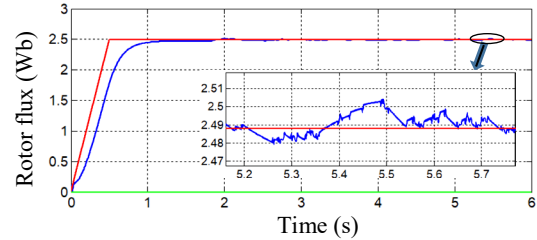


Fig. 7. Real rotor flux (in blue), prescribed rotor flux (in red) and q-axis component of the flux component (in green) in case of rotor flux estimation based on speed and stator currents, when $0.2\omega_N$ is prescribed.

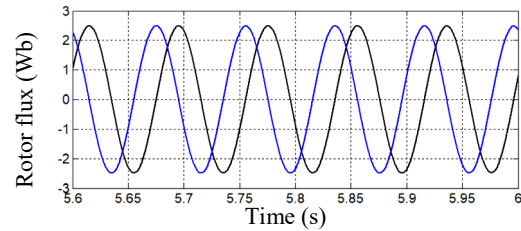


Fig. 8. α -axis component (in blue) and β -axis component of the rotor flux (in black) in case of rotor flux estimation based on speed and stator currents, when $0.2\omega_N$ is prescribed.

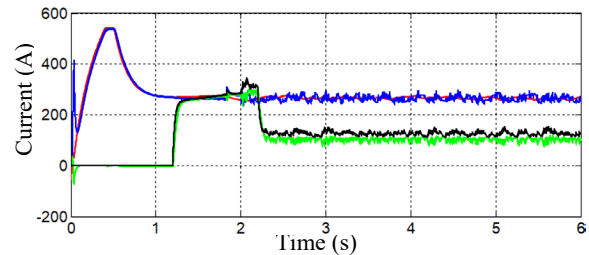


Fig. 9. Real i_{sd} (in blue); prescribed i_{sd} (in red); real i_{sq} (in green); prescribed i_{sq} (in black) in case of rotor flux estimation based on speed and stator currents, when $0.2\omega_N$ is prescribed.

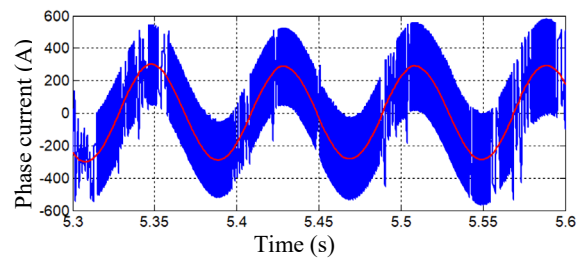


Fig. 10. Stator phase current (in blue) and its prescribed value (in red) in case of rotor flux estimation based on speed and stator currents, when $0.2\omega_N$ is prescribed.

Although it follows the sinusoidal evolution of the prescribed current, the stator current has a high degree of harmonic distortion at this low speed (Fig. 10).

2) Prescribed speed is $0.6\omega_N$

The second value of the prescribed speed taken into consideration is 740 rpm (about $0.6\omega_N$). First, the very good behavior of following the prescribed speed is highlighted (Fig. 11). The steady state error is below 0.14 %. The existence of a dynamic torque throughout the acceleration period followed by reaching the load torque are illustrated in Fig. 12. The prescribed rotor flux is also very well followed by the real one (Fig. 13). The components (prescribed and real) of the stator current in the rotating reference frame (d, q) are illustrated in Fig. 14. They are very close in values. As shown in Fig. 15, the phase stator current still has a high level of distortion, but lower than at the speed of $0.2\omega_N$.

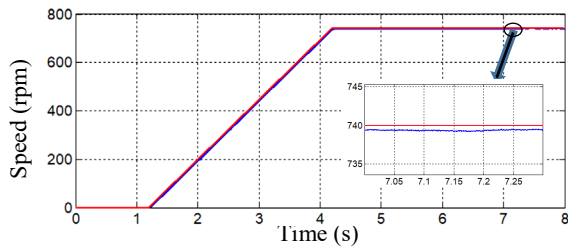


Fig. 11. Real speed (in blue) and prescribed speed (in red) in case of rotor flux estimation based on speed and stator currents, when $0.6\omega_N$ is prescribed.

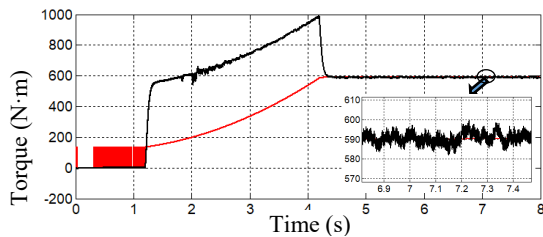


Fig. 12. Load torque (in red) and motor torque (in black) in case of rotor flux estimation based on speed and stator currents, when $0.6\omega_N$ is prescribed.

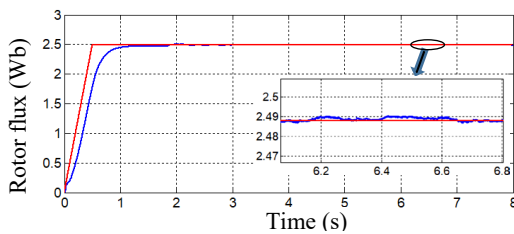


Fig. 13. Real rotor flux (in blue) and prescribed rotor flux (in red) in case of rotor flux estimation based on speed and stator currents, when $0.6\omega_N$ is prescribed.

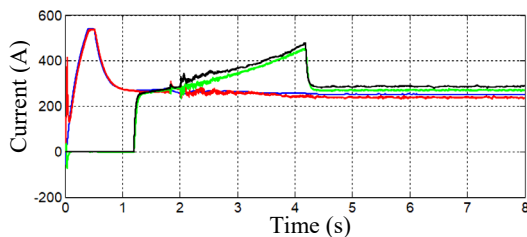


Fig. 14. Real i_{sd} (in blue); prescribed i_{sd} (in red); real i_{sq} (in green); prescribed i_{sq} (in black) in case of rotor flux estimation based on speed and stator currents, when $0.6\omega_N$ is prescribed.

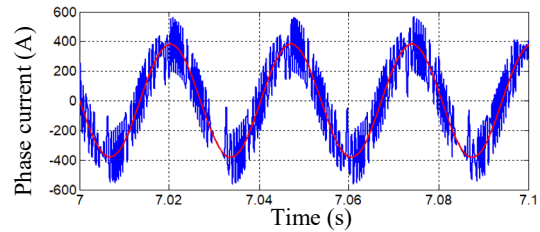


Fig. 15. Stator phase current (in blue) and its prescribed value (in red) in case of rotor flux estimation based on speed and stator currents, when $0.6\omega_N$ is prescribed.

3) Prescribed speed is ω_N

When the nominal value of the speed (1237 rpm) is prescribed, it is also accurately followed (Fig. 16). The load and motor torques are practically equal in steady state operation, as shown in Fig. 17. It can be seen that the imposed rotor flux is very well followed (Fig. 18).

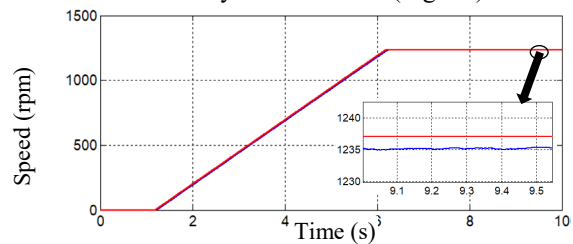


Fig. 16. Real speed (in blue) and prescribed speed (in red) in case of rotor flux estimation based on speed and stator currents, when ω_N is prescribed.

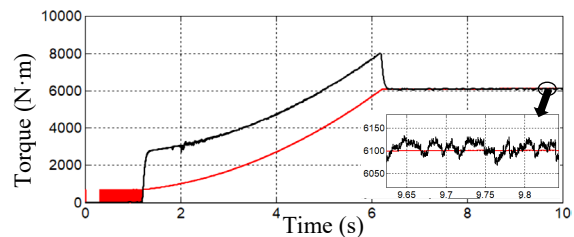


Fig. 17. Load torque (in red) and motor torque (in black) in case of rotor flux estimation based on speed and stator currents, when ω_N is prescribed.

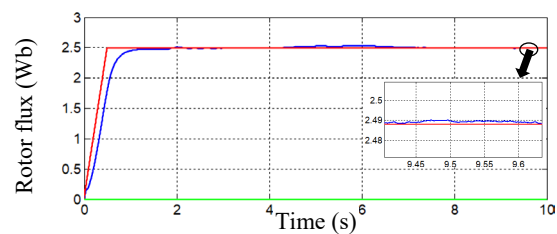


Fig. 18. Real rotor flux (in blue), prescribed rotor flux (in red) and q-axis component of the flux component (in green) in case of rotor flux estimation based on speed and stator currents, when ω_N is prescribed.

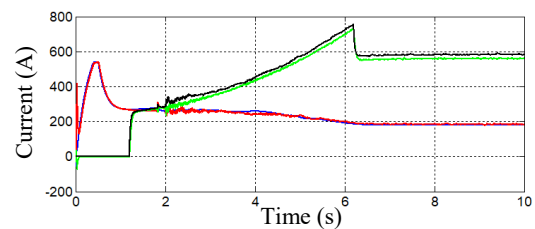


Fig. 19. Real i_{sd} (in blue); prescribed i_{sd} (in red); real i_{sq} (in green); prescribed i_{sq} (in black) in case of rotor flux estimation based on speed and stator currents, when ω_N is prescribed.

Fig. 19 shows the (d, q) stator current components and their prescribed values, which are very close to each other. As illustrated in Fig. 20, the magnetization inductance depends on the magnetization current. The stator current is closer to the prescribed value than at lower prescribed speeds (Fig. 21), with a lower total harmonic distortion factor (about 17%).

4) Prescribed speed is $1.6\omega_N$

The last value of the prescribed speed taken into consideration in the analysis is 1983 rpm (about $1.6\omega_N$). In this situation as well, the prescribed ramp speed is followed faithfully (Fig. 22). The equality between the torque developed by the induction motor and the load torque in steady state regime is very well illustrated in Fig. 23. At this high value of the prescribed speed, the prescribed rotor flux no longer has a constant value throughout the range of speed variation. It is 2.488 Wb when the speed is below the nominal value and then, it is reduced up to the value of 1.55 Wb, which is inversely proportional to the speed (Fig. 24). It can be seen that the real rotor flux accurately follows the prescribed value. The magnetization inductance evolution is shown in Fig. 25. The prescribed components of the stator current in the (d, q) reference frame are illustrated in Fig. 26 along with their real values, making evident very close values. From Fig. 27, it can be seen that the phase current is slightly more distorted than in the case of prescribing the nominal speed.

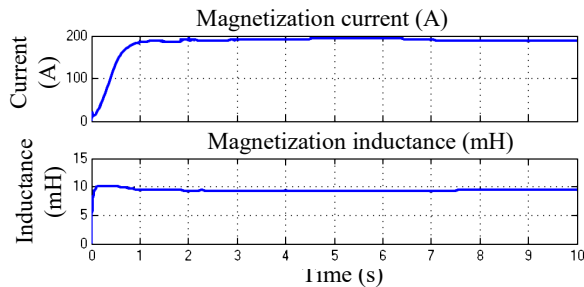


Fig. 20. Magnetization inductance in accordance with the magnetization current in case of rotor flux estimation based on speed and stator currents, when ω_N is prescribed.

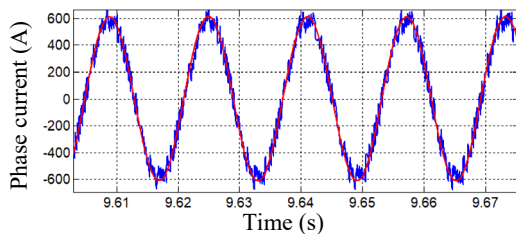


Fig. 21. Stator phase current (in blue) and its prescribed value (in red) in case of rotor flux estimation based on speed and stator currents, when ω_N is prescribed.

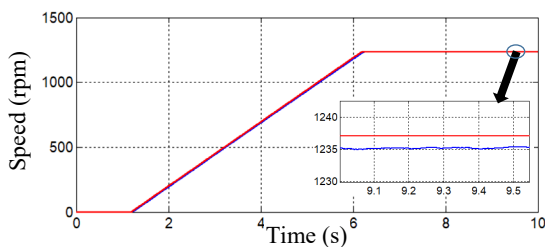


Fig. 22. Real speed (in blue) and prescribed speed (in red) in case of rotor flux estimation based on speed and stator currents, when $1.6\omega_N$ is prescribed.

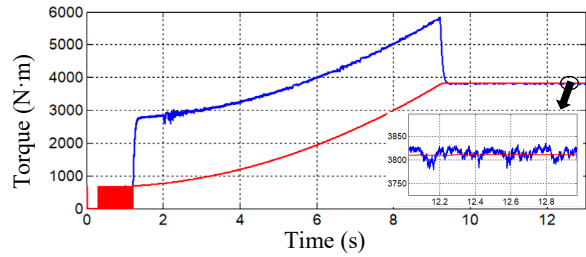


Fig. 23. Load torque (in red) and motor torque (in black) in case of rotor flux estimation based on speed and stator currents, when $1.6\omega_N$ is prescribed.

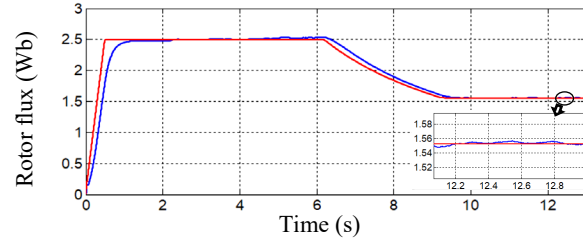


Fig. 24. Real rotor flux (in blue) and prescribed rotor flux (in red) in case of rotor flux estimation based on speed and stator currents, when $1.6\omega_N$ is prescribed.

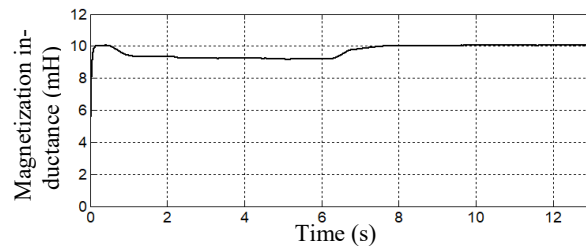


Fig. 25. The magnetization inductance evolution in case of rotor flux estimation based on speed and stator currents, when $1.6\omega_N$ is prescribed.

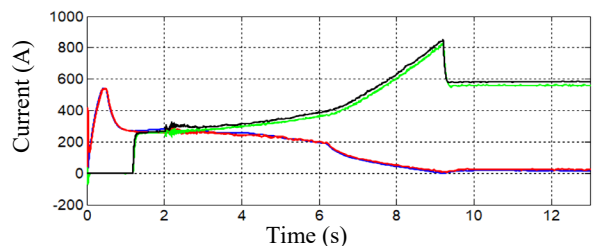


Fig. 26. Real i_{sd} (in blue); prescribed i_{sd} (in red); real i_{sq} (in green); prescribed i_{sq} (in black) in case of rotor flux estimation based on speed and stator currents, when $1.6\omega_N$ is prescribed.

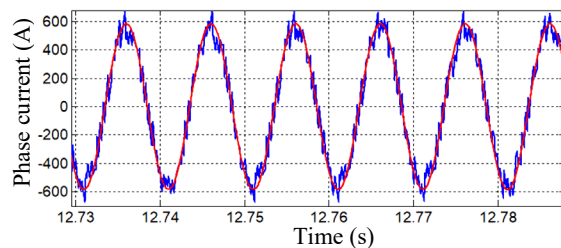


Fig. 27. Stator phase current (in blue) and its prescribed value (in red) in case of rotor flux estimation based on speed and stator currents, when $1.6\omega_N$ is prescribed.

B. Case of Rotor Flux Estimation on the Basis of Voltages and Stator Currents

As stated previously, other possibility for estimation the rotor flux consists in using the measured voltages instead the measured speed.

It should be mentioned that this version faces difficulties in implementation because the voltage supplied by the inverter is much distorted and its precise measurement is not simple. Moreover, there is no voltage sensor in the physical system on which the proposed control will be implemented.

However, by simulation, for all the prescribed speeds taken into consideration, it is shown that the estimated rotor flux is very close to the one obtained in the case of rotor flux estimation on the basis of measured speed and stator currents. Fig. 28, Fig. 29, Fig. 30 and Fig. 31 illustrate the estimated rotor flux for the four prescribed speeds ($0.2\omega_N$, $0.6\omega_N$, ω_N and $1.6\omega_N$) compared with those estimated through the other method.

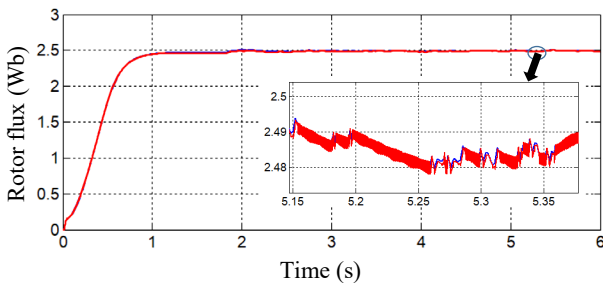


Fig. 28. Prescribed rotor flux in case of rotor flux estimation based on speed and stator currents (in blue) and in case of rotor flux estimation based on voltages and stator currents (in red), when $0.2\omega_N$ is prescribed.

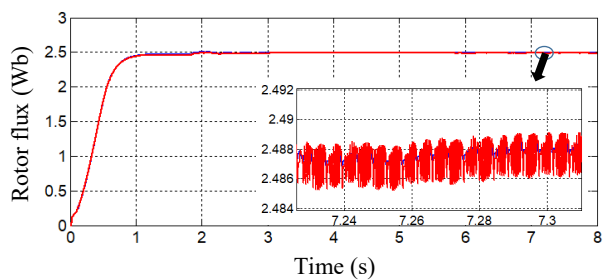


Fig. 29. Prescribed rotor flux in case of rotor flux estimation based on speed and stator currents (in blue) and in case of rotor flux estimation based on voltages and stator currents (in red), when $0.6\omega_N$ is prescribed.

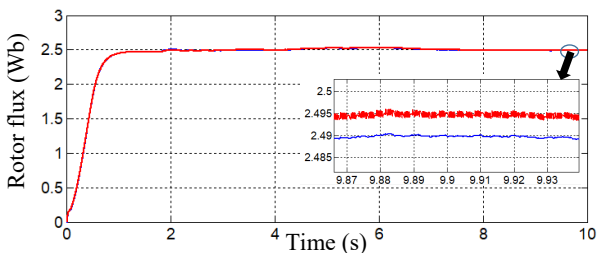


Fig. 30. Prescribed rotor flux in case of rotor flux estimation based on speed and stator currents (in blue) and in case of rotor flux estimation based on voltages and stator currents (in red), when ω_N is prescribed.

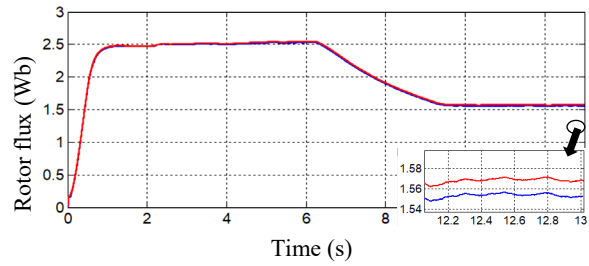


Fig. 31. Prescribed rotor flux in case of rotor flux estimation based on speed and stator currents (in blue) and in case of rotor flux estimation based on voltages and stator currents (in red), when $1.6\omega_N$ is prescribed.

If the values of the prescribed rotor flux calculated by the two methods are compared, it can be seen that, although they are very close, there are small oscillations of the prescribed flux in the case of rotor flux estimation based on voltages and stator currents, especially at low speeds (Fig. 28, Fig. 29, Fig. 30 and Fig. 31).

A possible alternative to measuring the distorted voltage could be its generation based on the inverter's IGBTs control signals.

When the waveforms of the measured and generated phase voltage are analyzed (Fig. 32), they appear to be identical at first glance.

Nevertheless, when the difference between the two-phase voltages is calculated, its time evolution (Fig. 33) shows that the phase voltage generated from IGBTs control signals is not very accurate.

As a natural consequence, the rotor flux estimated by using the calculated phase voltages from the control signals of the IGBTs is not acceptable, because it has large and unacceptable pulsations (Fig. 34).

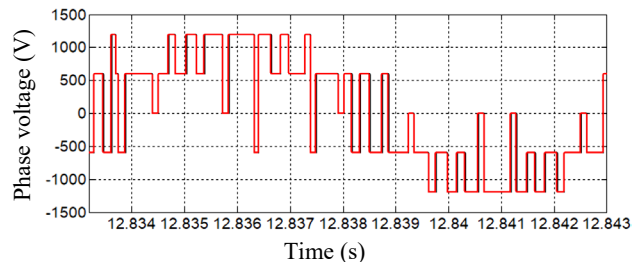


Fig. 32. Measured phase voltage (in red) and calculated phase voltage based on the control signals of the IGBTs (in black) when the prescribed speed is $1.6\omega_N$.

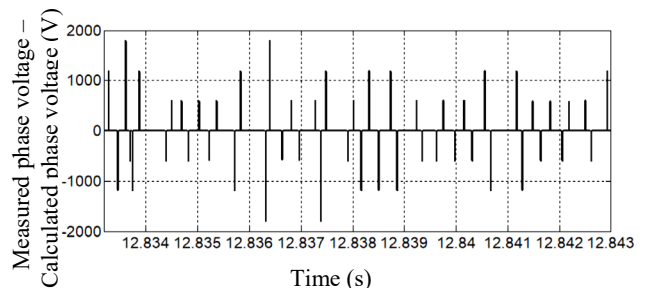


Fig. 33. Difference between the measured phase voltage and calculated phase voltage based on the IGBTs' control signals when the prescribed speed is $1.6\omega_N$.

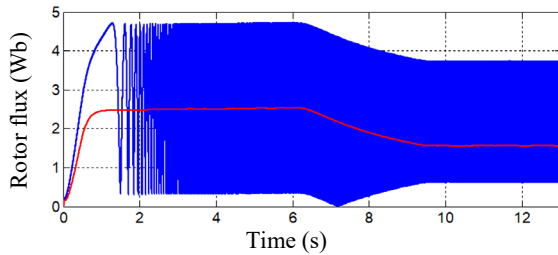


Fig. 34. Rotor flux (in blue) and its prescribed value (in red), when the rotor flux is estimated on the basis of the calculated phase voltage from the IGBTs' control signals and the prescribed speed is $1.6\omega_n$.

IV. CONCLUSIONS

From the analysis of the possibilities of estimating the rotor flux, it results that that use of the measured speed and stator currents leads to the best results, i.e. very good performance of the control system.

As a conclusion, it is the chosen method for rotor flux estimation, especially in the case of the induction motor used in the locomotive traction system on which vector control will be implemented.

The estimation of the rotor flux by using the IGBTs control signals is not a viable solution.

It is intended to implement the rotor flux-oriented control with rotor flux estimation based on the measured speed and stator currents for a railway traction motor in a Romanian company dealing with the modernization of locomotives.

Source of research funding in this article: Research program of the Department of Electromechanics, Environment and Applied Informatics, financed by the University of Craiova.

Contribution of authors:

First author – 50%

First coauthor – 20%

Second coauthor – 15%

Third coauthor – 15%

Received on October 29, 2023

Editorial Approval on November 30, 2023

REFERENCES

- [1] F. Blaschke, "A new method for the structural decoupling of ac induction machines," in *Conf.Rec.IFAC, Duesseldorf*, Germany, pp. 1-15, October 1971.
- [2] S. Laha, J. Dhali and P. K. Gayen, "Comparative performance between V/F and rotor flux-oriented controls of induction motor drive," in *Proc. 2023 IEEE Devices for Integrated Circuit (DevIC)*, Kalyani, India, 2023, pp. 1-6.
- [3] L. Di Leonardo, M. Popescu, M. Tursini and M. Villani, "Finite elements model co-simulation of an induction motor drive for traction application," in *Proc. 45th Annual Conference of the IEEE Industrial Electronics Society (IECON 2019)*, Lisbon, Portugal, 2019, pp. 1059-1065.
- [4] M. Popescu, A. Bitoleanu and C.V. Suru, "Synthesis of rotor field-orientation control for induction traction motor," in *Proc. 2021 International Conference on Applied and Theoretical Electricity (ICATE)*, Craiova, Romania, 2021, pp. 1-6.
- [5] I. Zhurov, S. Bayda and S. Florentsev, "Field-oriented control of the induction motor as part of the shunting locomotive powertrain considering core losses and magnetic saturation," in *Proc. 29th International Workshop on Electric Drives: Advances in Power Electronics for Electric Drives (IWED 2022)*, Moscow, Russian Federation, 2022, pp. 1-6.
- [6] L. di Leonardo, M. Popescu, G. Fabri and M. Tursini, "Performance evaluation of an induction motor drive for traction application," in *Proc. 45th Annual Conference of the IEEE Industrial Electronics Society (IECON 2019)*, Lisbon, Portugal, 2019, pp. 4360-4365.
- [7] M. Popescu, A. Bitoleanu and C. V. Suru, "Influence of locomotive wheels slipping on a traction system with rotor flux-oriented control and hysteresis current controllers," in *Proc. 2023 13th International Symposium on Advanced Topics in Electrical Engineering (ATEE 2023)*, Bucharest, Romania, 2023, pp. 1-6.
- [8] M. Popescu, A. Bitoleanu and C. V. Suru, "Estimation of the rotor flux in the traction systems with induction motors and field-oriented control," in *Proc. 14th International Conference and Exhibition on Electromechanical and Energy Systems (SIEMEN 2023)*, Chişinău, Moldova, 12-13 October 2023, pp. 1-6.
- [9] P. Mishra, R. Maheshwari and D. Patil, "Stabilization of rotor flux-oriented control of induction motor with filter by active damping," *IEEE Transactions on Industrial Electronics*, vol. 66, no. 12, pp. 9173-9183, Dec. 2019.
- [10] I. Ferdiansyah, L. P. S. Raharja, D. S. Yanaratri and E. Purwanto, "Design of PID controllers for speed control of three phase induction motor based on direct-axis current (Id) coordinate using IFOC," in *Proc. 4th International Conference on Information Technology, Information Systems and Electrical Engineering (ICITISEE)*, Yogyakarta, Indonesia, 2019, pp. 369-372.
- [11] Y. Zidani, A. Boulmane and D. Belkhatay, "Improvement of the indirect field oriented control for IM drives using fuzzy controllers," in *Proc. 6th International Conference on Electrical and Electronics Engineering (ICEEE)*, Istanbul, Turkey, 2019, pp. 45-49.
- [12] V. V. Puranik, V. N. Gohokar, "Simulation of an indirect rotor flux oriented induction motor drive using Matlab/Simulink," *International Journal of Power Electronics and Drive System (IJPEDS)*, vol. 8, no. 4, December 2017, pp. 1693-1704.
- [13] O. Buchholz and J. Böcker, "Gopinath-observer for flux estimation of an induction machine drive system," in *Proc. 2017 IEEE Southern Power Electronics Conference (SPEC)*, Puerto Varas, Chile, 2017, pp. 1-7.
- [14] S. Dutta, A. Yoo, Y. Shi and V. C. Peddi, "A comparison of induction machine rotor flux observers in stationary reference frame for rotor flux position estimation," in *Proc. 2022 IEEE Energy Conversion Congress and Exposition (ECCE)*, Detroit, MI, USA, 2022, pp. 1-8.
- [15] X. Huihui, Z. Feng, C. Wei, and P. Wei, "Study of a new rotor flux estimator for induction machine based on sliding mode control," in *Proc. IEEE Vehicle Power and Propulsion Conference (VPPC)*, Hangzhou, China, 2016.
- [16] H. Xie, F. Wang, W. Zhang, C. Garcia, J. Rodríguez and R. Kennel, "Sliding mode flux observer based predictive field oriented control for induction machine drives," in *Proc. 2020 IEEE 9th International Power Electronics and Motion Control Conference (IPEMC2020-ECCE Asia)*, Nanjing, China, 2020, pp. 3021-3025.
- [17] X. Wu et al., "Improved rotor flux observer with disturbance rejection for sensorless SPMSM control," *IEEE Transactions on Transportation Electrification*, 2023.
- [18] G. B. Reddy, G. Poddar and B. P. Muni, "Parameter estimation and online adaptation of rotor time constant for induction motor drive," *IEEE Transactions on Industry Applications*, vol. 58, no. 2, pp. 1416-1428, March-April 2022.
- [19] H. Swami and A. Kumar Jain, "Reducing dependency on rotor time constant in a rotor flux oriented vector controlled induction motor drive based on its static model," in *Proc. 2022 IEEE Electrical Power and Energy Conference (EPEC)*, Victoria, BC, Canada, 2022, pp. 430-437.
- [20] B. Kimiaghalam, M. Rahmani and H. Halleh, "Speed & torque vector control of induction motors with Fuzzy Logic Controller," in *Proc. 2008 International Conference on Control, Automation and Systems*, Seoul, Korea (South), 2008, pp. 360-365.

System for Monitoring Asynchronous Motors Powered at Variable Voltage

Monica-Adela Enache, Ion Vlad and Sorin Enache

University of Craiova/Faculty of Electrical Engineering, Craiova, Romania, senache@em.ucv.ro

Abstract – This paper presents some experimental aspects related to the operation of asynchronous motors powered at variable voltage. A modern system for actuation of low-power asynchronous motors is presented, equipped with a voltage and frequency converter. Also, a data acquisition system is presented, with a sampling frequency of up to 100 kHz, supervised by an acquisition program that allows the visualization of the variations of the main characteristic sizes of the motor. The program contains both graphic interfaces developed by the manufacturer and by the authors of the paper. This program solves, among other things, an electromagnetic compatibility problem. The experimental tests carried out with the help of this system (in permanent non-sinusoidal regime at various power supply frequencies) are detailed. Technical details of the main system components are provided. The tests are accompanied by photos taken during the experiments and many original explanatory graphics. The authors' contributions are mainly in the software area. Thus, in the original program, a series of windows for harmonic analysis and visualization of the characteristic phasors of the analyzed electrical quantities were implemented. The paper ends with the main conclusions resulting from the completion of the study and with a representative bibliography.

Cuvinte cheie: motor asincron, convertor de tensiune, sistem de achizitie de date, program de monitorizare, analiza armonica.

Keywords: asynchronous motor, voltage converter, data acquisition system, monitoring program, harmonic analysis.

I. INTRODUCTION

In practice, there are many situations that require adjusting the speed of asynchronous motors.

Among these, the most used are those that use voltage and frequency converters, or only voltage converters, which are the subject of an impressive number of papers published at prestigious conferences [1], [2], [3].

Dedicated data acquisition systems [4], [5], [6], with high sampling frequencies, can be used to monitor them.

The present paper belongs to this field.

A modern monitoring system for low-power electric machines is presented, with an application for an asynchronous motor with short-circuited rotor fed from a variable voltage source [7], [8].

A graphic interface that solves, among other things, an electromagnetic compatibility problem is detailed.

II. TEST STAND

The test stand used (sampling rates 100 kHz) was presented in detail in the paper [9].

From the multitude of blocks available, to complete the detailed research in this paper, the blocks from figures 1-5 were used.



Fig. 1. Overview.

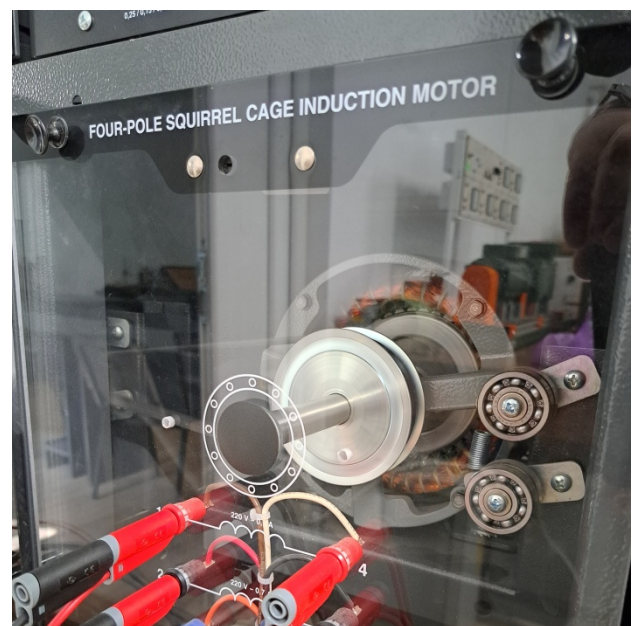


Fig. 2. Asynchronous Motor block.

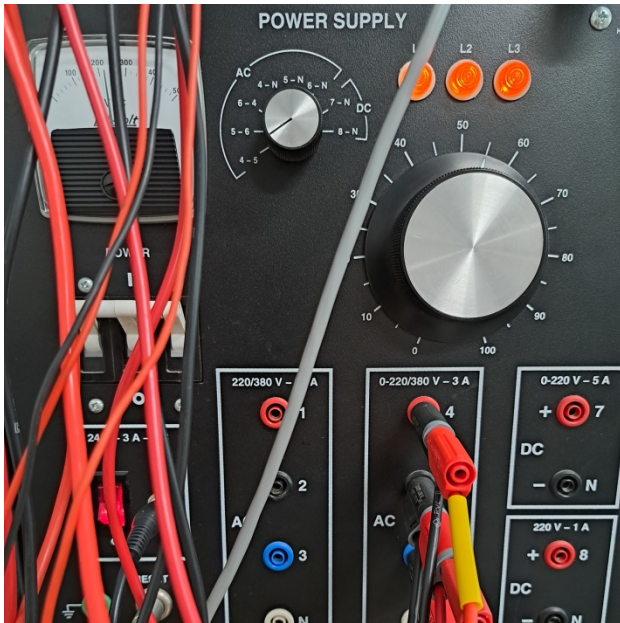


Fig. 3. Power Supply block.



Fig. 4. Dynamometer block.



Fig. 5. The Data Acquisition Interface block.

III. ASSEMBLY DIAGRAM AND MONITORING WINDOWS

To carry out the experiments, the mounting scheme from figure 6 was used.

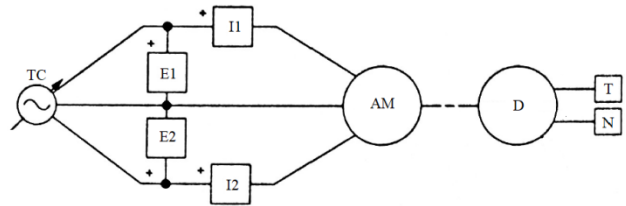


Fig. 6. Mounting scheme.

The meanings of the notations are the following:

- AM – asynchronous motor;
- D – dynamometer;
- TC – voltage converter;
- E1, E2 – voltage transducers;
- I1, I2 – current transducers;
- T – torque transducer;
- N – speed transducer.

The system includes a monitoring program [10], with visualization and analysis windows also made by the authors. The most important windows are included in figure 7 (Metering, Phasor Analyser, Harmonic Analyser and Spectrum Analyser).

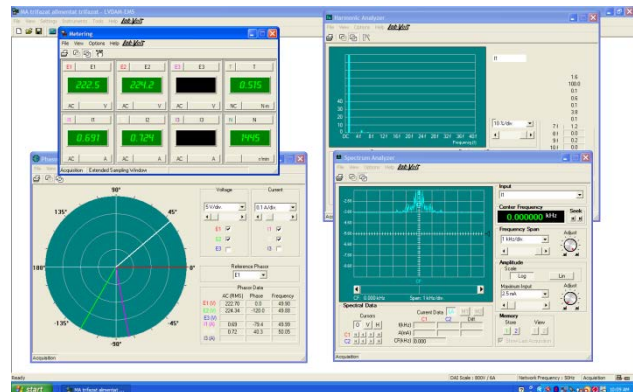


Fig. 7. The most important windows of the program.

Of these, the last three will be detailed for the practical situations considered relevant for the current research.

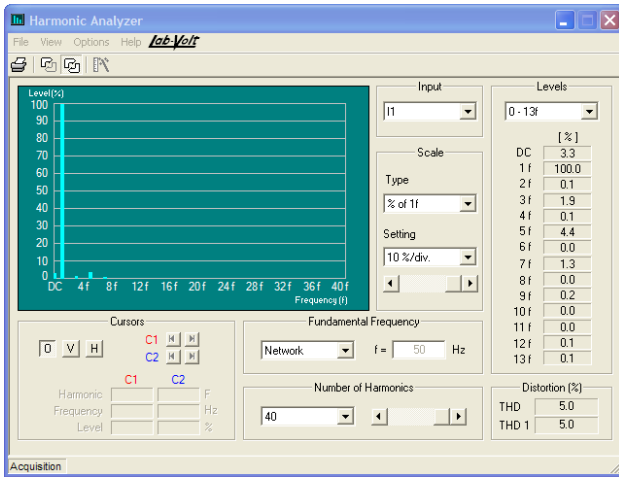
IV. EXPERIMENTAL DETERMINATIONS

With the help of the previously detailed assembly, a series of tests were carried out, considered relevant.

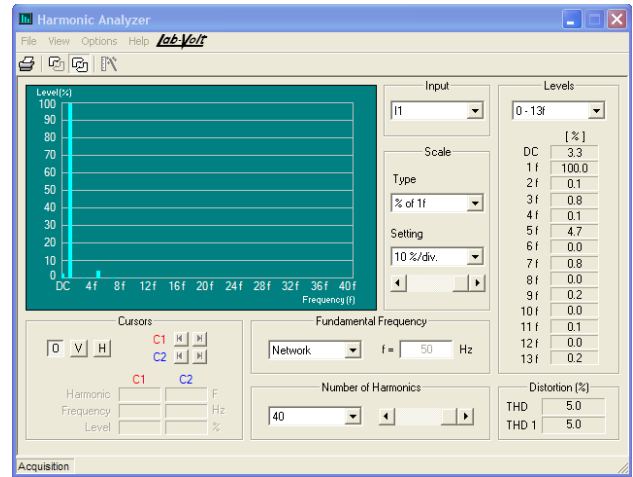
Three line voltages were preferred:

- 380 V (0 Nm and 1 Nm);
- 300 V (0 Nm and 1 Nm);
- 220 V (0 Nm and 1 Nm).

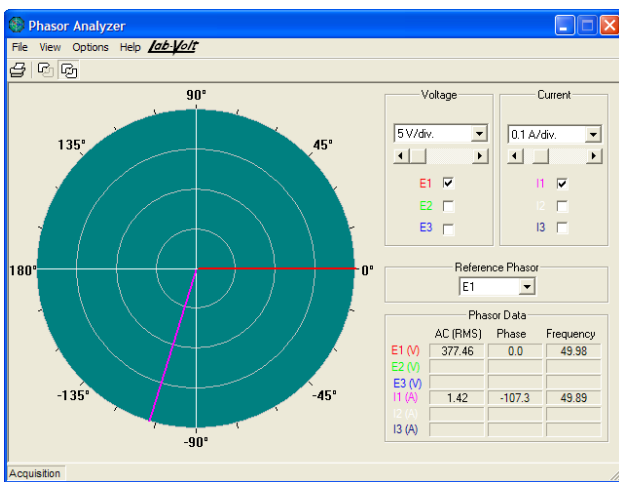
The graphic representations obtained are shown in figures 8, 9, 10, 11, 12 and 13.



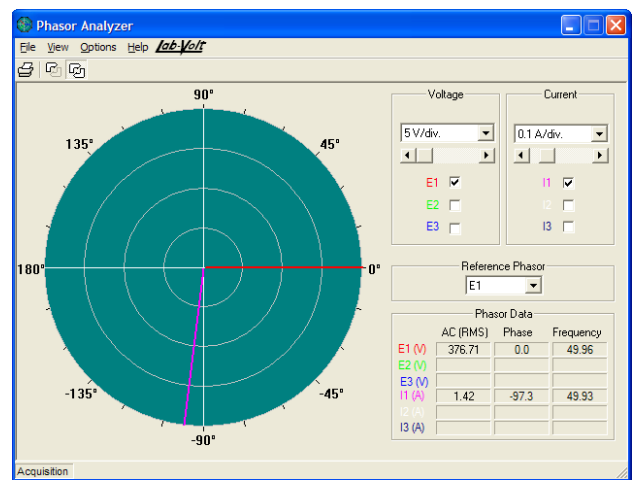
a)



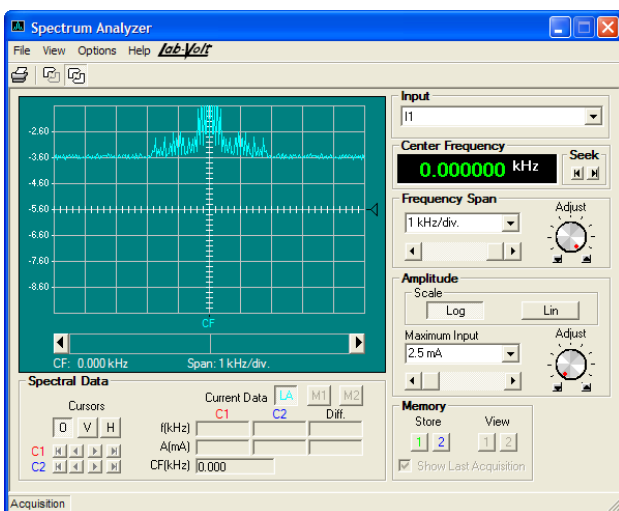
a)



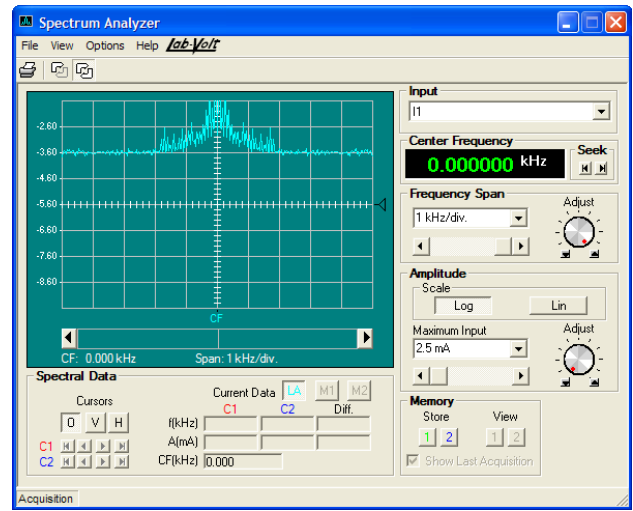
b)



b)



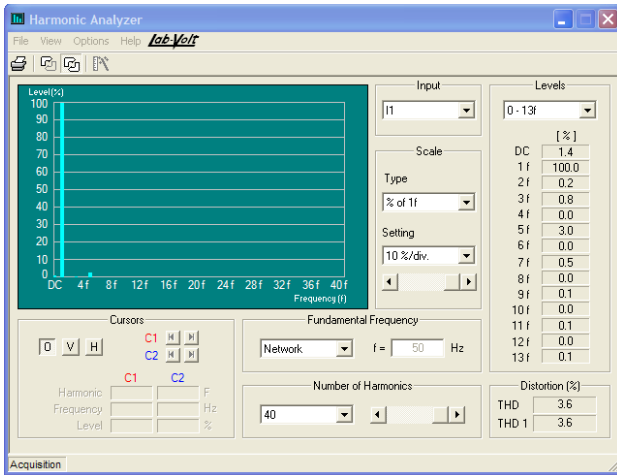
c)



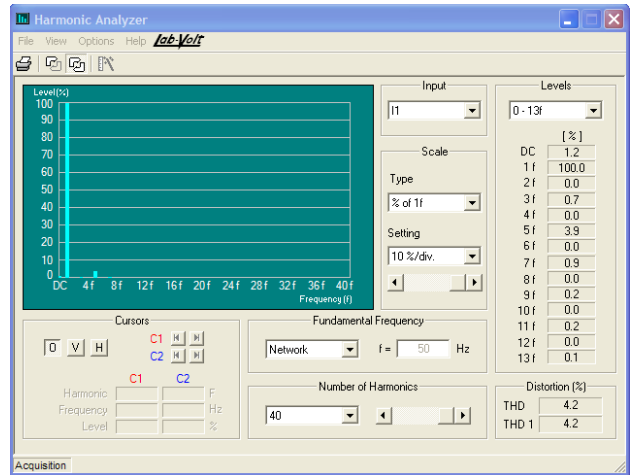
c)

Fig. 8. Representations obtained at 380 V, 0 Nm.

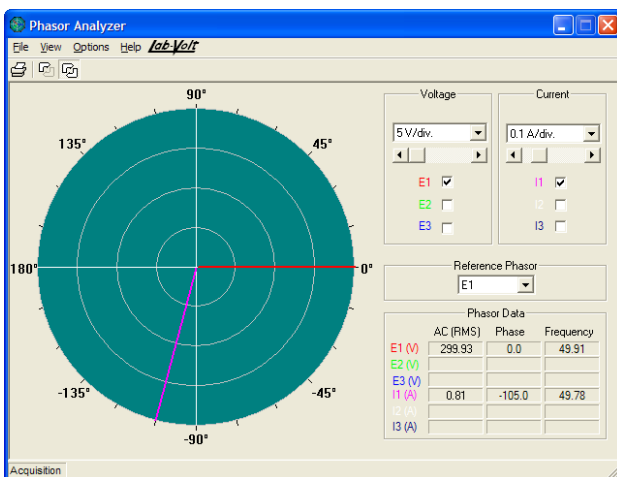
Fig. 9. Representations obtained at 380 V, 1 Nm.



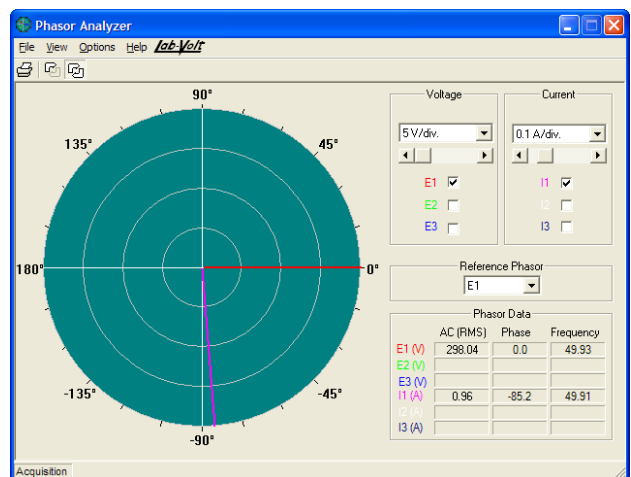
a)



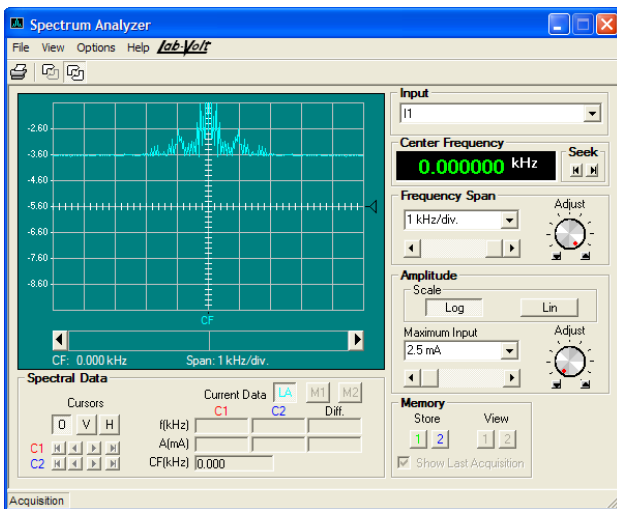
a)



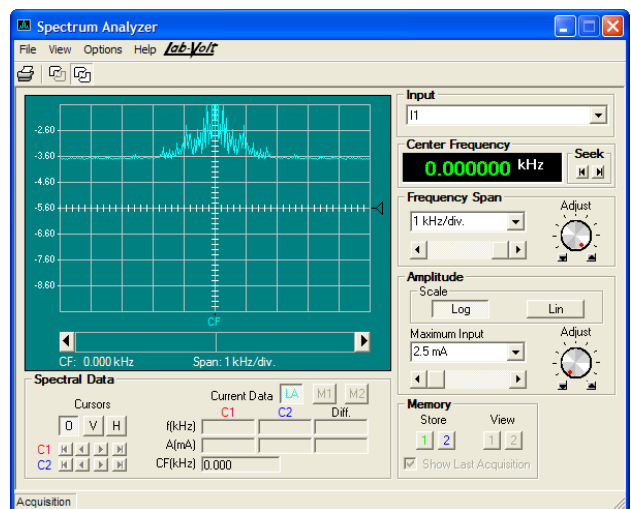
b)



b)



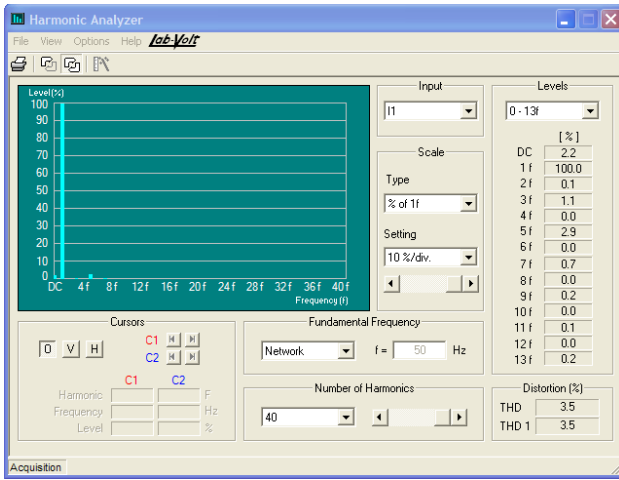
c)



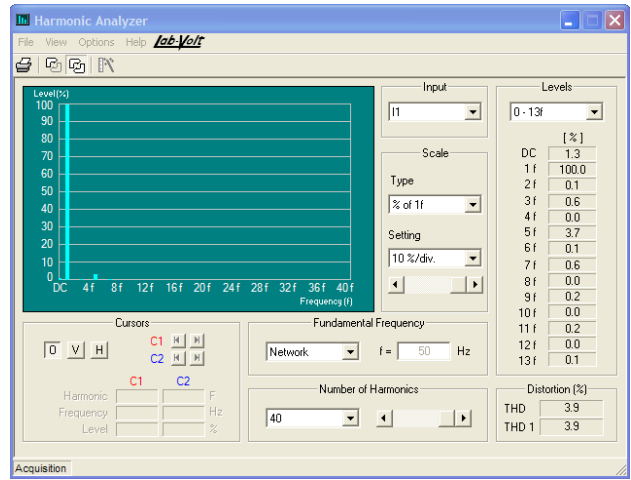
c)

Fig. 10. Representations obtained at 300 V, 0 Nm.

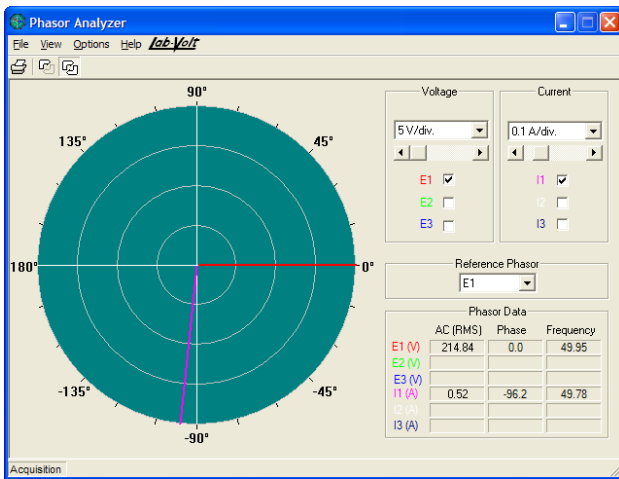
Fig. 11. Representations obtained at 300 V, 1 Nm.



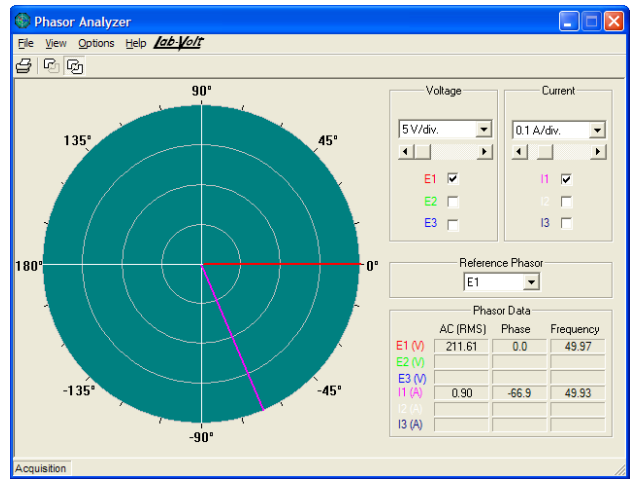
a)



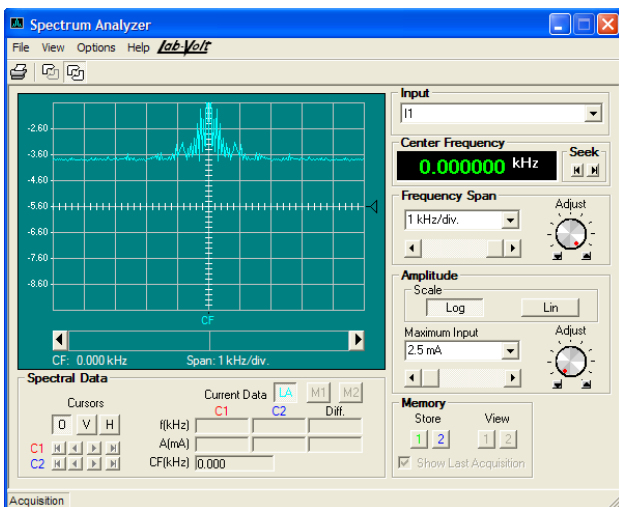
a)



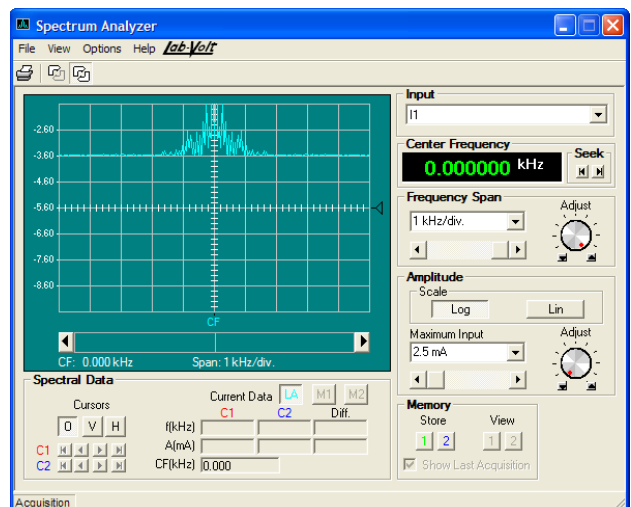
b)



b)



c)



c)

Fig. 12. Representations obtained at 220 V, 0 Nm.

Fig. 13. Representations obtained at 220 V, 1 Nm.

To facilitate the analysis of these representations, Table I was completed.

TABLE I.
CENTRALIZING DATA

Voltage [V]	Couple [Nm]	Harm. 3 [%]	Harm. 5 [%]	Harm. 7 [%]	The phase [o]
380	0	1,9	4,4	1,3	107,3
	1	0,8	4,7	0,8	97,3
300	0	0,8	3,0	0,5	105,0
	1	0,7	3,9	0,3	85,2
220	0	1,1	2,9	0,7	96,2
	1	0,6	3,7	0,6	66,9

V. CONCLUSIONS

The paper is an application of the use of a data acquisition and visualization program used on an actuation system with an asynchronous motor and variable voltage source.

Among the important contributions made by the authors in the paper, it should be stated that they added to the existing monitoring program, several modules for calculation and visualization of the phase shift angle of the phasors and harmonic analysis of non-sinusoidal quantities.

The program can be used in many practical situations (the paper presents a particular case considered to be representative).

Following the analyzes performed, according to Figures 8-13 and Table I, for the proposed application, the following conclusions were obtained:

- the current absorbed by the motor has a relatively important content of odd harmonics, in which the 5th order harmonic predominates;
- the importance of this harmonic increases as the load increases, regardless of the voltage value;
- for the other odd harmonics (the cases of the 3rd and 7th order harmonics were exemplified), as the load increases, their importance decreases;
- the phase shift angle between the current and the line voltage (obviously inductive), decreases when the load increases;
- the spectral analysis of the current highlights the important content of odd harmonics.

ACKNOWLEDGMENT

Source of research funding in this article: Research program of the Electrical Engineering Faculty financed by the University of Craiova.

Contribution of authors:

First author – 40%

First coauthor – 30%

Second coauthor – 30%.

Received on July 17, 2023

Editorial Approval on November 15, 2023

REFERENCES

- [1] C. Kang, F. Liu, "The design of material winding system based on tension control", *2021 IEEE 16th International Conference on Nano/Micro Engineered and Molecular Systems (NEMS)*, 2022.
- [2] B Tejaswini; E. Sheeba Percis, "Supremacy of Power Electronic Technologies and their Applications in Modern Operating Converters in Smart Grid", *2022 6th International Conference on Electronics, Communication and Aerospace Technology*, 2022.
- [3] H. Bouregba, M. Hachemi, S. Mekhilef, A. Ratni: "FFT analysis-based P&O with IC for 100 kW two stage grid-connected PV system: Comparative study", *2022 19th International Multi-Conference on Systems, Signals & Devices (SSD)*, 2022.
- [4] P. Deka, S. Deka, R. Kishore Roy, T. Bezboruah, "Development Of Weight Measurement System Based On Bend Sensor And Linear Compression Spring", *2023 4th International Conference on Computing and Communication Systems (I3CS)*, 2023.
- [5] H. Wu, Y. Liu, S. Ni, G. Cheng, X. Hu, "Loss Detection: Real-Time Packet Loss Monitoring System for Sampled Traffic Data", *IEEE Transactions on Network and Service Management*, Vol. 20, Issue 1, 2023.
- [6] M. Holub, O. Andrs, V. Stepanek, J. Kroupa, R. Huzlik, J. Tuma, J. Kovar, T. Marada, F. Bradac, "Experimental study of operational data collection from CNC machine tools for advanced analysis", *2022 20th International Conference on Mechatronics - Mechatronika (ME)*, 2022.
- [7] ***, *Virtual Laboratory and Equipments, User Guide*, Lab-Volt, 32359-E0, 2017.
- [8] ***, *Data Acquisition and Management System, User Guide*, Lab-Volt, 30328-E0, 2017.
- [9] S. Enache, A. Campeanu, I. Vlad, M. A. Enache, "Contributions Regarding Monitoring of Universal Fractional-Horsepower Commutator Motors", *Annals of Faculty of Engineering Hunedoara - International Journal of Engineering*, Tome XX [2022], Fascicule 4 [November], ISSN 1584-2665, pp. 175-178.
- [10] S. Enache, I. Vlad, M. A. Enache, "Program for Monitoring Operation Regimes of Low-Power Electrical Machines", *Annals of the University of Craiova, Electrical Engineering series*, No. 44, Issue 1, 2020, ISSN 1842-4805, pp. 55-60.

Influence of Electrical Circuit Parameter Changes on the Local Stability of a Three-Phase Cage Induction Motor Fed with Variable Frequency

Sorin Enache, Ion Vlad and Monica-Adela Enache

University of Craiova/Faculty of Electrical Engineering, Craiova, Romania, senache@em.ucv.ro

Abstract – The paper presents the mathematical support and the results of some simulations related to a new method of analyzing the stability of induction motors powered at variable frequency. After a brief introduction to the proposed issue, the mathematical model of the motor, written with relative values, is detailed. Taking this model as a starting point, a Matlab stability analysis program was created. By running this program, a series of graphs were obtained, detailed in the paper (two graphs are represented each, obtained for different conditions, which facilitate their comparison and obtaining conclusions). They refer to four specific cases regarding the modification of static inductance, rotor inductance, stator resistance and rotor resistance. Analyzing these graphs, the necessary conclusions were drawn. The conclusions are important, mainly in the design phase of the machine, to finalize the structure corresponding to the most stable operation of the drive system with asynchronous motor and static voltage and frequency converter. They highlight the influences of the most important parameters of the motor on the stability of the functioning of systems with such a structure. The paper ends with a representative bibliography for the proposed study.

Cuvinte cheie: motor asincron, frecventa variabila, stabilitate, model matematic, Matlab, simulari.

Keywords: induction motor, variable frequency, stability, mathematical model, Matlab, simulations.

I. INTRODUCTION

The problem of asynchronous motors powered at variable frequency is very topical due to the multiple practical applications that use this type of actuation [1]-[5], etc.

This all the more recently when there is a massive shift to the use of electric cars [6], [7], [8] etc.

The use of an unconventional power supply can lead to stability problems of the actuation system.

To avoid this problem, the stability analysis is required, the analysis quite popular in the current literature [9], [10], [11].

The present paper is part of this trend. The influences of the motor parameters on the stability are analyzed with the help of some modeling in the Matlab environment.

II. THE MATHEMATICAL MODEL IN RELATIVE VALUES

To achieve the proposed circuit, the mathematical model of the induction machine written in relative values was used [12].

The notations are those used in specialized literature:

$$\begin{aligned} \omega_s^* &= s_{ks}(\underline{\Psi}_s^* - k\underline{\Psi}_r^*) + \frac{d\underline{\Psi}_s^*}{dt^*} + j\omega_s^* \underline{\Psi}_s^* \\ 0 &= s_{kr}(\underline{\Psi}_r^* - k\underline{\Psi}_s^*) + \frac{d\underline{\Psi}_r^*}{dt^*} + j(\omega_s^* - \omega^*) \underline{\Psi}_r^* \\ h \cdot \frac{d\omega^*}{dt^*} &= -\frac{k}{x_{rt}^*} \text{Im}[(\underline{\Psi}_s^*)^* \underline{\Psi}_r^*] - m_r^* \end{aligned} \quad (1)$$

The condition is imposed that the pulsation changes in jumps with a small value.

In this case it is obtained:

$$\begin{aligned} \omega_s^* + \Delta\omega_s^* &= s_{ks}[\underline{\Psi}_s^* + \Delta\underline{\Psi}_s^* - k(\underline{\Psi}_r^* + \Delta\underline{\Psi}_r^*)] + \\ &+ \frac{d(\underline{\Psi}_s^* + \Delta\underline{\Psi}_s^*)}{dt^*} + j(\omega_s^* + \Delta\omega_s^*)(\underline{\Psi}_s^* + \Delta\underline{\Psi}_s^*) \\ 0 &= s_{kr}[\underline{\Psi}_r^* + \Delta\underline{\Psi}_r^* - k(\underline{\Psi}_s^* + \Delta\underline{\Psi}_s^*)] + \\ &+ \frac{d(\underline{\Psi}_r^* + \Delta\underline{\Psi}_r^*)}{dt^*} + \\ &+ j(\omega_s^* + \Delta\omega_s^* - \omega^* - \Delta\omega^*)(\underline{\Psi}_r^* + \Delta\underline{\Psi}_r^* + \Delta\underline{\Psi}_r^*) \end{aligned} \quad (2)$$

$$\begin{aligned} h \cdot \frac{d(\omega^* + \Delta\omega^*)}{dt^*} &= -\frac{k}{x_{rt}^*} \cdot \\ &\cdot \text{Im}\left\{(\underline{\Psi}_s^*)^* + \Delta(\underline{\Psi}_s^*)\right\} \cdot (\underline{\Psi}_r^* + \Delta\underline{\Psi}_r^*) - m_r^* \end{aligned}$$

The equations from (1) and (2) are processed accordingly.

It is obtained:

$$\begin{aligned} \Delta\omega_s^* &= (s_{ks} + j\omega_s^* + s) \cdot \Delta\underline{\Psi}_s^* - s_{ks} \cdot k \cdot \Delta\underline{\Psi}_r^* + \\ &+ j \cdot \underline{\Psi}_s^* \cdot \Delta\omega_s^* \\ 0 &= -s_{kr} \cdot k \cdot \Delta\underline{\Psi}_s^* + (s_{kr} + s) \Delta\underline{\Psi}_r^* + j(\Delta\omega_s^* - \Delta\omega) \underline{\Psi}_r^* \\ h \frac{d(\Delta\omega^*)}{dt^*} &= -\frac{k}{x_{st}^*} \text{Im}\left[(\underline{\Psi}_s^*)^* \cdot \Delta\underline{\Psi}_r^* + \underline{\Psi}_r^* \cdot \Delta(\underline{\Psi}_s^*)^*\right] \end{aligned} \quad (3)$$

(the operational variable was denoted with s).

In the following, a series of simplifications of the writing were made.

The following approximations can also be made:

$$j\underline{\Psi}_s^* = 1 \quad \text{and} \quad j\underline{\Psi}_r^* = k. \quad (4)$$

Under these conditions, the (3) relationships become:

$$0 = (s_{ks} + j\omega_s^* + s)\Delta\underline{\Psi}_s^* - s_{ks} \cdot k \cdot \Delta\underline{\Psi}_r^* \quad (5)$$

$$k(\Delta\omega^* - \Delta\omega_s^*) = -s_{kr} \cdot k \cdot \Delta\underline{\Psi}_s^* + (s_{kr} + s)\Delta\underline{\Psi}_r^*$$

Next, it is considered that the motor was running without load before changing the frequency.

In this case, due to the low frequency of the rotor current, its active component can be neglected.

So it can be written:

$$\Delta i_{dr}^* = \Delta i_{dr}^* + j\Delta i_{qr}^* \cong \Delta i_{dr}^* = \frac{\Delta\underline{\Psi}_r^* - k\Delta\underline{\Psi}_s^*}{dx_s^*} \quad (6)$$

By solving the system (5) relatively to $\Delta\underline{\Psi}_s^*$ and $\Delta\underline{\Psi}_r^*$ by replacing these relations in (6), after computations, it is obtained:

$$\Delta i_{dr}^* = \frac{s + j\omega_s^* + \varepsilon}{s^2 + (s_{ks} + s_{kr} + j\omega_s^*)s + s_{kr}(\varepsilon + j\omega_s^*)} \cdot k(\Delta\omega^* - \Delta\omega_s^*) \quad (7)$$

In the previous relation, the notation was used:

$$\varepsilon = (1 - k^2)s_{ks} = \frac{r_s^*}{x_s^*} = \frac{r_s^*}{x_r^*}. \quad (8)$$

When $\omega_s^* \geq 0,1$ it results that it can be considered (with approximation):

$$\left(\underline{\Psi}_s^*\right)^* = 1 \quad \text{and} \quad \underline{\Psi}_r^* = -jk \quad (9)$$

The Laplace transform is applied to relation (9).

It is obtained:

$$hs \cdot \Delta\omega^* = -\frac{k}{x_{st}^*} \text{Re}(\Delta\underline{\Psi}_r^* - k\Delta\underline{\Psi}_s^*), \quad (10)$$

The equivalent relation has the form:

$$hs \cdot \Delta\omega^* = -\frac{k}{x_{st}^*} \text{Re}(\Delta\underline{\Psi}_{dr}^* - k\Delta\underline{\Psi}_{ds}^*), \quad (11)$$

or:

$$hs \cdot \Delta\omega^* = -k\Delta i_{dr}^* \quad (12)$$

In what follows, using the previous relations, the stability of systems with such a structure will be analyzed.

III. STABILITY ANALYSIS

To analyze the stability of induction motors powered at variable frequency, a complex program was created [13].

The program, made in the Matlab environment, contains three modules that realize:

- the necessary calculations for the representations corresponding to the motor with real parameters;
- the necessary calculations for the representations corresponding to the motor with modified parameters;
- representation of comparative characteristics.

This program was used to study the influences of inductances (stator and rotor) and resistances (stator and rotor).

To carry out the simulations, a 1.1 kW induction motor with a short-circuited rotor was considered, with the following parameters:

$$R_s = 7,5 \, \Omega; \quad R_r' = 5,5 \, \Omega; \quad L_s = 0,529 \text{ H};$$

$$L_r' = 0,528 \text{ H}; \quad L_{sh} = 0,498 \text{ H}; \quad J = 0,004 \text{ kgm}^2.$$

The following numerical cases were considered:

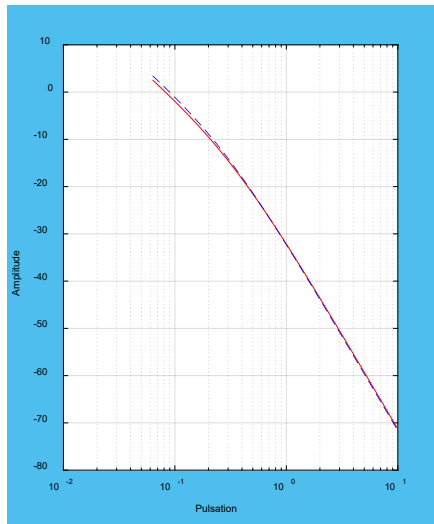
- A. Cases $L_s = 0,529 \text{ H}$, $L_s = 0,54 \text{ H}$;
- B. Cases $L_r = 0,528 \text{ H}$, $L_r = 0,54 \text{ H}$;
- C. Cases $R_s = 7,5 \, \Omega$, $R_s = 9 \, \Omega$;
- D. Cases $R_r = 5,5 \, \Omega$, $R_r = 7 \, \Omega$.

The graphs corresponding to the four cases are represented in figures 1-4.

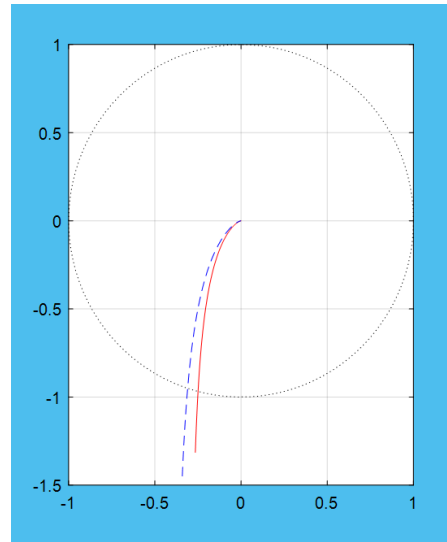
The following features are detailed:

- amplitude - pulsation;
- phase - pulsation;
- amplitude - phase;
- the hodograph.

A. Figures obtained for the case of changing the static inductance



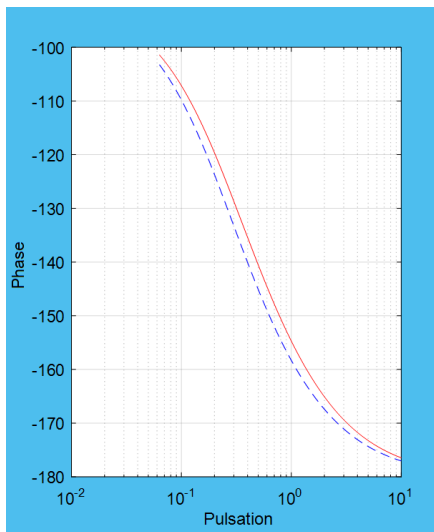
a)



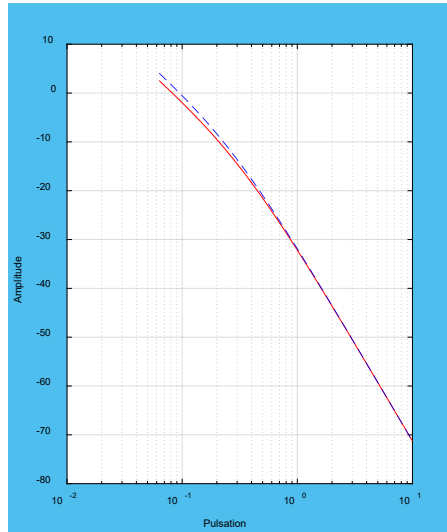
d) the hodograph

Fig. 1. Characteristics corresponding to the cases $L_s=0.529$ H (red), $L_s=0.54$ H (blue).

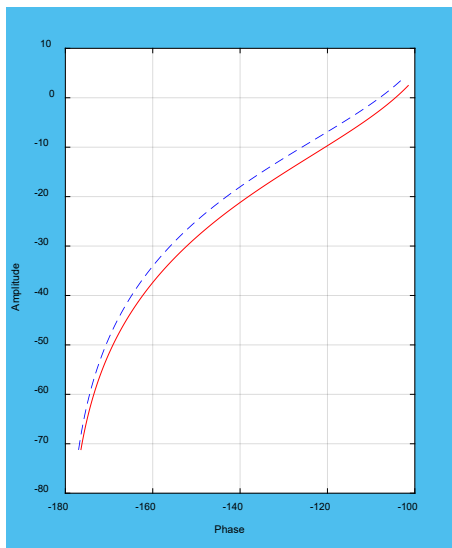
B. Figures obtained for the case of changing the rotor inductance



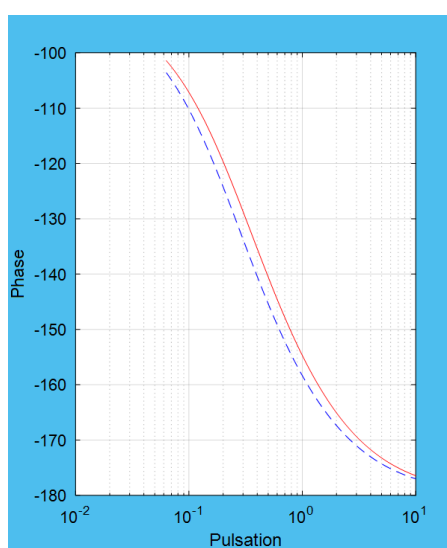
b)



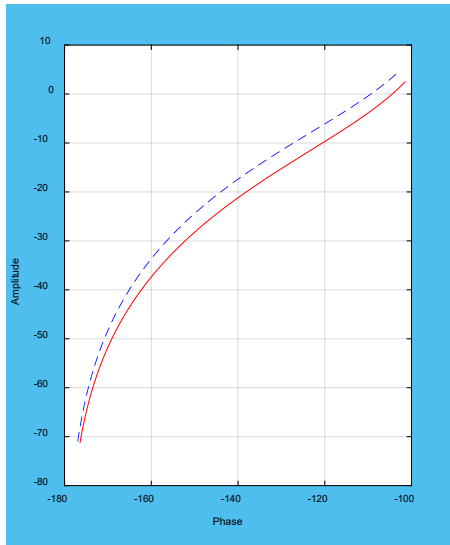
a)



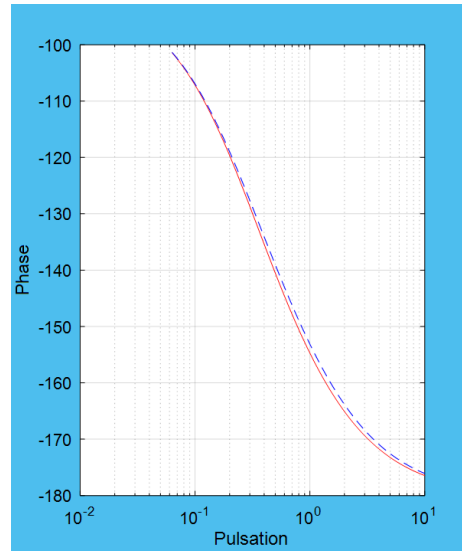
c)



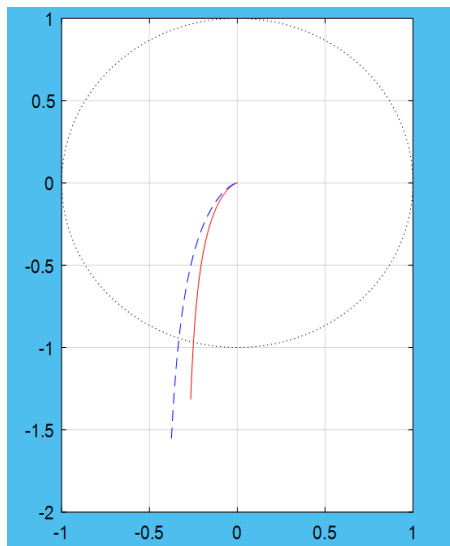
b)



c)



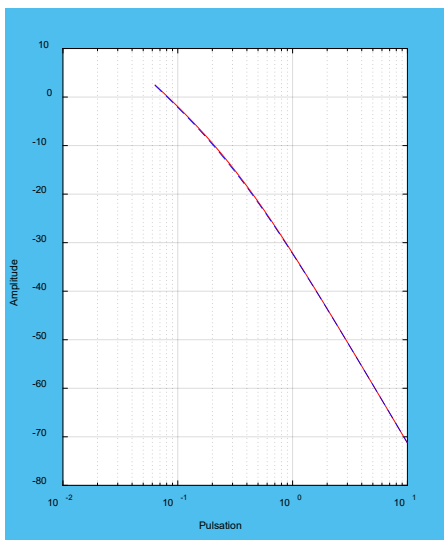
b)



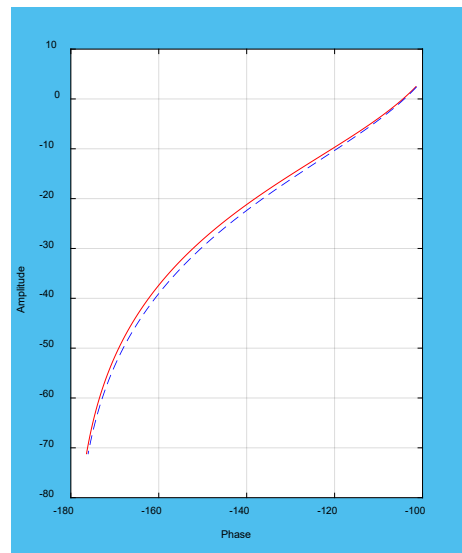
d) the hodograph

Fig. 2. Characteristics corresponding to the cases $L_r=0.528$ H (red), $L_r=0.54$ H (blue).

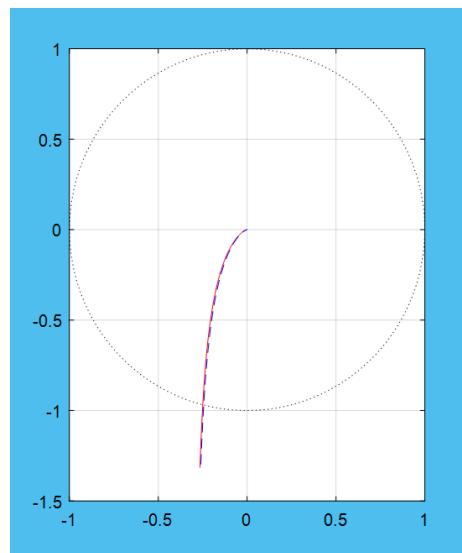
C. Figures obtained for the case of changing the stator resistance



a)



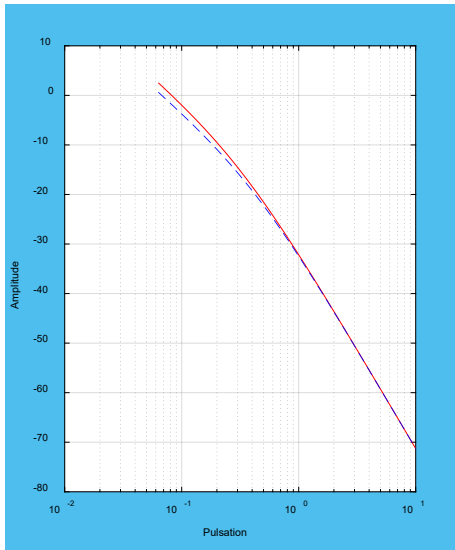
c)



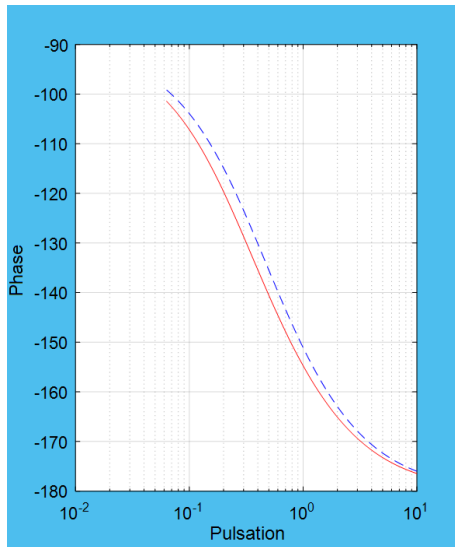
d) the hodograph

Fig. 3. Characteristics corresponding to the cases $R_s=7,5 \Omega$ (red), $R_s=9 \Omega$ (blue).

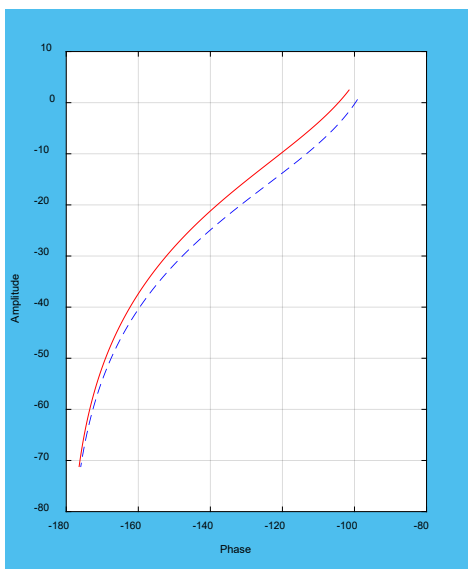
D. Figures obtained for the case of changing the rotor resistance



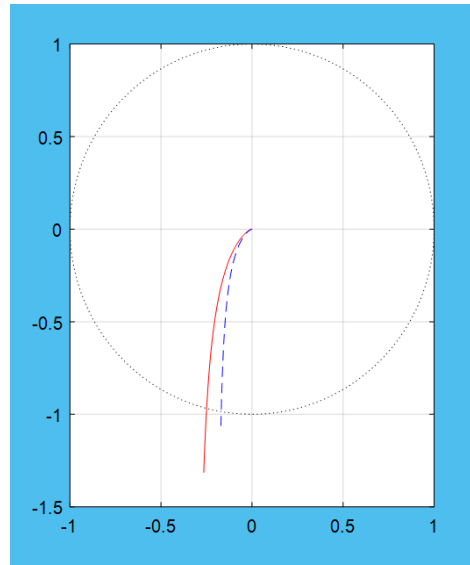
a)



b)



c)



d) the hodograph

Fig. 4. Characteristics corresponding to the cases $R_r=5,5 \Omega$ (red), $R_r=7 \Omega$ (blue).

IV. CONCLUSIONS

The characteristics in figures 1-4 provide a series of mathematical results, centralized in tables I and II.

TABLE I.
THE VALUES OF THE CHANGED PARAMETERS

Parameters	Abs. value	Phase margin
L_s	0,529	75,54
	0,54	71,94
L_r'	0,528	75,54
	0,54	70,62
R_s	7,5	75,54
	9	75,86
R_r'	5,5	75,54
	7	80,25

TABLE II.
THE PERCENTAGE VARIATIONS OF THE PARAMETERS

Parameters	Percent variation of the parameter	Percent variation of the phase margin
L_s	2,08	4,7
L_r'	2,27	6,5
R_s	20	1,3
R_r'	27,2	6,2

From the analysis of the previous results, the following conclusions were obtained:

- when the static inductance increases, the stability of the system decreases;
- when the rotor inductance increases, the stability also decreases;
- the increase in the value of the stator resistance determines the increase in stability;
- increasing the value of the rotor resistance also leads to increasing the stability of the system;
- the inductances influence the stability of the motor the most (with a plus for the rotor inductance);
- the smallest influence is the resistance of the stator winding.

ACKNOWLEDGMENT

Source of research funding in this article: Research program of the Electrical Engineering Faculty financed by the University of Craiova.

Contribution of authors:

First author – 40%;

First coauthor – 30%;

Second coauthor – 30%.

Received on July 10, 2023

Editorial Approval on November 29, 2023

REFERENCES

- [1] R.H. Nelson, T.A. Lipo, and P.C. Krause, "Stability analysis of a symmetrical induction machine," *IEEE Trans. Power App. Syst.*, vol. PAS-88, no. 11, pp. 1710–1717, Nov. 1969.
- [2] F. Fallside and A.T. Wortley, "Steady-state oscillation and stabilization of variable-frequency inverter-fed induction-motor drives," *Proc. IEE*, vol. 116, no. 6, pp. 991–999, Jun. 1969.
- [3] D.W. Novotny and J.H. Wouters, "Induction machine transfer functions and dynamic response by means of complex time variables," *IEEE Trans. Power App. Syst.*, vol. PAS-95, no. 4, pp. 1325–1335, Jul. 1976.
- [4] T.H. Chin, "Instability of variable frequency induction motor drives fed from voltage-source inverters," in *Conf. Rec. IEEE IAS Annu. Meeting*, 1985, pp. 704–709.
- [5] R. Ueda, et al., "Stability analysis in induction motor driven by V/f controlled general-purpose inverter," *IEEE Trans. Ind. Appl.*, vol. 28, no. 2, pp. 472–481, May 1992.
- [6] F. Xie, C. Qiu, Z. Qian, "Optimal Speed–Torque Control of Asynchronous Motor for Electric Cars in the Field-Weakening Region Based on Voltage Vector Optimization", *IEEE Transactions on Power Electronics*, Volume: 37, Issue: 1, 2022.
- [7] K. Ullah, M. Naeem, A. Hussain, M. Waqas, I. Haleemzai, "Evaluation of Electric Motor Cars Based Frank Power Aggregation Operators Under Picture Fuzzy Information and a Multi-Attribute Group Decision-Making Process", *IEEE Access*, Volume: 11, 2023.
- [8] M. S. Khan, A. Agrawal, "An Overview of Bi-Directional Charging Converter Topologies for Electric Vehicles and Fast Charging Stations analysis using Neural Network", *2023 International Conference on Computational Intelligence, Communication Technology and Networking (CICTN)*, 2023.
- [9] Ke Ji, "Harmonic Power Modeling for Converter-Driven Stability Study", *IEEE Transactions on Power Delivery*, 2023.
- [10] T. Wang, Y. Zhou, S. Yan, B. Wang, H. Zhang, "Output Impedance Modeling and Parameter Disturbance Stability Analysis of Photovoltaic Virtual Synchronous Generator", *2022 First International Conference on Cyber-Energy Systems and Intelligent Energy (ICCSIE)*, 2022.
- [11] Z. Xu, A. Zhang, R. Xu, X. Li, Y. He, X. Lei, "Research on Voltage Stability Control Method of SOFC Based on Fuzzy PI Algorithm", *2023 5th International Conference on Intelligent Control, Measurement and Signal Processing (ICMSP)*, 2023.
- [12] S. Enache, I. Vlad, *Induction machine. Basic notions. Dynamic processes*, Ed. Universitaria, Craiova, ISBN 973-8043-122-2, 2002.
- [13] S. Enache, I. Vlad, M. A. Enache, "Program for Monitoring Operation Regimes of Low-Power Electrical Machines", *Annals of the University of Craiova*, Electrical Engineering series, No. 44, Issue 1, 2020, ISSN 1842-4805, pp. 55-60.

Installation for Carrying out Thermal Tests on the Current Paths of Electrical Power Equipment

Gheorghe-Eugen Subțirelu*, Petre Pistol†, Adrian Vintilă†, Mihăiță Constantinescu*

* University of Craiova, Faculty of Electrical Engineering, Craiova, Romania, esubtirelu@em.ucv.ro

† National Institute for Research, Development and Testing in Electrical Engineering (ICMET) Craiova, Romania, petrepistol@icmet.ro

Abstract - Today's electrical networks, as part of the national power system, must meet a number of requirements imposed on power transmission and distribution equipment. The main requirements are: continuity of electricity supply to consumers, operational safety, quality of electricity supplied, development of networks, economic viability of investments, environmental impact requirements. In this context, the testing of the technical performance of the various elements that make up the electrical networks, both at the design stage and, in particular, at the certification stage, is of great importance and is regulated by internationally recognised technical standards and norms. The performance of tests under laboratory conditions requires the existence of specialised installations and equipment capable of generating the electrical parameters to which the various elements of electrical networks are subjected, for the purpose of performance testing and certification. The paper presents an installation for carrying out thermal tests on the current paths of electrical power equipment with a fully digital control system based on virtual instrumentation, which replaces the physical control panel made up of electronic modules and analogue devices. This enables the transition from primarily manual local control by the operator to remote control and eventually full automation of the thermal test process for medium and low voltage switchgear. By taking advantage of virtual instrumentation, the solution can be easily implemented and enhanced by integrating process control and computerisation applications.

Cuvinte cheie: curenți intensi, echipamente electrice de putere, instrumentație virtuală, sistem de comandă și control, teste de creștere a temperaturii.

Keywords: high currents, electrical power equipment, virtual instrumentation, command and control system, temperature rise tests.

I. INTRODUCTION

The temperature rise tests [1], [2] performed on low/medium voltage switchgear assemblies require a stable and highly efficient current source. The source should be capable of delivering a wide range of currents with greater accuracy than that required by the test standards [3]. There are several types of power supply suitable for the application, depending on the installed power, maximum current output and load voltage. Conventional sources use synchronous generators as voltage regulators, one for each phase of the source. These generators are simultaneously driven by a DC motor which sets the frequency of the voltages produced [4]. The effective value of the voltage, i.e. the currents generated by the source, is

controlled by the excitation currents of the three generators. This system has several drawbacks, including complex control and regulation of frequency and current amplitude, difficult maintenance, lower reliability, and operation with noise and mechanical vibration. Fig. 1 shows the schematic diagram of the installation for the thermal testing of the current paths of the electrical power equipment, in which the group of electrical machines is replaced by a set of three regulating autotransformers. The proposed installation is based on a three-phase stabilised AC power source capable of delivering high intensity 50 Hz sinusoidal currents, adjustable over a wide range, and is designed to perform temperature rise tests on low/medium voltage switchgear assemblies complying with SR EN 60439-1 and SR EN 62271-1.

The proposed installation includes, in addition to a stabilized AC power source, a computerized system for command, control, and regulation, as well as a system for measuring, acquiring, processing, and storing data that describes the thermal behavior of the tested equipment.

II. THREE-PHASE HIGH CURRENT SOURCE

A standard three-phase adjustable AC power source with automatic control consists of a source power scheme, a computerised control and automation system and a measurement, acquisition, processing and data storage system.

The main technical characteristics of the power source used in the electrical equipment testing laboratories are:

- rated supply voltage: 3 x 400Vac, 50Hz;
- rated installed power:
 - 225 kVA, three-phase balanced;
 - 75 kVA, single phase;
- maximum current per load: 10 kAef, for a balanced load with a maximum impedance of $6.5 \times 10^{-4} \Omega$.

A. Source power diagram

The power circuit of the adjustable three-phase AC power supply with automatic control is shown in Fig. 1 and includes:

1) Power supply cabinet (PSC)

The power supply cabinet is designed to supply the three-phase power circuit of the source as well as the control, measurement and protection circuits. It is equipped with a dedicated relay to monitor the power supply voltages from the low voltage network [5], [6].

2) Voltage regulating autotransformer group, type ATMU-75, consisting of three single-phase units

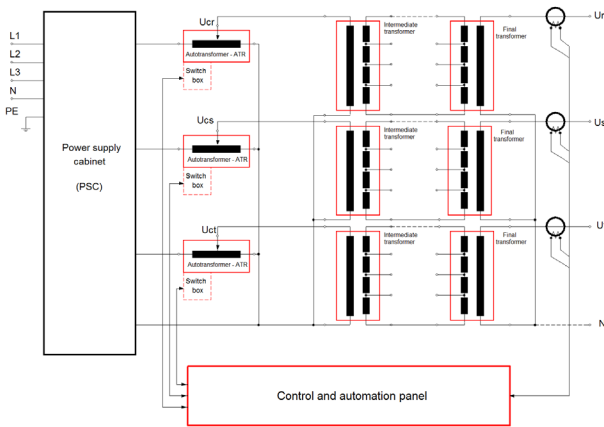


Fig. 1. Block diagram of the functions of the proposed system.

The three electrically controlled ATMU single-phase autotransformer units represent the elements of the power diagram that allow the control of the current flowing from the source. The autotransformers are oil cooled and have a unique design that is based on the magnetic flux beam splitting principle [7], [8] (Patent RO117053 (B1) / 28.09.2001, owned by ICMET Craiova). The design principle and construction details are presented in the following figures (Fig. 2...Fig. 5).

According to this principle, the voltage regulation step can be as small as desired without increasing the coil height. However, for technological reasons, it is limited to a maximum of 0.2 V, with a maximum voltage per turn of 2.4 V (voltage per turn in the classic design).

The voltage U_{AX1} obtained at the output terminals of the autotransformer is given by the relationship:

$$U_{AX1} = U_{AX} / N \cdot n + U_{AX1} / N \cdot k / K \quad (1)$$

where:

- U_{AX} is the nominal supply voltage of the autotransformer, i.e. 230V, 50Hz;
- N is the total number of turns of the autotransformer;

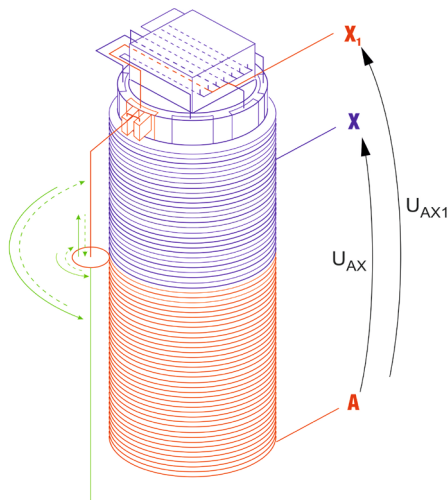


Fig. 2. Principle of beam splitting.

- n is the number of turns between the end A of the winding and the active roller of the current collector sliding shoe;
- K is the number of half-sections of the magnetic flux divider;
- k is the number of flux divider half-sections in the circuit of the last turn, corresponding to the position of the brush on the fixed collector.

$$n \leq N \quad (2)$$

$$k \leq K \quad (3)$$

The output voltage regulation step is given by the relationship:

$$\Delta U_{AX1} = U_{AX} / N \cdot 1/K \quad (4)$$



Fig. 3. Internal structure of the autotransformer showing the flux divider and slip ring collector.

Autotransformers are equipped with electrical systems to actuate and control the voltage and, implicitly, the slider position. The design principle and cursor position command and control allows the current source to introduce no harmonic distortion into the current waveform.



Fig. 4. Local autotransformer control and protection box.

The autotransformers have a high transformer ratio (230 V/0-250 V) and are equipped with local control and slider actuator protection boxes (Fig. 4), which allow:

- a) local *MANUAL* control of the slider;
- b) selection of the *LOCAL - REMOTE* control mode;
- c) autotransformer overload protection by monitoring the oil temperature in the tank;
- d) local monitoring and protection of the autotransformer drive system.



Fig. 5. Voltage regulating autotransformer group - three single-phase units.

3) Intermediate power transformer group, type TMAi-75 - three single-phase units

The three TMAi intermediate power transformers (Fig. 6) correspond to the voltage between the ATMU regulating autotransformers and the TMAf final transformers, in order to obtain accurate current regulation, corresponding to accuracy class 0.2, over a wide range of load impedances specific to the current paths inside the low and medium voltage distribution cabinets manufactured and tested by the beneficiary.

The intermediate transformers are air-cooled and the secondary is divided into four equal winding sections. The sections have the same rated current and can be connected in series, parallel or series-parallel by means of a manual selector with strap bands to obtain different transformation ratios.



Fig. 6. Intermediate power transformer group - three single-phase units.

4) Final power transformer group, type TMAf-75 - three single-phase units

The final power transformer block (Fig. 7) consists of three single-phase TMAf units. These transformers are air-cooled and the primary winding is divided into four equal sections, identical to the secondary windings of the TMAi transformers.

The sections have the same rated current and can be connected in series, parallel or series-parallel by means of a manual selector with strap bands to obtain different transformation ratios.



Fig. 7. Final power transformer group - three single-phase units

The high current secondary winding consists of three turns and is placed over the primary winding on the central column of the "shell" type magnetic core to optimise the electromagnetic coupling between the two windings.

The secondary winding consists of four copper bars, each 10x120 mm in cross section, arranged in parallel at a distance of 10 mm to optimise cooling. Additional cooling of the secondary windings is provided by a forced ventilation system, which is automatically controlled by a thermostat when the bar temperature exceeds 120° C, equivalent to insulation class F.

5) Busbar system

The source busbar system (Fig. 8) provides the transition of the source output terminals from the room where the power circuit elements are located to the adjacent room where the thermal tests on the distribution cabinets/cells are carried out. The 10,000/5A ratio current transformers used in the source control and automation circuit and the metering circuit are located on the system busbars. The bars are made from 10x120mm copper strips, arranged in parallel (across the width of the bar) 10mm apart to optimise cooling.



Fig. 8. Source output busbar system

III. COMPUTERISED COMMAND, CONTROL AND REGULATION SYSTEM

A. Hardware component of the system

Fig. 9 shows the hardware components of the proposed system [12].

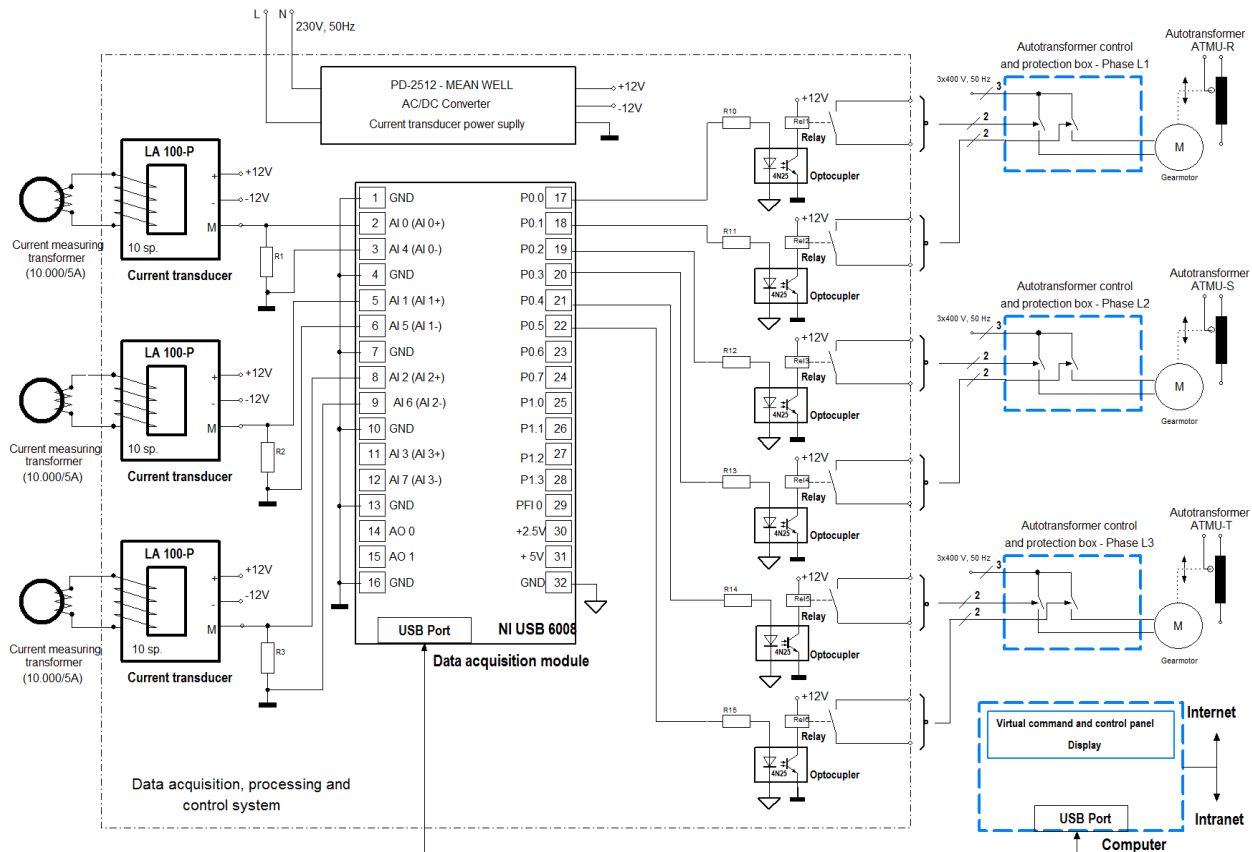


Fig. 9. Hardware component of the system.

The system hardware is built around a multifunctional DAQ device (NI-USB-6008). It provides analogue input/output capabilities, specifically 8 analogue inputs (12 bit, 10 kS/s), 2 analogue outputs (150 Hz) and digital inputs/outputs (12 DIO).

The instantaneous values of the three currents generated by the source are acquired in differential mode (Diff). Three voltages (from LEM-LA100P transducers) proportional to the three currents are applied to the inputs AI0, AI1, and AI2.

The six on/off digital output signals (P0.0...P0.5) are applied to the tap-changer control relays via optocouplers.

The PD 2512 dual source is used to power the LEM current transducers and optocouplers. Since the effective value of the primary current for the LEM current transducers is 100A, a few extra turns ($n=10$) are added.

B. Software component of the system

LabVIEW 2015 is used to create the virtual instrument that allows the user to communicate with the data acquisition module, process data, and control the system.

The front panel of the virtual instrument is divided into two sections [12]:

- the interface for setting the input parameters of the DAQ and the port (lines) where the digital output signals are located;
- the interface for controlling and monitoring the automation of the current source.

Fig. 10 shows the user interface of the program for communicating with the DAQ module. The block diagram of the hardware inputs/outputs of the USB-6008 module is shown. In the center (INPUT) there are the numerical controls (K1, K2, K3) for calibrating the measurement of the RMS values of the currents I1, I2, I3. In addition, the effective values of the currents are displayed both analytically and numerically.

On the right side (OUTPUT) there are controls for setting the digital output port P0 and the lines 0...5. LED indicators are used to signal the commands to increase/decrease the currents on each phase (for example: I1- decrease, I2+ I3+ increase).

The six lines of Port P0 are configured as active drive digital outputs, driving LEDs in optocouplers.

The main communication between the user and the system is done through the interface shown in Fig. 11. The display/signalling and control elements of the interface are horizontally grouped into three identical channels, one for each of the individual currents I1, I2 and I3. Each of these elements acts independently of the others.

The vertical toggle switches select the source operating mode (single phase, two phase or three phase). This is indicated by the LEDs I1, I2 or I3 lighting up. If they are off, the source will not generate power.

Next, the current value I (considered as the Process Variable, PV) is displayed in engineering units (EGU) and as a percentage (%) of the range.

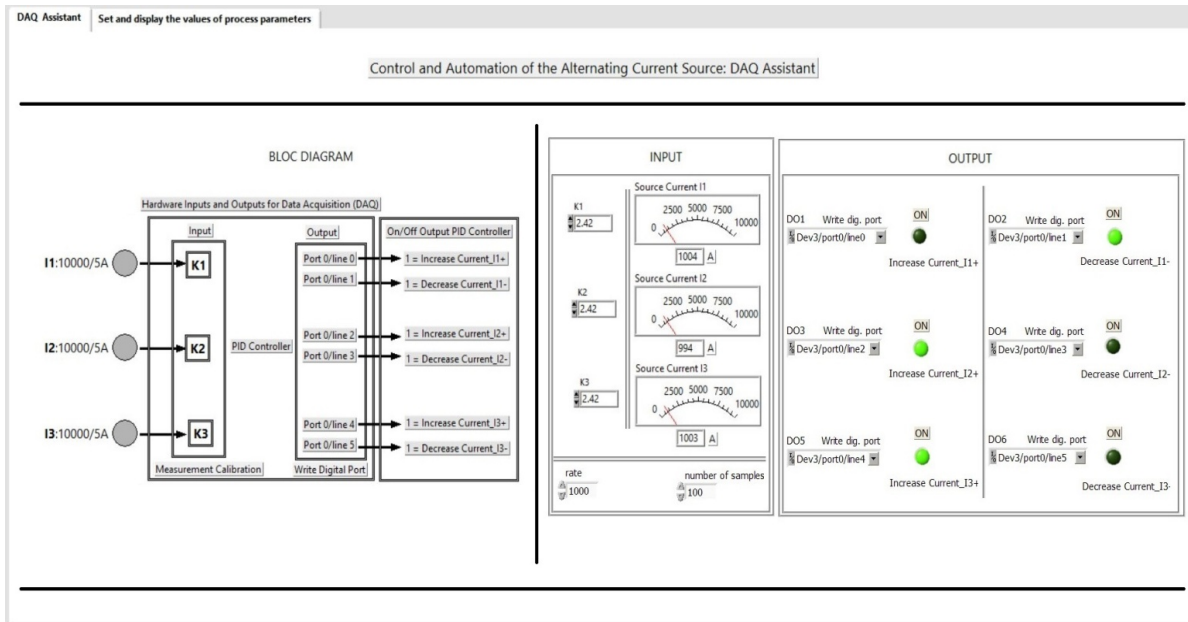


Fig. 10. The interface for configuring inputs/outputs and calibrating the source current measurement.

The current range (2-4-6-8 kA) is selected and displayed. In addition, the LED indicating that the upper limit has been exceeded is also displayed.

The specified current value is set using a horizontal pointer slide potentiometer and is displayed both in EGU units and as a percentage of the range.

The parameters of the PID controller are set: the proportional gain, the integral time and the derivative time. The result of the PID algorithm applied to the current control process is numerically displayed as a percentage (MV %).

The current control error is set between the limits of (-100, +100)% of the set point (SP) of the prescribed current by means of a vertical pointer slide. The current error value is displayed numerically, and any exceeding of the set limits is also displayed.

A hysteresis is applied to the upper and lower limits of the current error to avoid continuous on/off switching of the output.

The on/off outputs that control the current increase/decrease are indicated by two LEDs located on the right hand side of the front panel as shown in Fig. 11.

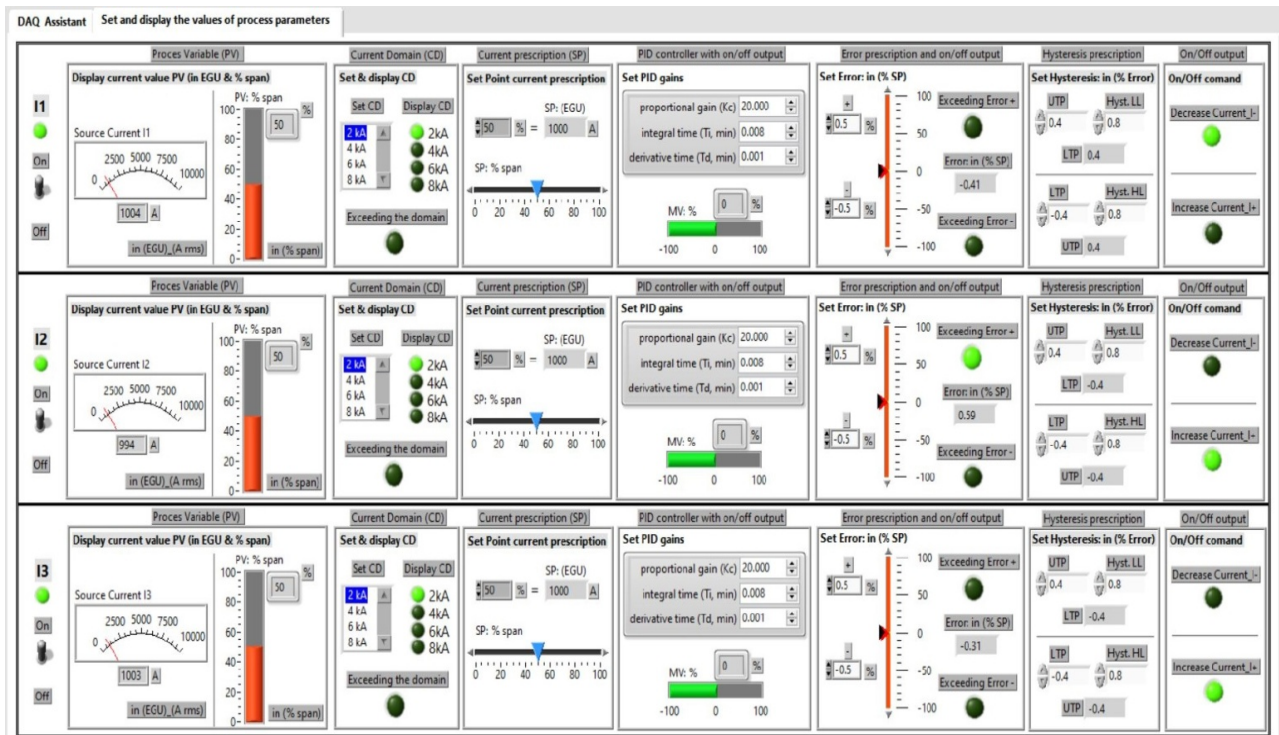


Fig. 11. The interface for setting and controlling the source parameters.

Fig. 12 shows a section of the block diagram where the acquisition parameters are set. This is done using the DAQ Assistant virtual instrument. The effective values are calculated from the instantaneous currents I1, I2, and I3. The constants K1, K2 and K3 are used to calibrate the measurement. Currents I1, I2, and I3 are process variables (PV) and inputs to the PID controller.

Fig. 13 shows a section of the block diagram where the output channels (digital output) are created to control the increase/decrease of the current on phase 1 (Increase Current I1+, Decrease Current I1-). A digital output channel consists of a single line.

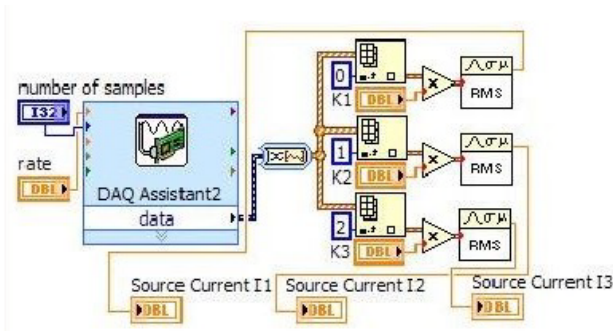


Fig. 12. Detail of the DAQ implementation for analogue inputs.

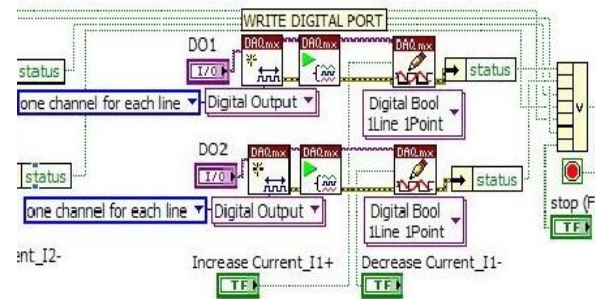


Fig. 13. Detail of the DAQ implementation for digital outputs.

To implement the current regulator function, a virtual instrument is used that implements a PID controller using a PID algorithm [13], [14], [15], [16].

To reduce the number of graphical connections in the block diagram, we have combined three virtual instruments into a single sub-VI: PID.vi, PID EGU to Percentage.vi, and PID Percentage to EGU.vi. The last two convert units of measurement based on the minimum and maximum range settings in EGU (see Fig. 14).

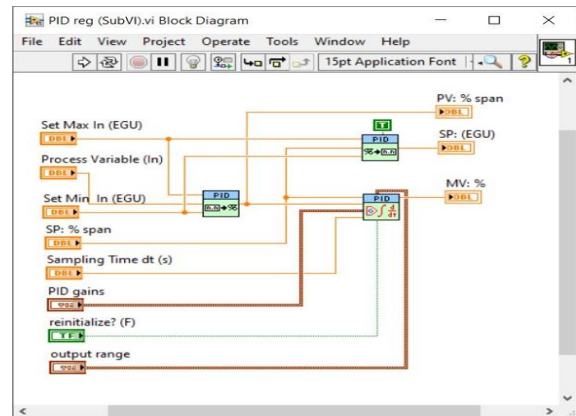


Fig. 14. The sub-VI for implementing the PID controller.

The graphical source code of the virtual instrument can be found in the Block Diagram (BD). Fig. 15 shows a detail of the block diagram with the functions of the proposed system.

All graphical elements are included in a repetitive structure (While Loop) which executes them until the logical conditions of True are met at the Loop Condition terminal.

The maximum current range of the source is selected using a case structure with four options: 2-4-6-8 kA.

To implement hysteresis software for the upper and lower error thresholds, the previous state of these values must be stored. A While loop using a shift register allows the previous output state to be stored for software implementation of hysteresis.

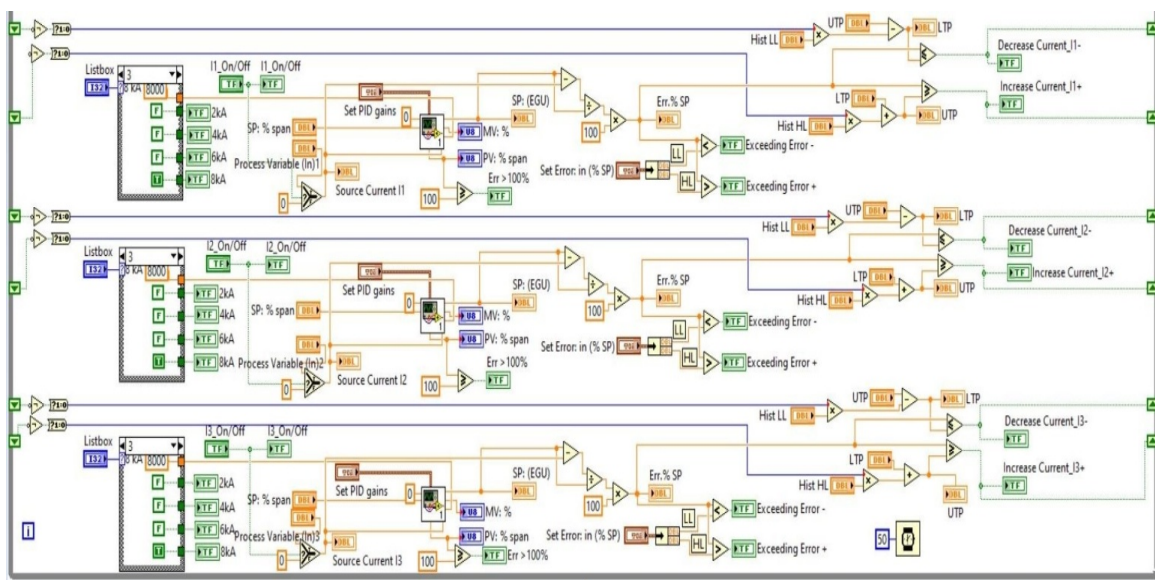


Fig. 15. The block diagram with the functions of the proposed system.

IV. MEASUREMENT, ACQUISITION, PROCESSING AND DATA STORAGE SYSTEMS[10]

The structure of the measurement, acquisition, processing and data storage system (Fig. 16) allows the acquisition of 8 sets of electrical measurements, each set represented by a three-phase current system and a three-

phase voltage system, and a maximum of 200 non-electrical signals (temperatures measured on the unit under test).

Currents are measured using current transformers as follows:

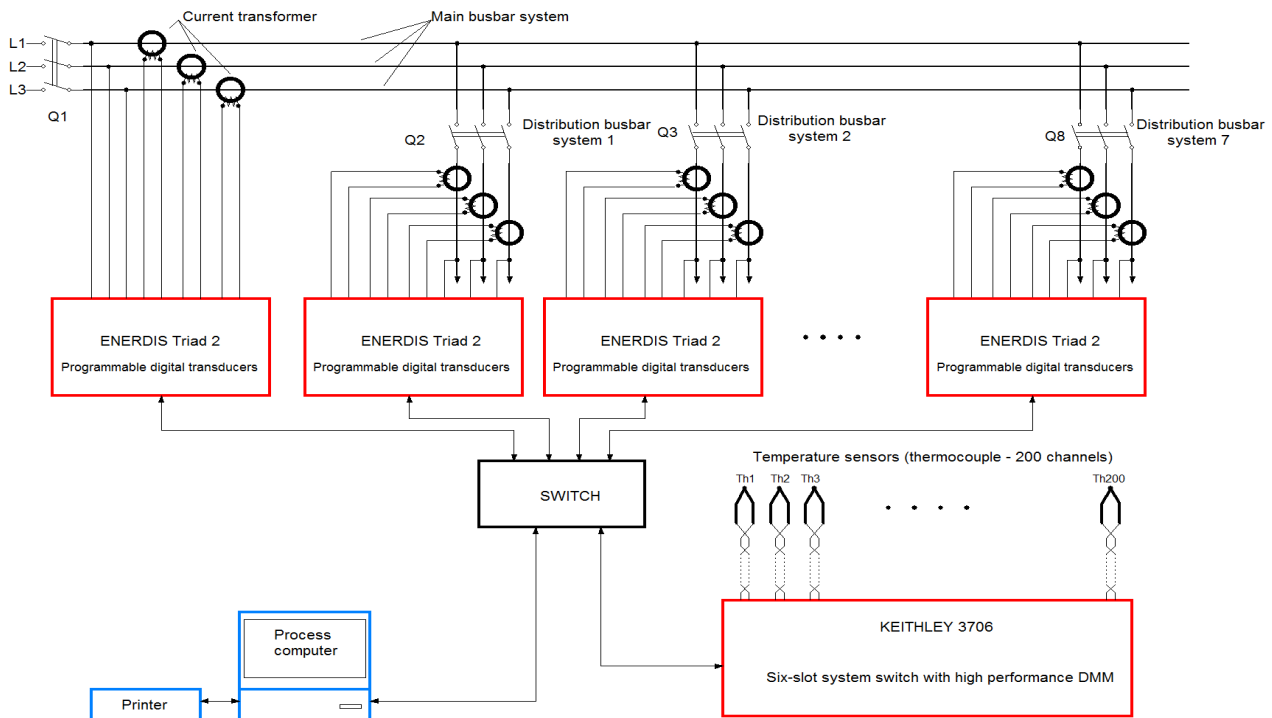


Fig. 16. Diagram of data measurement, acquisition, processing and storage systems.

- a set of three 10,000/5A ratio current transformers for measuring currents through the busbars of the switchboard(s) to be tested;

- seven sets of three measuring transformers with the appropriate transformer ratio selected to measure the currents through the busbars of the switchgear under test.

Electrical measurements are carried out using specialised ENERDIS Triad 2 equipment, which has the functions and facilities of an electrical energy analyser. The KEITHLEY 3706 measurement system is designed to acquire 200 temperature signals from T-type thermocouple sensors.

All signals are processed and transmitted in digital format via an RS 232/RS 485 serial interface to the process computer running a dedicated software application. The application allows real-time visualisation of the value of the various quantities in the process, graphical representation of their evolution over time, data storage and, at the end of the tests, the preparation of specific test bulletins for the certification of the DUTs [11].

V. RESULTS AND CONCLUSIONS

The verification of the performance of the computerised control system presented in this paper was carried out in a specialised laboratory at ICMET Craiova, where tempera-

ture rise tests on low and medium voltage switchgear are routinely performed. The high current source in the laboratory is designed according to the schematic diagram in Fig. 1, with autotransformers as control elements with fine (quasi-continuous) regulation of the voltage.

The following table shows the current control performance for the source equipped with the control, command and regulation system based on virtual instrumentation and numerical control algorithms.

TABLE I. EXPERIMENTAL RESULTS

No.	Current setting [A]	Measured current [A]		Error [%]	
		Reference measurement system	Digital control system	Regulating error	Measurement error
1	1000	1020	1015	2	-0.49
2	2000	1975	2005	-1.25	1.5
3	3000	3045	2995	1.5	-1.6
4	4000	4055	4005	1.375	-1.2
5	5000	5050	5035	1	-0.3

It is noted that the accuracy of detection and measurement of the current generated by the installation

was within the required accuracy class for all current ranges.

The three-phase stabilised AC power source, designed at ICMET Craiova in several versions since 1999, has been installed and commissioned at various beneficiaries in the country and abroad, as well as in the Institute's specialised laboratory. Modern technical solutions for automation and virtual control have been incorporated into this version to make operation as simple as possible, minimising human intervention. The proposed solution brings a significant reduction in the cost of implementing the high current source control, command and regulation system, a reduction in its dimensions and physical weight, automation of temperature rise tests, increased reliability and safety in the operation of the assembly, remote control of the process through specialised web applications, and offers the possibility of further software development through the integration of process monitoring and computerisation applications.

ACKNOWLEDGMENT

Source of research funding in this article: Research program of the Electrical Engineering Faculty financed by the University of Craiova.

Contribution of authors:

First author – 35%

First coauthor – 25%

Second coauthor – 25%

Third coauthor -15%

Received on July 17, 2023

Editorial Approval on November 15, 2023

REFERENCES

- [1] SR EN 62271-1:2011, "High-voltage switchgear and controlgear", August 2011.
- [2] E. Jezierski, Z. Gogolevski, Z. Kopczynski, I. Szmit, "Transformatoare electrice, Constructie si proiectare", Editura tehnica, Bucuresti, 1966.
- [3] Z. Sicheng, "Temperature rise test in Switching cabinet", University of Liverpool, 2018.
- [4] I. Gheorghiu, A. Fransua, "Tratat de masini electrice, Vol. II, Transformatoare", Editura Academiei, Bucuresti, 1970.
- [5] Gh. Hortopan, "Aparate electrice", Editura Didactica si pedagogica, Bucuresti, 1972.
- [6] R. Rudemberg, "Fenomene tranzitorii in sistemele electromagnetice", Editura Tehnica, Bucuresti, 1959.
- [7] Brevet de inventie nr. RO117053 (B1), "Transformator de tensiune cu raport variabil și control fin", 28.09.2001.
- [8] R. Kremer, "A guide to variable transformers", Phenix Technologies, Maryland, USA, 1995.
- [9] N. Edmond, "Măsurări electronice-Manualul inginerului electronist", Editura Tehnica, 1979.
- [10] R. Varbanescu, "Sisteme informatizate de măsurare", Editura MATRIX ROM, Bucuresti, 1999.
- [11] G. Ionescu, "Traductoare pentru automatizari industriale, vol. 1", Editura Tehnica, 1985.
- [12] G.E. Subtirelu, P. Pistol, A. Vintilă, M.D. Constantinescu, "Control, Command and Regulation System Based on Virtual Instrumentation for Three-Phase Alternating High Current Source", 14-th International Conference on Electromechanical and Energy Systems – SIELMEN, October 12-13, 2023, Chişinău – R. Moldova, ISBN 979-8-3503-1524-0/23, pp.1-6.
- [13] S. J. Shah, "Field Wiring and Noise Consideration for Analog Signals", NI Application Note 025, www.ni.com.
- [14] R. S. Vaidya, "Tips and Techniques in DAQ Triggering", NI Application Note 129, www.ni.com.
- [15] S. Chattopadhyay, G. Roy and M. Panda, "Simple Design of a PID Controller and Tuning of Its Parameters Using LabVIEW Software", Sensors & Transducers Journal, Vol. 129, Issue 6, June 2011, pp. 69-85.
- [16] T. R. Melo, J. J. Silva, J. S. da Rocha Neto, "Implementation of a Decentralized PID Control System on an Experimental Platform Using LabVIEW", IEEE Latin America Transactions, Vol. 15, Issue 2, February 2017, pp. 213-218.

Estimation of the Heating of Crimped Connections Based on Experimental Tests

Alin-Iulian Dolan

University of Craiova, Electrical Engineering Faculty, Craiova, Romania, adolan@elth.ucv.ro

Abstract – In this work, some analytical formulas based on experimental tests are presented that can be used to estimate the heating of the crimped connections used in construction of electrical machines, saving the experimenter from additional, long and expensive tests. The formulas are based on the energy balance equation and combine practical results obtained from previous steady-state heating cycles for a set of 6 crimped connections of the same type, at currents close to the nominal value. There are standards that allow the estimation of the heating of the elements in the circuit at small variations of the test current. Thus, based on the heating obtained at one value of the current, the heating at another, slightly different value can be estimated, without the need for the actual experiment. For a more accurate estimation, the variation with temperature of the electrical resistances of the 6 connectors must be taken into account, which allows the extension of the estimation range. In this case, if there are two heating cycles performed at two different values of the current, estimations can also be made at other values, much different from the two. A global temperature coefficient of resistance can be deduced that can simplify the formulas while keeping the precision, serving to estimate the average heating of the connectors. The formulas have been validated for several types of crimped connections used in the construction of electrical machines.

Cuvinte cheie: *conexiuni sertizate, încălzire, coeficient de variație a rezistenței cu temperatura, rezultate experimentale, mașini electrice.*

Keywords: *crimped connections, heating, temperature coefficient of resistance, experimental results, electrical machines.*

I. INTRODUCTION

Electrical machines such as motors and generators widely use crimp connections, which are permanent electrical contacts on which the reliability of the machine largely depends [1]. Crimping is a mechanical process often carried out with the help of hydraulic presses and its quality depends on a lot of factors, from the preparation of the cables and the choice of connectors, to the pressing itself.

Much research has been done over time to improve the performances of crimped connections, developing verification methods using ultrasonic inspection [2], [3] and thermography [4], analyzing the behavior at thermal shocks [5] or other factors that affect the contact resistance [6], modeling electric conduction [7] or temperature investigation for different types of crimping [8] with thermal modeling of heat transfer [9], [10]. For a quality pre-control of crimp contact, two solutions were proposed in [11] consisting in experimental determination of specific losses by calculating the initial rate of temperature or

checking reaching a critical temperature using on-level thermal indicator. To reduce of contact resistance and increase the reliability of crimped connections, useful solution was proposed in [12] by using two adjacent crimp indents in opposite sides instead of one crimp indents. In a recent work [13] is studied the influence of an improper crimped connection execution on crimping validation, analyzing the limits of variation of parameters so that it will not be compromised.

International standards such as [14] and [15] establish very clear methodologies for verifying the quality of crimped connections from an electrical, thermal and mechanical point of view.

In [16], a study of the influence of experimental measurements accuracy on coefficient δ called “initial scatter” which was performed, cumulating data from 6 crimped connections of barrel of terminal lug type, with different cross sections of cables and determining the quantities with the greatest influence. The paper [17] extends the researches on crimped connections of bimetallic through connector type by analyzing two pairs of cross sections. The obtained results can help the experimenter to pay more attention to measuring more influential quantities.

In [20], some useful formulas based on experimental determinations were presented that can be used to estimate the average heating of a set of 6 crimped connections, saving the experimenter from additional, long and expensive tests. The formulas were validated for several types of crimped connections used in the electrical machines.

In this paper, the results of two case studies used in [20] are detailed, highlighting graphically the differences between the estimations of the individual heatings of the connectors, obtained with the derived formulas.

II. ELECTRICAL TESTS OF CRIMPED CONNEXIONS

The standard [14] establishes formulas for determining the connector resistance factor, initial scatter (δ) and mean scatter (β) for different types of crimping: through connector, bimetallic through connector, branch connector, barrel of terminal lug, palm of terminal lug etc. (Fig. 1).

The initial scatter coefficient (δ) provides information on the behavior of the crimped connection immediately after installation before any aging effect begins. It is considered that 6 samples are sufficient to be tested to estimate the identification of a “family” of connectors. If the resistance factors for the type of connector tested are almost equal, it can be assumed that the same design and assembly technology will lead to the same result on a conductor of the same type. The mean scatter β has the same meaning as δ but takes into account the age of the connectors, assuming long-term operation at high temperatures.

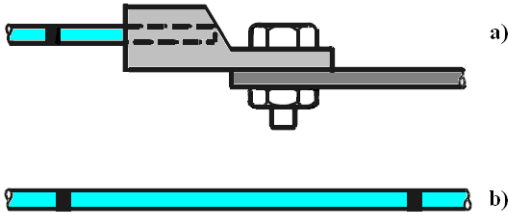


Fig. 1. Barrel of terminal lug (a) and reference conductor (b) [14].

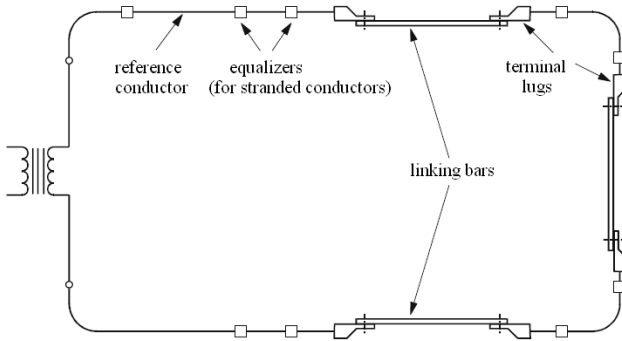


Fig. 2. Typical test circuit for barrel of terminal lugs [14].

For the experimental determinations of δ are used sets of 6 samples and reference conductors of each type involved in crimping. The measurements must make in direct current.

The influence of temperature on the resistance factor of the connector can be established after performing a large number of successive heating cycles in alternating current, by passing through the 6 samples in series (Fig. 2) with a current close to the rating one. Since during the tests high temperatures are reached both for the connectors and for the reference conductor, the use of thermoelectric thermometer is recommended for temperature measurement.

The standard provides for two preliminary heating cycles. The first cycle aims to determine the reference conductor temperature (θ_R) which will be used for subsequent heating cycles. The injected current into the test loop must be adjusted to ensure the condition $120^\circ\text{C} \leq \theta_R \leq 140^\circ\text{C}$ at equilibrium, defined as the time when the reference conductor and connectors do not vary in temperature by more than ± 2 K for 15 min.

The second heating cycle aims to determine the duration of a heating cycle by injecting a current into the test loop until the temperature of the reference conductor reaches the value θ_R for the duration t_1 and then cooling the connectors and the reference conductor to a temperature $\theta_0 \leq 35^\circ\text{C}$ on duration t_2 . The total period $t_1 + t_2$ constitutes the duration of a heating cycle.

A number of 1000 heating cycles is recommended [14], and after the first 250 cycles, every 75 cycles the maximum temperatures θ_{\max} of the connectors and the temperature θ_{ref} of the reference conductor are recorded and then the value of the mean scatter coefficient (β) is calculated. Comparing the temperatures θ_{\max} of the connectors with the simultaneously recorded temperature on the reference conductor θ_{ref} (which has a stable resistance) gives a rough idea of the "hot resistance" of each individual connector.

Being a long and expensive test, the heating test can be reduced to a single heating cycle, at current values that do not exceed the rating value, i.e. a current density of maximum 7 A/mm^2 , following only the maximum temperatures θ_{\max} reached of each connector, at equilibrium. Of course, in this case, the effect of the thermal stress on the crimped connections can only be ascertained in operation.

In the case of performing a single heating cycle, the manufacturer may request results regarding the maximum heating of the connectors obtained for several levels of current density, between $2 \div 7 \text{ A/mm}^2$. Based on the performed tests, empirical formulas can be derived for determining the heating of the same connectors at other current density values, thus saving the experimenter from additional tests, reducing both the cost and the duration of the tests.

The paper [20] presents useful empirically determined formulas on the basis of which the heating of the connectors can be estimated at theoretical values of the current density, different from those actually used. The formulas are experimentally validated.

The calculation is based on the equation of the energy balance in the unit of time at thermal equilibrium, which equates the Joule-Lentz losses with the heat flow transmitted to the surrounding environment by thermal convection:

$$R_i \cdot I^2 = \alpha \cdot \Delta\theta \cdot S_L = \alpha \cdot (\theta_{\max i} - \theta_{\text{amb}}) \cdot S_L \quad (1)$$

where I = RMS value of the current, R_i = electrical resistance of the i^{th} connector, $i = 1 \div 6$, modeled as a conductor of cross-section S , length L and lateral surface S_L , which reaches the steady-state temperature $\theta_{\max i}$, with global heat transfer coefficient α , at the ambient temperature θ_{amb} .

Writing the above equation for two slightly different values of the current I_1 and I_2 , neglecting the temperature variation of the resistance and of the global heat transfer coefficient, we obtain:

$$\begin{cases} R_i \cdot I_1^2 = \alpha \cdot \Delta\theta_{1i} \cdot S_L = \alpha \cdot (\theta_{1\max i} - \theta_{\text{amb}1}) \cdot S_L \\ R_i \cdot I_2^2 = \alpha \cdot \Delta\theta_{2i} \cdot S_L = \alpha \cdot (\theta_{2\max i} - \theta_{\text{amb}2}) \cdot S_L \end{cases} \quad (2)$$

$$\left(\frac{I_1}{I_2}\right)^2 = \frac{\Delta\theta_{1i}}{\Delta\theta_{2i}} = \frac{\theta_{1\max i} - \theta_{\text{amb}1}}{\theta_{2\max i} - \theta_{\text{amb}2}} \quad (3)$$

$$\Delta\theta_{2i} = \frac{I_2^2 \cdot \Delta\theta_{1i}}{I_1^2} \quad (4)$$

Therefore, having performed a heating test at current I_1 and $\theta_{\text{amb}1}$, for which the maximum temperature $\theta_{1\max i}$ was obtained for connector i , respectively, the heating $\Delta\theta_{1i}$, applying formula (4) it is possible to estimate the heating $\Delta\theta_{2i}$, which would be obtained at current I_2 , not much different from I_1 , for the same connector, in other ambient conditions $\theta_{\text{amb}2}$. The approximation is valid within the limits of $\pm 5\%$ variations of the current [18].

A global evaluation of the 6 connectors in the test loop should use information about all connectors, therefore instead of the heating of connector i at the current I_1 ($\Delta\theta_{1i}$), an average of the heatings of all connectors ($\Delta\theta_{1\text{mean}}$) at the same current I_1 can be considered [20]:

$$\Delta\theta_{1\text{mean}} = \frac{1}{6} \cdot \sum_{i=1}^6 (\theta_{1\text{max}i} - \theta_{\text{amb}1}) \quad (5)$$

$$\text{from where: } \Delta\theta_{2\text{mean}} = \frac{I_2^2 \cdot \Delta\theta_{1\text{mean}}}{I_1^2} \quad (6)$$

represents the average heating that would be obtained at current I_2 and $\theta_{\text{amb}2}$.

In the case of larger differences between the values of the currents I_1 and I_2 , the variation of the electrical resistance R_i (or resistivity ρ_i) of the connector with temperature must also be taken into account by the coefficients α_{Ri} [20]:

$$R_i = \frac{\rho_i \cdot L}{S} = \frac{\rho_{\text{Cu}20} \cdot [1 + \alpha_{Ri} \cdot (\theta_{\text{max}i} - 20^\circ\text{C})] \cdot L}{S} \quad (7)$$

Writing the energy balance equation for I_1 and I_2 and neglecting only the temperature variation of the global heat transfer coefficient, we obtain:

$$\begin{cases} R_{1i} \cdot I_1^2 = \alpha \cdot \Delta\theta_{1i} \cdot S_L = \alpha \cdot (\theta_{1\text{max}i} - \theta_{\text{amb}1}) \cdot S_L \\ R_{2i} \cdot I_2^2 = \alpha \cdot \Delta\theta_{2i} \cdot S_L = \alpha \cdot (\theta_{2\text{max}i} - \theta_{\text{amb}2}) \cdot S_L \end{cases} \quad (8)$$

$$\frac{1 + \alpha_{Ri} \cdot (\theta_{1\text{max}i} - 20^\circ\text{C})}{1 + \alpha_{Ri} \cdot (\theta_{2\text{max}i} - 20^\circ\text{C})} \cdot \left(\frac{I_1}{I_2}\right)^2 = \frac{\theta_{1\text{max}i} - \theta_{\text{amb}1}}{\theta_{2\text{max}i} - \theta_{\text{amb}2}} \quad (9)$$

$$\Delta\theta_{2i} = \frac{I_2^2 \cdot \Delta\theta_{1i} \cdot [1 + \alpha_{Ri} \cdot (\theta_{\text{amb}2} - 20^\circ\text{C})]}{I_1^2 \cdot [1 + \alpha_{Ri} \cdot (\theta_{1\text{max}i} - 20^\circ\text{C})] - I_2^2 \cdot \alpha_{Ri} \cdot \Delta\theta_{1i}} \quad (10)$$

Therefore, the heating $\Delta\theta_{2i}$ also depends on the coefficient α_{Ri} . The standard [14] indicates the value $\alpha_R = 0.004 \cdot \text{K}^{-1}$ for copper and aluminum conductors. In general, an electrical contact can have a value reduced by even a third of the coefficient α_R compared to the conductors that contributed to the formation of the contact [19]. From relation (10) it can be deduced:

$$\alpha_{Ri} = \frac{I_2^2 \cdot \Delta\theta_{1i} - I_1^2 \cdot \Delta\theta_{2i}}{I_1^2 \cdot (\theta_{1\text{max}i} - 20^\circ\text{C}) \cdot \Delta\theta_{2i} - I_2^2 \cdot (\theta_{2\text{max}i} - 20^\circ\text{C}) \cdot \Delta\theta_{1i}} \quad (11)$$

Based on the formulas (10) and (11), having carried out two heating tests at currents I_1 and I_2 for which the maximum temperatures $\theta_{1\text{max}i}$, respectively, $\theta_{2\text{max}i}$ were obtained, $i = 1 \div 6$, in ambient conditions $\theta_{\text{amb}1}$, respectively, $\theta_{\text{amb}2}$, the heatings $\Delta\theta_{3i}$ which would be obtained at current I_3 , different from I_1 and I_2 , in ambient conditions $\theta_{\text{amb}3}$, can be estimated:

$$\Delta\theta_{3i} = \frac{I_3^2 \cdot \Delta\theta_{1i} \cdot [1 + \alpha_{Ri} \cdot (\theta_{\text{amb}3} - 20^\circ\text{C})]}{I_1^2 \cdot [1 + \alpha_{Ri} \cdot (\theta_{1\text{max}i} - 20^\circ\text{C})] - I_3^2 \cdot \alpha_{Ri} \cdot \Delta\theta_{1i}} \quad (12)$$

The average heating of the 6 connectors at current I_3 and $\theta_{\text{amb}3}$ results:

$$\Delta\theta_{3\text{mean}} = \frac{1}{6} \cdot \sum_{i=1}^6 \Delta\theta_{3i} \quad (13)$$

A global temperature coefficient of resistance α_R for the 6 connectors in the test loop can be obtained by replacing all individual quantities in relation (11) with their averages [20]:

$$\Delta\theta_{2\text{mean}} = \frac{1}{6} \cdot \sum_{i=1}^6 (\theta_{2\text{max}i} - \theta_{\text{amb}2}) \quad (14)$$

$$\theta_{1\text{max mean}} = \frac{1}{6} \cdot \sum_{i=1}^6 \theta_{1\text{max}i} \quad (15)$$

$$\alpha_R = \frac{I_2^2 \cdot \Delta\theta_{1\text{mean}} - I_1^2 \cdot \Delta\theta_{2\text{mean}}}{\left[I_1^2 \cdot (\theta_{1\text{max mean}} - 20^\circ\text{C}) \cdot \Delta\theta_{2\text{mean}} - I_2^2 \cdot (\theta_{2\text{max mean}} - 20^\circ\text{C}) \cdot \Delta\theta_{1\text{mean}} \right]} \quad (16)$$

The global coefficient α_R can be used in (12), replacing individual coefficients α_{Ri} , to estimate the heatings $\Delta\theta_{3i}$ [20]:

$$\Delta\theta'_{3i} = \frac{I_3^2 \cdot \Delta\theta_{1i} \cdot [1 + \alpha_R \cdot (\theta_{\text{amb}3} - 20^\circ\text{C})]}{I_1^2 \cdot [1 + \alpha_R \cdot (\theta_{1\text{max}i} - 20^\circ\text{C})] - I_3^2 \cdot \alpha_R \cdot \Delta\theta_{1i}} \quad (17)$$

The average heating of the 6 connectors at current I_3 and $\theta_{\text{amb}3}$ results [20]:

$$\Delta\theta'_{3\text{mean}} = \frac{1}{6} \cdot \sum_{i=1}^6 \Delta\theta'_{3i} \quad (18)$$

Relations (4), (6), (11), (12), (13), (16), (17) and (18) save the experimenter from an additional test at the I_3 value of the current, saving time and energy.

III. CASE STUDIES

In the following, two case studies are presented in which barrel of terminal lug type crimped connections of different sections are subjected to a single heating cycle. In each test, the use of the proposed formulas is attempted and useful conclusions are drawn.

A. Case I

We consider the case of barrel of terminal lug type crimped connections of 185 mm² section for which the maximum temperatures of the connectors are requested during steady-state heating tests with current densities of 2, 3 and 4 A/mm², corresponding to the currents $I_1 = 370$ A, $I_2 = 555$ A and $I_3 = 740$ A. After carrying out the tests, overtemperatures ($\Delta\theta_i = \theta_{\text{max}i} - \theta_{\text{amb}}$) were obtained at thermal equilibrium for ambient temperatures $\theta_{\text{amb}1} = 27.2^\circ\text{C}$, $\theta_{\text{amb}2} = 27.2^\circ\text{C}$, respectively, $\theta_{\text{amb}3} = 28^\circ\text{C}$, and they are noted in Table I.

In the second test, a current of 560 A was used, which corresponds to a current density of 3.027 A/mm². For a correct reporting, it is necessary to estimate the values at 555 A using formulas (4) and (6), since the difference between the test currents is not too big (variation 0.89%). The estimation results are presented in Table II. In Table III and Table IV are presented the estimations with formulas (12), (13), respectively, (17), (18) with a better precision.

In Fig. 3 are shown the overtemperatures measured in the real tests, the estimations with (4), highlighted to the value 555 A and the range of applicability allowed by the

TABLE I.
OVERTEMPÉRATURES MEASURED IN REAL TESTS
FOR 370 A, 560 A, 740 A [20]

Current [A]	$\Delta\theta_i$ [K]						$\Delta\theta_{mean}$ [K]
	1	2	3	4	5	6	
370	15.9	16.5	16.0	16.7	16.0	16.1	16.20
560	38.5	38.1	37.7	37.6	37.1	38.7	37.95
740	66.3	67.5	66.6	67.9	66.4	69.4	67.35

TABLE II.
OVERTEMPÉRATURES ESTIMATED WITH (4), (6) FOR 555 A
BASED ON RESULTS FOR 560 A [20]

I_2 [A] / based on I_1 [A]	$\Delta\theta_i$ [K] (4)						$\Delta\theta_{mean}$ [K] (6)
	1	2	3	4	5	6	
555 / 560	37.8	37.4	37.0	36.9	36.4	38.0	37.275

TABLE III.
OVERTEMPÉRATURES ESTIMATED WITH (11), (12), (13), FOR 555 A AND 560 A BASED ON RESULTS FOR 370 A AND 740 A

I_3 [A] / based on I_1, I_2 [A]	$\Delta\theta_i$ [K] (11), (12)						$\Delta\theta_{mean}$ [K] (13)
	1	2	3	4	5	6	
555 / 370, 740	36.4	37.5	36.6	37.8	36.5	37.3	37.022
560 / 370, 740	37.1	38.2	37.3	38.5	37.2	38.0	37.711

TABLE IV.
OVERTEMPÉRATURES ESTIMATED WITH (16), (17), (18) FOR 555 A AND 560 A BASED ON RESULTS FOR 370 A AND 740 A

I_3 [A] / based on I_1, I_2 [A]	$\Delta\theta_i$ [K] (16), (17)						$\Delta\theta_{mean}$ [K] (18)
	1	2	3	4	5	6	
555 / 370, 740	36.5	37.1	36.6	37.3	36.5	38.1	37.025
560 / 370, 740	37.1	37.8	37.3	38.0	37.2	38.8	37.714

TABLE V.
ESTIMATION ERRORS OF (12), (13), (17), (18) COMPARED TO THE VALUES MEASURED IN REAL TEST FOR 560 A

Formulas	Errors ϵ_i [%]						ϵ_{mean} [%] (13), (18)
	1	2	3	4	5	6	
(12)	-3.74	0.15	-1.15	2.45	0.33	-1.70	-0.63
(17)	-3.54	-0.8	-1.05	1.11	0.25	0.35	-0.62

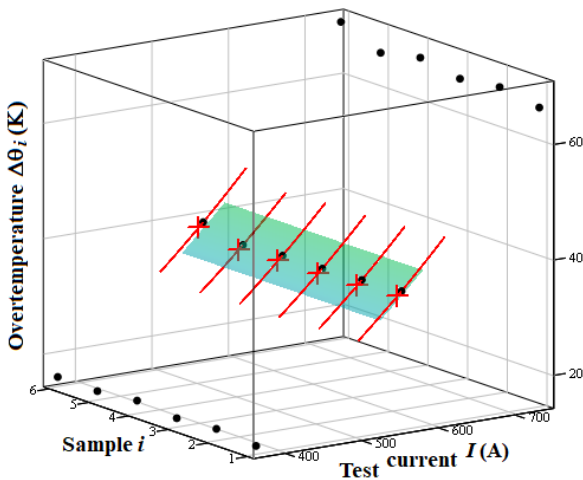


Fig. 3. Overtemperatures measured in real tests (black), estimated with (4) (red), highlighted to the value 555 A and the range of applicability (rainbow), for the case I.

standard [18]. In Fig. 4 and Fig. 5 are shown the estimations with (11), (12), respectively, (17), (18) highlighted to the same value and the range of applicability, visibly extended compared to the previous one.

Since three real heating tests were performed, the results of the second test can be used to validate the estimations using the purposed formulas. Thus, in Table V are done the errors ϵ of (12), (13), respectively, (17), (18) compared to the values measured in the real heating test for 560 A:

$$\epsilon_i = \frac{\Delta\theta_{3i} - \Delta\theta_{3i|560A}}{\Delta\theta_{3i|560A}} \cdot 100\% \quad (19)$$

$$\epsilon_{mean} = \frac{\Delta\theta_{3mean} - \Delta\theta_{3mean|560A}}{\Delta\theta_{3mean|560A}} \cdot 100\% \quad (20)$$

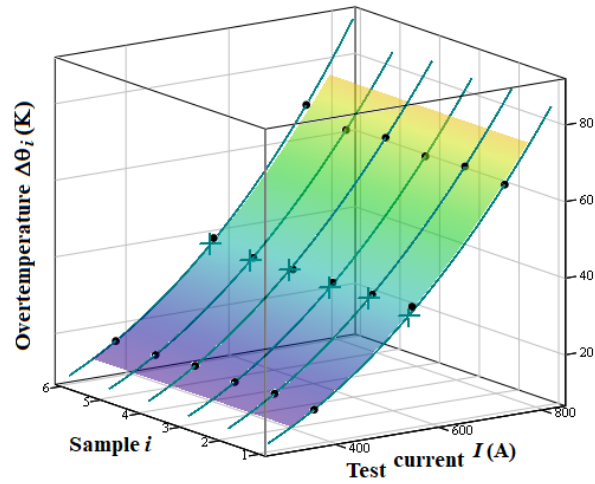


Fig. 4. Overtemperatures measured in real tests (black), estimated with (11) and (12) (green) and highlighted to the value 555 A and the range of applicability (rainbow), for the case I.

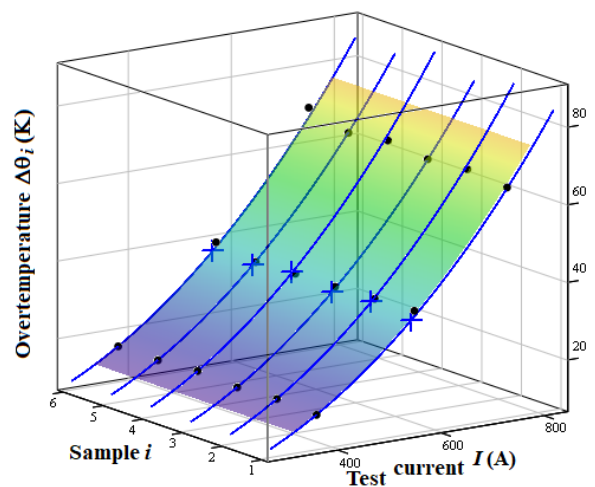


Fig. 5. Overtemperatures measured in real tests (black), estimated with (16) and (17) (blue) and highlighted to the value 555 A and the range of applicability (rainbow), for the case I.

The data show a good agreement with the real experiment, with average errors of -0.63% for (13) and -0.62% for (18). Also, it can be observed that the two formulas offer results close to each other. In Fig. 6 and Fig. 7 are highlighted the estimations with (11), (12), respectively, (17), (18) to the 560A.

The global temperature coefficient of resistance determined with (16) is $\alpha_R = 0.0007711639 \text{ K}^{-1}$. There is a decrease of 80.72% compared to the value of 0.004 K^{-1} [14].

In Fig. 8 are plotted the mean overtemperatures defined by relations (6) and (18) [20]. The points corresponding to the three real tests are also placed on the graph. The estimation of 37.714 K obtained with (18) at 560 A differs by 0.62% from the average real value 37.950 K . It is observed that the accuracy is quite good, although the current variations from 370 A to 560 A , or from 740 A to 560 A are 51.35% , respectively, -24.32% , i.e. much higher than $\pm 5\%$ [18]. At 555 A , an average heating of 37.275 K is estimated with (6) and of 37.025 K with (18), with an error between them of 0.67% . Obviously, the value obtained with (18) is much more precise.

B. Case II

We consider the case of barrel of terminal lug type crimped connections of 245 mm^2 section for which the maximum temperatures of the connectors are requested during steady-state heating tests with current densities of 4 and 5 A/mm^2 , corresponding to the currents $I_1 = 980 \text{ A}$ and $I_2 = 1225 \text{ A}$. After carrying out the tests, overtemperatures were obtained at thermal equilibrium for ambient temperature $\theta_{amb1} = \theta_{amb2} = 19^\circ\text{C}$ and they are noted in Table VI.

In the two tests, currents of 1005 A and 1140 A were used, which corresponds to current densities of 4.103 A/mm^2 and 4.654 A/mm^2 . For a correct reporting, it is necessary to estimate the values at 980 A and 1125 A .

As the variations of the currents from 1005 A to 980 A (-2.49%), respectively from 1140 A to 1125 A (1.32%) fall within the limits of $\pm 5\%$ [18], we can use formulas (4) and (6) and the estimation results are presented in Tables VII. For a greater precision, the use of formulas (12), (13) or (17), (18) led to the results shown in Tables VIII-IX.

In Fig. 9 are shown the overtemperatures measured in the real tests, the estimations with (4), highlighted to the value 980 A and 1125 A and the ranges of applicability allowed by the standard [18]. In Fig. 10 and Fig. 11 are shown the estimations with (11), (12), respectively, (17), (18) highlighted to the same values and the range of applicability, visibly extended compared to the previous ones, like in case I.

The global temperature coefficient of resistance determined with (16) is $\alpha_R = 0.0031139147 \text{ K}^{-1}$. There is a decrease of 22.15% compared to the value of 0.004 K^{-1} [14].

In Fig. 12 are plotted the mean overtemperatures defined by relations (6) and (18) [20]. The points corresponding to the two real tests are also drawn.

At 980 A , an average heating of 71.742 K is estimated with (6) and of 70.922 K with (18), with an error between them of 1.06% .

At 1125 A , an average heating of 101.394 K is estimated with (6) and of 100.540 K with (18), with an error between them of 0.85% . As before, the values obtained with (16) are much more precise.

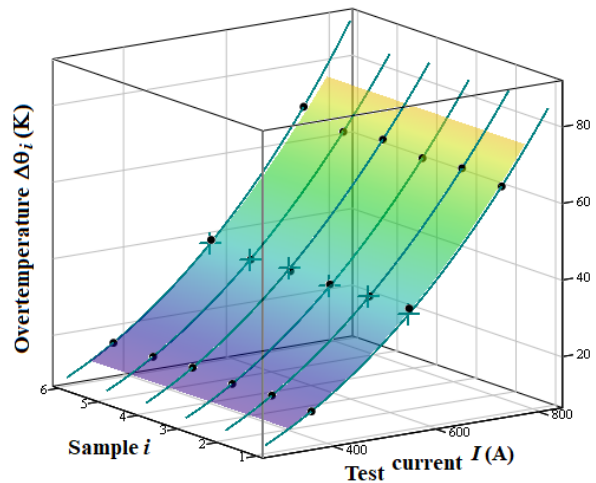


Fig. 6. Overtemperatures measured in real tests (black), estimated with (11) and (12) (green) and highlighted to the value 560 A and the range of applicability (rainbow), for the case I.

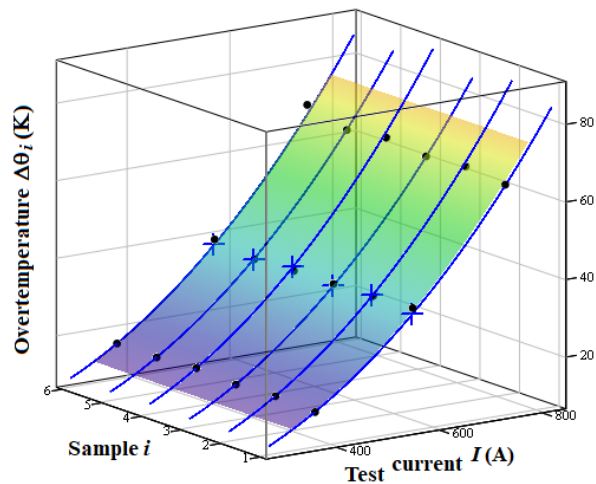


Fig. 7. Overtemperatures measured in real tests (black), estimated with (16) and (17) (blue) and highlighted to the value 560 A and the range of applicability (rainbow), for the case I.

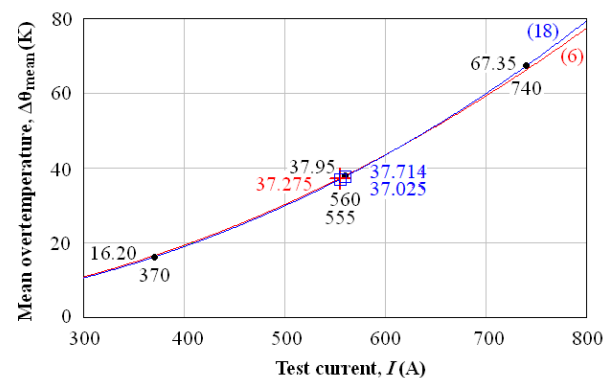


Fig. 8. Mean overtemperatures measured in real tests (black), estimated with (6) (red) and (18) (blue) [20].

TABLE VI.
OVERTEMPÉRATURES MEASURED IN REAL TESTS
FOR 1005 A, 1140 A [20]

Current [A]	$\Delta\theta_i$ [K]						$\Delta\theta_{mean}$ [K]
	1	2	3	4	5	6	
1005	75.6	76.1	75.2	76.1	74.9	74.8	75.450
1140	103.4	104.1	104.2	104.9	103.8	104.3	104.117

TABLE VII.
OVERTEMPÉRATURES ESTIMATED WITH (4), (6).FOR 980 A AND 1125 A
BASED ON RESULTS FOR 1005 A, RESPECTIVELY, 1140 A [20]

I_2 [A] / based on I_1 [A]	$\Delta\theta_i$ [K] (4)						$\Delta\theta_{mean}$ [K] (6)
	1	2	3	4	5	6	
980 / 1005	71.9	72.4	71.5	72.4	71.2	71.1	71.742
1125 / 1140	100.7	101.4	101.5	102.2	101.1	101.6	101.394

TABLE VIII.
OVERTEMPÉRATURES ESTIMATED WITH (11), (12), (13), FOR 980 A AND
1125 A BASED ON RESULTS FOR 1005 A AND 1140 A

I_3 [A] / based on I_1, I_2 [A]	$\Delta\theta_i$ [K] (11), (12)						$\Delta\theta_{mean}$ [K] (13)
	1	2	3	4	5	6	
980 / 1005, 1140	71.2	71.6	70.6	71.6	70.4	70.2	70.9
1125 / 1005, 1140	100.0	100.6	100.6	101.3	100.2	100.6	100.5

TABLE IX.
OVERTEMPÉRATURES ESTIMATED WITH (16), (17), (18) FOR 980 A AND
1125 A BASED ON RESULTS FOR 1005 A AND 1140 A [20]

I_3 [A] / based on I_1, I_2 [A]	$\Delta\theta_i$ [K] (16), (17)						$\Delta\theta_{mean}$ [K] (18)
	1	2	3	4	5	6	
980 / 1005, 1140	71.1	71.5	70.7	71.5	70.4	70.3	70.922
1125 / 1005, 1140	99.9	100.5	100.6	101.3	100.2	100.7	100.540

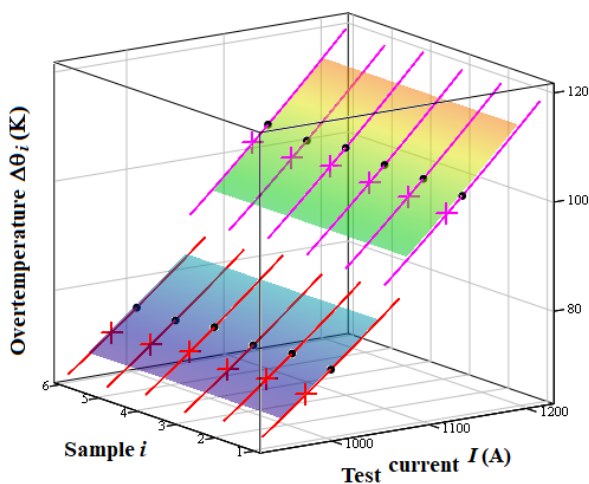


Fig. 9. Overtemperatures measured in real tests (black), estimated with (4) around the values 1005 A (red) and 1140 A (magenta) and highlighted to the value 980 A, respectively, 1125 A and the ranges of applicability (rainbow), for the case II.

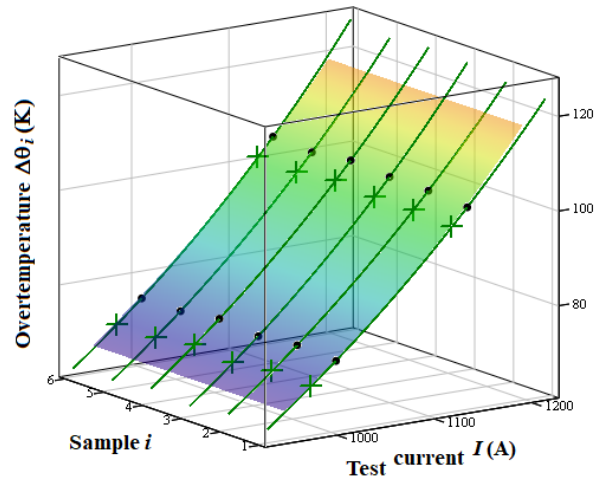


Fig. 10. Overtemperatures measured in real tests (black), estimated with (11) and (12) (green) and highlighted to the value 980 A, respectively, 1125 A and the range of applicability (rainbow), for the case II.

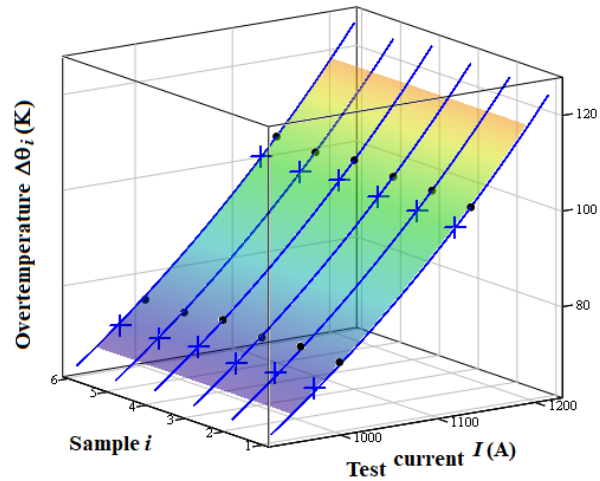


Fig. 11. Overtemperatures measured in real tests (black), estimated with (16) and (17) (blue) and highlighted to the value 980 A, respectively, 1125 A and the range of applicability (rainbow), for the case II.

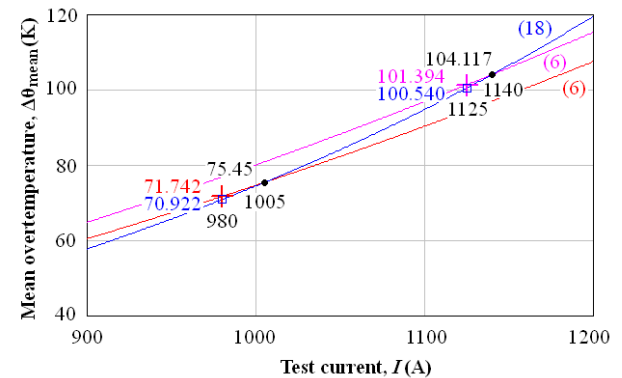


Fig. 12. Mean overtemperatures measured in real tests (black), estimated with (6) around the values 1005 A (red) and 1140 A (magenta) and highlighted to the value 980 A, respectively, 1125 A, estimated with (18) (blue) and highlighted to the same values, for the case II [20].

IV. CONCLUSIONS

The paper draws attention to some useful formulas for estimating the heating of crimped connections based on the experimental results obtained from previous tests. Some of the formulas can be applied to small variations of the test current ($\pm 5\%$), allowing estimations at a certain current if there are practical results for a close current. Other formulas, which take into account the temperature variation of the resistance of the connectors, allow the extension of the estimation range ($>5\%$), being able to make estimations at very different currents, based on known practical results for two different values of the current. In this case, a global temperature coefficient of resistance α_R can be deduced that can be used to estimate the average heating.

The formulas were tested with a fairly good precision on concrete cases of crimped connections used in the construction of electric machines. Values of the coefficients α_R lower values than those of the component conductors were determined, which is in accordance with the theory of electrical contacts.

The use of the proposed formulas can save the experimenter from additional tests, leading to a saving of energy and time.

ACKNOWLEDGMENT

Source of research funding in this article: Research program of the Electrical Engineering Department financed by the University of Craiova.

Received on July 09, 2023

Editorial Approval on November 25, 2023

REFERENCES

- [1] BS EN 60352-2:2006, Solderless connections, Part 2: crimped connections – general requirements, test methods and practical guidance, 2006.
- [2] E. Cramer, F. Daniel Perey, and T. William Yost, “Wire crimp connectors verification using ultrasonic inspection,” IV Conferencia Panamerica de END Buenos Aires, Octubre, 2007.
- [3] K. Elliott Cramer, F. Daniel Perey, and T. William Yost, “Wire crimp connectors verification using ultrasonic inspection,” IV Conferencia Panamericana de END, Buenos Aires, pp. 1-11, 2007.
- [4] M. Finc, T. Kek, and J. Grum, “Use of thermography and ultrasonic inspection for evaluation of crimped wire connection quality,” 18th World Conference on nondestructive testing, Durban, South Africa, 2012.
- [5] D.R. Liu, T. Bracket, and S. McCarthy, “Contact resistance comparison of good and bad crimp joints with tinned wires under thermal shock”, Electrical Contacts, Proceedings of the Forty-Seventh IEEE Holm Conference, pp. 35-43, 2001.
- [6] M. Mohd Ruzlin, A. H. Huzainie Shafi, and A.G. Ahmad Basri, “Study of cable crimping factors affecting contact resistance of medium voltage cable ferrule and lug,” 22nd International Conference of electricity distribution, Stockholm, Suedia, 2013.
- [7] G. Rosazza Prin, T. Courtin, and L. Boyer, “A new method to investigate electrical conduction in crimp joints. Influence of the compaction ratio and electrical model,” Electrical Contacts, Proceedings of the Forty-Eighth IEEE Holm Conference, pp. 246 – 251, 2002.
- [8] C.-F. Ocoleanu, A.-I. Dolan, G.A. Cividjian, and S. Teodorescu, “Temperature investigations in two type of crimped connection using experimental determinations,” International Journal of Mechanical, Aerospace, Industrial and Mechatronics Engineering, Vol. 8, No. 10, pp. 1633-1636, 2014, International Conference on Thermal Engineering, Barcelona, Spain, 2014.
- [9] C.-F. Ocoleanu, I. Popa, A.-I. Dolan, and V. Ivanov, “Magneto-Thermal Model for Crimped Connections,” Annals of the University of Craiova, Series: Electrical Engineering, No. 38, pp. 56-61, Universitaria Publishing House, 2014.
- [10] C.-F. Ocoleanu, I. Popa, A.-I. Dolan, and V. Ivanov, “Crimped Connections Heat Transfer Coefficient Law Determination Using Experimental and Numerical Results,” Proceedings of the XII-th IEEE International Conference on Applied and Theoretical Electricity - ICATE 2014, pp. 1-4, Craiova, Romania, October 23-25, 2014.
- [11] C.-F. Ocoleanu, G.A. Cividjian, and Gh. Manolea, “Solutions for quality pre-control of crimp contacts used in electric power systems and electrical machines,” 3rd International Symposium On Environment Friendly Energies And Applications, pp. 1-6, 2014.
- [12] C.-F. Ocoleanu, G.A. Cividjian, and Gh. Manolea, “Technological solution for increasing the quality of crimped connections,” 2015 IEEE 1st International Forum on Research and Technologies for Society and Industry Leveraging a better tomorrow (RTSI), Sept. 16-18, pp. 1-6, 2015.
- [13] C.-F. Ocoleanu, and A.-I. Dolan, “Experimental and Statistical Study of Connector Resistance Factor Influence on Crimping Validation Process,” 7-th International Conference on Renewable Energy Research and Applications - ICRERA 2018, Paris, France, Oct 14-17, pp.174-178, 2018.
- [14] BS EN 61238-1:2003, Compression and mechanical connectors for power cables for rated voltages up to 36 kV – Part 1: test methods and requirements, 2003.
- [15] B945-05, Standard Guide for Specification and Quality Assurance for the Electrical Contact of Crimped Wire Terminations.
- [16] A.-I. Dolan, and C.-F. Ocoleanu, “Influence of Experimental Measurements Accuracy on Connector Resistance Factor for Crimped Connections,” XVI-th IEEE International Conference on Applied and Theoretical Electricity – ICATE 2021, Craiova, Romania, May 27-29, 2021, pp. 1-5, 2021.
- [17] A.-I. Dolan, and C.-F. Ocoleanu, “Impact of Experimental Measurements Accuracy on Validation Process of Crimped Connections,” Annals of the University of Craiova, Series: Electrical Engineering, No. 45, pp. 16-23, Universitaria Publishing House, 2021.
- [18] IEC 60034-4, Rotating electrical machines - Part4: Methods for determining synchronous machine quantities from tests, 2008.
- [19] I. Popa, Electrical equipments - Theoretical bases (In Romanian), Universitaria Publishing House, 2017.
- [20] A.-I. Dolan, “Useful Experiment Based Formulas for Estimating the Heating of Crimped Connections,” Proceedings of the XIV-th IEEE International Conference on Electromechanical and Power Systems – SIELMEN 2023, October 11-13, pp. 1-5, Craiova-Chişinău, 2023.

An Example of Performance Achievement Based on Errors Analysis for Low-Cost Circuits Design

Constantin Daniel Oancea*, Daniel Bostan†, Viorel Constantin Petre*

* National University of Science and Technology Politehnica from Bucharest / Faculty of Electronics, Telecommunication and Information Technology, Bucharest, Romania, daniel.oancea@upb.ro

† RARTEL S.A., Bucharest, Romania, danielbostan@gmail.com

* National University of Science and Technology Politehnica from Bucharest / Faculty of Electrical Engineering, Bucharest, Romania, viorel.petre@upb.ro

Abstract - To create high-performance equipment, low-performance components, such as those from the old generations, can also be used. For example, if a conditioning stage (amplification/attenuation or filtering) is made with high-end components having increased performance, the costs are appropriate – using “classical” functional ones, the price of the equipment will become competitive. Low-cost devices may have features that do not make them attractive for inclusion in high-performance equipment but certain errors’ analysis may lead to practical and useful results. A converter circuit from PWM pulses to DC voltage was used. Experimental determinations were made using several types of operational amplifiers and errors analysis and correction was carrying out.

Cuvinte cheie: componente electronice, analiza si corectia erorilor, erori sistematice, microcontroler, calibrare, câstig.

Keywords: electronic components, errors’ analysis and correction, systematic errors, microcontroller, calibration, gain.

I. INTRODUCTION

Measurement errors are often seen as the fault of the human operator, by not respecting certain conditions for carrying out the measurements. However, the error can also be the result of systemic operational problems, constantly affecting the measurement. The presentation of these aspects leads to the prevention and/or correction of errors.

Errors due to human operators include usage errors (performing an operation incorrectly or the incorrect version of the standard operating procedure) and measurement errors (making a measurement error in a process). The consequences of the presence of errors can be costly or even dangerous, [1].

The existence of digital process measurement chains can easily introduce various errors. Thus, errors can come from the multiplexing part, from sampling and from the analog-to-digital conversion, which can accumulate. The use of a microcontroller implies the existence of a program, and it can be easily modified and updated, correcting possible implementation mistakes.

Measurement systems have many error components involved in the measurement and even when known and corrected, the uncertainty (with a lower estimate than the initial one) affects the final measurement value, generating

doubts about how well this result represents the measured quantity. Improper measurement can seriously affect quality-oriented companies because of the risks involved in making wrong decisions based on process control tools. Consequently, the effect of measurement uncertainty on the results must be carefully investigated, [2].

Systematic errors are easily observable and have a noticeable monotony (they can be constant or proportional to the measurement). Systematic errors are the first affecting the accuracy of a measurement. Sources of systematic errors result from observational error, imperfect instrument calibration, and environmental interference [3].

Systematic errors are different from random errors and they affect the aspect data which is reflected in obtaining false conclusions and interpretations. Measurements will deviate significantly from true values if systematic errors are present. A false positive conclusion or a false negative conclusion can be drawn about the relationship between the studied variables, [4].

A systematic error results in measurements of the same quantity differing in predictable ways. For each measurement, the result has the same sign and possibly the same amount compared to the true measurement. A systematic error can also be called a bias because the data is skewed in well-established ways that hide the true values. Offset errors and scale factor (gain) errors are two examples of quantifiable types of systematic errors.

Sources of bias can range from research materials to data collection procedures and analysis techniques. So they can come from all aspects of the measurement procedure.

Systematic errors can be mitigated by using procedures in the measurement process. For example, systematic errors can be observed in analog-to-digital and digital-to-analog conversions, but also in any other circuit where there is interference with an offset voltage, [5], [6].

For the detection of systematic errors, the obtained results may be compared with a known value or a theoretical value. Statistical methods can be used to analyze the data or the experimental setup can be changed to see if the error persists. Calibration of an instrument is another method of investigating systematic errors, which means comparing what the instrument records with the actual value of a known standard quantity. This procedure is done periodically for the instrument used and is done with a precise reference, [7], [8].

II. METHODOLOGY

A. Circuit design

The correction of systematic errors was analyzed for a circuit that transforms PWM pulses into direct voltage. The circuit has a mainly digital operation, using a microcontroller (PIC 18F452 from Microchip) and auxiliary circuits that use analog components such as operational amplifier and bipolar transistor. The design uses both digital and analog components; therefore it is possible to deal on both sides. Since we are talking about systematic errors, this is done only once, at the initial stage of setting up the device.

The structure of the considered device consists of a microcontroller and an output circuit, made around a low pass filter (LPF). The LPF is also a buffer for the output voltage, to isolate the output of the microcontroller and to protect it from overvoltage, Fig. 1.

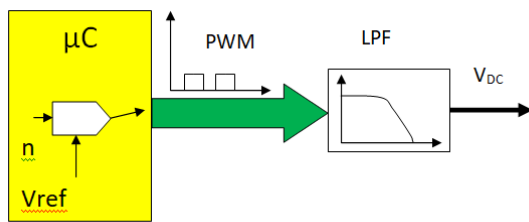


Fig. 1. The main components of the test equipment.

I used PWM, so that the method can also be used with microcontrollers that only have digital outputs.

The wiring diagram, in addition to the PWM signal generator microcontroller, consists of a 2nd-order low-pass filter, an output buffer and a bipolar power supply. A bipolar power supply was required because it is of interest to obtain a linear output voltage excursion, as much as possible (the transistor operates in the normal active region).

The entire device is powered from a 7V to 24V AC supply and the stabilized DC voltages are +12V and -5V to power the output buffer and +5V to power the microcontroller. It is not possible to feed the circuit with direct voltage, because it is not possible to obtain negative voltage. Additionally, a fuse and two diodes were provided which were used to protect the output against short circuit and overvoltage respectively, Fig. 2.

B. Application

The software of the microcontroller was developed in MPLAB IDE, using the specific assembly code, and was considered to display the information on the LCD, to observe the increment/decrement of the numerical values. The chosen resolution is 10 bits which corresponds to a step of ~4.88 mV. The execution speed is not critical, so any other microcontroller (or other brands) is suitable for using in the experiment - the only mandatory requirement is to have a PWM output mode.

A programming issue was displaying the decimal values corresponding to the 10-bits resolution of the digital-analog converter (DAC). That is because the microcontroller has an 8-bit memory configuration and the 10-bits

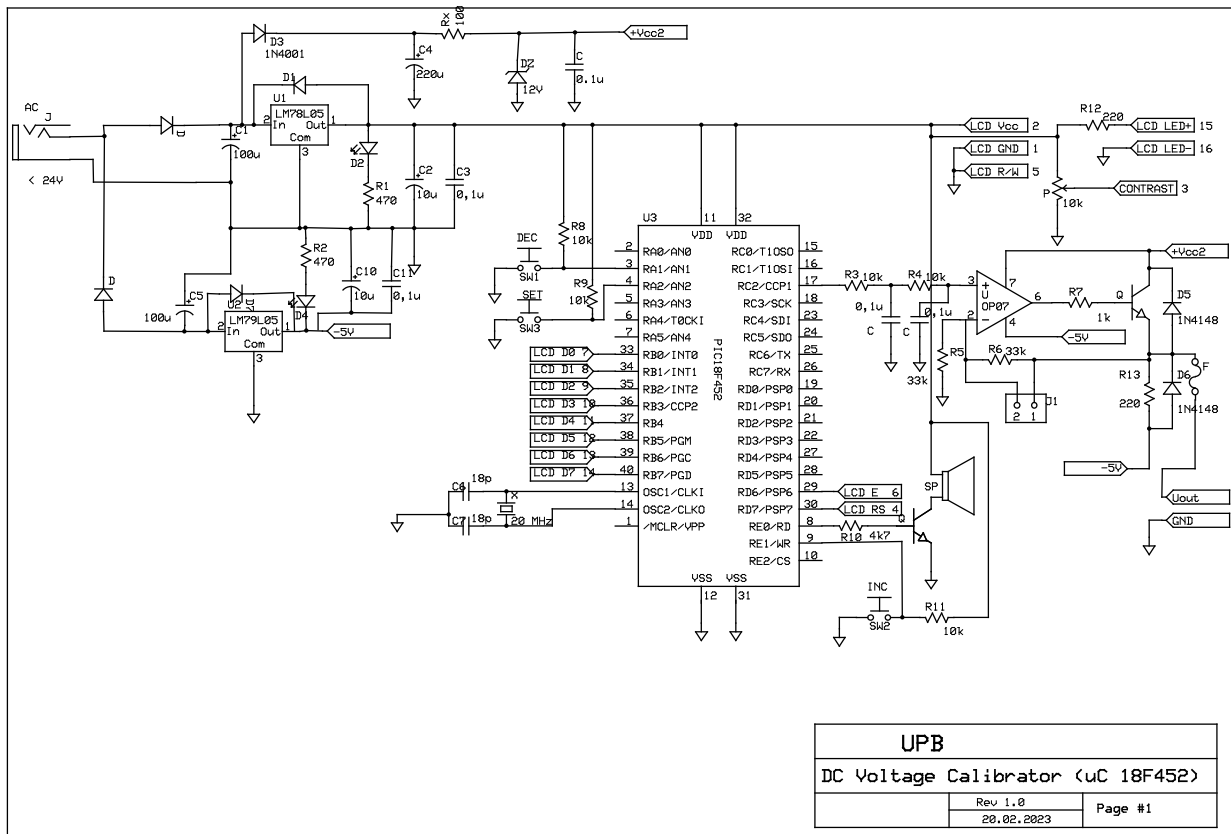


Fig. 2. The Complete schematics of proposed circuit.

DAC values are stored in two different memory locations (8-bits + 2-bits) - handling these extra 2-bits requires advanced programming skills. Other code sequences such as timing, initializing the LCD display, displaying characters on the LCD, and sending the number to the output port (via registers) were used, [9].

C. Experimental setup

Experimental determinations and all tests were performed using PIC 18F452 microcontroller. It is a multi-function microcontroller with PWM output and five I/O ports. It can operate in two DAC modes: 8-bit and 10-bit. In order to have the best resolution, the 10-bit option was used.

For testing the circuit, three different types of manufacturers for the operational amplifier of the output buffer were used, Table I.

TABLE I.
THE CONVERSION CHARACTERISTIC FOR DIFFERENT TYPES OF THE OUTPUT BUFFER

No.	Output voltage [V]		
	OP07	βA741	UA741
0	0.0012	0.0011	0.0023
1	0.0061	0.0061	0.0072
10	0.0505	0.0505	0.0516
50	0.2479	0.2479	0.2490
250	1.2357	1.2358	1.2367
500	2.4728	2.4731	2.4738
750	3.7125	3.7129	3.7136
1000	4.9548	4.9553	4.9559
1023	5.0692	5.0698	5.0703

As presented, the following parameters are established (initially):

- the step (4.88 mV),
- full-scale (depend by operational amplifier used (OP07 / βA741 / UA741) : from 0.0012 / 0.0011 / 0.0023 V to 5.0692 / 5.0698 / 5.0703 V),
- the percentage resolution (0.09669 / 0.09864 / 0.09669%) for this digital-to-analog converter.

The OP07 operational amplifier is a high-quality integrated circuit (lower offset voltage than the 741 family of circuits; 60 μV and 1 mV respectively).

The comparison of working frequencies is not relevant because both operational amplifiers work at approximately 20 kHz, a frequency far below the limit (e.g. 0.6 MHz for OP07).

The PWM module inside the PIC18 microcontroller uses a timer to control the signal frequency and duty cycle, [10]. The period of the generated PWM signal is given by (1).

$$PWM_{period} = (PR2 + 1) \cdot 4 \cdot TOSC \cdot TMR2_{prescale_value} \quad (1)$$

Where PR2 is the value loaded into the period register and TOSC is the clock period of the peripheral clock.

To estimate duty cycle of signal must use register CCP1L and CCP1CON value.

$$PWMDuty_{cycle} = \frac{CCP1L}{CCP1CON < 5: 4 >} \cdot TOSC \cdot TMR2Prescale_Value \quad (2)$$

Where CCP1L represents 8 bits MSB and CCP1CON 2 bits LSB (4 and 5). These registers can be programmed to count up or down. The parameters for this project are summarized as follows:

- PWM_frequency= 19531.25 Hz
- TOSC= 51.2 us
- Timer used = Timer2
- TMR_prescaler_value= 124

To estimate the necessary correction, the error was computed, Table II.

TABLE II. ERROR OF SOME SAMPLED DATA

No.	Error [%]		
	OP07	βA741	UA741
0	0.02	0.02	0.05
1	0.02	0.02	0.04
10	0.02	0.02	0.04
50	0	0	0.02
250	-0.08	-0.08	-0.06
500	-0.13	-0.13	-0.11
750	-0.13	-0.13	-0.11
1000	-0.09	-0.08	-0.07
1023	-0.08	-0.07	-0.06

The used formula used is a typical one for D/A conversion, [6], [7].

$$\varepsilon = \frac{Vm - Vi}{Vref} \cdot 100 \quad (3)$$

Where Vm is the measured output voltage, Vi is the ideal output voltage (computed with D/A conversion formula) and Vref is the reference voltage, which in this case it is 5.0733 V.

$$\frac{N}{Nref} = \frac{V}{Vref} \quad (4)$$

The output characteristic and the error diagrams reveal differences between experimental results, Fig. 3, Fig. 4.

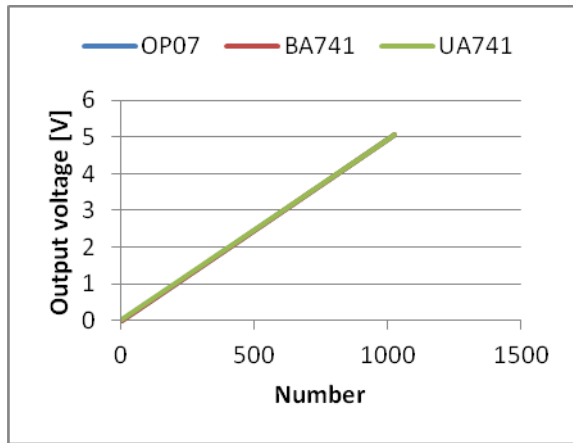


Fig. 3. The output characteristic with different operational amplifiers.

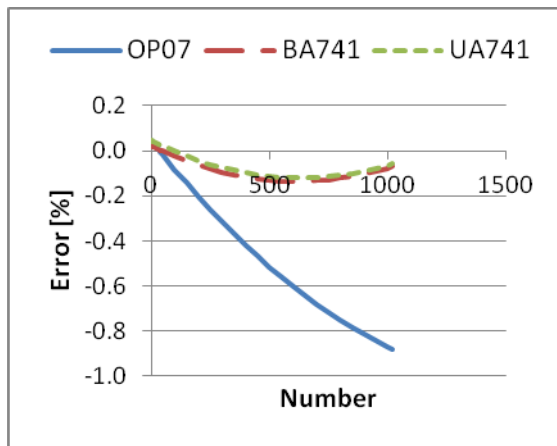


Fig. 4. The output characteristic error.

After errors' analysis and for performance improvement using error correction, we chose the circuit having the operational amplifier OP07 as output buffer, Table III.

The first step was the determination of the experimental output error, (5). The error plot shows that we are dealing with systematic offset errors and thus, they can be corrected by displacement. For β A741 and UA741 IC, Table IV and Table V present some computed correction.

The second step was to find the corresponding voltage for the error correction, (6).

The third step was to calculate the difference between the newest (preferred) voltage and the original voltage (measured voltage). Therefore, we considered using a constant voltage of approximately 0.003V in this case.

The meanings of the quantities are: ϵ correction is the necessary correction, in percent, based on minimum and maximum error computed with (1); $V_{\text{correction}}$ is the expression of ϵ correction in volts and V is the theoretical/ideal voltage of D/A converter, from (2). The number 5.0733 represents the reference voltage of the DAC

$$e_{\text{correction}} = \epsilon - \frac{(\epsilon_{\text{min}} - \epsilon_{\text{max}})}{2} \quad [\%] \quad (5)$$

$$V_{\text{correction}} = e_{\text{correction}} \cdot 5.0733/100 + V \quad (6)$$

This voltage resulting from the difference between the corrected and the measured value, 0.003V, is constant. This value is used to shift the output characteristic to reduce the maximum error from the initial rate, Fig. 5.

TABLE III
SOME COMPUTED CORRECTION FOR OP07

No.	OP07		
	New error (forced)[%]	Corresponding voltage [V]	Difference between the new output voltage and initial output voltage [V]
0	0.08	0.0042	0.0030
1	0.08	0.0091	0.0030
10	0.08	0.0535	0.0030
50	0.06	0.2509	0.0030
250	-0.02	1.2387	0.0030
500	-0.08	2.4758	0.0030
750	-0.08	3.7155	0.0030
1000	-0.03	4.9578	0.0030
1023	-0.02	5.0722	0.0030

TABLE IV
SOME COMPUTED CORRECTION FOR β A 741

No.	β A 741		
	New error (forced)[%]	Corresponding voltage [V]	Difference between the new output voltage and initial output voltage [V]
0	0.0779	0.0040	0.0028
1	0.0787	0.0090	0.0029
10	0.0741	0.0534	0.0029
50	0.0550	0.2508	0.0029
250	-0.0228	1.2387	0.0030
500	-0.0723	2.4760	0.0032
750	-0.0725	3.7158	0.0033
1000	-0.0214	4.9582	0.0034
1023	-0.0128	5.0727	0.0035

Thus, the absolute maximum value is approximately 0.08%, from the initial value of 0.142%. Practically, the characteristic will be "centered", symmetrical to the axis.

This additional voltage can be generated internally, by software or externally, by applying a voltage to the operational amplifier that shifts the potential from the output. This correction can be done before using the device, into initial calibration phase.

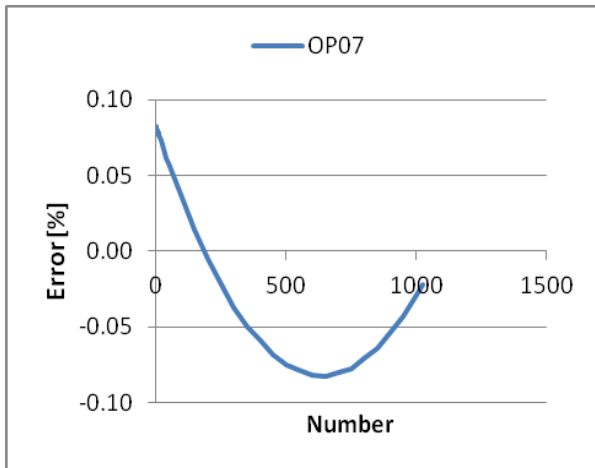


Fig. 5. New error after correction, OP07.

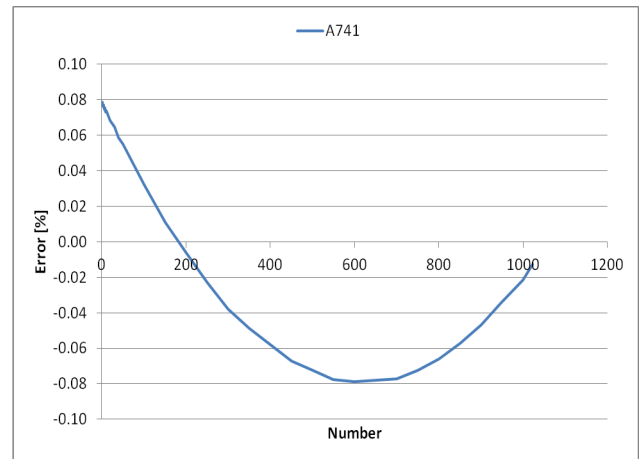


Fig. 6. New error after correction, A741.

TABLE V
SOME COMPUTED CORRECTION FOR UA741

No.	UA741		
	New error (forced)[%]	Corresponding voltage [V]	Difference between the new output voltage and initial output voltage [V]
0	0.08321	0.0042	0.0030
1	0.08204	0.0091	0.0030
10	0.07744	0.0535	0.0030
50	0.05833	0.2509	0.0030
250	-0.02342	1.2386	0.0029
500	-0.07682	2.4757	0.0029
750	-0.07701	3.7155	0.0030
1000	-0.02792	4.9578	0.0030
1023	-0.02126	5.0722	0.0030

Program correction can be implemented if the digital-to-analog conversion step is smaller than the required correction. In our case it is 0.003V compared to 0.0049V.

New error plot for A741 and UA741 was generated after correction, Fig. 6, Fig. 7.

From Table IV, in case of use A741 operational amplifier, the difference between initial and new output voltage is not a constant but also difference is very small. This is because systematic errors it was not completely eliminated, having several causes.

Comparing initial errors, Fig. 4, with new errors, Fig. 5, Fig. 6, Fig. 7, it is obviously the efficiency of method proposed.

The error tends to be reduced by half, close to the error of the measuring equipment.

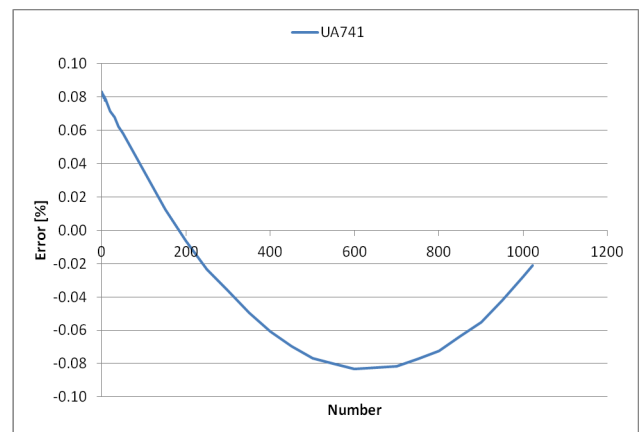


Fig. 7. New error after correction, UA741.

III. CONCLUSIONS

The presented method is useful when developing equipment or a device with low quality components, with reduced costs. After an initial analysis of the device/equipment performance, one chooses which method (software or hardware) is better to reduce systematic errors. For this, an imposed error is estimated, which is usually half of the original error. Then the voltage corresponding to this error is determined and finally it is checked if the differences, for the values of interest, are the same or very close. Depending on the results, it is decided whether the correction is made in the auxiliary electronic circuits of the microcontroller or internally, by changing the number used for conversion. There is also the possibility that the correction methods act on hardware and software simultaneously.

The solution used is chosen after analyzing the operation of the scheme, because the performance of the components used is important. If, for example, the compensation voltage exceeds the value of the converter, then the correction can be done by software. If this offset is less than the voltage step at the output, then the error correction can only be done by hardware.

Obviously, there is also the possibility of combining the two methods.

The experimental setup, Fig. 8, used in this case is a DC voltage generator, synthesized by the PWM technique, but one can imagine any other configurations, like signal generator or current source.

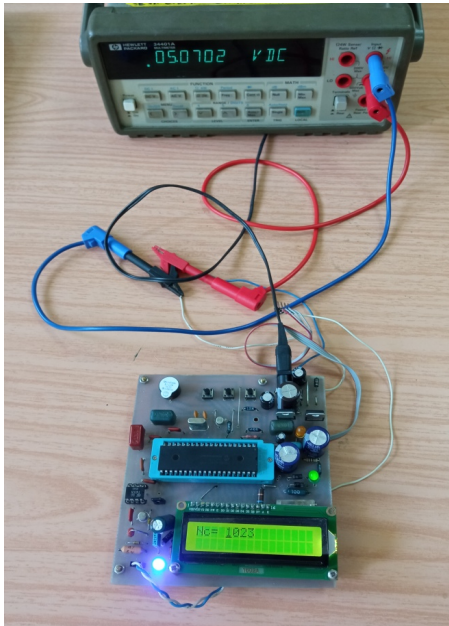


Fig. 8. Experimental setup.

A HP 34401A voltmeter with a measurement resolution of 0.1 mV was used to measure the voltages, which is adequate to validate the proposed method.

From the experimental data it is found the possibility of completely eliminating the systematic errors, when using the OP07 and UA741 integrated circuits. It's not the same when using A741, because it seems to be supplementary causes of systematic errors.

By using the microcontroller, additional functions can be performed, such as communicating with a computer or designing a more complex menu in the program through which certain settings of the operation of the microcontroller can be configured, including an adjustment of the offset of the generated output signal.

When testing the method one must take in consideration to correlate the device tested performance (in terms of errors) with the used measurement equipment.

To increase the degree of automation, a data acquisition board with appropriate performance (e.g. resolution/number of bits) can be used to allow the reading of the generated voltage, assistance from the automatic cal-

culaton and other possibilities (storage, filtering) of using digital information.

ACKNOWLEDGMENT

Source of research funding in this article: Research program of the National University of Science and Technology Politehnica, Bucharest.

Contribution of authors:

First author – 70%

First coauthor – 15%

Second coauthor – 15%

Received on July 23, 2023

Editorial Approval on November 28, 2023

REFERENCES

- [1] G. E. Couto, P. C. Oprime, "The Importance of Measurement Uncertainty Analysis on Statistical Quality Control" In: Thomé, A.M.T., Barbastefano, R.G., Scavarda, L.F., dos Reis, J.C.G., Amorim, M.P.C. (eds) Industrial Engineering and Operations Management. IJCIEOM 2020. Springer Proceedings in Mathematics & Statistics, vol 337. Springer, Cham., pp 205–213.
- [2] D. Macii, D. Petri, "Guidelines to manage measurement uncertainty in conformance testing procedures", IEEE Transactions on Instrumentation and Measurement, v. 58, n. 1, p. 33–40, (2008).
- [3] A. M. Helmenstine, "Random Error vs. Systematic Error." ThoughtCo, Aug. 28, 2020, thoughtco.com/random-vs-systematic-error-4175358, last accessed 07.21.2023.
- [4] F. Attivissimo, A. Cataldo, L. Fabbiano, N. Giaquinto, Systematic errors and measurement uncertainty: An experimental approach. Measurement, 44(9), 1781-1789, 2011.
- [5] J.-A. GOULET, I. F. C. SMITH, Structural identification with systematic errors and unknown uncertainty dependencies. Computers & structures, 128: 251-258, 2013.
- [6] Y. YANG, S. ZHANG, Adaptive fitting of systematic errors in navigation. Journal of Geodesy, 79: 43-49, 2005.
- [7] P. Bhandari, "Random vs. Systematic Error | Definition & Examples", Scribbr. Retrieved July 19, 2023, from <https://www.scribbr.com/methodology/random-vs-systematic-error/> last accessed 07/21/2023.
- [8] V. Petre, "Introduction to microcontrollers and programmable automata", "Introducere in microcontrolere si automate programabile", MatrixRom Publishing House, 2010.
- [9] C. Ionescu Golovanov, Measurement of electrical quantities in the power system, Măsurarea mărimilor electrice în sistemul electroenergetic, Technical Press and Romanian Academy Press, 2009.
- [10] C. Zet and C. Fosalau, "Generating Programmable Analog Signals using FPGA," 2019 International Conference on Electromechanical and Energy Systems (SIELMEN), Craiova, Romania, 2019, pp. 1-4.

Integrated System for Remote Health Status Monitoring and Analysis

Marian-Ștefan Nicolae *, Florentina-Fulgina Bîzîc †, Nicolae-Leonide Sîrbu †, Iurie Nucă ** and Raluca-Cristina Presură (Nicolae)**

* University of Craiova/IEEA, Craiova, Romania, nmarianstefan@yahoo.com

† University of Craiova, Faculty of Electrical Engineering, Craiova, Romania

** University of Craiova, Electrical and Energetic Eng. Doctoral School Dept., Craiova, Romania

Abstract - With the emergence of new types of diseases and viruses that can affect the human immune system, different types of vaccines and treatments have been developed to combat the new threats. Various technical methods have been developed to monitor the health status of a patient suffering from a certain ailment in order to certify the efficacy of a given treatment scheme. A way to monitor the health condition of a patient is proposed, based on the Arduino platform. The prototype can transmit data collected from a sensorial system and store them to a web server. The system is designed to monitor human body temperature with three temperature sensors placed on the head, body and lower limbs to obtain the average body temperature; an oximeter sensor for simultaneously monitoring the heart rate and the blood oxygen level of a patient; and two sensors for measuring indoor air quality, namely a gas sensor and a temperature and humidity sensor. This last sensor determines if a given bacteria or virus can thrive in the environment. A specialized software program was used to create the remote health monitoring prototype, which was subsequently manufactured using a 3D printer. The prototype is resilient and efficient, being appropriate for long-term use.

Cuvinte cheie: monitorizarea stării de sănătate, comanda unui sistem de senzori, soluție IoT integrată.

Keywords: health status monitoring, sensorial system control, integrated IoT solution.

I. INTRODUCTION

The literature in the area of health status monitoring offers a variety of solutions. Our capacity to solve problems, interact with one another, and handle everyday issues has undergone a paradigm shift as a result of new trending technologies like powerful industrial microcontrollers, Internet of Things (IoT), cloud computing, machine learning (ML), among others [1].

Temperature, breathing, and heartbeat (or pulse) are just a few of the human vital indicators that a remote health monitoring system can identify.

In [2] is suggested to use a mobile application-based health monitoring system. The suggested technology gives the patient's doctor and family members access to the patient's location and some current health parameters. With the help of graph tools, mobile applications may monitor their surroundings and connect to the internet via 3G or 4G wireless cellular networks.

A system that can collect patients' heart rates and body temperatures and save data in the cloud is provided in [3].

When compared to an electrocardiogram (EKG) equipment, the system underwent testing and displayed a similar accuracy.

The field of telemedicine has also advanced quickly, and the present research focus is on remote monitoring and the detection and analysis of human health status indicators [4].

II. HEALTH MONITORING SYSTEM COMPONENTS

An IoT-based patient health monitoring system using ESP8266 and Arduino is developed, able to process and transmit data collected from a sensorial system to a remote server. The system was designed with a dedicated program for a 3D printer, and the prototype was then realized to prove the usability of the proposed solution.

The proposed system is able to measure the heart rate/pulse (BPM), as well as the blood oxygen level (SpO₂), using the MAX30100/102 pulse oximeter sensor. Some DS18B20 temperature sensors are used to measure the average body temperature. The temperature and humidity inside a room are detected with a DHT11 Humidity and Temperature sensor. The MQ-135 sensor is needed for monitoring the noxious gas levels that can affect the air quality inside a room.

The monitoring system is made of the components from Fig. 1. The IoT platform used for the data storage and analysis is ThingSpeak [6].

Arduino UNO is a development board based on the ATmega328 microcontroller. The Arduino UNO has 14 digital input/output pins (of which 6 can be used as PWM outputs), 6 analog inputs, a 16 MHz quartz oscillator, a USB connection, a power jack, an ICSP jack [7].

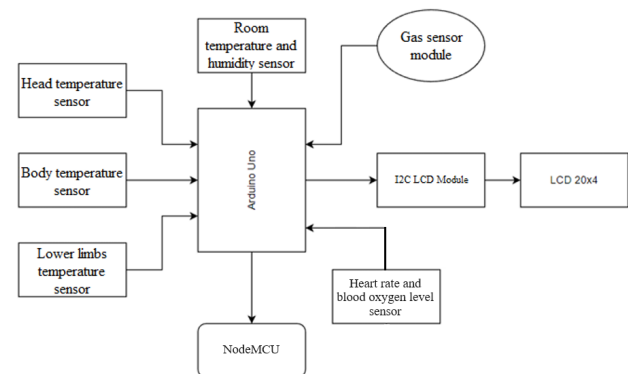


Fig. 1. The block diagram of the proposed health monitoring system.

NodeMCU is an open source IoT platform used for adding networking capabilities to Arduino UNO. At first it included ESP8266 Wi-Fi SoC firmware from Espressif Systems and hardware based on the ESP-12. Later, support for the ESP8266/ESP32 was added [8], [9]. The NodeMCU development board is depicted in Fig. 2.

We use three DS18B20 temperature sensors to measure the average temperature of the human body, collecting data from the head, body and lower limbs.

Similarly, a patient needs to be kept in a room having a certain temperature and humidity level. Hence, the patient does not feel uncomfortable in the room. To do this we also need to monitor the room temperature and humidity. So we use the DHT11 Humidity and Temperature sensor.

The pulse sensor is an essential component of the system, allowing the user's heart rate to be constantly monitored [10]. The data obtained from this sensor provided valuable information about the person's cardiovascular health, as well as the level of physical activity and effort exerted during exercise. Detection of heart rhythm abnormalities, such as tachycardia or bradycardia, could signal serious health problems and the need for immediate medical intervention.

On the market are available many different types of health monitoring systems, including those based on Arduino and Zigbee technology for widespread health monitoring. The technology of the testing system should be optimized nonetheless, as there are now more health testing data available.

Systems that employ sensors, link gadgets, and the Internet to achieve a better level of automation can be created thanks to remote servers like ThingSpeak. IoT has the ability to completely change patient management and monitoring in the healthcare industry [5]. Silent monitoring is essential in an intensive care unit, as even a small delay in deciding how to treat a patient might result in death or lifelong health issues.

Emergency warnings may be delivered to medical personnel and caregivers in the event of changes in a patient's health, to enable timely intervention. This technique makes it feasible to identify medical emergencies before they become serious.

In Fig. 3 are gathered the main electronic components of the proposed system, along with the required supply voltage sources and the connections between them.

The Internet of Things (IoT) is a system of "connected things". Things generally include an embedded operating system and an ability to communicate with the Internet or neighboring things. One of the key elements of a generic IoT system that connects different "things" is an IoT service. An interesting implication of the "things" that comprise IoT systems is that the things themselves cannot do anything. At a minimum, it should have the ability to connect to other "things".

The real power of IoT is harnessed when things connect to a "service" either directly or through other "things". In such systems, the service plays the role of an invisible manager, providing capabilities ranging from simple data collection and monitoring to complex data analysis.

ThingSpeak IoT software allows users to create new and private channels to collect analyzed data. Analysts can read data from public channels and then transfer them to custom channels [6]. The platform allows users to write

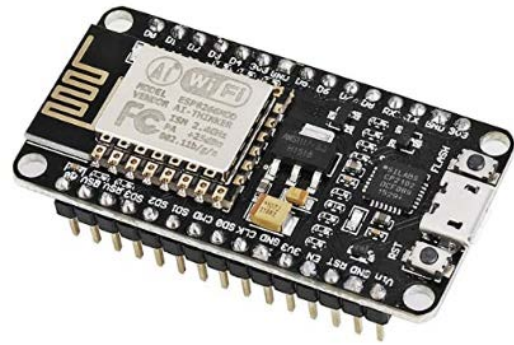


Fig. 2. Top view of NodeMCU [9]

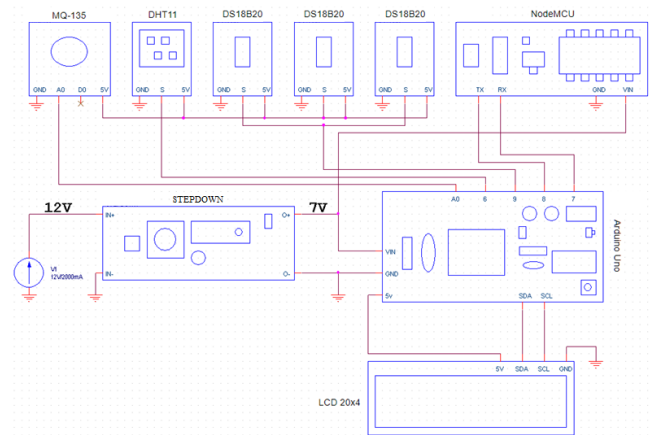


Fig. 3. Simplified electronic diagram of the proposed circuit.

data to their ThingSpeak channels in various formats such as REST API, MATLAB, MQTT or with third-party applications. These protocols allow experts to share telemetry information.

Meteorologists can read temperature and humidity data from various weather channels and view the results on their private channels. Using MATLAB, they visualize trends, plot histograms, calculate dew points from raw data, and forecast changes in weather patterns.

ThingSpeak IoT helps users share analyzed data with public channels. The settings panel allows users to view more options on their channels. The tab shows sharing options that will allow the user to set their channel as private, public (everyone can see it), or shared with specific users. Professionals can also import or export data on their channels.

The DS18B20 from Fig. 4, a waterproof digital temperature sensor, is a reliable temperature sensor that provides an adjustable 9 to 12-bit thermometer using a 1-wire interface [11].



Fig. 4. The prototype of the DS18B20 sensor used for measuring the average body temperature [11].

Data is sent to/from the DS18B20 via a 1-wire interface, so only one wire (ground) needs to be connected from a central microprocessor to the DS18B20. It provides power for reading, writing and temperature conversions. The values can be derived from the data bus itself, without the need for an external power supply.

Because each DS18B20 contains a unique serial number on silicon, multiple DS18B20s can exist on the same 1-wire bus [12]. This allows temperature sensors to be placed in various places.

The MQ-135 air quality sensor from Fig. 5 is used to measure the air quality inside the room where the patient is placed [13]. Gas levels may be transmitted to an LCD screen or to a ThingSpeak channel, on which various warning messages may be displayed.

The air quality is constantly monitored with the developed system, so that the amount of toxic gas, smoke or alcohol cannot become dangerous for the patient. In case the gas level is exceeded, an alarm is triggered.

A thermistor is a sensitive thermal resistor that uses resistance values to determine temperature. It is comprised of a semiconductor, and when subjected to temperature changes, its physical resistance changes.

The DHT11 sensor from Fig. 6 is used for measuring ambient temperature and humidity, factors that decide whether the environment is conducive to certain bacteria or viruses [14].

The MAX30100 pulse sensor from Fig. 7 is a combined heart rate and blood oxygen sensor [16]. The sensor is meant to monitor blood oxygen levels and the pulse using photoplethysmography, a non-invasive technique.

The sensor is an integrated photodetector and LED emitter. Infrared (IR) and red light are emitted by the LED emitter, and the photodetector gauges how much light is reflected off the user's skin. For the purpose of detecting variations in blood vessel volume during the pulse, photoplethysmography is used. The sensor detects fluctuations in the absorption of infrared and red light as the pulsing blood moves through the arteries.

An oled display is used to display information about heart rate [bpm] and the oxygen saturation [SpO₂] collected from the oximeter, as in Fig. 8.



Fig. 5. MQ-135 gas sensor module [13].

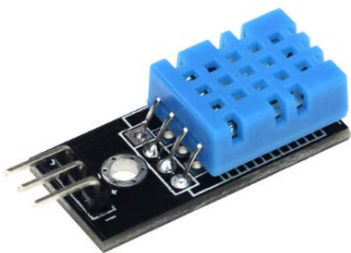


Fig. 6. DHT11 sensor module [15].

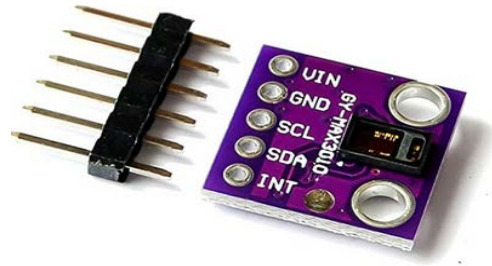


Fig. 7. The structure of the MAX30100 pulse sensor [17].



Fig. 8. The OLED Display used to monitor the pulse sensor [18].

III. DESIGN OF THE HEALTH MONITORING SYSTEM

The proposed system is based on two Arduino boards and a NodeMCU, and has four different components that act as a whole for the health monitoring.

Each subsystem was previously developed and tested with Fritzing, an open-source hardware package that makes electronics available to anybody as a creative environment [19].

After developing and testing each subsystem, they were added together as parts of the health monitoring system.

A. Body Temperature Sensor Subsystem

In Figure 8 is depicted the 2D schematic of the body temperature sensor, consisting of:

- the Arduino UNO development board;
- 16x2 LCD display. An I²C was used to save pins. By using it, only two pins to power the display were used, and opened up the possibility to connect other sensors to the display. To use I²C, it was necessary to use the related library in the code;
- the DS18B20 sensor, to which a 4.7k Ω resistor was connected. This resistor was used to enable the sensor's internal pull-up resistor to ensure proper communication between the sensor and the microcontroller.

The body temperature sensor is an important component of the monitoring system. It allows the detection and monitoring of fever, a significant indicator of infections and other conditions.

By monitoring the body temperature in real time, the system can provide early alerts if the temperature rises above the normal limit, signaling possible respiratory infections or systemic diseases. Thus, it can contribute to prompt intervention and initiation of appropriate treatment.

A pull-up resistor is a resistor connected between a signal line and a positive voltage source (VCC) for the purpose of providing a logic high (HIGH) level on that line in the absence of an active command.

B. Ambient temperature sensor subsystem

The subsystem used for monitoring the ambient temperature and humidity, based on a DHT22 sensor, is depicted in Fig. 9. As with the subsystem used to determine the body temperature, in addition to the sensor itself, a switch powered from digital pin number 8 of the Arduino UNO board was added, aiming to reduce the waiting time for the sensors to display on the LCD, making it more practical to select any sensor and use it as long as needed.

The ambient temperature and humidity sensor brings an extra dimension to the health monitoring. It was designed to measure the level of humidity and air pollution in the environment. Air quality and humidity levels can affect a person's respiratory health and overall well-being. By detecting and monitoring high levels of humidity or the presence of air pollutants, the system can provide warnings or recommendations related to improving air quality and preventing respiratory ailments.

C. Gas sensor subsystem

The subsystem of the gas sensor MQ-135 from Fig. 10 was designed to display the gas level on the LCD. An LED was also added to digital pin number 5 of the Arduino UNO board. Pin 5 was defined as an output pin, to which a 1 k Ω resistor was added, in order to limit the current that passes through the led and to protect it against any overvoltage.

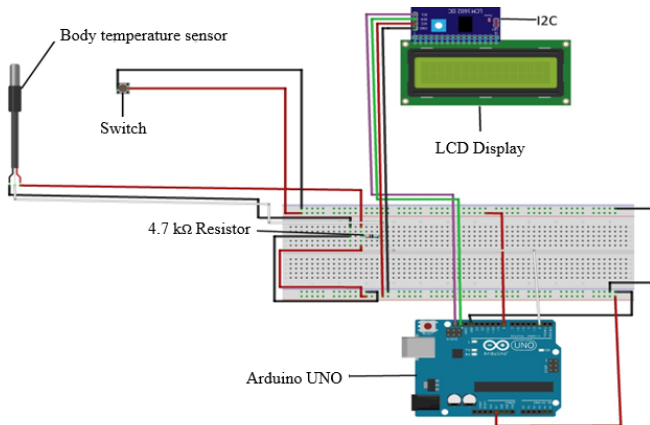


Fig. 9. Diagram of the body temperature sensor subsystem.

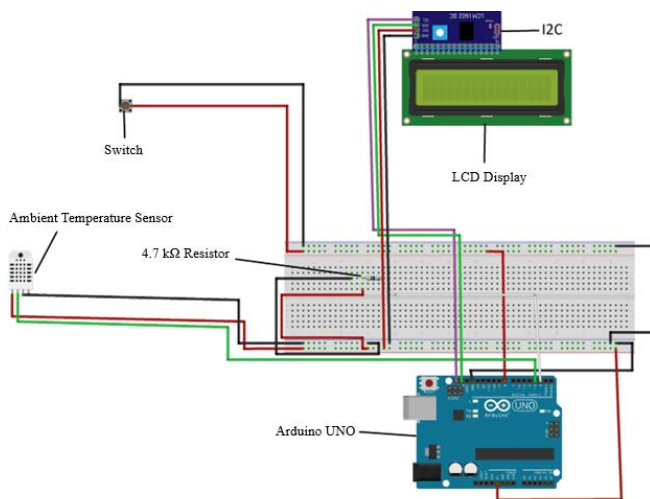


Fig. 10. Diagram of the ambient temperature sensor subsystem.

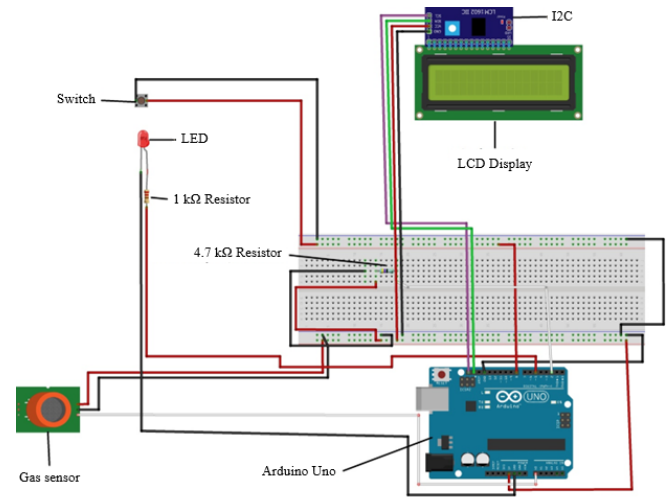


Fig. 11. Diagram of the gas sensor subsystem.

The use of the gas sensor is an important measure to prevent and manage the increased levels of polluting gases in the air. This sensor can detect the gas level in the room and issue warnings or alerts if the detected value is above the permissible limit. This aspect is of particular importance in preventing accidents caused by gas leaks, as well as in promoting a responsible and healthy approach to the quality of the air breathed by the patient.

D. Pulse monitoring subsystem

The pulse monitoring sensor subsystem from Fig. 11 differs from the other subsystems, as it could not be implemented on the same Arduino Uno board. With a second board available, a separate circuit was implemented, due to the limited memory capacity of the first board, which started to create interference between the pulse sensor, ambient temperature sensor and the LCD display.

The new Arduino board offers enough space to implement an OLED display that would display the desired information separately from the other sensors, as in Fig. 12. An OLED display was chosen due to its additional functions, such as creating an animation. The second Arduino board is powered from the first board with a 5V voltage.

E. The Whole Health Monitoring System

The main components of the whole health monitoring system are depicted in Fig. 13. These are a pulse monitoring sensor (MAX30100), three body temperature sensors

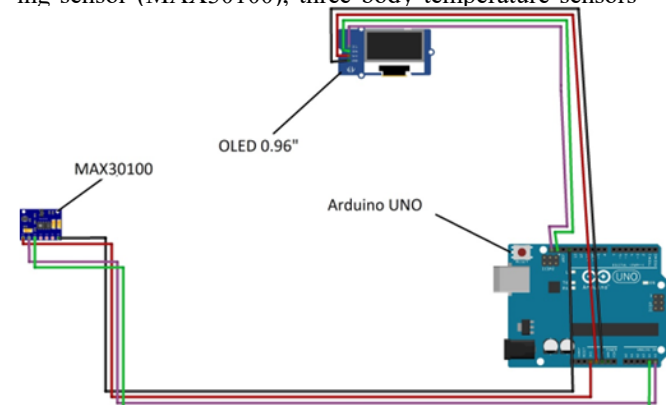


Fig. 12. Diagram of the pulse monitoring subsystem.

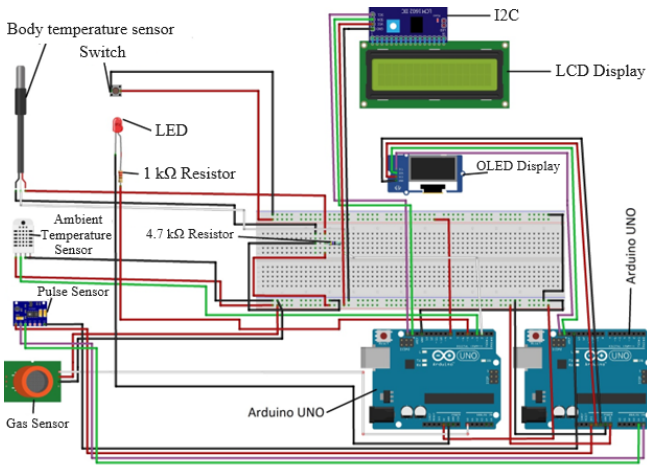


Fig. 13. Main components of the health monitoring system.

(DS18B20), an ambient temperature and humidity sensor (DHT22), a gas detection sensor (MQ-135), two Arduino UNO development boards, one LCD display (16x2), one I2C circuit, one OLED display, one Switch, some LEDs and some 4.7kΩ and 1kΩ resistors.

IV. DEVELOPMENT OF THE PANEL AND PREPARATION FOR 3D PRINTING

The designed health monitoring system was further developed, in order to integrate all the components in a prototype, with the aid of a 3D printer.

At first, a sketch with the panel size of 200x200mm was created. Then the mounting holes with a diameter of 5mm and the holes for the temperature sensors and the MQ-135 sensor, as in Fig. 14, were added.

The extrude function was used to raise the wall by 3mm. The sketch was designed using the Fusion 360 software package, as in Fig. 15.

In Fig.16.a) is depicted the final design, while Fig.16.b) depicts the sketch imported by the 3D printer software package.

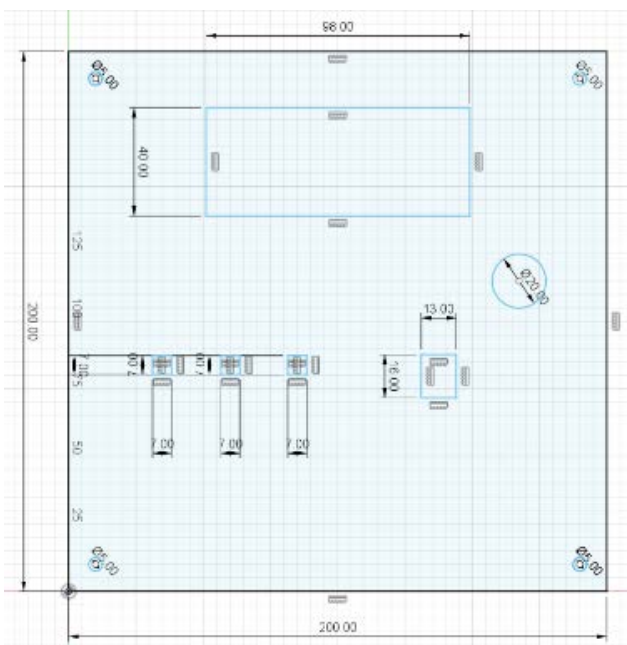


Fig. 14. 2D view of the panel in Fusion 360.

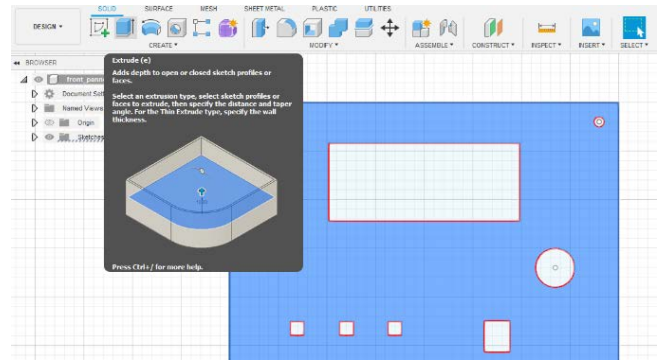


Fig. 15. Sketch design steps.

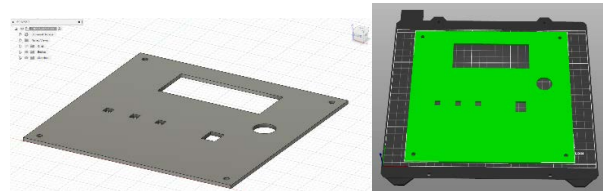


Fig. 16. The final 3D design of the sketch with Fusion 360 – (a) and The design imported by the 3D printer software – (b).

After compiling the data for a print with a layer thickness of 0.2mm, we get a print time of 6 hours and 41 minutes and a print material consumption of 132.58 grams.

V. THE EXPERIMENTAL SETUP AND THE RESULTS COLLECTED FROM THE THINGSPEAK IOT PLATFORM

The system developed according to the Fritzing design was successfully implemented, and an overview of the laboratory prototype is depicted in Fig. 17.

The sensor readings were correct, so the next step was to build the health monitoring system from Fig. 17, as a compact solution that may be used under real world conditions.

The system was built by adding together the 3D printed mechanical components with the electric and electronic parts. In this manner, a robust and compact system was obtained, suitable for long-term use.

Data provided by the developed health monitoring system can be stored and displayed on a personal computer, using the Arduino IDE and an LCD, or remotely, via a ThingSpeak channel, provided by the MATLAB server.

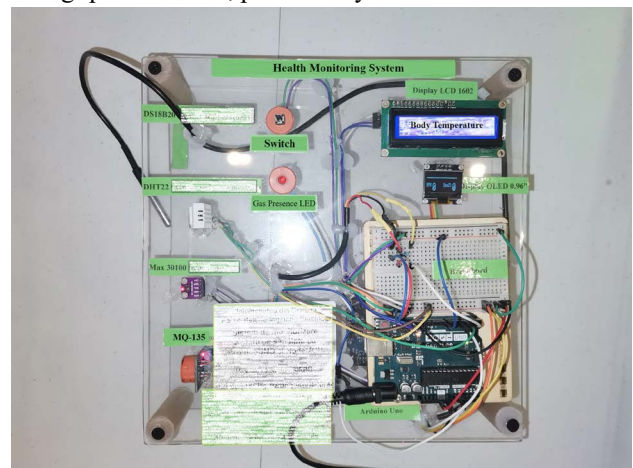


Fig. 17. Overview of the implemented health monitoring system.

In Fig. 18 may be noticed the variation of the room temperature over time, resulted from the data collected by a ThingSpeak channel.

Fig. 19 depicts the variation of the average body temperature, based on data collected from the three sensors.

One or more persons can permanently examine the data gathered from the three temperature sensors on the ThingSpeak channel to keep an eye on the patient's condition.



Fig. 18. The experimental IoT system built for health monitoring.

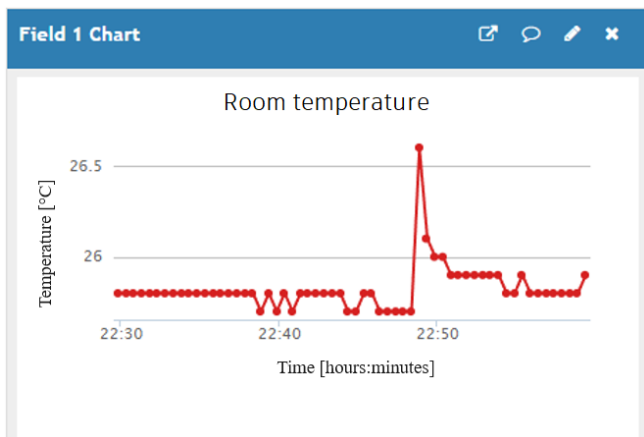


Fig. 19. Time variation of the room temperature [6].

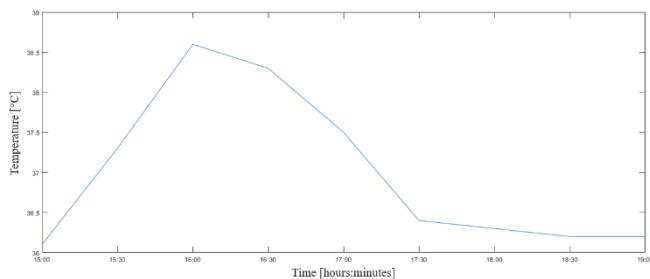


Fig. 20. The average human body temperature.

In case a threshold value imposed for one of the sensors is exceeded, an alarm may be triggered.

CONCLUSIONS

Such a system has several benefits. Real-time monitoring of the body temperature, pulse and oxygen level, on one hand, and room temperature, humidity and air quality, on the other hand, allows for the prompt identification of any changes or abnormalities that may indicate health issues requiring immediate attention.

By using the personalized notifications and advice provided by the system, users can take the necessary steps to maintain their health condition and prevent problems.

Room environment is also important, being monitored in order to ensure that it contains no smoke, while the temperature and humidity are ideal for a patient.

The suggested health monitoring solution is resilient and an effective way to remotely monitor certain vital signs that could point to a patient's health changing.

In addition to the obvious benefits for people, such a system can aid in the gathering of data for study and analysis. The monitored data can be utilized to spot patterns and trends in the development of health status and can offer important details to help with better condition diagnosis and care.

Based on the collected data, the system can provide a preliminary result, according to which the patient is infected or not.

The possibility of storing data collected from such a system for a longer period of time may lead to proving whether a treatment is effective or not.

ACKNOWLEDGMENT

Source of research funding in this article: Research program of the Electrical Engineering Department financed by the University of Craiova.

Contribution of authors:

First author – 30%

First coauthor – 20%

Second coauthor – 20%

Third coauthor – 15%

Fourth coauthor – 15%

Received on November 3, 2023

Editorial Approval on November 15, 2023

REFERENCES

- [1] A. Nduka, J. Samual, S. Elango, S. Divakaran, U. Umar and R. SenthilPrabha, "Internet of Things Based Remote Health Monitoring System Using Arduino," 2019 Third International conference on I-SMAC (IoT in Social, Mobile, Analytics and Cloud) (I-SMAC), Palladam, India, 2019, pp. 572-576.
- [2] E. O. Tartan and C. Ciflikli, "An Android Application for Geolocation Based Health Monitoring, Consultancy and Alarm System", 2018 IEEE 42nd Annual Computer Software and Applications Conference (COMPSAC), Tokyo, Japan, 2018.
- [3] E. A. -A. Karajah and I. Ishaq, "Online Monitoring Health Station Using Arduino Mobile Connected to Cloud service: "Heart Monitor" System," 2020 International Conference on Promising Electronic Technologies (ICPET), Jerusalem, Palestine, 2020, pp. 38-43.

- [4] X. Zhang and L. Liu, "Technical Optimization of Physical Fitness and Mental Health Monitoring System under the Background of Big Data," International Conference on Forthcoming Networks and Sustainability in AIoT Era (FoNeS-AIoT), Nicosia, Turkey, 2021, pp. 105-109.
- [5] P. Anirudh, G. A. E. S. Kumar, R. P. Vidyadhar, G. Pranav and B. A. Aumar, "Automatic Patient Monitoring and Alerting System based on IoT", 2023 8th International Conference on Communication and Electronics Systems (ICCES), Coimbatore, India, 2023, pp. 328-331.
- [6] [***https://thingspeak.com/](https://thingspeak.com/) accessed on August 25th 2023.
- [7] [***https://store.arduino.cc/products/](https://store.arduino.cc/products/) accessed on August 25th 2023.
- [8] [***https://en.wikipedia.org/wiki/NodeMCU](https://en.wikipedia.org/wiki/NodeMCU) accessed on April 28th 2023
- [9] [***https://www.amazon.in/Easy-Electronics-NodeMcu-Development-Board/dp/B06XYRS6KC](https://www.amazon.in/Easy-Electronics-NodeMcu-Development-Board/dp/B06XYRS6KC) accessed on April 28th 2023.
- [10] M. A. A. Razali, M. Kassim, N. A. Sulaiman and S. Saaidin, "A ThingSpeak IoT on Real Time Room Condition Monitoring System", IEEE International Conference on Automatic Control and Intelligent Systems (I2CACIS), Shah Alam, Malaysia, 2020, pp. 206-211.
- [11] [***https://images.theengineeringprojects.com/image/webp/2019/01/Introduction-to-DS18B20.jpg.webp?ssl=1](https://images.theengineeringprojects.com/image/webp/2019/01/Introduction-to-DS18B20.jpg.webp?ssl=1) accessed on April 28th 2023.
- [12] Z. Runjing, X. Hongwei and R. Guanzhong, "Design of Temperature Measurement System Consisted of FPGA and DS18B20," 2011 International Symposium on Computer Science and Society, Kota Kinabalu, Malaysia, 2011, pp. 90-93.
- [13] [***https://www.optimusdigital.ro/en/gas-sensors/1128-module-sensor-de-gaz-mq-135.html](https://www.optimusdigital.ro/en/gas-sensors/1128-module-sensor-de-gaz-mq-135.html) accessed on August 28th 2023.
- [14] N. Karna, D. L. Lubna and S. Y. Shin, "Air Quality Measurement Device Using Programmable Quadcopter Drone Towards Internet of Drone Things", 2021 International Conference on Information and Communication Technology Convergence (ICTC), Jeju Island, Korea, Republic of, 2021, pp. 753-758.
- [15] [***https://www.jiomart.com/p/homeimprovement/srs-sprout-robotic-solutions-dht11-temperature-and-relative-humidity-sensor-module-diy-kit/599558122](https://www.jiomart.com/p/homeimprovement/srs-sprout-robotic-solutions-dht11-temperature-and-relative-humidity-sensor-module-diy-kit/599558122) accessed on August 28th 2023.
- [16] [***https://www.electronicwings.com/components/max30100-pulse-oximeter-and-heart-rate-sensor](https://www.electronicwings.com/components/max30100-pulse-oximeter-and-heart-rate-sensor) accessed on September 1st 2023.
- [17] [*** https://www.sigmanortec.ro/senzor-puls-optic-gy-max30102](https://www.sigmanortec.ro/senzor-puls-optic-gy-max30102) accessed on November 2nd 2023.
- [18] [*** https://cleste.ro/ecra-oled-0-96-inch.html](https://cleste.ro/ecra-oled-0-96-inch.html) accessed on November 2nd 2023.
- [19] [***https://fritzing.org/](https://fritzing.org/) accessed on August 28th 2023.

Equipment for the Detection of People Falling

Constantin-Daniel Oancea

National University of Science and Technology Politehnica Bucharest, Bucharest, Romania, daniel.oancea@upb.ro

Abstract - There are people whose state of health requires permanent supervision. There are a number of medical or aging-related conditions that can have quite an impact on the daily life of these people, therefore, in order to provide them with proper assistance and care, various health monitoring devices have been developed. This article proposes the use of advanced technologies with the help of which we can observe and record the changes in the position of a person with such problems. The equipment has a sensor that can determine the position of the body by measuring the height from the ground. The device can be integrated into a belt or bracelet to record data in real time. This data is analyzed and interpreted by means of a program. The program can detect changes in posture, providing notifications and alerts when the person has suffered a fall. Greatly simplifying surveillance, the device also provides an objective assessment of a person's balance ability. Since each person has a specific posture and movement, the developed device must be tested and adapted to adjust the coefficients in the program, to avoid the triggering of false events.

Cuvinte cheie: stare de sanatate, gradient de presiune, echilibru posturii.

Keywords: state of health, pressure gradient, posture balance.

I. INTRODUCTION

Many older adults experience balance problems and dizziness. Problems can be caused by certain medications, balance disorders, or other medical conditions. Balance problems are one of the reasons older people fall. Maintaining good balance as you get older and learning to prevent falls can help with walking, ensuring independence and carrying out daily activities. Several of the body's organs, including muscles, bones, joints, eyes, balance organ in the inner ear, nerves, heart, and blood vessels, must function normally for normal balance to exist. When they don't work well, they can cause balance problems for people. Many medical conditions can cause balance problems. Also, aging is a degenerative process that affects most organs and therefore balance problems are more present in the elderly people. This device helps those responsible for the care and assistance of patients, and sends alerts in case of important changes in position (such as after a fall), so that it can be observed by anyone who has access to the created web interface. The device have an advanced technology (in terms of design and algorithm) capable to detect the variation of pressure in direct correlation with height, combining a very good precision sensor, whose essential role is to measure parameters such as body position, [1], [2]. Data is broadcast in real time, in specified time interval, signaling when there is a problem. Equipment can distinguish between fall of person and the small pressure variations that the sensor can detect when the person in question moves, climbs stairs, etc. The device is created in such a way that it reaches a minimalistic

size so that it can be integrated as easily as possible into a bracelet or a belt. With the help of software that provides not only alarms or the detection of abnormal changes in movement posture, but also an objective assessment of the balance of the person concerned. An unusual change in posture is identifying by permanently measuring distance toward ground. If essential changes happen, the warning signal is triggered.

II. SENSITIVE DEVICE USED

A. Sensors

Almost every aspect of life, including safety, surveillance, monitoring and general awareness, requires the development and use of sensors. The use of equipment and devices for diagnosis, monitoring, patient care and public health ensures greater safety and objectivity in decision-making. Smart sensors are those that process data and obtain relevant information, such as time evolution of parameters outside intervals or connectivity to a repository for data storage. Proximity sensors, for example, come in a variety of varieties, including capacitive, photoelectric, magnetic, and inductive. For the considered device, height measurement is used, for which, in a first phase, sensors can be used to measure the distance. Distance sensors are often confused with proximity sensors for their similar functions, the functions of each sensor can be misunderstood most of the time.

In the present work, a pressure sensor is used, which uses the phenomenon of pressure drop with height increase. Thus, the pressure gradient is monitored and if a certain limit is exceeded, this is signaled. Pressure gradient sensors are devices used to measure the pressure difference between two points in a fluid or gas. Medical, aviation and other industrial applications are areas where these sensors can be used. Gradient sensors work by detecting pressure differences between two points in a fluid or gas. Pressure gradient sensors are divided into two types: piezoelectric sensors and differential pressure sensors. The pressure difference is measured by piezoelectric sensors, which convert the pressure into an electrical signal. The sensors are extremely sensitive and can detect very small pressure variations. Differential pressure sensors, on the other hand, use a measuring element that is sensitive to the pressure difference between a reference and the measuring point. Because they have lower sensitivity, these sensors are cheaper and easier to manufacture than piezoelectric sensors, [3]. Air pressure is determined by the weight of the air column at that point, or it can be said that it is determined by the density of the atmospheric air column at that point. It is considered that the atmospheric pressure varies depending on the temperature. If we consider that the air column at a point decreases as the altitude increases, the result is a decrease in atmospheric pressure with height, Fig. 1, [4].

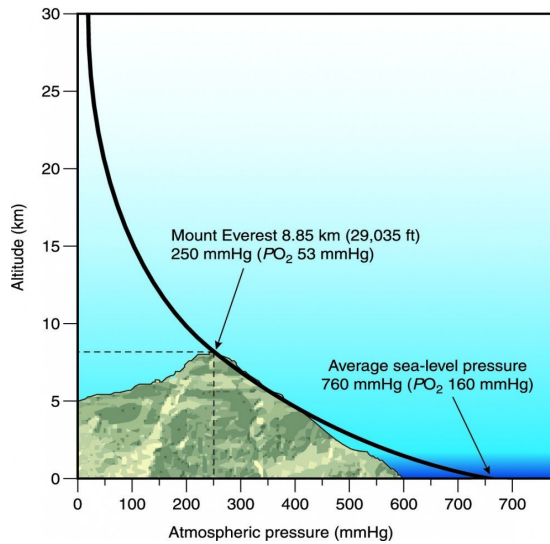


Fig. 1. Pressure gradient vs. altitude, [4].

At sea level, the average atmospheric pressure is about 1013 hPa, which is equal to 1 atmosphere (atm) or 14.7 psi. (pounds per square inch). Make sure that depending on the weather conditions, the atmospheric pressure can vary a lot in time and altitude. In general, if the weather conditions are stable, the atmospheric pressure decreases by approximately 1 hPa for every 8 meters of altitude, [5], [6]. Information about the pressure sensor used and how it works is present in the next section.

B. SPL06-001 Sensor

The sensitive pressure sensor SPL06-001 with high accuracy is to measure the pressure in the atmosphere and make the difference between any abnormality such as normal walking, wind, climbing stairs, etc. and a fall. The SPL06-001 sensor is a miniaturized digital barometric pressure sensor as well as a temperature sensor. The sensor is characterized by high precision, and is great for mobile and portable devices. This pressure sensor is based on a capacitive sensing principle that ensures high accuracy during temperature changes. The internal signal processor of this sensor converts the output of the pressure and temperature sensors into 24-bit results. Pressure sensor accuracy is ± 0.006 hPa (or ± 5 cm) (high precision mode), according with specifications, [9], [10], [11].

III. APPLICATION

The code is written in Python, chosen for its simplicity and for the fact that this programming language has the possibility of intrinsically managing a website. The application starts with the import of the libraries, each one being important for its function. Communication between the sensor and the Raspberry Pi is done via SMBus, a two-wire interface based on the I2C protocol, is used to communicate with the I2C sensor.

The "time" library provides functions to handle the necessary timings. The "ctypes" library is used to define certain data types in communication with certain hardware devices. The last but the most important is request library can make requests to web servers, with the help of sending and transmitting data through HTTP and HTTPS protocols (It can be used Django or Flask framework).

The pressure values will be continuously read through the infinite while loop, and if there are different values in the list, the pressure value will be added to the event list and a corresponding text will be displayed. The algorithm will check if the message is negative, clear the past values displayed and add the current value, which may indicate a new patient fall. The user interface can be as intuitive as possible, easy to use, in the form of a web interface, Fig. 2.

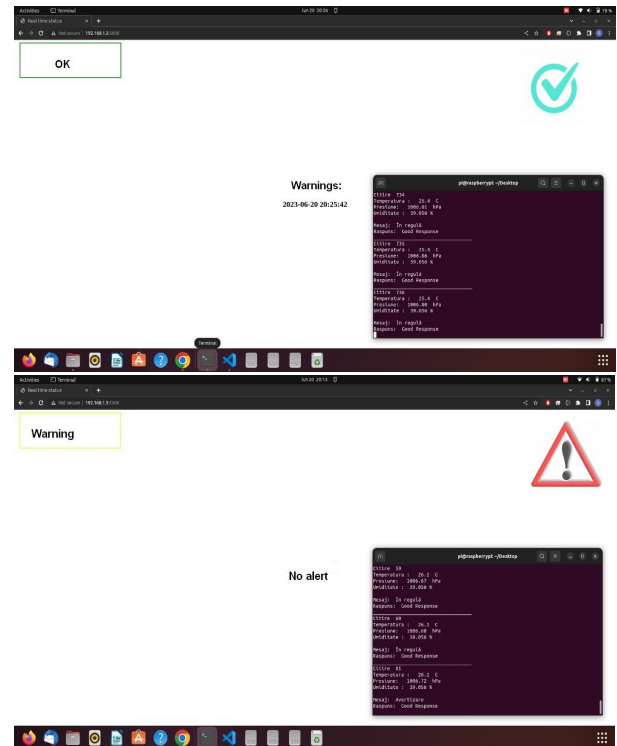


Fig. 2. Aspects of interfaces (OK – top; Warning – bottom).

In the lower right part you can see the event log. There are also visual warning elements on the interface (distinctive signs), but the application can be easily expanded for external warnings (sounds and optics).

IV. EQUIPMENT DESIGN

The two main components of the equipment are the pressure sensor and the embedded system such as Raspberry Pi or equivalent, Fig. 3. The sensor and Raspberry Pi are connected via digital interface. Raspberry Pi has the role of a small computer on which the application is located. The sensor data can be transmitted to a web interface, or to an alarm, which has the role of signaling any type of patient fall. The web interface will not only receive the sensor data, but also the alerts that will be able to confirm the alert and remain on record to know the date and time of each such event, Fig. 4. In the flowchart, "A" represents the current reading and "B" represents the average of the previous readings. When the device is turned on, the first step it will go through is calibration. Calibration is done through the first readings of the pressure sensor, which establishes the reference value for the current location and current conditions, and ends up having approximately the same pressure after each reading. After calibration, normal sensor readings will follow that will arrive in the ready

state, each reading being compared to an average of thirty units less than the current value, [6], [7].

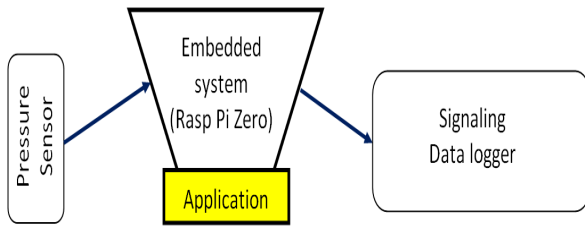


Fig. 3. Block diagram of equipment.

If the reading is less than the threshold of three units (as the difference), the circuit will resume reading, so that the next reading will be taken to the initial state, where it will be compared with a value that is at least ten units higher. If this condition is not met the reading resumes and if the current reading is greater by at least thirty units then the reading will enter the "warning" state.

These values were chosen empirically, for a stable operation of the equipment. These thresholds can be modified and customized depending on the patient.

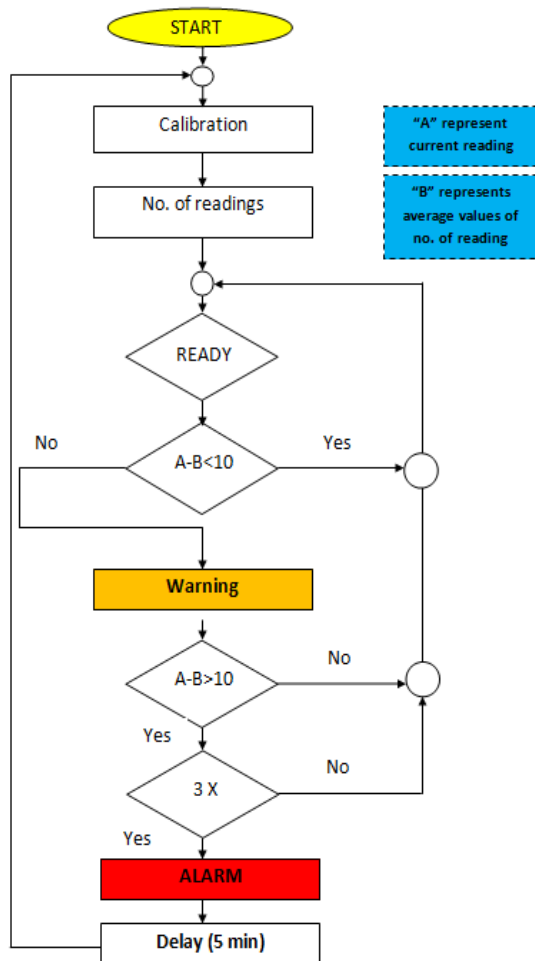


Fig. 4. Flow chart of application.

The threshold is set to every ten centimeters so as to result in an average, to have an average error that represents the pressure differences in the atmosphere, whether we are talking about normal walking, climbing the stairs or going down them, [8].

The warning state shows us that the value transmitted by the sensor is quite high and that it can only represent an anomaly so that it would return to the ready state again, or if there are at least three consecutive readings that end up entering the warning state, these will alert in real time an alarm, representing the patient's fall.

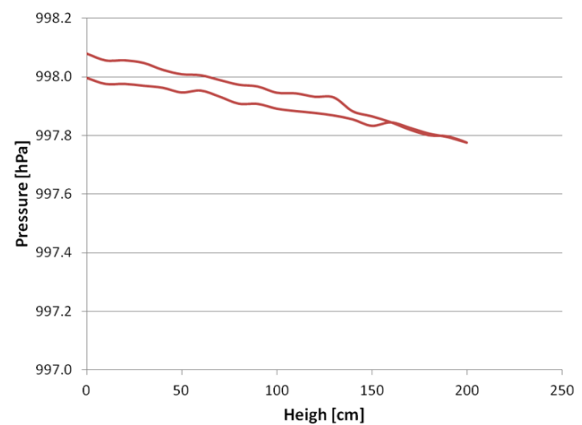


Fig. 5. Experimental results.

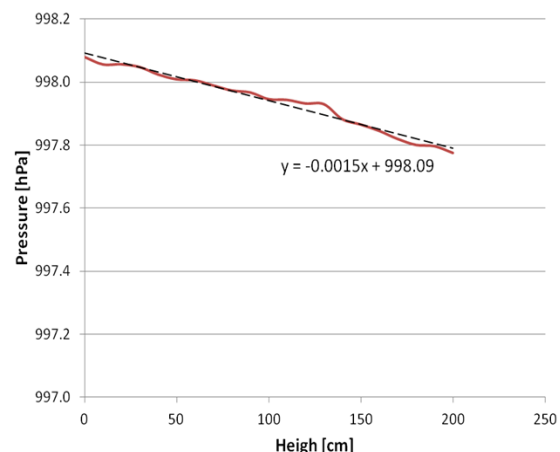


Fig. 6. Experimental data in ascending and descending order, to highlight hysteresis errors.

In the situation where the sensor has reached the alarm state, the data to be read and passed through the same process are no longer taken into account, the alarm representing the most important point at which a reading can reach. The alarm condition lasts until cleared by resetting the sensor and repeating all of the above steps, or lasts up to five minutes if not cleared by restarting the calibration process. After the five minutes in which the alarm is not turned off by anyone, it will be recorded on the applica-

tion with the date and time it occurred, even if it will no longer be in an alarm state, so that it can be viewed at a later time.

V. RESULTS AND COMMENTS

After fully understanding the operation of the sensor and the variation of pressure with height, measurements were made readings every 10 cm until 200 cm, Fig. 5. The actual value that the sensor reads to observe the rise and fall of pressure, at different heights, was obtained by averaging, the sensor being influenced by events such as sudden movements, gusts of wind, etc.

From these experimental results became, by linear regression, an ideal characteristic, presented on the same picture, Fig. 5. This can be useful when develop application, to increase estimation of events occurs. The presence of the hysteresis error was also analyzed, Fig. 6.

As can be seen, this is present especially towards the initial value (0 cm) from where the evaluation is made. The pressure drop with height is not smooth, due to various factors (the sensor provides a very good resolution on 24 bits of the pressure measurement, which causes excessive sensitivity to any influence such as air movement or positioning accuracy in front of the landmark). Arithmetic average is the most suitable because it can be easily seen that although different phenomena occur, it is kept as correct, there is the possibility of events that change the pressure at a certain height especially during normal walking, events such as sudden movement or walking more quickly and this leading to an error in the measurements. A series of averages were done to see which one is the most suitable, such as shifting average which is the calculation method that is based on consecutive values.

Another possible formula is the statistical average, which selects the median value of the entire data read. A possible comparison between these values leads to improved performance by choosing the best averaging method. Hysteresis error uses the classic formula, applied in the worst case (here at 0 cm height), (1). Hysteresis error occurs when the measured value (such as pressure) is increasing or decreasing and may not be the same in both directions, [11], [12], [13]. In this case, this error is about 27%. Even this error is significant, it can be reduced, but it is also useful to avoid any false alarm (decreased sensitivity).

$$\epsilon_h [\%] = \frac{|p_{mM} - p_{mm}|}{|p_{max} - p_{min}|} * 100 \quad (1)$$

The explanations of quantities are: $|p_{mM} - p_{mm}|$ is the absolute maximum difference of pressure, observed from the graphic representation; $|p_{max} - p_{min}|$ represents absolute difference between maximum and minimum pressure for which the variation characteristic was established.

Experimental setup consists of a measuring tape, Raspberry Pi Zero W to which the pressure sensor is connected, a plier set that allows positioning (from 10 by 10 cm) on the measuring tape, Fig. 7.

Data acquired use two relation to make mean of measured pressure: median (statistical) and average (arithmetic) formulas, Table I.

There is some difference between results because mean formula is different.



Fig. 7. Aspect of experimental setup, to establish pressure vs. height correlation

Also was use relative pressure because this value is used by algorithm to make decision.

TABLE I.
SOME SAMPLES OF DATA ACQUIRED

Height [cm]	Pressure [hPa]			
	Statistical	Relative statistical	Average	Relative average
100	997.9746	0.217674	997.9463	0.170828
110	997.9578	0.200874	997.9440	0.168592
120	997.8901	0.133167	997.93256	0.157092
130	997.9107	0.153807	997.9302	0.154794
140	997.8777	0.120766	997.8826	0.107219
150	997.8836	0.126652	997.8656	0.090145

Considering a pressure sensor, hysteresis would be the error in the measured value immediately after pressure is applied to the sensor, before the system responds. Once the pressure sensor eventually reaches a steady state, the error is reduced. This error can be reduced in this application by increasing the interval between readings, the measurement time, but this may affect the response time. The sooner the occurrence of an event in which a difference in a patient's posture is observed, the better the delayed intervention of the medical staff will be avoided. The device can be made in a more compact way, using the smallest representative of the Raspberry Pi family, the Raspberry Pi Pico. Components of entire equipment are reasonable in terms of weight and sizes, Fig. 8, Fig. 9, Fig. 10.

The device can be used alone or expanded with the sampling of other signals, outline more complex equipment for patient monitoring.



Fig. 8. Sensors, Raspberry Pi Zero and power bank.

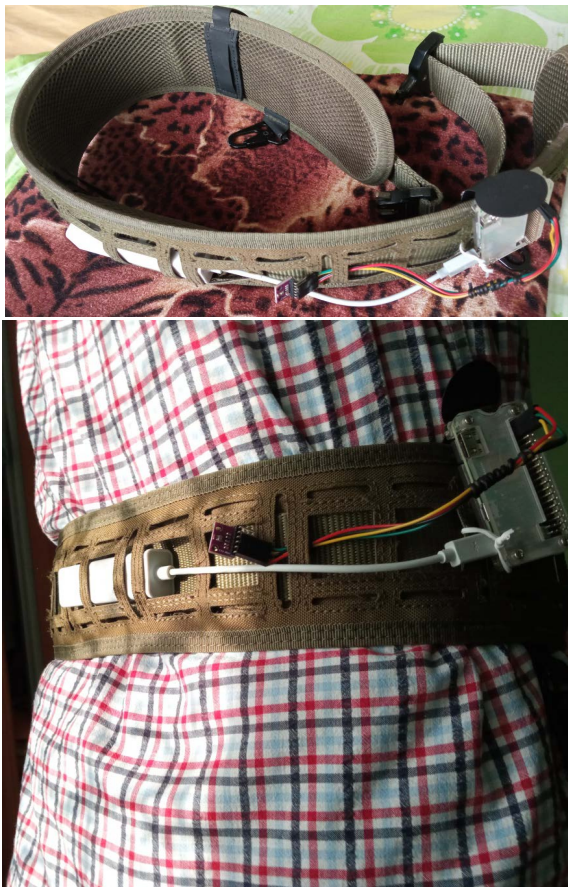


Fig. 9. Fixing the equipment on the belt.

The entire equipment can be carried in the pocket, belt or bracelet. The power bank supply with 5 V the equipment and ensure an operating time according with its capacity. According with specifications Raspberry Pi Zero consumption is about (various versions and situation): idle - ~ 65 mW, W idle - ~ 0.6 W, 2 W idle - ~ 1.4 W, stressed - ~ 1 W, W stressed - ~ 1.85 W, 2 W stressed - ~ 2.9 W. If go further we have possibility to use Raspberry Pi Pico, and in this case we have, at power supply of 3.3 V, the following results: WiFi connected: 43 mA, WiFi connected and answering remote ping requests: around 60mA.



Fig. 10. Bracelet version of balance monitoring device.

For example, a power bank of 5000mAh can be use in condition of 1.5 W consumption (intensive use of Raspberry Pi Zero board) almost 24 hours (ideal condition and not complete discharge the power bank because this operation can damage it). In case of using Raspberry Pi Pico, three weeks is operating time. An optimization is needed between operation time, charging of battery, and weight of equipment.

Because of low-voltage operating (3.3 – 5 V), the equipment is safe in operation. To avoid short circuit between sensor pads and GPIO pins, or bending them, the hardware components must be fixed in a box.

VI. CONCLUSIONS

Equipment developed use low-cost components and software application use friendly programming IDE (Python). Also the design of the equipment took into account that it should be robust and accurately signal any event that indicates an important change in a patient's posture.

Was choosing Python for integrated web framework; more than two possibilities to use this facility: Django and Flask. Django is high-level, full-stack framework used for quickly developing clean-looking apps. Flask is a micro web framework written in Python. It is classified as a micro framework because it does not require particular tools or libraries.

To detect changes in distance to the ground, pressure sensors was chosen, because has been exploited the gradient of pressure vs. the height (altitude). In the development of the algorithm, situations that can generate false alarms were taken into account, such as climbing stairs and occasional pressure variations (such as those due to opening a door). This differentiation between the situations that appear was solved by means of mediation, repeating data reading and counting operations. Quantitatively, these operations were established experimentally.

Remarkable is the accuracy of pressure sensors SPL06-001; actually was necessary to decrease this accuracy (24 bits) because o stability of readings.

Also a hysteresis error was noted, but is beneficial in this case because for small variation (e.g. for stepping movement), the signal is more stable.

Developments of the application can be considered the possibility of adjusting the parameters in the program interface, the possibility of presenting events in the form of a diagram, and the extension of the application to mobile devices.

To increase duration of operation it is possible to deactivate some unnecessary peripheral like LED indicator on Raspberry Pi board, or use Wi-Fi connection only when is needed. Also it is possible to use idle facility of Raspberry Pi board, and in this case operation time can increase significant (one week in case of Raspberry Pi Zero).

Entire developed equipment is a starting point for improvements.

ACKNOWLEDGMENT

Source of research funding in this article: Research program National University of Science and Technology Politehnica Bucharest

Received on June 30, 2023

Editorial Approval on November 17, 2023

REFERENCES

- [1] D. Andritoi, C. Luca, I. Onu, C. Corciova, R. Fuior, A. Salceanu, D.-A. Iordan, "The Use of Modern Technologies in Post-COVID-19 Cardiopulmonary Rehabilitation", *Applied Sciences*. 2022; 12(15):7471.
- [2] C. Corciova, R. Ciorap, D. Matei, A. Salceanu, "Design an Impedance Plethysmography System for Measuring Limb Blood Flow", in: Jobbágy, Á. (eds) 5th European Conference of the International Federation for Medical and Biological Engineering. IFMBE Proceedings, vol 37. Springer, Berlin, Heidelberg, 2011.
- [3] A. M. Bădescu, O. Fratu, A. Frujină, S. Halunga, I. Marcu, *Wireless Sensor Network for Wildlife Monitoring*, *Environmental Engineering & Management Journal (EEMJ)* . Nov2011, Vol. 10 Issue 11, p1625-1634. 10p.
- [4] <https://www.scienceabc.com/eyeopeners/ears-pop-airplane-takes-off-landing-air-pressure-difference.html> last accessed Nov. 4th 2023 [3]
- [5] S. Jena, and A. Gupta, "Review on pressure sensors: a perspective from mechanical to micro-electro-mechanical systems", *Sensor Review*, Vol. 41 No. 3, pp. 320-329, 2021.
- [6] M. V. Paulet, O. M. Neacsu and A. Salceanu, "Wireless monitoring system of the heart rate," 2014 International Conference and Exposition on Electrical and Power Engineering (EPE), Iasi, Romania, 2014, pp. 581-584.
- [7] C. Fosalau, I. A. Iftode and C. Zet, "A New Respiratory Rate Sensing Principle Based on Magnetic Amorphous Wire Micro-transformers," 2021 International Conference on e-Health and Bioengineering (EHB), Iasi, Romania, 2021, pp. 1-4.
- [8] C. Fosalau, C. Zet and D. Petrisor, "Implementation of a landslide monitoring system as a wireless sensor network," 2016 IEEE 7th Annual Ubiquitous Computing, Electronics & Mobile Communication Conference (UEMCON), New York, NY, USA, 2016, pp. 1-6
- [9] E. A. Haering, Jr., "Air Data Measurement and Calibration", NASA Technical Memorandum, December 1995.
- [10] D. Tandeske, "Pressure Sensors: Selection and Application", CRC Press, 1990.
- [11] <https://www.avnet.com/wps/portal/abacus/solutions/technologies/sensors/pressure-sensors/> last accessed 07/09/2023
- [12] D. Mihai, "Designing an experimental platform for the air pressure in a small tank by digital control," 2016 International Conference on Applied and Theoretical Electricity (ICATE), Craiova, Romania, 2016, pp. 1-8.
- [13] C. Ionescu Golovanov, *Measurement of electrical quantities in the power system*, Măsurarea mărimilor electrice în sistemul energetic, Technical Press and Romanian Academy Press, 2009.

Experimental Study of the Pressure Exerted in the Body of a High-Voltage Fuse and Metal Enclosed Switchgear

Cristian-Eugeniu Sălceanu, Cătălin Dobrea, Daniel Constantin Ocoleanu, Daniela Iovan
National Institute for Research, Development and Testing in Electrical Engineering – ICMET Craiova, Romania,
lmp@icmet.ro, pramlmp@icmet.ro, pdaniela@icmet.ro

Abstract - This article presents the importance of analyzing the breakdown behaviour of high voltage fuses and highlights the pressure values at the fuse ends. The theoretical basis, test scheme structure, design and sizing elements of fuse components, and numerical simulations performed in Matlab/Simulink are presented. The extinguishing environment is not modelled as it is considered to be a vacuum. Starting with the oldest overcurrent protection device and continuing with the importance of high voltage fuses for operational safety, the study presents the behaviour of high voltage fuses during short-circuit current interruption. The key element is the value of the pressure on the contacts of fuses, which is often ignored in favour of the pressure of the middle element. When fuses change from solid to liquid state the inner parts are hotter than the outer parts and melt first, and the melting zone extends to the periphery. The study found that the pressure is much higher and is an important value for designers. Experiments showed that the maximum pressure is reached during the arcing period, a significant finding for the design process of the contacts of a high-voltage fuse. The research was then extrapolated to check the pressure in metal enclosed switchgear containing fuse combinations.

Cuvinte cheie: *siguranțe de înaltă tensiune, presiune, curent de scurtcircuit, timp de arc electric, element fuzibil, celule electrice, combinație separator-siguranțe fuzibile*

Keywords: *high-voltage fuses, pressure, short-circuit current, arcing time, fuse element, switchgear, load break switch-fuse combination.*

I. INTRODUCTION

The oldest protection device against high currents is the fuse and today it is still the main protection used in many applications due to its high reliability at voltages starting from 7.2 kV to 66 kV. The design of fuses is apparently simple, but the phenomena that occur during its operation are quite complex. For this reason, fuse research and development has tended to rely on empirical methods, requiring a great deal of expensive experimentation and testing. To overcome this, the current global trend is to turn this empirical research into science.

Standards used by the applications with fuses are constantly improved, but the basic parts remained unchanged for more than half of century [1-5]. Electrical systems nowadays require higher short-circuit power concentration and space limitation; therefore, modern fuses operate at the maximum technical limits for which they were designed. Increasing of the safety requirements

mean safety limits decrease and the smallest selection error can have serious consequences [6-12].

Fuses are found in many electrical circuits around the world and their main function is to protect electrical equipment such as distribution transformers, motors and capacitor banks from overload currents.

One of the global objectives is to design fusible seals that will operate safely in air with limited heat dissipation when used in gas insulated switchgear.

The fuse has to detect and isolate the faulty equipment from the rest of the circuit, therefore it is connected in series with the protected equipment. The simplest fuse consists of a metal wire connected between two insulated supports. Modern fuses are encased in a ceramic enclosure and the fuse wires are mounted inside an insulating support, they are also equipped with a striker, a signaling device that also acts as an actuator for other electrical devices. The ceramic casing is filled with an arc-quenching exothermic material that is most commonly quartz sand. Other metal components may be made of copper, iron, brass, and can be silver-plated or nickel-plated and must be capable of functioning under the thermal, mechanical, or electrical conditions encountered in service.

Medium-voltage switchgear equipped with load-break switches and fuses (combinations) in metal enclosures are common and reliable, and their design limits the mechanical effects of excessive pressure surges. In order to assess the effects of pressure on the metal envelope, experiments were carried out on the unsuccessful opening of fuses which were deliberately designed with defects and which did not limit short-circuit currents, thus creating pressure in the metal envelope.

II. LITERATURE REVIEW

The behavior of fuses at maximum breaking current has been extensively analyzed over time. The fuse wire melting process is shown in Fig. 1.

At the end of the liquid phase (the pre-arc period) the voltage increases exponentially, as shown in Fig. 1. The moment when the voltage rate begins to increase abruptly marks the beginning of the arc period. Heat continues to grow even though the current has dropped up to that moment. The metallic coherence within the wire is interrupted, before the material is completely vaporized, and an arc is formed [1,3, 9-16]. Researches [8,13] have shown that devices without serious manufacturing defects and with symmetry within tolerable limits will most likely melt in the central region, as suggests the temperature distribution on the metal element.

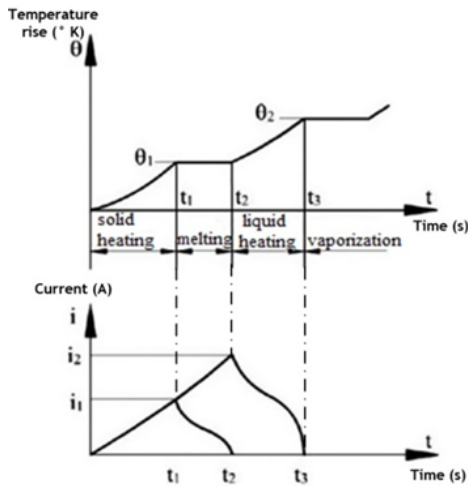


Fig. 1. Fuse wire melting process

Quartz sand fuses with metal parts. Fuse melting leads to metal droplets and vapors that dissipate into the rest of the ceramic casing, creating a gap and instantly initiating the arc [14].

Thermal ionization of the containing medium contributes to arc formation. If there is only air in the ceramic case, when the arc flashes expand, they create both high temperature and high pressure in the plasma, therefore an active medium. The size of the arc is a rapidly changing as a function of the burning rate of the metal parts (arc elongation). This process leads to rapid increase in the electrical resistance of the arc and its eventual extinction [1-3,7,9]. Another study of plasma-wall interaction [6] shows that the electrical conductivity of the plasma σ is basically given by the current (i) and the voltage (u), assuming that the plasma fills the ceramic casing with a given radius R :

$$\sigma = \frac{i}{u} \frac{l}{\pi R^2} \quad (1)$$

Doubts arise whether this phenomenon will occur regularly or whether the cylinder of liquid will explode under the mechanical action of vapor pressure. [3, 9, 16, 17]. From specialized literature it is known that a cylindrical wire completely melted by an electric current passing through is subjected to a pressure directly related to the surface energy and a magnetic pressure created by the electric current. The magnetic pressure will be higher at the smaller diameter of the fused wire. A cylindrical, current-carrying liquid conductor stretched in air deforms into a series of globules (wavelets) as a result of surface tension and magnetic pressure. Small arcs will occur between these globules if the source voltage of the circuit is high enough. This phenomenon is called "multiple arcs" [1-3, 10, 16]. For this situation the following equations have been used for the calculation of the magnetic pressure:

$$P_B = \frac{B^2}{2\mu_0} \quad (2)$$

$$B = \mu_0 \frac{I}{2\pi r} \Leftrightarrow P_B = \frac{\mu_0 I^2}{8\pi^2 r^2} \quad (3)$$

where μ_0 is the magnetic permeability constant:

$$P_B = \left(\frac{10^{-7}}{2\pi r^2} \right) I^2 = kI^2 \quad (4)$$

This parabolic equation explains the graph: $P_B = f(I)$.

The evaporation process of the molten wire creates a column of metal vapor in an air environment that expands very rapidly due to the pressure created by this vapor [16]. Theoretical and experimental studies of melting wires have shown that fusible elements can overheat in the liquid state after reaching the evaporation temperature under atmospheric conditions [18-20]. At the actual evaporation temperatures, the metal vapor column has a much higher resistance than that of the fusible element at the same temperature but in liquid state. The safety resistance in this case is determined by the cross-section of the metal vapor column, the length of the column and the specific resistance of the ionized metal vapor. Experiments have shown that the cross-section of the metal vapor column is dependent on the current [1, 2, 16-23].

Arcing occurs in the metal vapor column and it is a self-sustained electrical discharge in which the plasma is at high temperature, high pressure, and the surrounding environment is in local thermodynamic equilibrium. The most important characteristic of the arc is its temperature [1-3, 16, 23]. Under these conditions, a low electric field strength is required to maintain a high electron density and also there is little electrode drop [1-3, 23].

In the literature, the methods used to determine plasma temperature are generally those described in [2, 6, 22], but research findings vary. The work of these authors focuses on materials other than copper, such as silver and aluminum.

Chikata et al along with Cheim and Howe [7] estimate that the temperature remains constant throughout the phenomenon at about 20000 K and 24000 K, and the electron density is about 10^{18} cm^3 . Saquib [20] noticed a drop from the maximum temperature of 22000 K generated by the arc to 15000 K 4.1 ms later. Maximum electron density was $2 \times 10^{18} \text{ cm}^3$.

In paper [6] the values obtained point a maximum temperature at about 21000 K and a decrease to 11000 K at the end of the arc period, the temperatures are evaluated using the Boltzmann diagram, the electronic density differentiated by other researchers has a maximum value of $2 \times 10^{19} \text{ cm}^3$. In the experiments and research of M.J. Taylor were observed and described the fragmentation of exploding wires and the formation of plasma [24-26]. During his experiments, he mainly used capacitor-based pulsed power supplies and also made time measurements of the voltage on the wire and the current. The wire material used was high purity copper (99.9%) with larger geometric characteristics (1.0 mm in diameter, with a length ranging from 150 to 180 mm). These experimental results showed the change in resistance and plasma formation and expansion of the current and voltage waveforms of the used pulses by X-ray imaging, photographic study and measurement [27-32]. Detail of the development of plasma spots was studied using photographic images.

There are papers [35] which highlight the conflicting claims of [37] to [33] and explain the consequences with regard to the use of fuses in combination with circuit breakers containing sulphur hexafluoride as an extinguishing medium. In fact, important and well-

established applications for fuses are virtually excluded by [37].

Alternative proposals for resolving the conflicting situation in International Standards are presented.

In the medium-voltage ring network configuration, the typical medium-voltage switchgear of medium-voltage and low-voltage substations is a compact and often non-extendable 3-function RMU, consisting of two interrupting switchgear units plus a protection unit connected to the medium-voltage/low-voltage transformer. The protection unit can be a combination circuit breaker-fuse or a circuit breaker. For such public distribution applications, the protection of medium-voltage/low-voltage transformers by a combined medium-voltage circuit-breaker/fuse provides an optimised solution. The circuit breaker/fuse has its place in smart grid investments [35].

The main objective of the paper [36] is to experimentally investigate the DC switching characteristics of a combination DC circuit breaker. The DC circuit breaker is a combination of a DC isolator and a fuse and is preferred in some DC switching applications.

III. EXPERIMENTAL TESTING FOR PRESSURE VERIFICATION

It has been observed that the temperature level of the phenomena caused by breaking is between 2000 K±3000 K and the current densities can subject any material to excessive stresses.

This article presents an experiment in which the values of the pressure exerted from the inside on the fusible fuse contacts and the porcelain outer casing are evaluated. The fuse is a classic design where the extinguishing medium is quartz sand.

The lower end of the fuse (without striker) has a special port to accommodate a pressure transducer (Fig. 2).



Fig. 2. High voltage fuse bottom contact

It was then fitted with an STS Sirmach ATM pressure sensor – Fig. 3.

The pressure sensor used in the experiments and mounted on the high-voltage fuse (Fig. 3) has the following technical characteristics: pressure measuring range: 2÷25 bar; analogue output: 0÷10 V; supply voltage: 15÷30 Vdc; operating temperature: -25÷85°C; accuracy: $\leq 0,5 / \leq 0,25 / \leq 0,1$; response time: ≤ 1 ms.

The acquisition system (Fig. 4) consisted of single-channel HV 6600 analog-to-digital converters (ADC) coupled via fiber optics to a high-speed transient recorder (TR) with a sampling rate of 25 MS/s at 16-bit resolution.

The acquisition system has an analog +/-0-100 VDC input, fully galvanically isolated with fiber optics and high immunity to electromagnetic interference. Perception software platform compatible with HBM GENESIS ac-

quisition system. The correlation between pressure and voltage in the experiment: $2\div 25 \text{ bar}/0\div 10\text{V} \Rightarrow 2,3 \text{ bar/V} \Rightarrow p = 2,3 * (P_{out}) + 2$ pressure sensor.

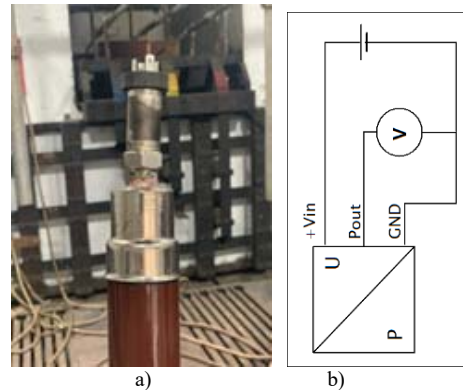


Fig. 3. Pressure sensor (a) pressure sensor mounted on high voltage fuse; (b) pressure sensor wiring diagram

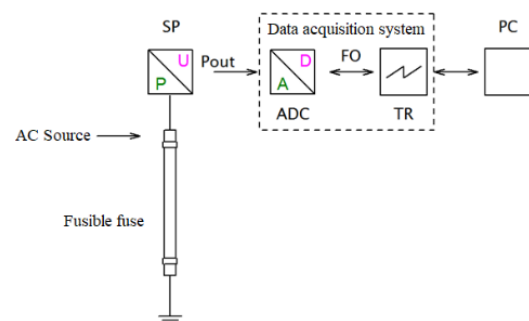


Fig.4. Data acquisition system

The circuit shown in Fig. 5 was used in the experiments and consists of: G - high current AC source 2500 MVA generator; XR - shock coils with 400 mΩ; MB1, MB2, MM – switchgear (MB1-master breaker computer controlled, MB2 – master protection breaker set to work after 200 ms, MM – master maker set to close in the zero of voltage to obtain the maximum peak of current); T - 80 MVA step-up transformers; R-C - transient recovery voltage regulation circuit (200 mΩ and 87 μF); O1 - current measurement; O2 - transient recovery voltage measurement; O3 - source voltage measurement; O – the tested fuse (24 kV, 25 kA, 50 A) equipped with pressure measurement as in Fig. 4.

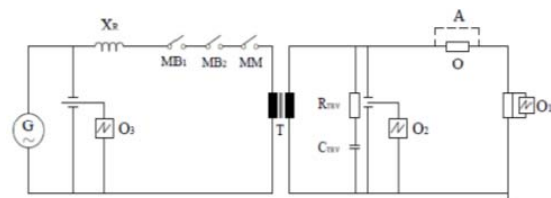


Fig.5. Circuit used in experiments

The signals from the current, voltage, and pressure transducers are acquired by an automatic measuring system and further processed.

Before the experiments, the same circuit was developed in MATLAB Simulink and the oscillograms in Fig. 6 were obtained.

The extinguishing environment was not modelled in the simulation because it was considered empty. The voltage and current values, taking into account the connection at

an angle of $\varphi=18$ electrical degrees, are consistent with the assumed values, but the values obtained for the pressure are several times higher than the assumed value.

As we have already seen, the stresses that act on the porcelain casing of a fuse when an overcurrent occurs are: dielectric, thermal and mechanical, due to the pressure that builds up inside.

Almost everything is known about the dielectric stresses caused by operating overvoltage, but very little is known about the thermal and mechanical stresses, because the design of thermal and pressure transducers needs to be adapted. Making this structural adjustment is not easy, and these expensive transducers can be destroyed if the fuse blows.

Also, any design modification of the fuse body that deviates from the standard conditions and its characteristics may affect the breaking behavior, but there is no alternative.

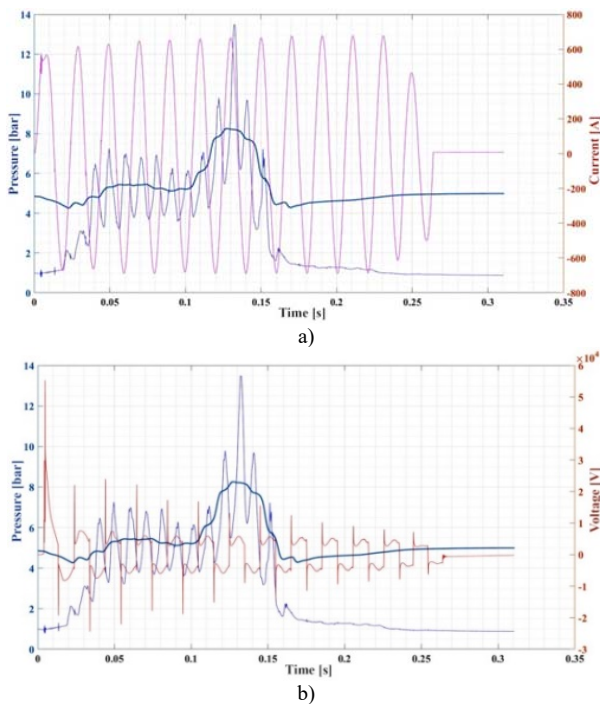


Fig. 6. Oscillograms obtained from pressure simulations as a function of current (a) and voltage (b)

Measuring the pressure inside the fuse body can only be done invasively, and it is known that the porcelain casing of fuses is tested at a static pressure that can withstand several tens of atmospheres, but the processes during the breaking of a current are dynamic, resulting in much higher pressure shocks that lead to its rupture. Normally, when the current is correctly interrupted, the pressure in a fuse does not exceed 2 bar when the fuse melts, which is completely harmless for the casing and the caps, regardless of the arc energy developed, except, of course, for the thermal stress.

What happens inside the fuse if the arc fails to extinguish within 3-4 ms after being initiated? This can be seen graphically in Fig. 7 when a pressure surge in excess of 30 bar occurs with devastating effects on the fuse and surrounding equipment. In the experiment shown in Fig. 7, a breaking test is performed for a current of 14 kA_{rms}, assumed at a voltage of 36 kV_{rms} under the conditions defined by [33].

In the first part of the experiment, the fuse tries to limit the short-circuit current to a value of 5.6 kA in accordance with its limiting characteristic, but the conditions for extinguishing the arc in 3-4 ms were not met, and since the arc energy is high, 165 kA²s, it leads to the explosion of the fuse. It can be seen how the high energy creates a pressure surge of more than 30 bar, causing the fuse body to break and the arc to last until the end of the test.

For comparison with Fig. 7, Fig. 8 shows an ideal test in which the fuse interrupts with minimal arc energy (area A) and another test, Fig. 9, in which a higher energy B is developed that cannot generate dangerous pressure on the fuse body.

Fig. 10 shows a low-amplitude (500A_{rms}) current breaking test for a fuse also equipped with a pressure transducer. The fuse, according to the limiting characteristic, should cut the current in about 10 ms, but it fails and the arc lasts for 260 ms, leading to thermal rupture of the fuse body (see Fig. 11) without the pressure exceeding 3.5 bar and pulverizing the fuse body, as happened in the experiment in Fig. 7.

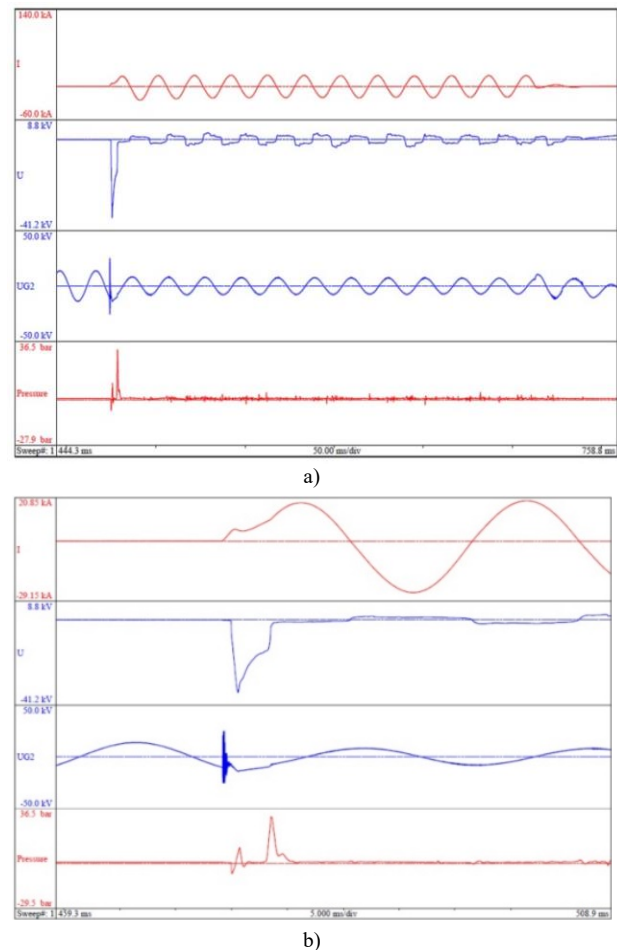


Fig. 7. Oscillogram obtained from practical experiment (a) full duration of the current; (b) zoom on the occurrence of current

Values obtained at a current making angle of $\varphi=48.4^\circ$: $I_f=5.6$ kA; $I_{rms}=14.1$ kA; $t_k=0.24$ s; $P=31.4$ bar; $U_c=35.4$ kV; $t_{pa}=0.8$ ms; $t_{arc}=3.5$ ms; $E_{total}=170.4$ kA²s; $E_{arc}=165$ kA²s.

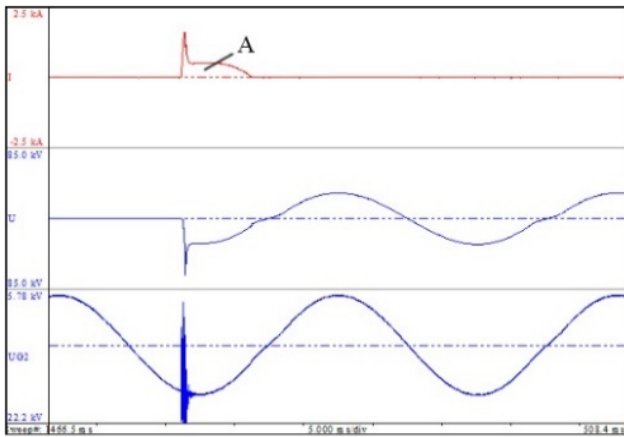


Fig. 8. Normal fuse behavior

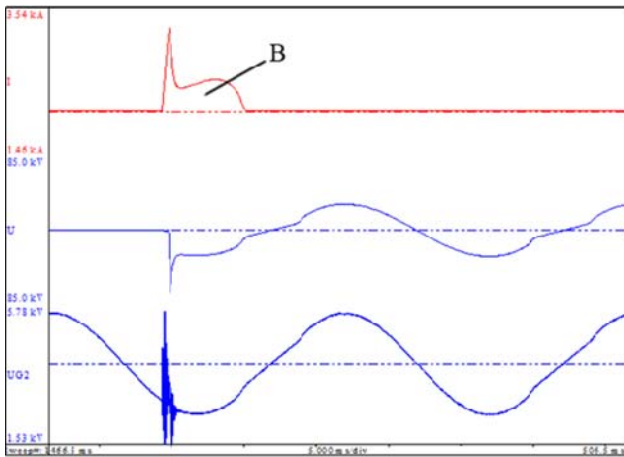


Fig. 9. Experiment on the release of high energy

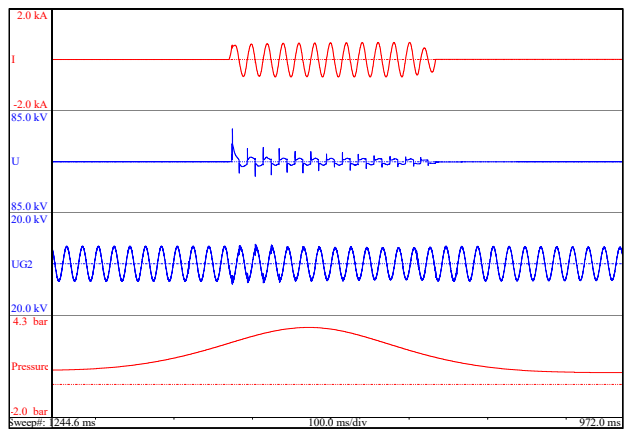


Fig. 10. Experiment for checking pressure

Fig. 10 shows the values obtained at a making angle of $\phi=7.1^\circ$: $I_{pk}=0.57$ kA; $U_c=55.2$ kV; Energy = 55.1 kA²s; $t_k=0.26$ s; $P=3.3$ bar.

The real-life values obtained are higher (the pressure is 31.4 bar compared to 8 bar obtained in simulation, rest of the values are similar) than those obtained in simulation, because in the simulation it was not considered the extinguish environment.

The literature points that the maximum pressure point is in the middle of the fuse, proven wrong by real life experiments with pressure measurements and high-speed video recording. The maximum pressure is obtained at the extremities of the fuse.

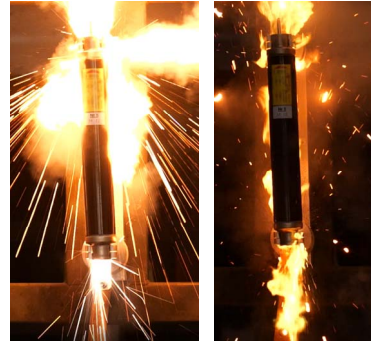


Fig. 11. Experiment for checking pressure

IV. EXPERIMENTS TO VERIFY THE PRESSURE IN SWITCHGEAR WITH FUSE COMBINATIONS

It is well known that successful breaking of high currents does not create dangerous pressures in the fuse body. For the purpose of the experiments, fuses were designed with imperfections so that they could not limit and break the current, and the metal envelope of the switchgear was fitted with a membrane to limit the pressure during the short-circuit. Pressure transducers have also been fitted to the body of the metal envelope to measure envelope pressures.

The values of these pressures generated in the envelope depend very much on the value of the short-circuit currents and their duration as well as the shape and volume of the envelope.

The values of these pressures are not known in the theory, because the electric arc that generates the pressure has an unpredictable evolution due to the electric circuit, the insulating parts and the ferromagnetic walls of the envelope and the electromagnetic forces that occur.

In addition to the pressure transducers, the sealed metal envelope is equipped with a valve (diaphragm) that bursts at a certain pressure level, preventing it from reaching values of tens of bars and limiting its disintegration with consequences and losses in the installation.

The experiments include tests strictly complying with the requirements at different parameters: $I=16$ kA_{rms}, $U=24$ kV_{rms}; 36 kV_{rms}, in single-phase and three-phase circuits, following the behaviour of the envelope under pressure.

The position of the experimental test equipment and the fuse socket is shown in Fig. 12.



Fig. 12. Distribution switchgear in experimental circuit for pressure testing. Fuse placement on a side phase.

A single phase experiment is shown in Fig. 13. A single fuse placed on a side phase ignites the arc in the enclosure at $I=16$ kA_{rms}, arc voltage drop $U=0.5$ kV_{rms}, $t=1$ s and produces an energy of 280 MA²s, resulting in a pressure shock $P=1.5$ bar.

Within 20 ms of the pressure shock, the diaphragm (pressure valve) operates and limits the effect of the pressure on the envelope.

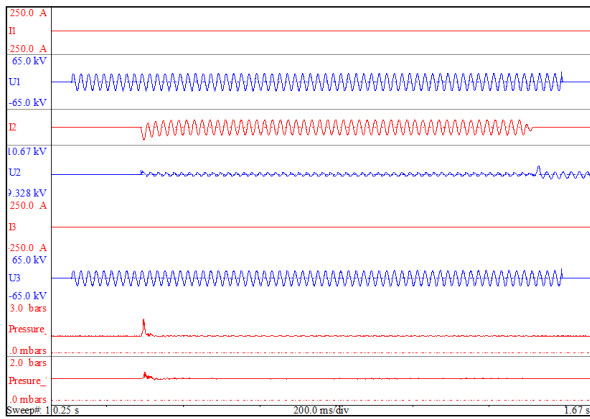


Fig. 13. Single phase experiment to check the pressure on the first lateral phase

The second experiment, shown in Fig. 14, is also a single phase test on an intermediate phase with the parameters $I = 16 \text{ kA}_{\text{rms}}$, $U = 0.5 \text{ kV}_{\text{rms}}$, $W = 283 \text{ MA}^2\text{s}$, $t = 1 \text{ s}$.

Two pressure transducers were mounted on this test specimen, one close to the fuse and the other as far away as possible, and the pressure values $P_1 = 2.44 \text{ bar}$, $P_2 = 1.5 \text{ bar}$ were recorded, proving that the extremely dynamic pressure manifests itself dangerously close to the arc, as in the first experiment. The pressure valve operates in 20 ms, preventing the metal envelope from exploding.

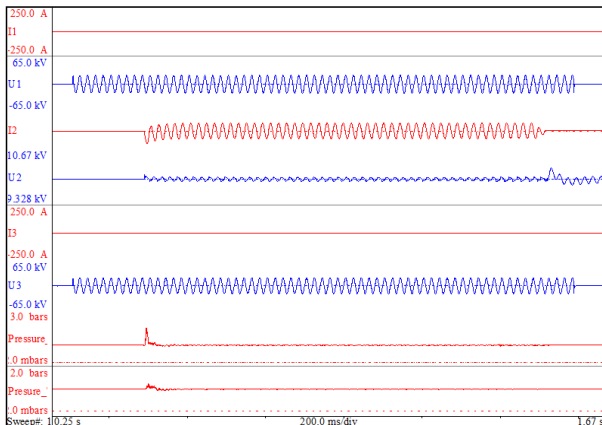


Fig. 14. Single phase experiment to check the pressure on the second lateral phase

The three-phase test (three fuses were installed) with parameters $I = 15 \text{ kA}_{\text{rms}}$, $U = 0.6 \text{ kV}_{\text{rms}}$, $t = 0.5 \text{ s}$, giving an energy $W = 118 \text{ MA}^2\text{s}$, $P = 4.5 \text{ bar}$, is shown in Fig. 15. The pressure membrane works and limits the effects of pressure, but as in all experiments, the arc does not extinguish and continues to produce thermal and electrodynamic effects until the end of the test.

The experiment in Fig. 16 is similar to the previous one with the parameters $I = 16.5 \text{ kA}_{\text{rms}}$, $U = 0.55 \text{ kV}_{\text{rms}}$, $t = 0.5 \text{ s}$, $W = 130 \text{ MA}^2\text{s}$, $P = 4.72 \text{ bar}$, and the result is similar and the pressure valve works after about 80 ms, releasing the pressure.

In the experiment in Fig. 17, a three-phase test is carried out with three fuses in the circuit, producing a three-phase arc with the parameters $I_{\text{med}} = 16 \text{ kA}$, $U = 0.5 \text{ kV}$, $W = 300 \text{ MA}^2\text{s}$, $t = 1 \text{ s}$. Two pressure shocks of about 4 bar are produced, because the pressure valve did not release all the pressure, being locked in the middle

position, then the pressure began to rise again for 100 ms, and when it was high enough, it completely released the discharge surface, limiting the destruction of the metal envelope.

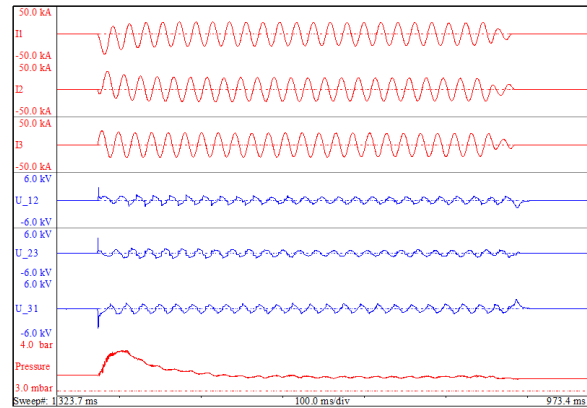


Fig. 15. Three-phase experiment for pressure verification

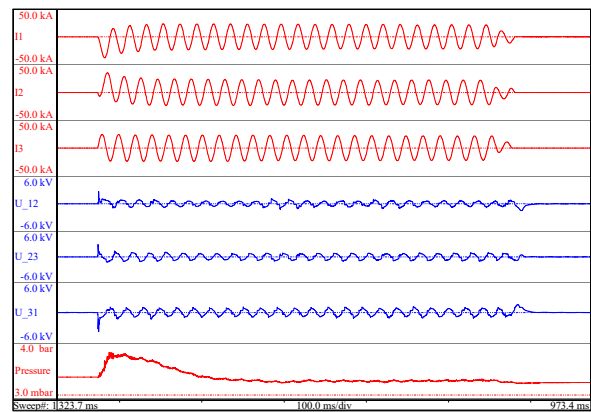


Fig. 16. Three-phase experiment for pressure verification

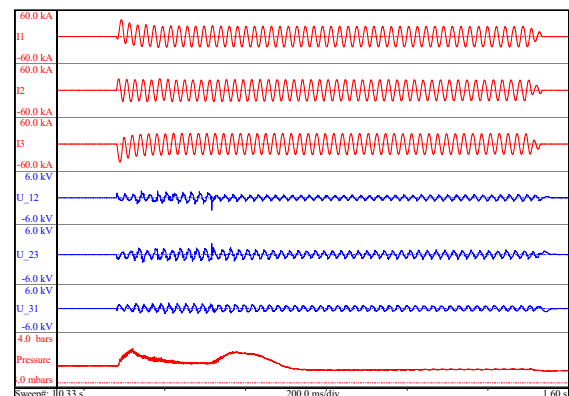


Fig. 17. Three-phase experiment for pressure verification

In all the experiments carried out so far, the pressure relief valve (diaphragm), set at a value above 2.5 bar, has functioned correctly, limiting the effects of an arc. However, there are also situations where it is not properly adjusted and the pressures in the metal envelope are devastating, as shown visually in Fig. 18.

Fig. 19 shows the oscilloscope recording for the destructive test, using similar parameters to the previous experiments: $I = 16 \text{ kA}_{\text{rms}}$, $U = 0.55 \text{ kV}_{\text{rms}}$, $W = 290 \text{ MA}^2\text{s}$, $t = 1 \text{ s}$, the pressure was not immediately released, resulting in the destruction of the switchgear.



Fig. 18. Destructive experiment for pressure verification - photo steps

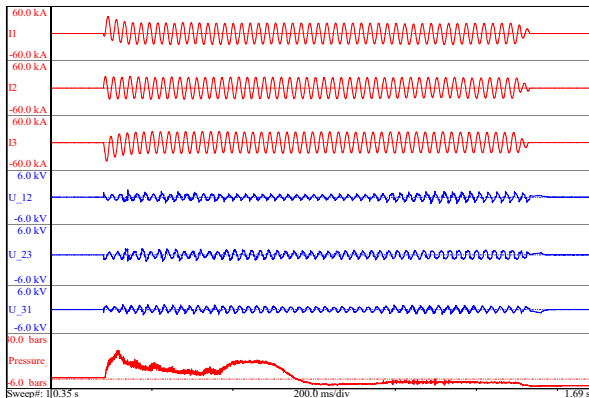


Fig. 19. Three-phase destructive experiment for pressure verification

On the basis of tests carried out on distribution switchgear containing fuse/load break switch combinations, the following pattern of events can be observed. In the first phase, the short-circuit current causes the fuse temperature to rise from a nominal value to the first-state transition point in the material. An increase in resistivity can therefore be estimated as a small linear gradient of increase and is manifested as a slight increase in voltage from the zero values recorded at the element terminals. This voltage rise occurs approximately at the beginning of a half sine period. The fact that the voltage increases non-linearly with resistivity indicates that the material is in the same state of matter as before, but the transition from solid to solid melting point is about to occur. A sudden increase in voltage lasting 0.2 ms indicates that the liquefaction temperature has been reached.

V. CONCLUSIONS

This article presents the importance of analyzing the breaking behavior of high-voltage fuses and emphasizes the pressure values at the ends of the fuses, important values in the design process.

The waveforms obtained can be divided into the pre-arc period and the arc period. A series of initial conditions were replicated in this study and their results were observed in the experiments. Parameters that control a potential outcome are the sinusoidal quadrant where the preliminary arc starts, the surface imperfections and internal crystalline structure of the copper wire, the surrounding environment, the geometry of the conductive fuse relative to the materials, and finally the quality and geometry of the rest of the device. The geometry of the fuse material was simple and all fuses used the same type

of fuse elements, providing a common reference for the rest of the parameters.

Based on the presented experiments, it can be observed a pattern of events. First, the short-circuit current causes the temperature of the fuse to rise from a nominal value to the transition point from the first state of the material. Thus, an increase in resistivity can be estimated as a small linear gradient of increase manifested by a slight increase in the voltage at the element's terminals. This voltage rise occurs approximately at the beginning of the first half of the sine wave period.

The fact that the voltage increases in a non-linear manner due to resistivity indicates that the material is in the same state of matter as before, but the transition from the solid to the melting point is about to occur. A sudden voltage increase in 0.2 ms indicates that the pour point has been reached.

As fusible elements go from solid to liquid the inner parts are hotter than the outer parts and melt first. Then the melting zone extends to the periphery.

At melting temperature, the resistivity of the molten material is much higher than the solid material one, and increases as melting continues. (Specific resistivity data for copper are: solid at melting point 10.2×10^{-6} Ohm-cm, liquid at melting point 21.3×10^{-6} Ohm-cm, and molten 13.8×10^{-6} Ohm-cm) [3, 7-10].

As it can be observed from the figures, the step increase in voltage is followed by another voltage increase that can last 2~6 ms.

Whether this increase is linear, a combination of linear increases of any duration depends on the phase of the sine wave and the power that passes through the wire and is converted. The equations for the temperature distribution estimation on the fusible elements can be found in the literature [8].

One of the key findings is the value of the pressure exerted on the caps of a high-voltage fuse, which has not been tested before. It also confirms the theory that the pressure at the ends of the fuse is directly proportional to the recovery voltage.

Analysis of fusible elements after experimental testing and fulgurite distribution confirms that the electrical conductivity of quartz sand to a fused conductor is very low at the pressures evaluated.

Experiments have shown that the maximum pressure is reached during the arcing period, an important finding for a high-voltage fuse contacts design and for a full understanding of the phenomena that occur inside it during the opening of the electrical circuit.

The evolution of fuse element disintegration over different time periods can be controlled by controlling the Joule energy in the fuse wires, which is directly proportional to the pressure in the fuse contacts.

The scientific contribution consists in the calculation and realization of the test circuit for pressure verification, solution for creating the experimental model, study of the most unfavorable situation, solution for the acquisition of the pressure values and the results interpretation.

ACKNOWLEDGMENT

This work was developed with funds from the Ministry of Research, Innovation and Digitization of Romania as part of the NUCLEU Program: PN 23330201.

First author – 70%
 First coauthor – 10%
 Second coauthor – 10%
 Third coauthor – 10%

REFERENCES

- [1] D. R. Barrow, A. F. Howe, and N. Cook, "The chemistry of electric fuse arcing," *IEE Proc. A.*, 1991, 138, 1, pp. 83-88.
- [2] L.A.V. Cheim and A.F. Howe, "Spectroscopic observation of high breaking capacity fuse arcs," *IEE Proc. Sci. Meas. Technol.*, 1994, 141, 2, pp. 123-128.
- [3] A. Wright, and P.G. Newbery, "Electric fuses," IEE Peter Peregrinus Ltd, 1995, 2nd ed.
- [4] J.G. Leach, P.G. Newbery, and A. Wright, "Analysis of high-rupturing-capacity fuselinks prearcing phenomena by a finite differential method," *IEE Proc.*, 1973, 120, 9, pp. 987-993.
- [5] V.N. Narancic, and G. Fecteau, "Arc energy and critical tests for HV current-limiting fuse," *Ibid*, pp. 236-251.
- [6] W. Bussière, E. Duffour, P. André, R. Pellet, and L. Brunet, "Experimental assessment of temperature in plasma wall interaction," *The European Physical Journal D-Atomic, Molecular, Optical and Plasma Physics*, 2004, 28, pp. 79-90.
- [7] T. Chicata, Y. Ueda, Y. Murai and T. Miyamoto, "Spectroscopic observations of arcs in current limiting fuse through sand," *Proc. of Inter. Conf. on Electric Fuses and their Applications*, Liverpool (UK), 1976, pp. 114-121.
- [8] C.S. Psomopoulos, and C.G. Karagiannopoulos, "Temperature distribution of fuse elements during prearcing period," *Electric Power Systems Research*, 2002, 61, pp.161-167.
- [9] R. Rüdénberg, "Transient performance of electric power system - phenomena in lumped networks," MIT Press, 1970, pp. 431-453.
- [10] C.S. Psomopoulos, and C.G. Karagiannopoulos, "Measurement of fusible elements during current interruption and interpretation of related phenomena," *Measurement*, 2002, 32, pp. 15-22.
- [11] A.J. Chapman, "Heat Transfer", Maxwell Macmillan International (Ed.), 4th ed., 1989.
- [12] M.S. Agarwal, A.D. Stokest, and P. Kovitas, "Prearcing behavior of open fuse wire," *J. Phys. D: Appl. Phys.*, 1987, 20, pp. 1237-1242.
- [13] A. T. Pleëca, "Thermal Analysis of the Fuse with Unequal Fuse Links Using Finite Element Method," *World Academy of Science Engineering and Technology*, 2012, 6, pp. 1186-1194.
- [14] W. Bussière, "Estimation of the burn-back rate in high breaking capacity fuses using fast imagery," *Journal of Physics D: Applied Physics*, 2001, 34, pp. 1007.
- [15] W. Bussière, and A. Pascal, "Evaluation of the composition, the pressure, the thermodynamic properties and the monatomic spectral lines at fixed volume for a SiO₂-Ag plasma in the in the temperature range 5000-25 000 K," *Journal of Physics D: Applied Physics*, Vol. 34, No. 11, 2001, pp. 1657-1664.
- [16] L. Vermij, "The voltage across a fuse during the current interruption process," *IEEE Trans. Plasma Sc.*, 1980, 8, pp. 460-468. V.T. Morgan, "Rating of conductors for sort-duration currents," *Proc. IEE*, 1971, 118, pp. 555-570.
- [17] D.V. Lebedev, "Explosion of a metal by an electric current," *Sov. Phys. - JETP*, 1957, 5, pp. 243-252.
- [18] I.M. Vitkovitsky, and V.E. Scherrer, "Recovery characteristic of exploding wire fuses in air and vacuum," *J. Appl. Phys.*, 1981, 52, pp. 3012-3015.
- [19] T.L. Berger, "Effects of surrounding medium on electrically exploded aluminum foil fuses," *IEEE Trans. Plasma Science*, 1980, 8, pp. 213-216.
- [20] M.A. Saqib, and A.D. Stokes, "Time resolved spectrum of the fuse arc plasma," *Thin Solid Films*, 1999, 345, 1, pp. 151-155.
- [21] Y. Bajda, and O. Grechko, "Multiphysics calculation of fuses of medium voltage measuring transformers", *Bulletin of NTU KhPI Series Problems of Electrical Machines and Apparatus Perfection The Theory and Practice*, 2023, pp.3-10. 10.20998/2079-3944.2023.1.01.
- [22] Y.P. Raizer, "Gas Discharge Physics," Springer-Verlang, (Ed.), 1991, pp 128-161, pp. 245-288, pp. 288-291.
- [23] M.J. Taylor, "Formation of plasma around wire fragments created by electrically exploded copper wire," *J. Phys. D.: Appl. Phys.*, 2002, 35, 7, pp. 700-709.
- [24] M.J. Taylor, "Current diversion around a fragmenting wire during the voltage spike associated with exploding wires," *Proc. of Inter. Conf. on Electric Fuses and their Applications*, Gdansk (PL), 2003, pp. 1-9.
- [25] M.J. Taylor, J. and Dunnett, "A description of the wire explosion process for ETC plasma generators," *IEEE Transactions on Magnetics*, 2003, 39, 1, pp. 269-274.
- [26] C.-E. Salceanu, M. Nicola, C.-I. Nicola, D. Ocoleanu, C. Dobrea, D. Iovan, and S. Enache, "Experimental Study on the Behavior of Aluminum Fuse Element Inside 24 kV, 50 kA High-Voltage Fuses", *Energies* 2022, 15, 7171. <https://doi.org/10.3390/en15197171>.
- [27] C. -E. Salceanu, M. Nicola, D. Ocoleanu, D. Iovan and S. Enache, "Experimental Study of HBC Fuses with Aluminium Fuse Element at Minimum Rated Breaking Current," 2021 International Conference on Applied and Theoretical Electricity (ICATE), Craiova, Romania, 2021, pp. 1-6, doi: 10.1109/ICATE49685.2021.9465000.
- [28] M.L. Coffman, "Exploding Wire," W G Chace and H K Moore (Ed.), 1964, pp. 89-102.
- [29] Y. MeĠBar, and R. Harel, "Electrical explosion of segmented wires," *Journal of Applied Physics*, 1996, 79, 4, pp. 1864-1868.
- [30] A. Lukyanov, and S. Molokov, "Flexural vibrations induced in thin metal wires carrying high currents," *Journal of Physics D: Applied Physics*, 2001, 34, pp. 1543-1552.
- [31] P. Graneau, "Wire explosions," *Physics Letters*, 1987, 120A, pp. 77-79.
- [32] IEC 60282-1:2002 High-voltage fuses –Part 1: Current-limiting fuses.
- [33] Powell, J.D., and Thornhill, L.D.: 'Current distribution and plasma properties in injectors for electrothermalchemical launch', *IEEE Transactions on Magnetics*, 2001, 37, 1, pp. 183-187
- [34] Lukyanov, A., and Molokov, S.: 'Flexural vibrations induced in thin metal wires carrying high currents', *Journal of Physics D: Applied Physics*, 2001, 34, pp. 1543-1552
- [35] H. Bessei, "Incorrect use of fuse characteristics in IEC 62271-105 restricts H.V. fuse application in ring main units," 2007 8th International Conference on Electric Fuses and their Applications, 2007, pp. 185-189, doi: 10.1109/ICEFA.2007.4419985
- [36] S. Liu et al., "DC current interruption by a combination of electric fuse and vacuum switch," 2015 3rd International Conference on Electric Power Equipment – Switching Technology (ICEPE-ST), 2015, pp. 246-250, doi: 10.1109/ICEPE-ST.2015.736833
- [37] IEC 62271-105:2012, High-voltage switchgear and controlgear – Part 105: Alternating current switch-fuse combinations for rated voltages above 1 kV up to and including 52 kV.

Comparative Performance Analysis of Photovoltaic Power Plants – a Case Study

Mihaita Linca*, Ion Popa†, Constantin Vlad Suru* and Florin Ravigan*

* Faculty of Electrical Engineering, University of Craiova, Craiova, Romania
mlinna@em.ucv.ro, vsuru@em.ucv.ro, florin.ravigan@gmail.com

† ELCO SA, Tg. Jiu, Romania, cristip77@yahoo.com

Abstract - The aim of this paper is the comparative study of the behavior and performances of two photovoltaic power plants of different installed power, but which uses identical equipment. The difference in size is being given by the number of specific equipment used (the power inverters and solar panels). The plant behavior was investigated, as the injected active power is dependent on the available sunlight to the photovoltaic panels (and a larger plant leads to a larger panel area), as well as the influence of the power plants to the power grid, given the fact that a large power plant will inject more active power, and the grid local power transformer must be able to accept this power. The power plants efficiency was also investigated, as typically, the bigger the plant, the higher the efficiency must be. But, the efficiency depends on the generated active power (which must be high, to have a good efficiency) and in the case of photovoltaic power plants, the produced power depends on the available sunlight, and again, the bigger the plant, the bigger the panel area susceptible to be shaded. This gives the fact that although the injected power is higher for the bigger power plant, if the power of each inverter is below the rated power, the overall efficiency is lower compared to the small power plant which works at the rated power.

Cuvinte cheie: *fotovoltaic, central electrică, radiație solară.*

Keywords: *photovoltaic, power plant, solar radiation.*

I. INTRODUCTION

Nowadays renewable energy is increasingly used due to its potential benefits, mainly the reduction in greenhouse gas emissions, by reducing the dependence on fossil fuels used in classical power plant (coal and gas) [1].

Although solar energy is considered to be convenient, it has specific costs and issues, given by the solar power plant equipment. On one hand, the investment cost must be amortized, and on the other hand the solar power plant is based on static converters. Therefore, before the plant lifetime is reached and the equipment must be recycled, (resulting in an amount of waste) the solar power plant gives electric pollution during its lifetime. This is because the solar energy is injected to the power grid only by means of power inverters, which are injecting voltage and current harmonics to the grid [2-7].

Another problem is caused by the generated energy availability, which is directly dependent on the solar radiation. Consequently, the solar power plants can produce electricity only during sunny days. When the sky is cloudy the solar plants production drops, and during nighttime the production is halted [8-9].

Considering the convenience of installing solar power plants in Romania region, the country is located in a geographical area which gives good solar coverage, having 210 sunny days per year with a solar energy annual flow between 1000 kWh/sqm/year and 1300 kWh/sqm/year [8][10].

As a function of the intensity of solar radiation (H_i) in the horizontal plane, Romania is in the European sunshine zone B, considered to be advantageous to produce electricity by means of solar energy.

Romania is divided into three areas, dependent to the geographical area [8]:

- The red zone, for $H_i > 1650$ kWh/sqm/year, which includes the southern areas: Oltenia, Muntenia, Dobrogea and the south of Moldova;
- the yellow zone with H_i between 1300 and 1450 kWh/sqm/year: the Carpathian and sub-Carpathian regions of Muntenia and Oltenia, Transylvania, the middle and the northern part of Moldova;
- the blue zone which includes the mountain regions - radiation intensity between 1150 and 1300 kWh/sqm/year.

The paper aims the comparative study of two photovoltaic power plants installed in Romania (low-power and high-power) on the same urban location.

After the introduction, the studied power plants are detailed in the second chapter, and in the third chapter, the experimental data is presented and evaluated. Finally, the conclusions are drawn.

II. THE POWER PLANTS

The two photovoltaic power plants taken into consideration are both located in the urban area of Tg. Jiu, Romania, in the Gorj County.

The first plant is residential, connected to the public power grid, at about 250 m from the power transformer, among home consumers, mainly apartment flats. However, the rated power is relatively high, for a residential plant. The main parameters of this plant are:

- Rated power: $P_N = 50$ kW;
- Number of panels: 108;
 - Panel rated power: 540 W;
- Number of inverters: 1;
 - Inverter rated power: 50 kW.

The second studied power plant is also located in Tg. Jiu area, but in the industrial zone, and is connected to the

power grid directly to the power transformer. The main parameters of this power plant are:

- Rated power: $P_N = 250 \text{ kW}$;
- Number of panels: 466,
 - Panel rated power: 540 W;
- Number of inverters: 5;
 - Inverter rated power: 50 kW.

The photovoltaic panel type used for both plants is LR5-72HPH-540M, with the following rated parameters:

- Max power: $P_{\max} = 540 \text{ W}$;
- Open circuit voltage: $V_{OC} = 49.5 \text{ V}$;
- Max power voltage: $V_{mp} = 41.65 \text{ V}$;
- Short-circuit current: $I_{SC} = 13.85 \text{ A}$;
- Max power current: $I_{mp} = 12.97 \text{ A}$;
- Efficiency $\eta = 21.1 \%$.

The power inverter used for both plants is SUN2000-50KTL-M0, with the following rated values:

- output power: $S_N = 50 \text{ kVA}$;
- output voltage: $U_N = 220/230 \text{ V (3f+N)}$;
- output current: $I_N = 76/72.2 \text{ A}$;
- power grid frequency: $f_N = 50/60 \text{ Hz}$;
- max harmonic distortion: $\text{THD} = 3\%$;
- max input voltage: $U_{dcN} = 1100 \text{ V}$;
- max MPPT input current: $I_{dcN} = 22 \text{ A}$.

The 50 kW power plant uses one power inverter with the corresponding 108 photovoltaic panels organized on 6 rows each with 18 panels.

The 250 kW power plant uses the same configuration of panels, for each of the 5 inverters.

III. EXPERIMENTAL RESULTS

The electric and energetic parameters of the two considered power plants had been recorded in August, 2023. It can be seen that the data was recorded during the “good” period of the year, when the solar radiation is the highest.

The analyzed data was recorded by the power inverters, given their capability to measure, compute and record (for a time step of 5 minutes) a comprehensive number of quantities:

- The power grid RMS voltage (phase and line voltages);
- The power grid RMS current;
- Active power injected to the power grid;
- Reactive power;
- Power factor;
- Generated energy to the power grid;
- Frequency;
- Photovoltaic panels voltage;
- Photovoltaic panels current;
- Inverter efficiency.

The data was recorded when the power inverters had been online, therefore, when the solar radiation was sufficient for the inverter to start and connect to the power

grid. The time intervals when the inverters had been disconnected from the power grid (during night time for example) had not been recorded. Therefore, each daily recording starts after the sunrise (the solar radiation is high enough for the inverters to start), and stops at dusk (the solar radiation is too low and the inverters stop).

The first recorded quantity, the three-phase power grid current RMS values are illustrated in Fig. 1. It is observed that the RMS values of the three-phase currents are practically equal, no differences being observed qualitatively. As expected, the current RMS value is pulsing, having its maximum value at each mid-day, and the corresponding minimum values at each morning and evening. Moreover, the cloudy days can be identified, from the switching like pattern. It must be noticed that although the both plants are located in the same town, the injected current is not the same (keeping the proportions) – not only that the production evolution in time is not the same, but the switching due to clouds is different.

The power grid voltages are illustrated in Fig. 2. One can see that the phase voltages are not symmetrical, although the currents are, showing the fact that the power grid voltage is asymmetrical.

This does not mean that the photovoltaic plant does not affect the power grid. To better observe the voltage and current daily evolution, a detailed view is illustrated in Fig. 3.

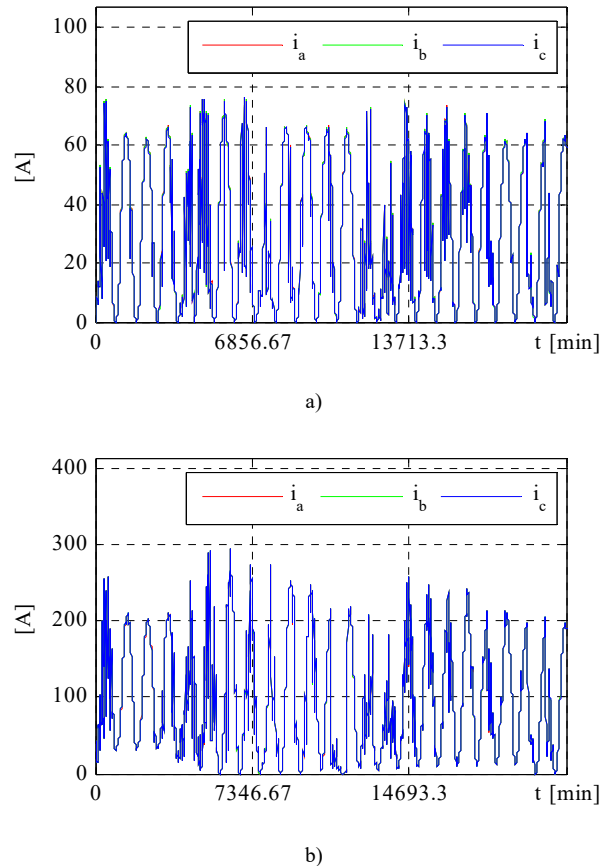


Fig. 1. The RMS current injected to the power grid for one phase: a) 50 kW plant, b) 250 kW plant.

An interesting fact is the effect of the current affecting the voltage as a function of plant coupling point to the

power grid. It results that although the current injected to the grid by the 250 kW plant is greater, because the plant connects directly to the power transformer, the voltage increase is lower, compared to the 50 kW power plant which is connected to the grid at considerable distance from the power transformer. In fact, for the latter, the voltage variation and asymmetry are considerable higher, given the long lines and the single phase residential consumers.

A similar conclusion can be drawn regarding the current switching due to shading, for which the voltage is more affected by the low-power plant.

The active power injected to the power grid is illustrated in Fig. 4. Because the voltage variation is low, the active power shape reflects the injected RMS current shape.

On the other hand, the measured reactive power at the point of coupling to the power grid is practically zero, as it can be observed in Fig. 5.

The power factor is illustrated in Fig. 6. For most of the time, the power factor is unitary, except for some short moments. Comparing the low values of the power factor with the active and reactive power (for the same moments of time) it appears that the low value of the power factor coincides with very low values of active power. Also, considering the fact that this low-power factor values are scarce and with no cyclic repetition, they are probably measurement errors.

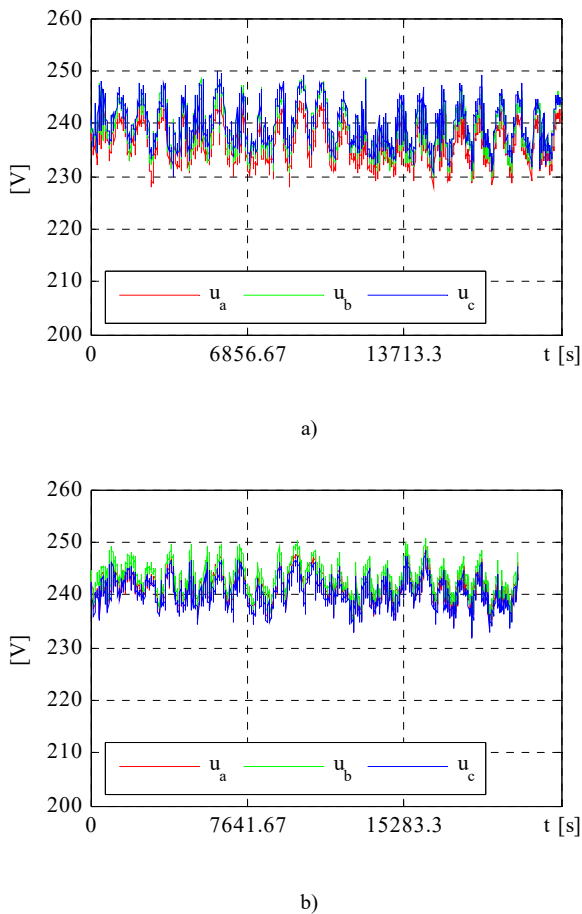


Fig. 2. The power grid voltages: a) 50 kW plant, b) 250 kW plant.

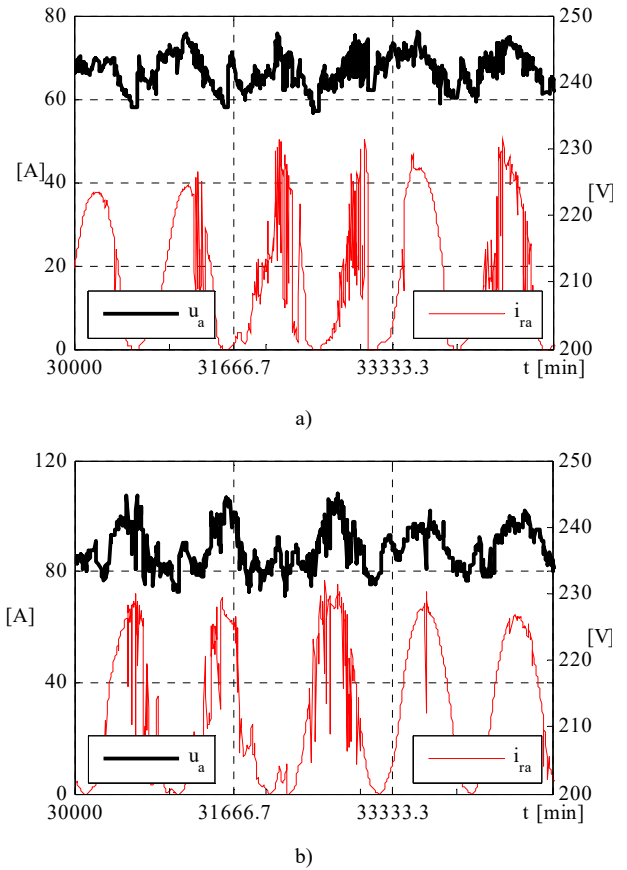


Fig. 3. Detail of the grid current and voltage on phase a: a) 50 kW plant, b) 250 kW plant.

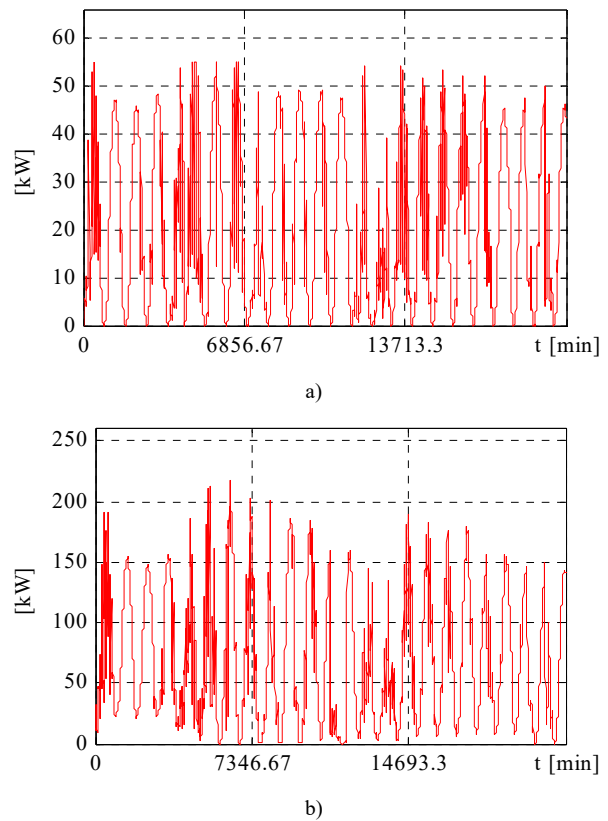


Fig. 4. The active power injected to the power grid for the recorded timespan: a) 50 kW plant, b) 250 kW plant.

The produced energy by the two power plants is illustrated in Fig. 7. The typical daily evolution of the injected active power is visible, given the produced energy ripple. Also, the successive cloudy days are visible, when the produced energy is slackened.

The voltages corresponding to the rows of photovoltaic panels for the 50 kW plant are presented in Fig. 9. It can be seen that the voltages corresponding to the 6 rows of panels are relatively equal, with little differences, except for the cloudy days, to which bigger differences appear as only some of the panels are shaded.

The conclusion is confirmed by the current of each row of photovoltaic panels, given in Fig. 9. It shows that the voltage ripple and difference between rows is higher when the panels are shaded, so the current is low value and high ripple.

The voltages corresponding to the rows of photovoltaic panels for the 250 kW plant are presented in Fig. 10 and the currents are given Fig. 11.

In this case, the number of illustrated voltages and currents is considerably higher, as the plant uses 5 inverters, each with 6 rows of panels.

At the same time, because of the high number of panels, the probability that some of the panels are shaded while other is not, increases. Therefore, the panel row voltage variation as well as the current row variation is much higher for the case of the 250 kW plant.

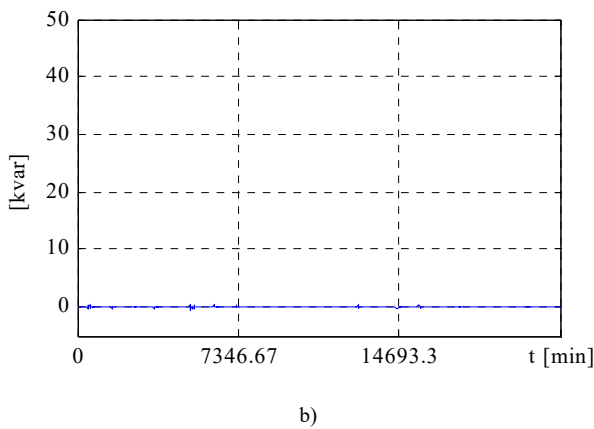
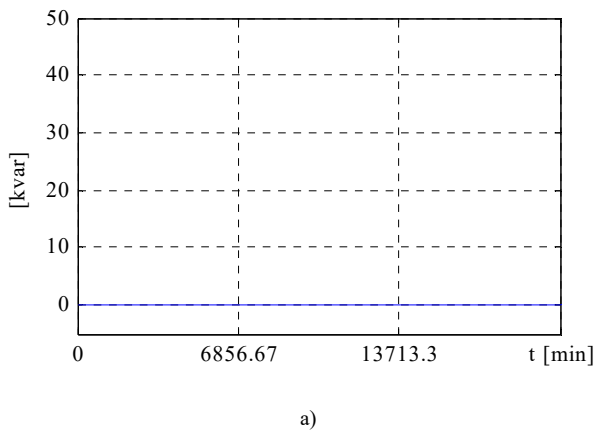


Fig. 5. The reactive power injected to the power grid for the recorded timespan: a) 50 kW plant, b) 250 kW plant.

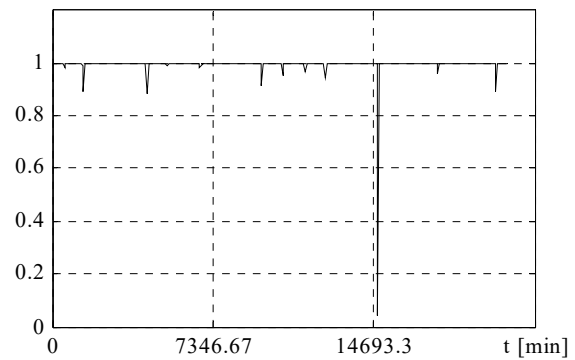
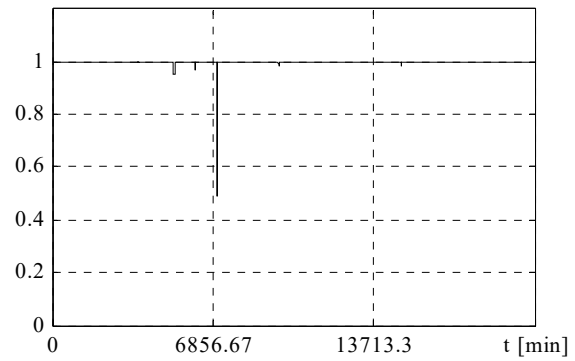


Fig. 6. The power factor for: a) 50 kW plant, b) 250 kW plant.

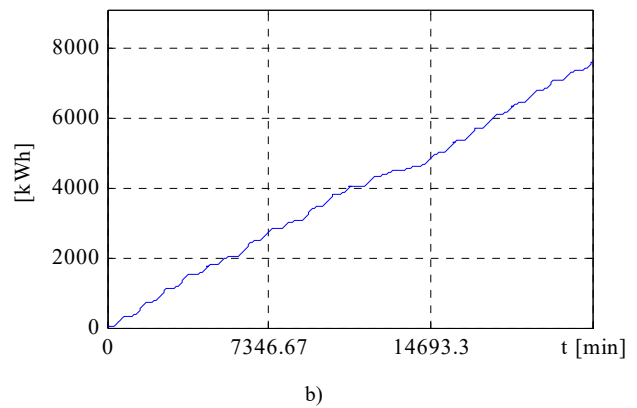
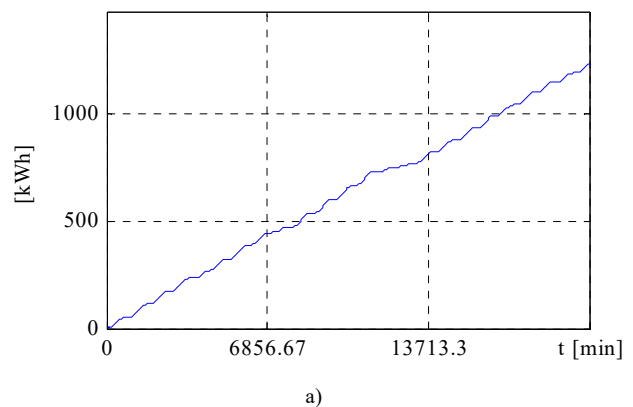
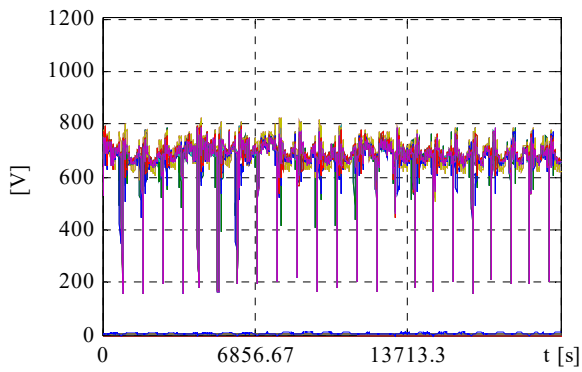
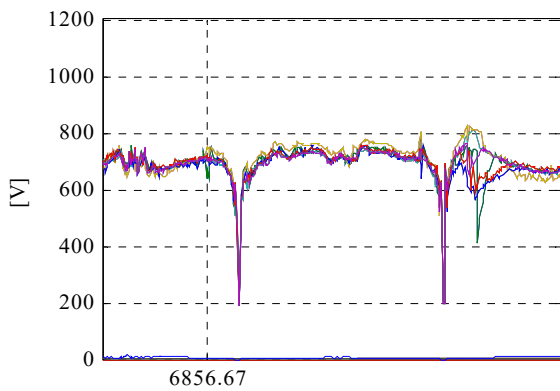


Fig. 7. The produced energy for the recorded timespan: a) 50 kW plant, b) 250 kW plant.

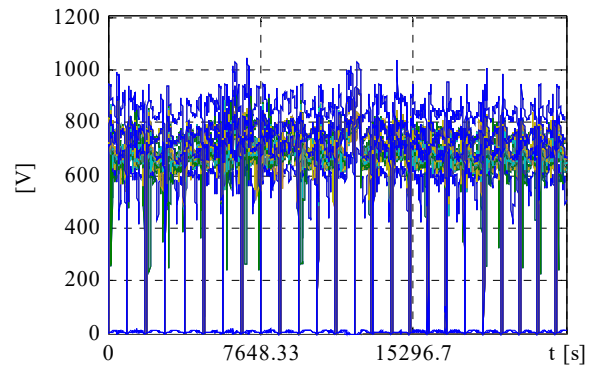


a)

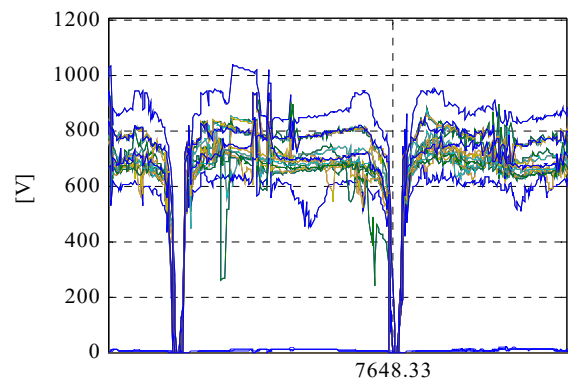


b)

Fig. 8. The output voltage of each row of photovoltaic panels for the 50 kW plant: a) for the recorded timespan, b) detailed view.

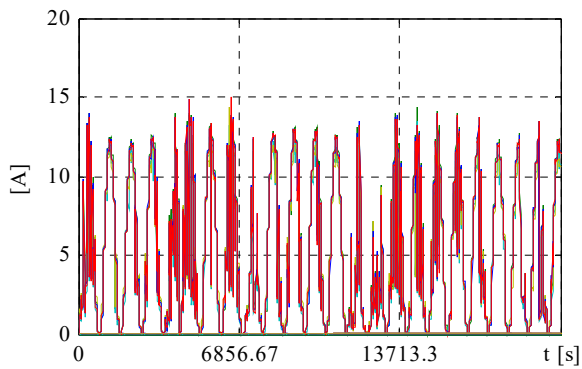


a)

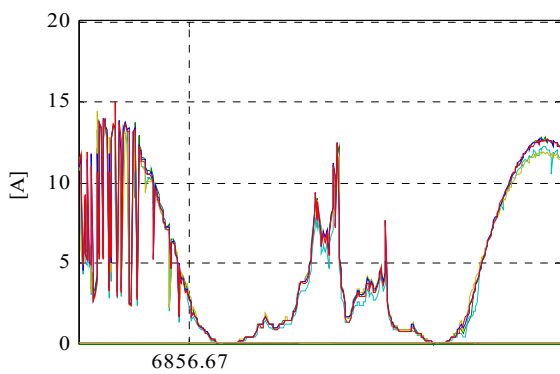


b)

Fig. 10. The output voltage of each row of photovoltaic panels for the 250 kW plant: a) for the recorded timespan, b) detailed view.

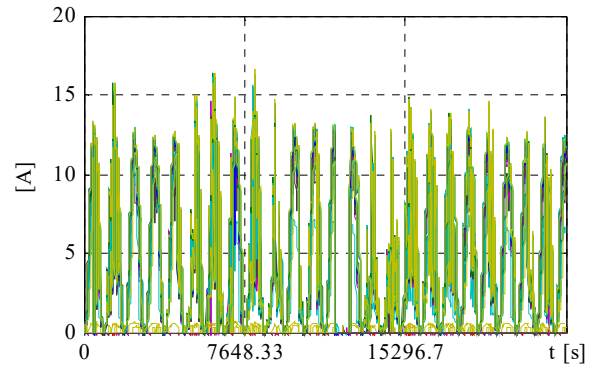


a)

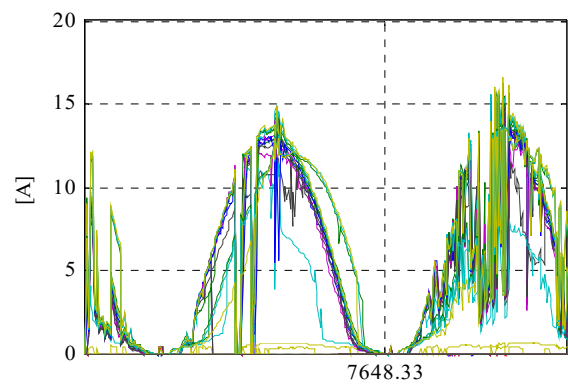


b)

Fig. 9. The output current of each row of photovoltaic panels for the 50 kW plant: a) for the recorded timespan, b) detailed view.



a)



b)

Fig. 11. The output current of each photovoltaic row of panels: a) for the recorded timespan, b) detailed view.

Another issue which is due to the plant size is the higher rate of breakdowns which is shown by the panel rows voltage and current. Because of the high number of panels, some of the connections are broken, so the row voltage increases to the open circuit value.

The power inverters efficiency is illustrated in Fig. 12, for the two considered power plants. The efficiency is high, close to 100% when the produced power is high, close to the rated value, and it lowers when the inverter approaches the idle regime (at the start and the end of each day, or in cloudy days). The efficiency of each of the plant 5 inverters is shown in Fig. 12-b. The efficiency evolution during the day, and during the month, is not identical for the 5 inverters, as the high area of panels is differently shaded. The highest efficiency of the low-power plant is 98.7% and the lowest is 74.3%. For the high-power plant, the highest efficiency is 95.5% and the lowest is 61.6%, although the average minimum is 64.9%.

The typical efficiency of a power plant is higher for higher power, which is contradicted by the obtained results. The explanation of these is given by the two plants injected power. As seen in Fig. 4, a and b, it results that the small power plant works close to the rated power, even at the maximum datasheet power of 55 kW, for some days. The high-power plant works considerably below its rated power of 250 kW (at an averaged percent of 80% of the rated power), for the same days and day moments, despite the fact that both plants are located in the same town.

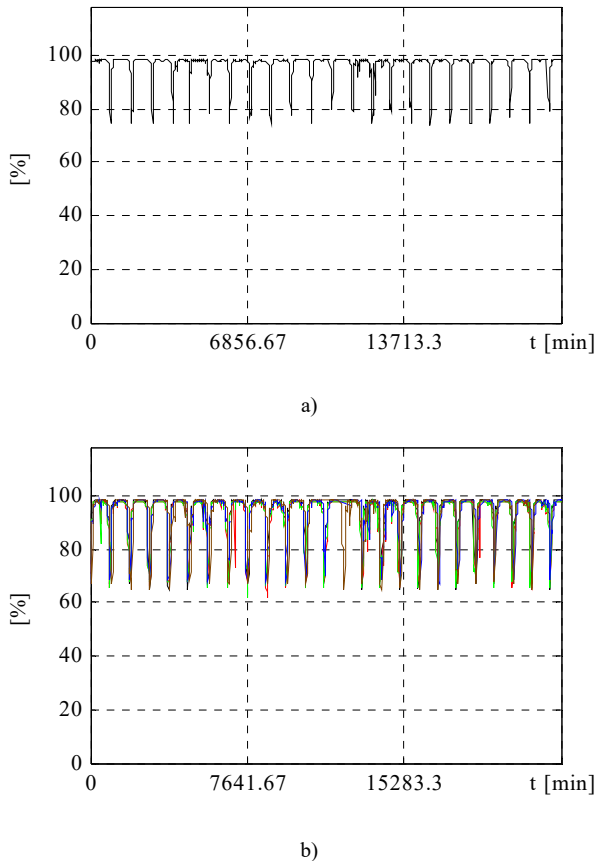


Fig. 12. The inverter efficiency: a) for the 50 kW plant, b) for the 250 kW plant.

This is further explained in Fig. 9 and Fig. 11, which show that the panel row currents are different for the high-power plant, meaning that the solar radiation is not the same for all the panels/inverters.

Therefore, each of the five inverters of the high-power plant is working below its rated power, as proven in Fig. 13 and Fig. 14, respectively.

Another important fact is that the power inverters are pure sine which means that they give sinusoidal voltage at their output (very important for the inverter to work, synchronized to the power grid). At the same time, in order to obtain sinusoidal output voltage, the inverter is connected to its load (power grid) by means of important reactive harmonic filters.

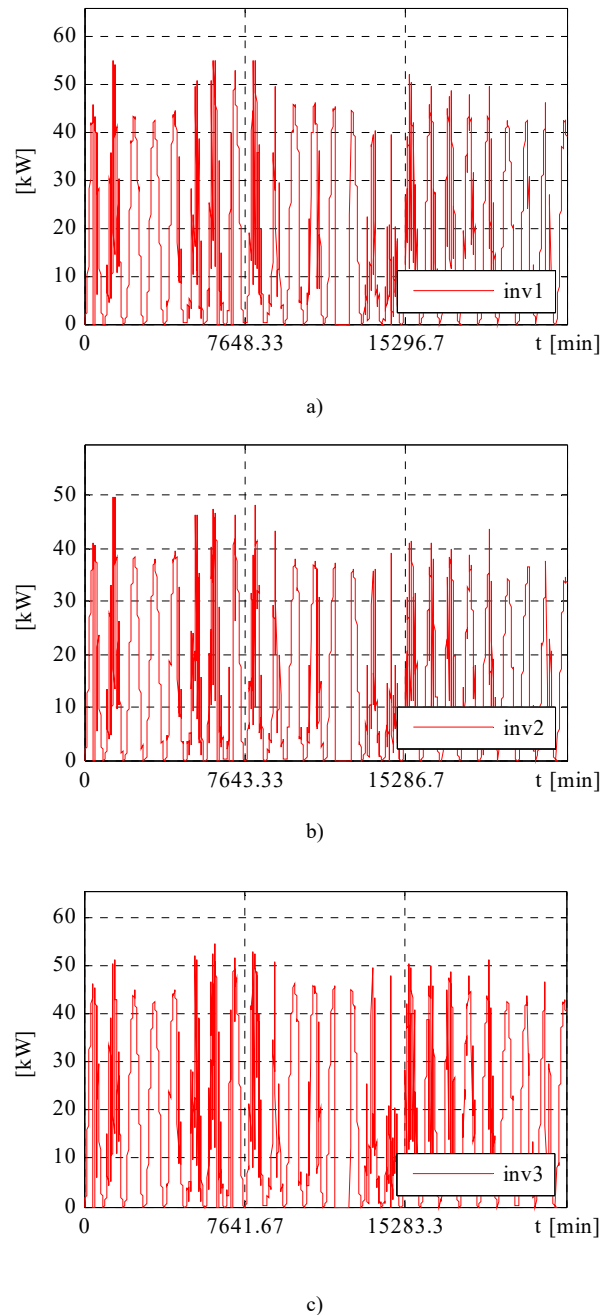
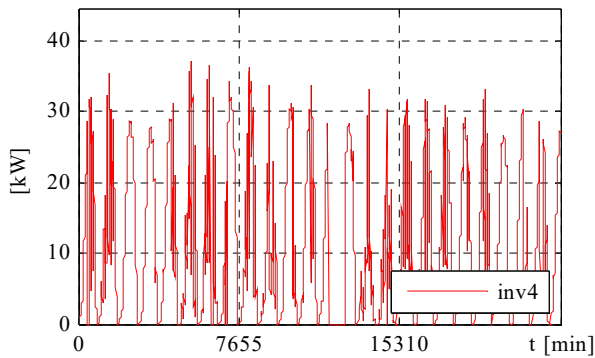
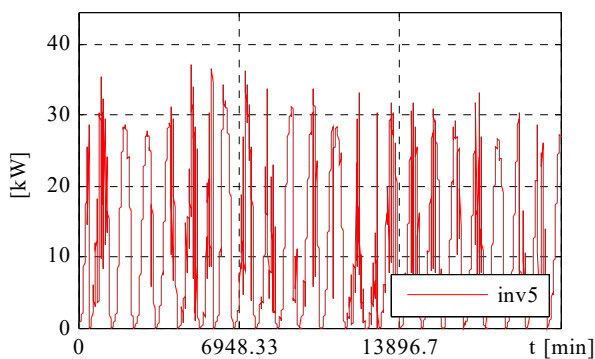


Fig. 13. The power injected to the power grid of the first three inverters of the 250 kW power plant.



d)



e)

Fig. 14. The power injected to the power grid by the other two inverters of the 250 kW power plant.

The passive harmonic filters give a relatively high value reactive current which flows between the inverter and the harmonics filter, irrespective to the load current (even at idle operation), increasing the inverter conduction and switching losses (compared rectangular wave inverter). This leads to a lower power inverter efficiency, compared to a classic rectangular wave inverter. Moreover, the pure sine inverter uses not only the passive harmonic filters to obtain pure sinusoidal wave, but also a “multipulse” PWM modulation method (like the classical sinusoidal PWM modulation), which gives higher switching losses, compared to the rectangular wave inverter, which output only one pulse per half period.

CONCLUSIONS

The efficiency of a power plant depends on its size, and surprisingly, the smaller plant showed higher efficiency than the bigger plant. For photovoltaic power plants, the efficiency decreases as the plant is low on production and the production is low when the photovoltaic panels are not receiving direct sunlight. The bigger the plant, the higher the total panel surface is, so the higher is the probability that some of the panels to be shaded by thin, scattered clouds. And the injected active power is much lower and unstable in cloudy days.

A demand for photovoltaic power plants consists of the pure sine power inverters which must output sinusoidal voltage with low harmonic distortion, in order to work

synchronized to the power grid voltage. Of course, this gives the advantage that the solar power inverter can inject only active power to the grid, with an insignificant amount of reactive and distortion power. At the same time, it gives the disadvantage that in order to obtain pure sinusoidal voltage, large passive harmonic filters are necessary at the inverter output. These filters require an important current to flow from the inverter even at idle operation, resulting in higher inverter losses. Another disadvantage of small distributed photovoltaic power plants is the power grid voltage increase, even more so when the plant is connected to the grid away from the power transformer.

ACKNOWLEDGMENT

Source of research funding in this article: Research program of the Electrical Engineering Faculty financed by the University of Craiova.

Contribution of authors:

First author – 40%

First coauthor – 20%

Second coauthor – 20%

Third coauthor – 20%

Received on July 10, 2023

Editorial Approval on November 27, 2023

REFERENCES

- [1] https://ec.europa.eu/eurostat/statistics-ex-plained/index.php?title=Archive:Statistici_privind_energia_din_surse_regenerabile&oldid=365442
- [2] S. Ștefanescu and A. Botezan, "Over Grid Connection of Non Dispatchable Utility Photovoltaic Power Plants in Romania," 2019 8th International Conference on Modern Power Systems (MPS), Cluj-Napoca, Cluj, Romania, 2019, pp. 1-4, doi: 10.1109/MPS.2019.8759705.
- [3] A. Burgio, D. Menniti, A. Pinnarelli and N. Sorrentino, "The reliability evaluation of a power system in presence of photovoltaic and wind power generation plants and UPS," 2007 9th International Conference on Electrical Power Quality and Utilisation, Barcelona, Spain, 2007, pp. 1-6, doi: 10.1109/EPQU.2007.4424163.
- [4] S. ștefanescu and A. Botezan, "Over Grid Connection of Large Photovoltaic Power Plants in Romania," 2018 International Conference and Exposition on Electrical And Power Engineering (EPE), Iasi, Romania, 2018, pp. 1070-1073, doi: 10.1109/ICEPE.2018.8559794.
- [5] <https://www.sistemulenergetic.ro/>
- [6] B. Lu et al., "Damping Injection Control Strategy of Low Frequency Oscillation in Photovoltaic Power Plant," 2021 International Conference on Power System Technology (POWERCON), Haikou, China, 2021, pp. 1707-1712, doi: 10.1109/POWERCON53785.2021.9697675.
- [7] R. Aihara, A. Yokoyama, F. Nomiya and N. Kosugi, "Impact of operational scheduling of pumped storage power plant considering excess energy and reduction of fuel cost on power supply reliability in a power system with a large penetration of photovoltaic generations," 2010 International Conference on Power System Technology, Zhejiang, China, 2010, pp. 1-6, doi: 10.1109/POWERCON.2010.5666528.
- [8] <https://www.panourisolareconstanta.ro/harta-radiatia-solara-in-romania>
- [9] Oprea, C: Radiatia solara aspecte - teoretice si practice, ISBN 973-03915-1, Bucuresti, 2005.
- [10] <http://free-energy-monitor.com/index.php/energy/fotovoltaiac>

Modelling, Simulation and Implementation on dSpace 1103 of the Direct Power Control in a Three-Phase Shunt Active Power Filter System

Mihaiță-Daniel Constantinescu, Mihaela Popescu, Gheorghe-Eugen Subțirelu and Ionuț-Cosmin Toma
University of Craiova, Faculty of Electrical Engineering
mconstantinescu@em.ucv.ro, mpopescu@em.ucv.ro, esubtirelu@em.ucv.ro, ctoma@em.ucv.ro

Abstract— This article describes a control method called "direct power control" designed specifically for parallel active power filters. The purpose of this method is to attenuate harmonics in the supply current and offset reactive power problems. The main goal is to bring the active power and reactive power back to the reference values through hysteresis control. The output of the hysteresis controller is combined with the switching table to regulate active and reactive power in real time by determining the optimal switching configuration of the inverter. This study proposes a novel switching table design based on analyzing the impact of the inverter switching vector on the instantaneous reactive and active power derivatives. The goal is to reduce the number of commutations by eliminating zero vectors while maintaining the required DC bus voltage using anti-windup techniques based on PI controllers.

Cuvinte cheie: *controlul direct al puterii(DPC), filtru activ, filtru activ de putere, putere reactivă.*

Keywords: *Direct Power Control (DPC), power quality, active power filter, active power, reactive power, switching table*

I. INTRODUCTION

Having the primary objective of enhancing the power quality of power sources and achieving unity power factor, the Voltage Source Inverters (VSIs) continue to play a significant role in various grid-connected applications. These applications encompass active power filters, and distributed generation systems utilizing renewable energy sources such as wind and photovoltaic power [1], [2].

The widespread adoption of static converters in both industrial and household devices, along with the use on an increasingly large scale of non-linear loads, has led to a significant power quality degradation especially through the current waveforms. This deterioration adversely impacts the reliability of power electronic equipment. Active power filters, with their diverse series, shunt, and hybrid configurations, have emerged as an appealing substitute for passive filters due to their advantages [1]. Usually, a three-phase Shunt Active Power Filter (SAPF), which employs a three-phase VSI is connected in parallel with the mains and non-linear loads at the Point of Common Coupling (PCC). The SAPF's purpose is to reduce current harmonics as much as possible, compensate reactive power, and maintain system stability. The effectiveness of SAPF relies on its power structure design, adopted control strategies, and the resilience of its controllers. Different control methods, such as some based on instantaneous

reactive power theory and voltage-oriented control (VOC), have been explored to ensure optimal SAPF operation under varying conditions [1], [3]–[5].

Over the past decade, the Direct Power Control (DPC) method and others derived from it, such as Virtual Flux-DPC and DPC-Space Vector Modulation, were applied for PWM rectifiers and SAPFs [6]–[17]. Some of these applications have directly utilized Noguchi's switching table for DPC [6]. For the improvement of SAPF performance, the authors of [7] proposed an algorithm to compensate the harmonic current, redefined the switching functions, and dynamically adjusted the hysteresis bandwidths of the comparators. Different switching lookup tables for DPC used in an AC-DC converter were analyzed in [8].

In [9], a direct power control strategy for SAPF was presented, including experimental validation to illustrate the good dynamics of the system. Appropriate dynamic response of the supply current and DC voltage is also illustrated in [10].

The use of the direct power control in different applications, such as rectifiers, grid connected inverters and SAPF is well reviewed in [11].

Some new or improved switching tables to be used in DPC implementation are discussed in [12]–[16]. Also, the solution of using multiple switching tables for DPC is addressed in [17] and [18].

In the case of operation under non-ideal grid conditions, replacing the classical static look-up tables with the predictive DPC for the selection of the switching vector is proposed in [19].

In order to regulate DC-link voltage, a new control method using an anti-windup fractional order proportional-integral differentiator (AW-FOPID) controller is the solution proposed in [20]. A short response time in the DC-link voltage evolution, as well as small overshoots and undershoots are highlighted.

To compensate the harmonic currents in a grid-connected photovoltaic system, the hysteresis control and the DPC are the two methods analyzed comparatively in [21]. The superior performances related to the DPC method are highlighted.

Aiming to reduce the instantaneous active and reactive power ripples when conventional DPC is used, the replacement of the hysteresis controllers and switching table by a fuzzy inference system is proposed in [22]. In this way, a smother control is obtained.

This paper is focused on the implementation of the Direct Power Control algorithm in the control of a three-

phase SAPF system for the compensation of the current harmonics and reactive power. First, the system is described through its configuration, the calculation of the instantaneous powers, the hysteresis controllers and the switching table. Then, modelling, simulation and implementation of the system operation are presented in section III. For the experimental implementation of the control strategy, the dSPACE DS1103 PPC Controller Board working with MATLAB-SIMULINK RTW was used and some experimental results are presented in section IV. At the end of the work, some final conclusions are drawn.

II. SYSTEM DESCRIPTION

A. System Configuration

The power configuration of the SAPF system based on DPC is shown in Fig. 1. The ultimate goal is to compensate both the current harmonics and the reactive power so that the power factor at the supply side to be as close as possible to one.

The active power filter can operate as a controlled current source and it is required to deliver a supply current waveform that closely aligns with the reference current.

To establish the reference current, it is necessary to establish a balance between the instantaneous power provided by the source and the active power filter, and the load power. If notations p_s and q_s are used for the real instantaneous power and imaginary instantaneous power respectively at the supply side, for the purpose of offsetting the reactive power and eradicating harmonic currents, these powers should be $p_s = \bar{p}_l$ and $q_s = 0$ after compensation. p_l is the instantaneous power of the load and \bar{p}_l is its average value.

If p_f and q_f denote the real and imaginary instantaneous power provided by SAPF and q_l is the instantaneous reactive power of the load, the following relationships can be expressed.

$$p_s = \bar{p}_l; \quad q_s = 0; \quad (1)$$

$$p_f = p_l - p_s = \bar{p}_l + \bar{p}_l - p_s = \bar{p}_l + \bar{p}_l - \bar{p}_l = \bar{p}_l \quad (2)$$

$$q_f = q_l - q_s = q_l \quad (3)$$

The oscillatory component of p_l should be supplied by the active power filter, whereas q_l must be entirely sourced from the active power filter. This approach enables the attainment of power compensation as well.

B. Instantaneous Powers Calculation

Based on the supply voltages and currents, the instantaneous active and reactive powers can be computed as the real and imaginary parts of the instantaneous apparent power or by using directly the measured quantities, as follows [6]:

$$p = e_a i_a + e_b i_b + e_c i_c \quad (4)$$

$$q = \frac{1}{\sqrt{3}} [(e_a - e_b)i_c + (e_b - e_c)i_a + (e_c - e_a)i_b] \quad (5)$$

In order to increase the system reliability by reducing the number of the used sensors, Noguchi formulated the so called sensorless DPC which is based on the estimated voltage in the point of common coupling [16], [22].

However, it should be noted that, in this approach, the time derivatives of the measured currents are used and the effect can be the increase of the harmonic distortion of the current [16].

C. Hysteresis Controllers

As shown in Fig. 1, two hysteresis band controllers are used in order to keep the instantaneous active and reactive powers into a desired band. Their inputs are the power errors, respectively the differences between the reference and calculated values of the active and reactive powers:

$$\begin{cases} \Delta p = P_{ref} - p \\ \Delta q = Q_{ref} - q \end{cases} \quad (6)$$

As illustrated in Fig. 2, the outputs of the hysteresis band controllers depend on the input errors (Δp and Δq) and the imposed hysteresis band for the active and reactive powers ($HB(p, q)$). The following expressions summarize the behavior of the hysteresis controller with respect to power error limits [16]:

$$\begin{aligned} \Delta(p, q) &> HB(p, q) \\ -HB(p, q) &\leq \Delta(p, q) \leq HB(p, q) \\ \frac{d(\Delta(p, q))}{dt} &< 0; \quad \Delta(p, q) = 1 \end{aligned} \quad (7)$$

$$\begin{aligned} \Delta(p, q) &< -HB(p, q) \\ -HB(p, q) &\leq \Delta(p, q) \leq HB(p, q) \\ \frac{d(\Delta(p, q))}{dt} &> 0; \quad \Delta(p, q) = 0 \end{aligned} \quad (8)$$

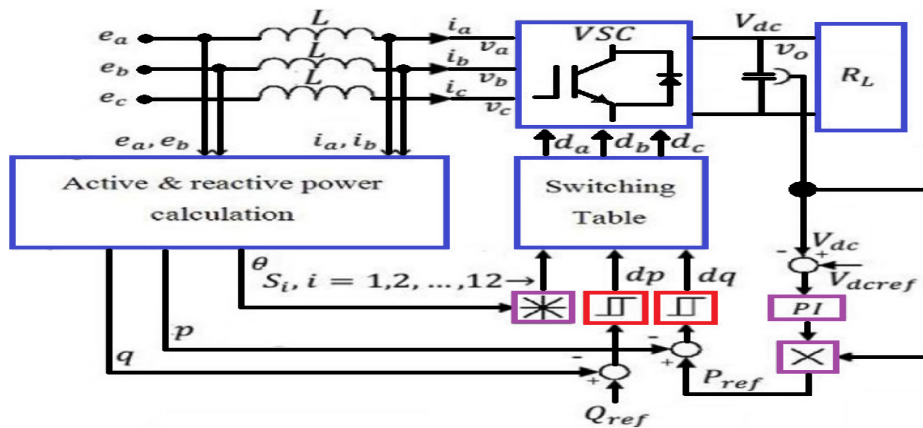


Fig. 1. Configuration of SAPF system based on DPC.

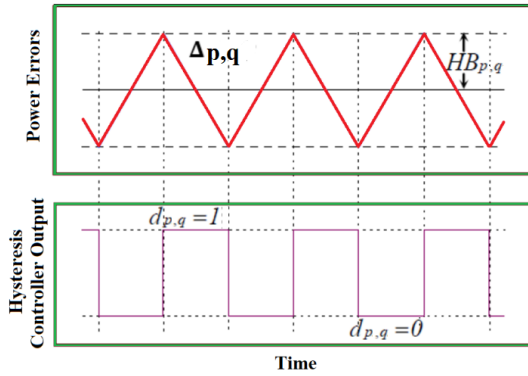


Fig. 2. Behavior of the hysteresis power comparator.

These outputs of the hysteresis controllers, together with the identified sector number of the voltage vector are the inputs of the switching table which will determine the appropriate switching of the inverter.

D. Switching Table

The look-up table, commonly referred to as the switching table (ST) is a crucial component in the DPC technique. It was initially used in publications relating to the Direct Torque Control (DTC) of the induction motor [23].

ST plays an essential role in selecting the states of the VSI's power semiconductor devices to efficiently regulate the active and reactive powers. This component is used to determine how the transistors in the VSI are activated and deactivated to achieve the desired power values.

Using a switching table in direct power control offers advantages such as simplifying control, eliminating internal current control loops and PWM modulators, which can lead to a more efficient and faster implementation of the control technique.

In the context of DPC, in order to regulate the active and reactive powers to their reference values, quick and precise decisions need to be made regarding the switching states of the semiconductor devices in the VSI. This is where the switching table comes into play, providing clear instructions on how transistors or IGBTs should be turned on or off at each moment to fulfill the control objectives.

Usually, the switching table is prepared in advance and contains all possible switching combinations, each with its role in adjusting the active and reactive powers. It can be created based on certain criteria, such as errors related to the active and reactive powers or the position of the voltage vector.

Using these criteria, the DPC control decides which switching combinations to activate in order to achieve the desired regulation.

The primary goal when designing an ST is to ensure the accurate tracking of the two instantaneous powers. However, certain degrees of flexibility are present when pursuing this objective, affording the designer the option to alternatively emphasize dynamic properties or system efficiency [17].

Furthermore, the operational mode of the converter (either rectifier or inverter) or the grid sequence (positive or negative) should also be factored into the design process due to the impracticality of developing a single ST capable of delivering optimal performance across all these scenarios.

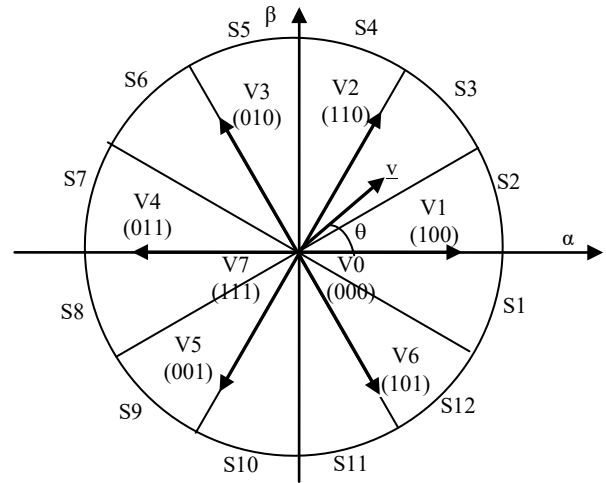


Fig. 3. Sectors and voltage vectors in the stationary reference frame.

To conceive the ST, the stationary reference frame α - β is divided into 12 sectors (Fig. 3). The number of the sector where the voltage vector is located can be simply determined by using same comparators [24].

The DC voltage control block gives the prescribed active power and the prescribed reactive power is an external quantity.

The hysteresis controllers outputs are the digitized signals d_p and d_q . Based on d_p , d_q and the number of the sector located for the voltage vector, the ST detailed in Table I gives the control signals of the converter's transistors [6], [8].

III. MODELLING, SIMULATION AND IMPLEMENTATION OF THE SYSTEM OPERATION

The simulation of the SAPF system operation is based on the specific model conceived for the whole system in the MATLAB - SIMULINK environment (Fig. 4). It consists of several dedicated blocks for: the three-phase power supply, the non linear load which is an uncontrolled rectifier with RLC load, the PWM VSI, the control algorithm implementing the direct power control.

Fig. 5 illustrates the structure of the block named "Algorithm Control", according to the direct power control principles.

To highlight the correct operation of the control system, the waveforms of the phase voltage and supply current after compensation are illustrated Fig. 6. It must be specified that the supply current (in red in Fig. 6) is multiplied by 2 for qualitative identification. It can be seen that the compensated supply current is almost sinusoidal. For comparison, Fig. 7 shows the waveforms of the phase voltage and the high distorted load current.

TABLE I. SWITCHING TABLE FOR THE ADOPTED DPC

d_p	d_q	θ_1	θ_2	θ_3	θ_4	θ_5	θ_6	θ_7	θ_8	θ_9	θ_{10}	θ_{11}	θ_{12}
1	0	101	111	100	000	110	111	010	000	011	111	001	000
	1	111	111	000	000	111	111	000	000	111	111	000	000
0	0	101	100	100	110	110	010	010	011	011	001	001	101
	1	100	110	110	010	010	011	011	001	011	101	101	100

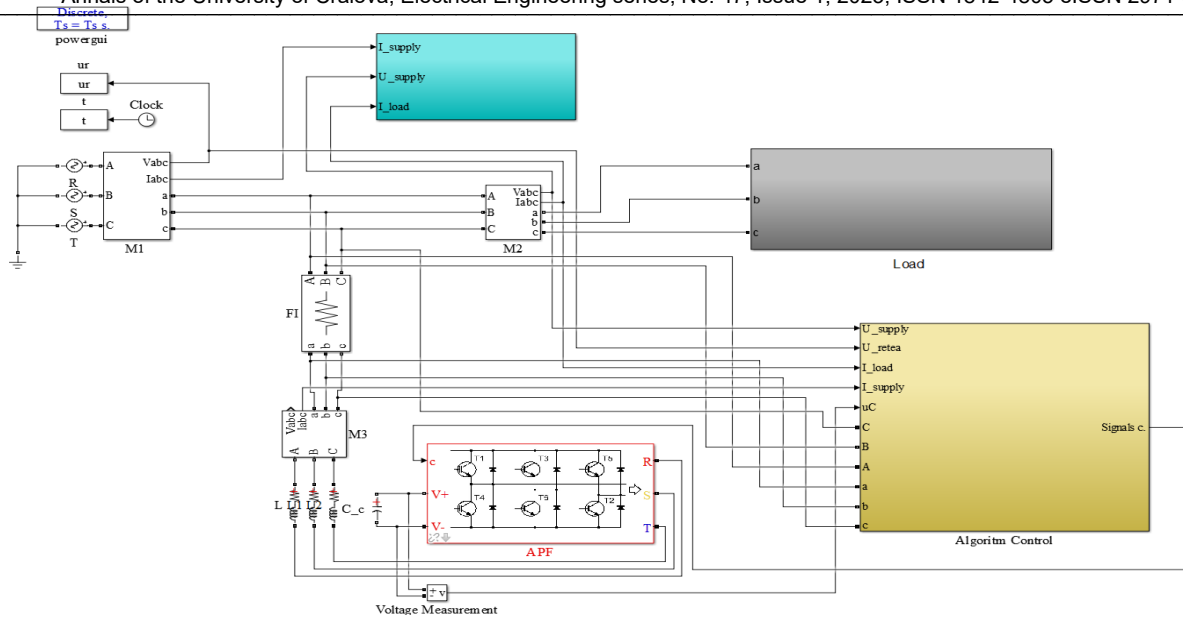


Fig. 4. The Matlab Simulink model of the SAPF compensation system with DPC.

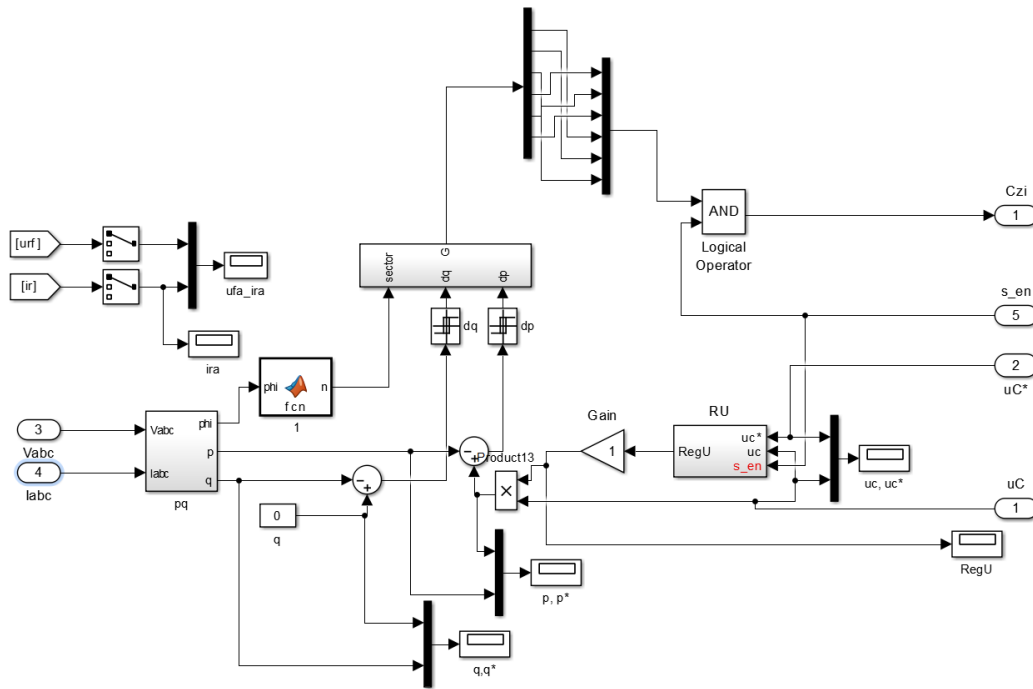


Fig. 5. The structure of the DPC block.

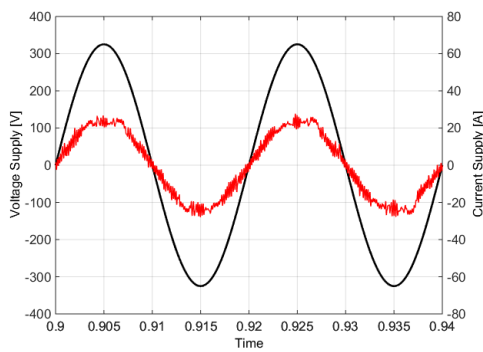


Fig. 6. Waveforms of the phase voltage and supply current, after compensation.

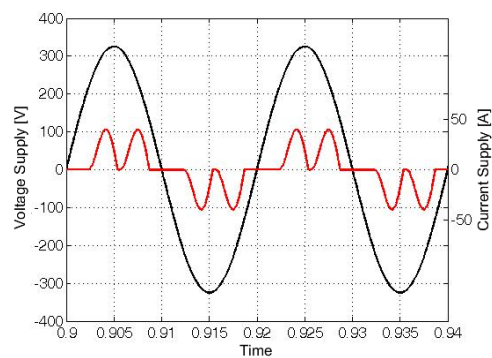


Fig. 7. Waveforms of the phase voltage and distorted load current.

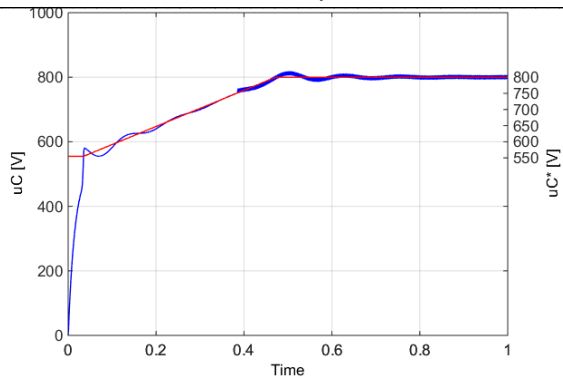


Fig. 8. The time evolution of the actual DC voltage across the capacitor (in blue) and its prescribed voltage (in red).

To illustrate the correct operation of the DC-voltage control loop, the actual voltage across the capacitor (in blue) and its prescribed value (in red) are shown in Fig. 8. It can be seen the faithful tracking of the prescribed value and that there is practically no steady state error, compared to the imposed value of 780 V.

IV. EXPERIMENTAL VERIFICATION

The experimental verification was done on a test bench for the SAPF system within the Research Centre for Electrical Engineering of the University of Craiova.

The control strategy is executed through a single-board dSPACE DS1103 PPC Controller Board, with integrated development environment of MATLAB-SIMULINK RTW, provided by MathWorks, Inc. The adopted sampling time used in the experimental tests is 25 μ s, and experimental results are derived using identical parameters as those used in the simulation.

A picture of the conceived user interface by using Control Desk 5.3 is shown in Fig. 9. Both experimental results and the control panel are illustrated, as follows. The supply phase

voltage and current after compensation are shown in the top left figure. It can be seen that they are in phase and the current is very close to the sinusoidal form, so the active filtering results are very good. The total harmonic distortion (THD) factor of the compensated current is about 7.2 %. Below these waveforms, the phase supply phase voltage and the distorted load current are displayed. In the bottom left figure, the three phase currents at the supply side after compensation are shown proving the balanced operation. In the upper-right corner, the control options for the algorithm are displayed, followed by the DC capacitor voltage (prescribed and actual values) waveforms.

An additional analysis was performed using a Fluke 41B harmonic analyzer for same measurements and experimental acquisitions. The results shown in Fig. 10 – Fig. 15 correspond to a load current of about 10 A. Thus: the acquired supply current after compensation is shown in Fig. 10; its harmonics spectrum is shown in Fig. 11; the numerical values associated with this current are shown in Fig. 12. With reference to the supply voltage, Fig. 13 illustrates its waveform, Fig. 14 its harmonics spectrum and Fig. 15 the associated numerical values.

It must be specified that the supply voltage available in the experiments has a small harmonic distortion of about 1.8 %.

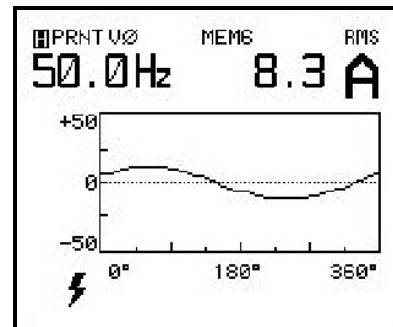


Fig. 10. Acquired supply current after compensation.

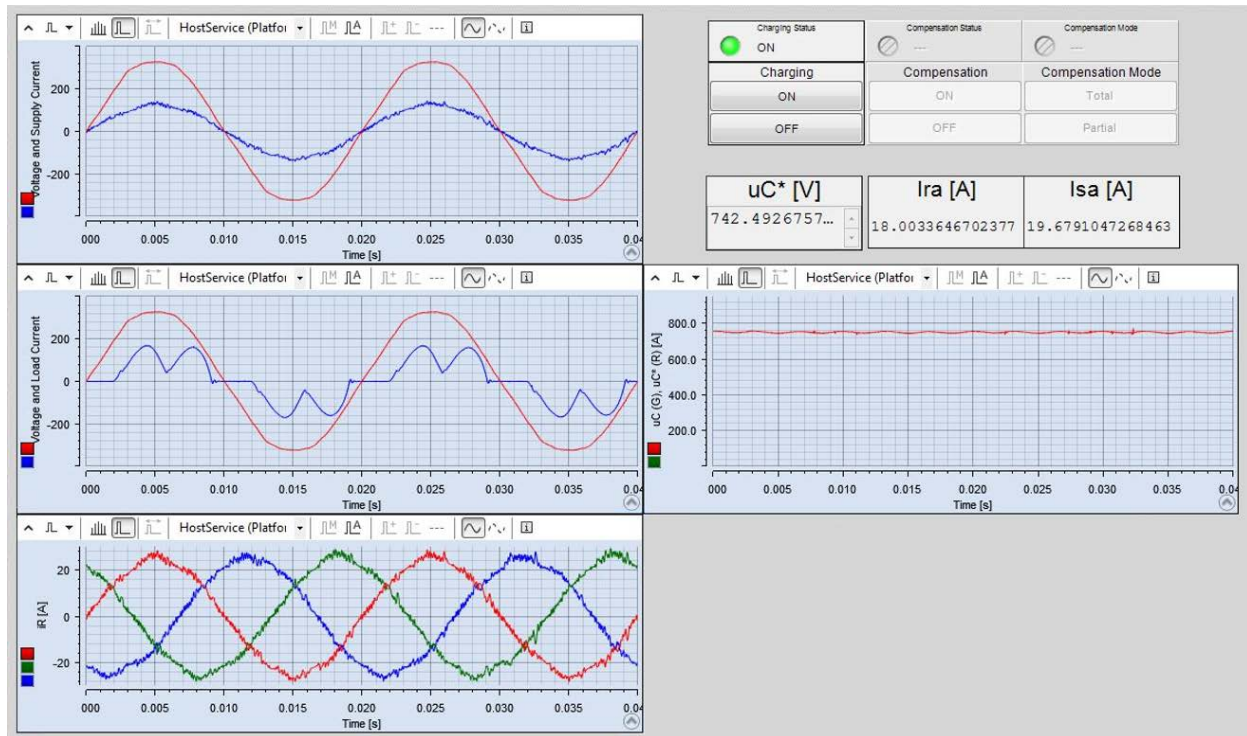


Fig. 9. The dSPACE Control Desk user interface.

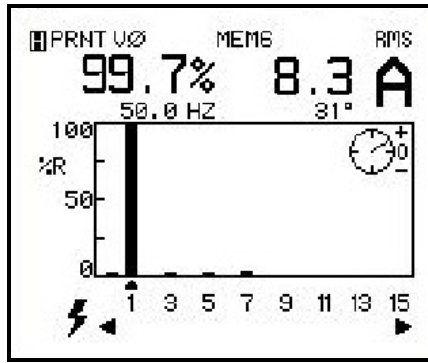


Fig. 11. Harmonics spectrum of the supply current after compensation.

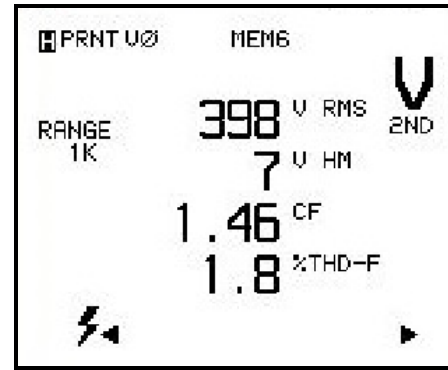


Fig. 15. The screen with the numerical values related to the supply voltage.

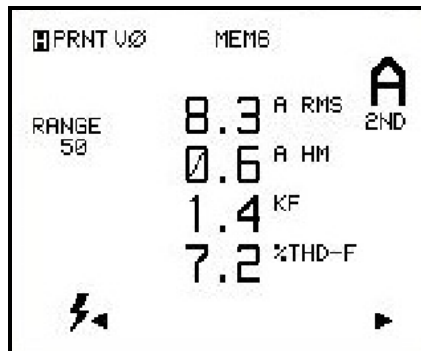


Fig. 12. The screen with the numerical values related to the supply current after compensation.

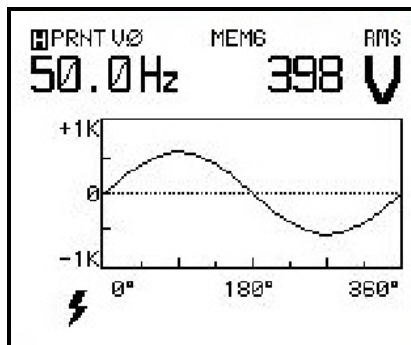


Fig. 13. Acquired supply voltage.

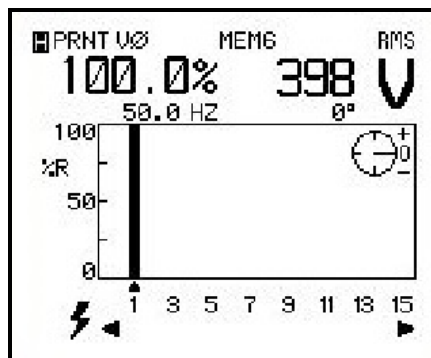


Fig. 14. Harmonics spectrum of the supply voltage.

V. CONCLUSIONS

This paper described an application of the direct power control in a three-phase shunt active filtering system.

Both the modeling and experimental implementation of this specific control algorithm are relatively simple and effective at low currents.

In order to confirm the control strategy's great performance, numerous simulation are conducted, demonstrating how the non-sinusoidal load current can be changed to a quasi-sinusoidal current after the active filtering application.

Since the reactive power is zero after compensation and the active power closely follows its reference, an almost unity power factor is assured.

The simulation results are validated by the experimental results.

The experimental results were obtained within the Research Centre for Electrical Engineering of the University of Craiova, by using the dSPACE 1103 interface.

ACKNOWLEDGMENT

Source of research funding in this article: Research program of the Electrical Engineering Department financed by the University of Craiova.

Contribution of authors:

First author – 40%

First coauthor – 20%

Second coauthor – 20%

Third coauthor – 20%

Received on July 18, 2023

Editorial Approval on November 26, 2023

REFERENCES

- [1] D. Li, T. Wang, W. Pan, X. Ding, and J. Gong, "A comprehensive review of improving power quality using active power filters," *Electric Power Systems Research*, 199, 2021, 107389.
- [2] J. R. Rodriguez, J. W. Dixon, J. R. Espinoza, and J. Pontt, "PWM regenerative rectifiers: state of the art," *IEEE Trans. Ind. Electron.*, 2005, 52, (1), pp. 5–22.
- [3] A. Kusko, M. T. Thompson, *Power Quality in Electrical Systems*, McGraw Hill Professional, 2007.

- [4] T. Ohnishi, "Three-phase PWM converter/inverter by means of instantaneous active and reactive power control," *Proc. IEEE IECON'91*, Kobe, Japan, October/November 1991, pp. 819–824.
- [5] H. Akagi, E.H. Watanabe, and M. Aredes, "Instantaneous power theory and applications to power conditioning," *IEEE Press Series on Power Engineering*, 2007, 1st edn.
- [6] P. Noguchi, H. Tomiki, S. Kondo, and I Takahashi, "Direct power control of PWM converter without power-source voltage sensors," *IEEE Trans. Ind. Appl.*, 1998, 34, (3), pp. 473–479.
- [7] B. S. Chen and G. Joós, "Direct power control of active filters with averaged switching frequency regulation," *IEEE Trans. Power Electron.*, vol. 23, no. 6, pp. 2729–2737, Nov. 2008.
- [8] F. Tlili, F. Bacha, "Comparative study based on different switching lookup tables for Direct Power Control of three-phase AC/DC converter," *2020 4th International Conference on Advanced Systems and Emergent Technologies*, pp. 152–157.
- [9] A. Chaoui, J. -P. Gaubert, F. Krim and L. Rambault, "Direct Power Control of shunt active filter," *2007 European Conference on Power Electronics and Applications*, Aalborg, Denmark, 2007, pp. 1–11.
- [10] S. Chen and G. Joos, "Direct power control of three phase active filter with minimum energy storage components," *Proc. IEEE APEC'01*, Anaheim, USA, March 2001, pp. 570–576.
- [11] T. A. Trivedi, R. Jadeja, P. Bhatt, "A review on Direct Power Control for applications to grid connected PWM converters," *Engineering, Technology & Applied Science Research*, vol. 5, no. 4, 2015.
- [12] J. Alonso-Martinez, G. Carrasco JE, and S. Arnaltes, "Table-based direct power control: a critical review for microgrid application," *IEEE Trans. Power Electron.*, 2010, 25, (12), pp. 2949–2961.
- [13] A. Baktash, A. Vahedi, and M. A. S. Masoum "Improved switching table for direct power control of three-phase PWM rectifier," *Proc. Australasian Universities Power Engineering Conference*, Perth, Australia, December 2007, pp. 1–5.
- [14] A. Bouafia, J. P. Gaubert, and F. Krim, "Analysis and design of new switching table for direct power control of three-phase PWM rectifier," *Proc. Power Electronics and Motion Control Conf.*, Poznan, Poland, September 2008, pp. 703–709.
- [15] J. Hu, and Z. Q. Zhu, "Investigation on switching patterns of direct power control strategies for grid-connected dc-ac converters based on power variation rates," *IEEE Trans. Power Electron.*, 2011, 26, (12), pp. 3582–3598.
- [16] B. Essoussi, A. Moutabir, B. Bensassi, A. Ouchatti, Y. Zahraoui, B. Benazza, "Power quality improvement using a new DPC switching table for a three-phase SAPF," *International Journal of Robotics and Control Systems*, vol. 3, no. 3, pp. 510–529, 2023.
- [17] J. G. Normiella, J. M. Cano, and G. A. et al. Orcajo, "Optimization of direct power control of three-phase active rectifiers by using multiple switching tables," *Proc. Int. Conf. Renewable Energies and Power Quality (ICREPQ'10)*, Granada, Spain, March 2010.
- [18] H. Jingjing, Z. Aimin, C. Xiaojun, Z. Hang, and W. Jianhua, "A novel direct power control strategy of double hysteresis and multiple switching tables for rectifiers," *Proc. Int. Conf. Advanced Power System Automation and Protection (APAP)*, Beijing, China, October 2011, pp. 36–41.
- [19] A. Rath and G. Srungavarapu, "An advanced shunt active power filter (SAPF) for non-ideal grid using predictive DPC," *IETE Technical Review*, vol. 40, no. 4, pp. 1–14, Oct. 2022.
- [20] Boudechiche, M. Sarra, O. Aissa, J.-P. Gaubert, B. Benlahbib, and A. Lashab, "Anti-windup FOPID-based DPC for SAPF interconnected to a PV System Tuned Using PSO Algorithm," *European Journal of Electrical Engineering*, vol. 22, no. 4-5, pp. 313–324, Oct. 2020.
- [21] Z. Chelli, A. Lakehal, T. Khoualdia, and Y. Djeghader, "Study on Shunt Active Power Filter control strategies of three-phase grid-connected photovoltaic systems," *Periodica Polytechnica Electrical Engineering and Computer Science*, vol. 63, no. 3, pp. 213–226, Aug. 2019.
- [22] M. Kadem, A. Semmah, P. Wira, and S. Dahmani, "Fuzzy logic-based instantaneous power ripple minimization for direct power control applied in a shunt active power filter," *Electrical Engineering*, vol. 102, no. 3, pp. 1327–1338, Sep. 2020.
- [23] I. Takahashi and T. Noguchi, "A new quick-response and high-efficiency control strategy of an induction motor," *IEEE Trans. Ind. Appl.*, 1986, 22, (5), pp. 820–827.
- [24] M. D. Constantinescu, M. Popescu, G. -E. Subtirelu and I. -C. Toma, "Application of the Direct Power Control in a three-phase shunt active power filter system," *2023 International Conference on Electromechanical and Energy Systems (SIELMEN)*, Craiova, Romania, 2023, pp. 1-6.

Data-Driven Control of the Second Order Inertial Systems with Astatism

Irina Cojuhari

Technical University of Moldova, Chişinău, Republic of Moldova, irina.cojuhari@ati.utm.md

Abstract - In order to realize an efficient synthesis of the control algorithm, it is necessary to be known the mathematical model of the control object. This paper deals with the problem of data-driven control of second order astatic inertial systems with, or without time delay, that supposes an experimental identification of the mathematical model in the closed-loop and algorithm for synthesis the PD and PID controllers. The control algorithm was synthesized according to the maximum stability degree method with iterations. The closed-loop identification method and control algorithms of the PD and PID controllers were verified by computer simulation in MATLAB and there are obtained good results in model estimation and in the tuning of the PD and PID controllers.

Cuvinte cheie: *identificarea în buclă închisă, control bazat pe date, PD și PID regulator, modelarea matematică, modele de obiecte cu inerție și astatism.*

Keywords: *closed-loop identification, data driven control, PD and PID controllers, mathematical modelling, second order inertial systems with astatism.*

I. INTRODUCTION

In the realm of control systems engineering, traditional methods of tuning the proportional-integral-derivative (PID) controllers often rely on mathematical models. The mathematical models present the center of the design and synthesis the controllers, and while these models work well, when the underlying system dynamics are well understood and predictable, but they can give not so good results for the case of complex, uncertain and nonlinear systems [1]. This limitation has led to the emergence of data-driven control, a novel and powerful approach that leverages real-world data to develop control algorithms and optimize system performance in real time of the system operation [2-4].

Data-driven control refers to a control strategy that utilizes data-driven modelling techniques to design control algorithms and this strategy has gained popularity in recent years due to its ability to handle complex and nonlinear systems, where the traditional control methods may give not so good results. It is particularly useful when the underlying physics of the system are not well understood or when the system's behavior changes over time [16].

The applications of data-driven control span across various industries and fields. From the manufacturing processes and robotics to autonomous vehicles, and this strategy has shown promise in enhancing system performance, reducing energy consumption, improving safety, and handling complex environments.

Key features of data-driven control include model identification based on data analysis, adaptive control mechanisms that adjust in real-time the tuning parameters, and the ability to optimize control strategies using historical and real-time data. In this control strategy various identification methods are used to approximate the dynamics of the process with different transfer functions, where the model identification supposes the approximation of the process with mathematical model from observed input/output data [5]. In the control systems the control object model estimation can be realized by the two different approaches: in the open-loop and in the closed-loop. In an open-loop system identification, the control input is applied to the system, but the system's output is not used to influence the control action. Essentially, the system operates without any feedback control. Open-loop identification methods involves analyzing the system's response to different inputs and disturbances and presents some simple assumptions where the process dynamics is approximated by the model of object with inertia first or second order with, or without time delay.

Opposite to the open-loop identification, there are developed over 30 years the closed-loop identification methods, where the control input is adjusted based on the system's output, creating a feedback loop. This allows to the system to regulate itself and maintain desired performance. Closed-loop identification takes into account the interaction between the control action and the system's response. In both open-loop and closed-loop model identification, the goal is to find a mathematical model that accurately predicts how the system responds to inputs and disturbances. These models can subsequently be used for controller design, system analysis, or optimization [6-7].

The purpose of this paper, is to focus attention on the data-driven control of the second order inertial systems with astatism with, or without time delay. This supposes the model identification in the closed-loop and algorithm for synthesis the PD and PID controllers. The controllers were proposed to be synthesized according to the maximal stability degree method with iterations (MSDI), that offers to the system high performance and good robustness.

II. DATA-DRIVEN CONTROL OF THE SECOND ORDER INERTIAL SYSTEM WITH ASTATISM

A. Closed-Loop System Identification of the Second Order Inertial Systems with Astatism

The data-driven control strategy involves deriving control actions directly from observed data and system behavior, rather than relying solely on a pre-existing, fully known mathematical model.

Many industrial processes operate under feedback control. Due to unstable behavior of the control object, or necessary of the safety of operation, experimental data can be acquired only under closed-loop. Closed-loop identification methods have been proposed by the Karl Johan Åström et al. (1970), Gustavsson et al. (1977), Söderström and Stoica (1989), Lennart Ljung et al. (1999), Tore Häggglund et al. (2000), Graham C. Goodwin (2011), Sudhahar et al. (2020) [5-10]. The closed-loop identification methods are oriented to solve the consistency problem of identification, considering the situation that the control object and the disturbance signal are taken into account in the identified model [11-15].

In the author paper [17], it was proposed an algorithm for identification of the astatic system in the closed-loop, where the transfer function that approximates the control object is:

$$H(s) = \frac{k}{s(T_1s+1)(T_2s+1)} = \frac{k}{a_0s^3 + a_1s^2 + a_2s}, \quad (1)$$

where T_1, T_2 are time constants; k is transfer coefficient of the system; $a_0 = T_1T_2$, $a_1 = T_1 + T_2$, $a_2 = 1$.

The identification algorithm in the closed-loop consists from the following steps:

1. Analysis of the process, that involves identifying the key characteristics that define the nature of the system.
2. Implementation of the feedback control system with P controller.
3. Variation of the proportional tuning parameter $k_p > 0$, until the system achieves the limit of stability and further determination the value of critical transfer coefficient k_{cr} and period of oscillations – T_{cr} .
4. Calculation of the natural frequency value according to the relation:

$$\omega_n = \frac{2\pi}{T_{cr}}. \quad (2)$$

5. Calculation of the system transfer coefficient according to the relation:

$$k = \lim_{t \rightarrow \infty} \frac{y_{st} - y_{initial}}{u - u_{initial}}, \quad (3)$$

where y_{st} is the steady-state output value, $y_{initial}$ is the initial value of the output response, u – input signal, $u_{initial}$ is the initial value of the input signal.

6. Calculation the parameters' values of the control object (1):

$$\begin{cases} a_0 = \frac{1}{\omega_n^2}; \\ a_1 = \frac{k_{cr}k}{\omega_n^2}; \\ a_2 = 1. \end{cases} \quad (4)$$

B. Closed-Loop System Identification of the Second Order Inertial Systems with Astaticism and Time Delay

For the case of the astatic system with time delay, in the author paper [17], it was proposed an algorithm for system identification in the closed-loop, where the transfer function that approximates the control object is following:

$$H(s) = \frac{ke^{-\tau s}}{s(T_1s+1)(T_2s+1)} = \frac{ke^{-\tau s}}{a_0s^3 + a_1s^2 + a_2s}, \quad (5)$$

where T_1, T_2 are time constants; k is transfer coefficient of the system; τ - time delay; $a_0 = T_1T_2$, $a_1 = T_1 + T_2$, $a_2 = 1$.

The identification algorithm of the astatic system with time delay in the closed-loop is following:

1. Analysis of the process, that involves identifying the key characteristics that define the nature of the system.
2. Implementation of the feedback control system with P controller.
3. Variation of the proportional tuning parameter $k_p > 0$, until the system achieves the limit of stability and further determination the value of critical transfer coefficient k_{cr} and period of oscillations – T_{cr} .
4. From the undamped transient response of the closed loop system determination the value of time delay - τ .
5. Calculation of the natural frequency value according to the relation (2).
6. Calculation of the system transfer coefficient according to the relation (3).
7. Calculation the parameters' values of the control object (5):

$$\begin{cases} a_0 = \frac{a_2\omega_n - k_{cr}k \sin \tau\omega_n}{\omega_n^3}; \\ a_1 = \frac{k_{cr}k \cos \tau\omega_n}{\omega_n^2}; \\ a_2 = 1. \end{cases} \quad (6)$$

C. Synthesis the PD Controller to the Model of Object with Inertia Second Order and Astaticism

It is considered that the control system is presented in the Fig. 1 and it is formed from the controller with transfer function $H_R(s)$ and control object (1).

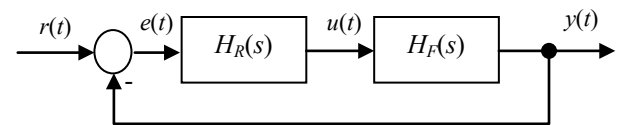


Fig. 1. Structural scheme of the automatic control system.

The PD controller is described by the transfer function [1]:

$$H_R(s) = k_p + k_d s, \quad (7)$$

where the tuning parameters of PD controller - k_p , k_d .

One of the tuning methods of the controllers is maximum stability degree (MSD) criterion [18] and according to this criterion the value of stability degree is calculate by the expression:

$$J = \frac{a_1}{na_0}, \quad (8)$$

where the n is the order of the closed-loop characteristic equation with respectively controller.

Next, utilizing the MSD method with iterations [19], there are calculated expressions for tuning parameters of the PD controller:

$$k_p = \frac{1}{k}(a_0J^3 - a_1J^2 + a_2J) + k_dJ, \quad (9)$$

$$k_d = \frac{1}{k}(-3a_0J^2 + 2a_1J - a_2), \quad (10)$$

where J is the stability degree of the system.

From the expression (8) is calculated the value of system stability degree

$$J = \frac{a_1}{3a_0},$$

and according to this expression, the analytical expressions for calculation the tuning parameters of the PD controller (9)-(10) can be rewritten in the following way:

$$k_p = \frac{a_1^3}{27ka_0^2}, \quad (11)$$

$$k_d = \frac{a_1^2 - 3a_0a_2}{3ka_0}. \quad (12)$$

According to the expressions for calculation the values of control object's parameters (4), the expressions (11)-(12) can be rewritten as:

$$k_p = \frac{k_{cr}^3 k^2}{27\omega_n^2}, \quad (13)$$

$$k_d = \frac{k_{cr}^2 k^2 - 3\omega_n^2}{3k\omega_n^2}. \quad (14)$$

D. Synthesis the PID Controller to the Model of Object with Inertia Second Order and Astatism

The control algorithm PID is described by the following transfer function [1]:

$$H_R(s) = k_p + \frac{k_i}{s} + k_d s, \quad (15)$$

where the tuning parameters of PID controller - k_p , k_i , k_d .

The analytical expressions for calculation the tuning parameters of the PID controller were obtained in concordance with MSD method with iterations [19]:

$$k_p = \frac{1}{k}(4a_0J^3 - 3a_1J^2 + 2a_2J) + 2k_dJ, \quad (16)$$

$$k_i = \frac{1}{k}(-a_0J^4 + a_1J^3 - a_2J^2) - k_dJ^2 + k_pJ, \quad (17)$$

$$k_d = \frac{1}{k}(-6a_0J^2 + 3a_1J - a_2), \quad (18)$$

where J is the stability degree of the system.

From the expression (8) it is calculated the value of system stability degree

$$J = \frac{a_1}{4a_0}.$$

And in concordance with the value of stability degree, the analytical expressions (16)-(18) can be rewritten as:

$$k_p = \frac{a_1^3}{16ka_0^2}, \quad (19)$$

$$k_i = \frac{a_1}{256ka_0^3}, \quad (20)$$

$$k_d = \frac{3a_1^2 - 8a_0a_2}{8ka_0}. \quad (21)$$

According to the expressions for calculation the value of control object's parameters (4), the expressions (19)-(21) can be rewritten as:

$$k_p = \frac{k_{cr}^3 k^2}{16\omega_n^2}, \quad (22)$$

$$k_i = \frac{k_{cr}\omega_n^4}{256}, \quad (23)$$

$$k_d = \frac{3k_{cr}^2 k^2 - 8\omega_n^2}{8k\omega_n^2}. \quad (24)$$

E. Synthesis the PID Controller to the Model of Object with Inertia Second Order, Astatism and Time Delay

The control algorithm PID is described by the transfer function (15) and the control object is described by the transfer function (5). The analytical expressions for calculation the tuning parameters of the PID controller were obtained in concordance with MSD method with iterations [19]:

$$k_p = \frac{e^{-\tau J}}{k}(-\tau a_0 J^4 + (\tau a_1 + 4a_0)J^3 - (a_2\tau + 3a_1)J^2 + (25) + 2a_2J) + 2k_dJ,$$

$$k_i = \frac{e^{-\tau J}}{k}(-a_0J^4 + a_1J^3 - a_2J^2) - k_dJ^2 + k_pJ, \quad (26)$$

$$k_d = \frac{e^{-\tau J}}{2k}(-\tau^2 a_0 J^4 + (\tau^2 a_1 + 8\tau a_0)J^3 - (\tau^2 a_2 + 6a_1\tau + (27) + 12a_0)J^2 + (4a_2\tau + 6a_1)J - 2a_2)$$

where J is stability degree of the system.

F. Algorithm for Data Driven Control

According to the procedure of experimental identification in the closed-loop of the astatic system with inertia second order and analytical expressions for calculation the tuning parameters, the algorithm for data-driven control of the astatic systems with inertia is following:

1. P control algorithm establishment.
2. Achievement the undamped transient response by the variation the proportional tuning parameter $k_p > 0$.
3. Data extraction from step response as T_{cr}, k_{cr}, k, τ and calculation the value of natural frequency ω_n .
4. Model object chosen and parameter estimation by the (4) or (6) expressions in dependency of time delay presence.
5. Tuning the PD controller by the expressions (9)-(10), or PID controller by the expression (18)-(20), or (25)-(27).

III. APPLICATION AND COMPUTER SIMULATION

A. Closed-Loop System Identification and Control of the Second Order Inertial Systems with Astatism

To verify the proposed algorithm, it is considered that the control object is described by the following transfer function:

$$H(s) = \frac{2}{s(2s+1)(3s+1)} = \frac{2}{6s^3 + 5s^2 + s}. \quad (28)$$

Next, the control system with P controller was simulated and k_p tuning parameter was varied until it was achieved the system response presented in Fig. 2.

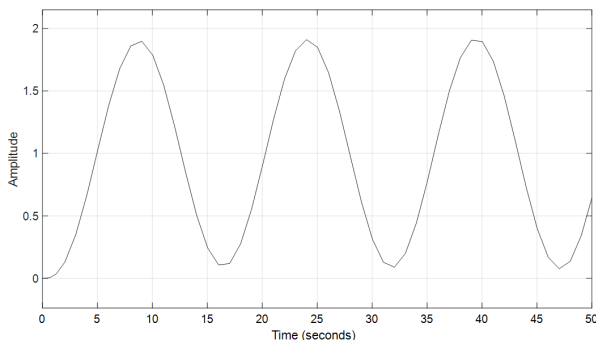


Fig. 2. Undamped step response of the closed-loop system.

There are obtained the following parameters:

$$k_{cr} = 0.42, T_{cr} = 15.314 \text{ s}, \omega_n = 0.4101.$$

Based on the expressions (4), there are calculated the transfer function of the control object:

$$H(s) = \frac{2}{5.9459s^3 + 4.99s^2 + s}. \quad (29)$$

In the Fig. 3, it is presented the comparison between original step response of the open loop system described by the transfer function (28) – curve 1 and identified transfer function (29) – curve 2.

From Fig. 3, it can be observed that the algorithm for identification in the closed loop offers good estimation of the mathematical model.

Next, to the identified transfer function (29), it is proposed to tune the PD controller according to the (13)-(14) expressions. In the Table I, there are presented the calculated values of the tuning parameters and it was done the comparison with MSDI method, parametrical optimization (PO) from MATLAB and genetic algorithm (GA).

In case of genetic algorithm, the fitness function was designed based integral square error (GA1) and integrated time absolute error (GA2).

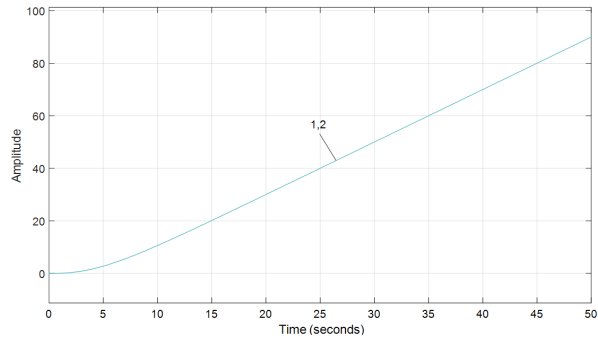


Fig. 3. Comparison of the system step responses in the open loop.

TABLE I.
SYSTEM PERFORMANCE AND TUNING PARAMETERS OF THE PD CONTROLLER

No	Method	J	k_p	k_d	t_s	t_r	σ
1	Proposed Method of Tuning		0.065	0.199	22.2	22.2	-
2	MSDI	0.29	0.064	0.193	22.7	22.7	
3	MSDI	0.36	0.049	0.147	32.1	32.1	
4	PO		0.206	0.886	14.3	3.1	7.5
5	GA1		3.302	35.01	13.1	0.33	69
6	GA2		3.008	26.84	14.6	0.54	70

In Fig. 4, it is presented the step responses of the automatic control system with PD controller.

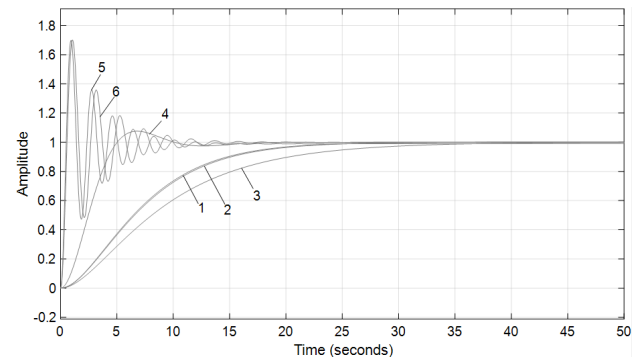


Fig. 4. Step response of the automatic control system with PD controller tuned by: 1 – proposed method of tuning; 2 – MSDI method; 3 – MSDI; 4 – parametrical optimization from MATLAB; 5 – GA1 (fitness function ISE); 6 – GA2 (fitness function ITAE).

In case of using the genetic algorithm, there were obtained oscillated transient responses with high overshoot more than 20%.

Next, it was proposed to be tuned the PID controller to the identified model of object (29) based on the analytical expressions (22)-(24). The obtained results are presented in the Table II and there was done the comparison with MSDI method, parametrical optimization from MATLAB and genetic algorithm, where fitness function was designed based integral square error (GA1) and integrated time absolute error (GA2). Tuning parameters of the PID controller and system performance are presented in the Table II.

TABLE II.
SYSTEM PERFORMANCE AND TUNING PARAMETERS
OF THE PID CONTROLLER

No	Tuning Method	J	k_p	k_i	k_d	t_s	t_r	σ
1	Proposed Method of Tuning		0.1	4.640 5e-05	0.28	19.7	11.5	2.8
2	MSDI	0.2	0.10	0.005	0.27	43.1	8.2	26
3	MSDI	0.28	0.07	0.001	0.21	122	13.5	8.4
4	PO		0.2	0.006	0.92	45	4	10
5	GA1		0.25	0.014	18.17	18	0.48	57
6	GA2		5.89	0.008	67.62	11.76	0.32	83

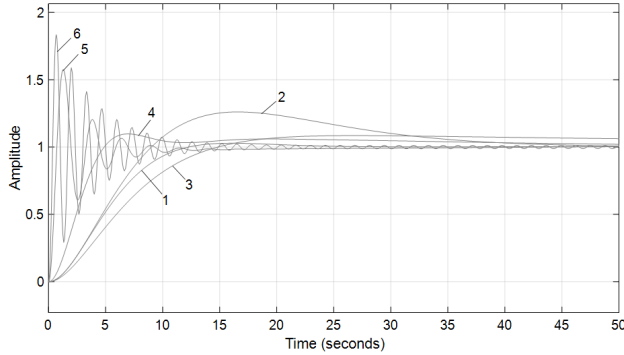


Fig. 5. Step response of the automatic control system with PID controller tuned by: 1 – proposed method of tuning; 2 – MSDI method; 3 – MSDI method; 4 – parametrical optimization from MATLAB; 5 – GA1 (fitness function ISE); 6 – GA2 (fitness function ITAE).

B. Closed-Loop System Identification and Control of the Second Order Inertial Systems with Astatism and Time Delay

It is given the control object described by the following transfer function:

$$H(s) = \frac{3e^{-10s}}{s(5s+1)(2s+1)} = \frac{3e^{-10s}}{10s^3 + 7s^2 + s}. \quad (30)$$

According to the identification algorithm, the control system with P controller was simulated and k_p tuning parameter was varied until it was achieved the system response presented in Fig. 6.

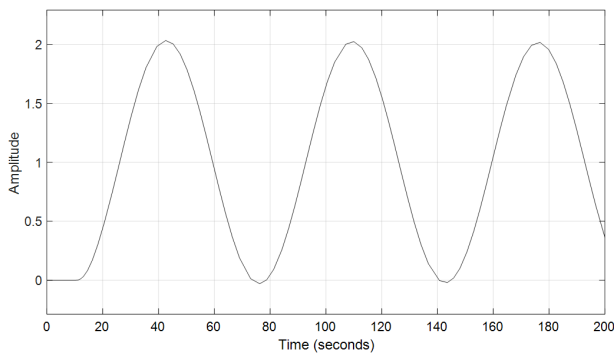


Fig. 6. Undamped step response of the closed-loop system.

Based on the step response presented in the Figure 6, there are obtained:

$$k_{cr} = 0.0355, T_{cr} = 67.418 \text{ s.}, \tau = 10 \text{ s.}, \omega_n = 0.0932.$$

Based on the expressions (6), there are calculated the transfer function of the control object:

$$H(s) = \frac{3e^{-10s}}{9.51s^3 + 7.31s^2 + s}. \quad (31)$$

The comparison between original step response of the open-loop system described by the transfer function (30) (curve 1) and identified transfer function (31) (curve 2) is presented in the Figure 7.

From Fig. 7, it can be concluded that the identification algorithm in the closed-loop offers so good model estimation.

Next, to the identified transfer function (31), it was proposed to be tuned PID controller according to the (25)-(27) expressions.

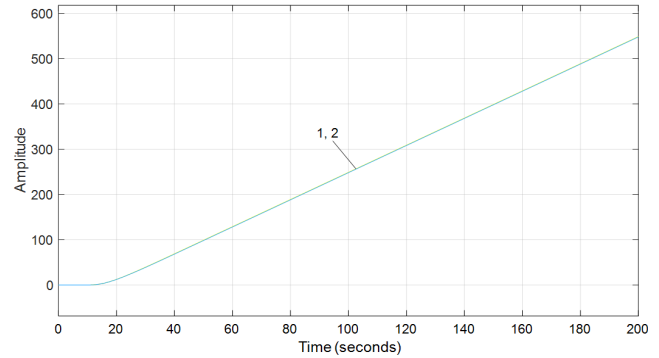


Fig. 7. Comparison of the system step responses in the open loop.

The obtained results are presented in the Table III and there was done the comparison with parametrical optimization (PO) from MATLAB. The genetic algorithm did not give the satisfactory results for the case of tuning the PID controller.

TABLE III.
SYSTEM PERFORMANCE AND TUNING PARAMETERS
OF THE PID CONTROLLER

No	Tuning Method	J	k_p	k_i	k_d	t_s	t_r	σ
1	MSDI	0.08	0.016	0.00026	0.09	141	15	39
2	MSDI	0.1	0.015	0.0002	0.08	176	17	32
3	PO		0.016	7.9136e-05	0.11	351	17	12

In the Figure 8, it is presented the computer simulation of the control system with PID controller tuned by the MSDI method – curve 1 and curve 2, parametrical optimization – curve 3.

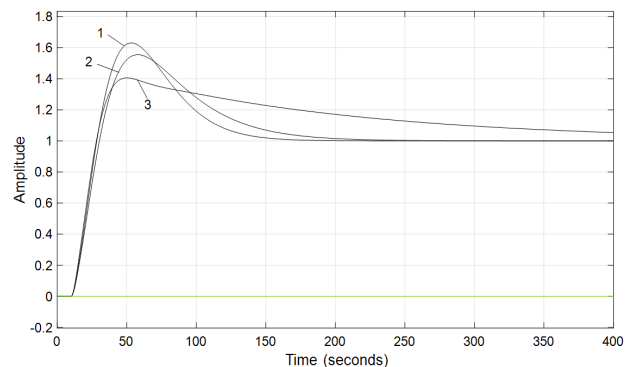


Fig. 8. Step response of the automatic control system with PID controller tuned by: 1 – MSDI method; 2 – MSDI method; 3 – parametrical optimization from MATLAB.

IV. CONCLUSIONS

Traditional control methods and algorithms often depend on accurate mathematical models to design controllers, data-driven approaches leverage the availability of data to achieve control objectives. This paper introduced a new algorithm for data-driven system identification and control of the second order inertial systems with astaticism and with, or without time delay. The algorithm's foundation lies in a stepwise approach, commencing with system identification, that is performed within a closed-loop, leveraging the undamped step response of the system and based on the parameters, that are obtained from the undamped step response, there are calculated the mathematical model that approximates the inertial system with astaticism.

Next according to data-driven control algorithm, there are proposed simple analytical expressions for calculation the tuning parameters of the PD and PID controllers. The expressions for tuning the PD and PID controllers were obtained based on the MSD method with iterations. The closed-loop identification and synthesis methods was verified by computer simulation and the obtained results were compared with parametrical optimization from MATLAB and genetic algorithm. The proposed procedure of data driven control of second order inertial systems with astaticism can be implemented as auto-tuning method of the PD or PID controller and offers to the control system so good performance and high robustness.

ACKNOWLEDGMENT

This work was supported by the project 22.00208.5007.12/PD I "Models and algorithms for control and behaviour approach of the interoperable systems" and by the project 20.80009.5007.26 „Models, algorithms and technologies for the control, optimization and security of the Cyber-Physical systems”.

Received on July 12, 2023

Editorial Approval on November 19, 2023

REFERENCES

- [1] I. Dumitrache, *Control engineering (in romanian)*. Bucharest: Politehnica P, V. 1, 2016.
- [2] T. Zhang, M. Ye, "Data-driven control for complex systems: Concepts, algorithms, and applications," in *Science China Technological Sciences*, 61(1), 2018, pp. 36-49.
- [3] H. Wang, D. M. Hausenloy, S.S. Ge, "Data-driven control: From data-intensive to data-driven control in theory and practice," *IEEE Transactions on Cybernetics*, 47(11), pp. 3895-3911.
- [4] C. H. Lee, J. M. Velni, L. Xie, "Data-driven control: Concepts, algorithms, and applications," in *Annual Reviews in Control*, 46, 2018, pp. 106-120.
- [5] J. Ertveldt, J. Sanchez-Medina, Z. Jardon, M. Hinderdael, P. Guillaume, "Experimental identification of process dynamics for real-time control of Directed Energy Deposition," in *Procedia CIRP*, Vol. 111, 2022, pp. 321-325. 10.1016/j.procir.2022.08.031.
- [6] S. Sharma, B. Verma, P. K. Padhy, "Closed-loop identification of stable and unstable processes with time-delay," in *Journal of the Franklin Institute*, 359(7), 2022, pp. 3313-3332.
- [7] J. Kurek, "Identification of inertial model for astatic system," in *Proceedings of the 18th International Conference on Methods & Models in Automation & Robotics (MMAR)*, Miedzyzdroje, Poland, 2013.
- [8] P. Van den Hof, "Closed-loop Identification," *IFAC Proceedings Series*, 3, 1997, pp. 1547-1560.
- [9] W. Jianhong, R.A. Ramirez-Mendoza, "The practical analysis for closed-loop system identification," in *Cogent Engineering*, 7:1, 2020, pp. 1-16.
- [10] A. Ebadat, *Experiment Design for Closed-loop System Identification with Applications in Model Predictive Control and Occupancy Estimation*. Doctoral thesis, Stockholm, Sweden, 2017.
- [11] J. Linder, M. Enqvist, "Identification of systems with unknown inputs using indirect input measurements," in *International Journal of Control*, 90:4, 2017, pp. 729-745.
- [12] J. C. Agüero, G. C. Goodwin, P. M.J. Van den Hof, "A virtual closed loop method for closed loop identification," *Automatica*, Volume 47, Issue 8, 2011, pp. 1626-1637.
- [13] U. Forssell, L. Ljung, "Closed-loop identification revisited," *Automatica*, Volume 35, Issue 7, 1999, pp. 1215-1241.
- [14] A. Ingimundarson, T. Häggglund, "Closed-Loop Identification of a First-Order Plus Dead-Time Model with Method of Moments," *IFAC Proceedings Volumes*, Volume 33, Issue 10, 2000, pp. 929-934.
- [15] K. J. Åström, P. Eykhoff, *System Identification. (Technical Reports TFRT-7011)*. Department of Automatic Control, Lund Institute of Technology (LTH), 1970.
- [16] I. Cojuhari, "Data-Driven Model Identification and Control of the Inertial Systems," in *Intelligent Control and Automation*, 14, 2023, pp. 1-18. doi: 10.4236/ica.2023.141001.
- [17] I. Cojuhari, "Closed-Loop System Identification Approach of the Inertial Models," in *Applied Mathematics*, 14, 2023, pp. 107-120. doi: 10.4236/am.2023.142006.
- [18] I. Fiodorov, "Synthesis Algorithms of Controllers for Automatic Control Systems with Maximum Stability Degree," in *Annals of the University of Craiova, Electrical Engineering*, series 2013, 37, 2013, pp. 139-143.
- [19] B. Izvoreanu, I. Fiodorov, M. Pisarenco, "Comparative Analysis of Controllers Tuning Methods to Models of Objects with Inertia," in *Buletinul Institutului Politehnic din Iași, Tomul L(LIV), Fasc. 5A, Electrotehnică, Energetică, Electronică*, 2004, pp. 63-68.

The Design of a Location Monitoring System for a Fleet of Electric Scooters

Florin Ravigan, Mihăiță Lincă and Laurențiu Alboteanu

University of Craiova/Faculty of Electrical Engineering, Craiova, Romania, ravigan.florin@gmail.com

University of Craiova/Faculty of Electrical Engineering, Craiova, Romania, mlnca@em.ucv.ro

University of Craiova/Faculty of Electrical Engineering, Craiova, Romania, lalboteanu@em.ucv.ro

Abstract - The development of geolocation systems (geostationary satellite networks), as well as devices capable of receiving signals and processing the data coming from them, makes possible the implementation of location monitoring systems for various purposes. Whether it's about security or optimizing travel times or routes, these systems are based on information in the form of global coordinates (latitude and longitude) from satellite systems or cell towers. The design of such a system is presented in this paper, being a good guide in the design and implementation of such a system, regardless of the application. Both, the hardware part (the designed equipment) and the software part (the backend component running on a virtual private server, as well as a mobile application) are presented in this paper. In the development of the system, was used only location provided by information from satellites, without using GSM cell signals. The entire system has been successfully tested in different GSM signal conditions as well as various locations to see the influence of environmental parameters on performance. The system described in the paper can be the starting point for the development of other systems for a variety of applications that require the management of the location of some devices.

Cuvinte cheie: geolocație, microcontroller, sateliti, framework, full-stack.

Keywords: geolocation, microcontroller, satellites framework, full-stack.

I. INTRODUCTION

As is known, positioning systems use networks of geostationary satellites that emit signals to the Earth's surface where they are received by the equipment that can process them. Currently, four global positioning systems are fully operational: the U.S. Navigation Signal Timing and Ranging (NAVSTAR) GPS, Russia's Global Navigation Satellite System (GLONASS), the EU's system named Galileo, and China's Bei Dou Navigation Satellite System. Japan and India are also well on their way with their regional systems, the Quasi-Zenith Satellite System (QZSS) and the Indian Regional Navigation Satellite System (IRNSS), respectively[1].

The most popular and widely used are the GPS and GLONASS systems. They emit signals that ensure positioning accuracy of a few meters for the general public, but also commercial signals for positioning with an error of only a few centimeters.

To receive signals from satellites, are used electronic devices consisting of an electronic control unit equipped with a dedicated antenna.

A GPS or GNSS antenna is a device designed to receive and amplify the radio signals transmitted on specific frequencies by satellites and convert them to an electronic signal for use by a receiver.

This receiver is represented by a dedicated electronic device with an integrated microprocessor that most of the time has a built-in component that ensures the connection to a mobile phone network and can be configured through a set of AT commands.

The picture below presents a board equipped with that kind of unit from Simcom(China) and a GPS active antenna.

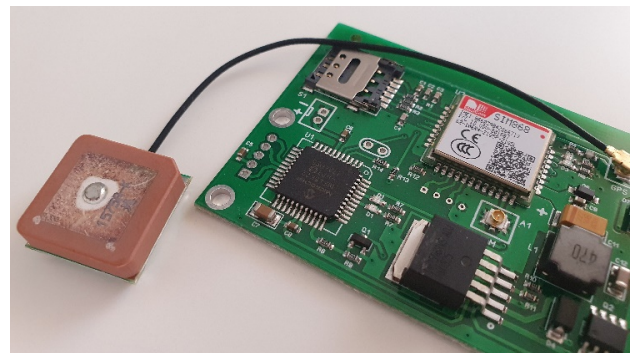


Fig.1 The GPS module with a dedicated antenna

II. THE SYSTEM'S ARCHITECTURE

The role of this system is to connect a two-wheeled electric vehicle to the Internet network through which to transmit a series of data (location, battery level), as well as to receive various commands (software update for controllers, on/off, or lock commands).

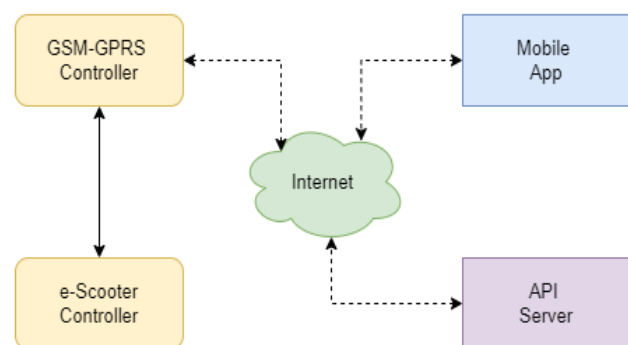


Fig.2 The block diagram of the entire system

To realize these tasks, the system is composed of several hardware and software components. The block diagram of the entire system is shown in the following figure.

The GSM-GPS Controller is a dedicated controller designed for the acquisition of the location and the Internet connection is plugged into a serial communication port to the vehicle controller which runs a firmware that is specially modified for this application.

The mobile application, which will be described later, allows viewing the data sent by this controller, as well as interacting with it.

The API server is represented by a software package developed in PHP and JavaScript run by Apache2 under Debian Linux on a VPS(virtual private server).

Next, the structure and operation mode of all these components will be presented.

III.HARDWARE DESCRIPTION

A. The GSM-GPS Controller

That controller(fig.3) is designed around of PIC18F45K22 microcontroller from Microchip. This microcontroller fulfills several distinct tasks:

- initializes and communicates with the Simcom SIM868 GPS-GPRS module,
- processes the data coming from it
- ensures serial communication with the vehicle's main controller.

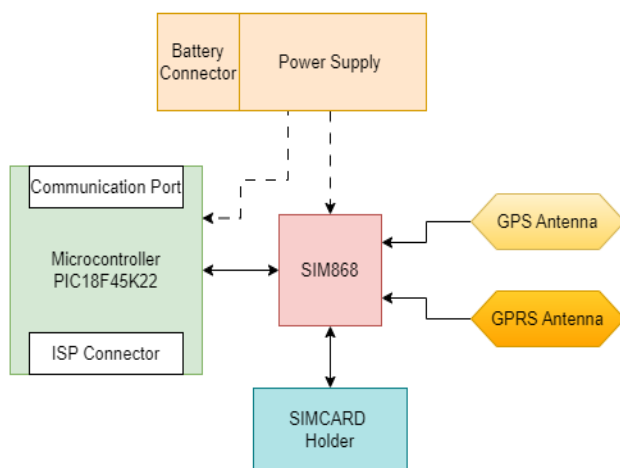


Fig.3 The GSM-GPS Controller Schematic

The microcontroller is a high-performance 16-bits RISC CPU. Its main features are:

- A C Compiler Optimized Architecture;
- Up to 1024 Bytes Data EEPROM;
- Up to 64 Kbytes Linear Program Memory Addressing;
- Up to 1024 Bytes Data EEPROM;
- Up to 16 MIPS Operations;
- 16-bit Wide Instructions, 8-bit Wide Data Path
- Priority Levels for Interrupts

Two serial ports of the microcontroller are used to communicate simultaneously with the SIM868 as well as with the main controller of the scooter (located in the scooter's display element).

All the code run by PIC18F45K22 was written in C language and compiled with the CCS Compiler.

SIM868 module is the complete Quad-Band GSM/GPRS module which combines GNSS(GPS/GLONASS/BDS) technology for satellite navigation. It has strong extension capability with interfaces including UART, USB 2.0, and GPIO[2].

Designed for a global market, SIM868 is integrated with a high-performance GSM/GPRS engine and a GNSS engine.

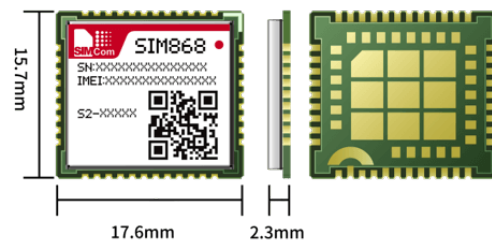


Fig.4 SIM868's dimensions

It has low power consumption, embedded TCP/UDP protocols, and multi-constellation GNSS receiver support: GPS, GLONASS, and Bei Dou.

This module can also be used to find the location using the intensity of the GSM signals coming from the cell towers. Also, using the capabilities to make calls and send SMS, a set of short messages can be designed to configure certain system parameters. However, there is a limitation, namely that, when the GPRS connection to the Internet is initiated, the voice and SMS services cannot be used.

The only limitation of this model is that it cannot operate in 4G and 5G networks. For these networks, it can be successfully replaced by the Simcom SIM7070G model.

The entire operation of the SIM868 is controlled through AT commands.

The "AT" or "at" or "aT" or "At" prefix must be set at the beginning of each Command line. To terminate a Command line enter <CR>.

Commands are usually followed by a response that includes "<CR><LF><response><CR><LF>".

Communication between the microcontroller and SIM868 is done using a master-slave protocol through AT commands at a transfer rate of 115200 bps. The response time to AT orders is of the order of tens of milliseconds.

Both the microcontroller and the GSM-GPS module require a supply voltage of 3.3V. Since the energy source is the scooter's battery, whose voltage is between 36V and 48V, a buck DC to DC Converter was used.

The XL7005a model was chosen, due to its capabilities. It has the following features [3]:

- Maximum Input Voltage 100V
- Output Adjustable from 1.25V to 20V

- Maximum 0.4A Output Current

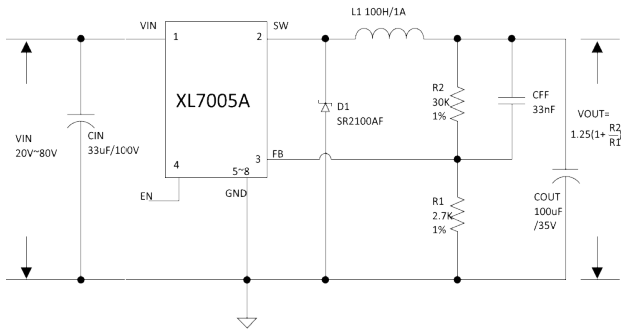


Fig.5 XL7005A usage diagram

For radio communication, as shown in Figure 3, two antennas are needed: one for GSM communication and one for receiving GPS signals.

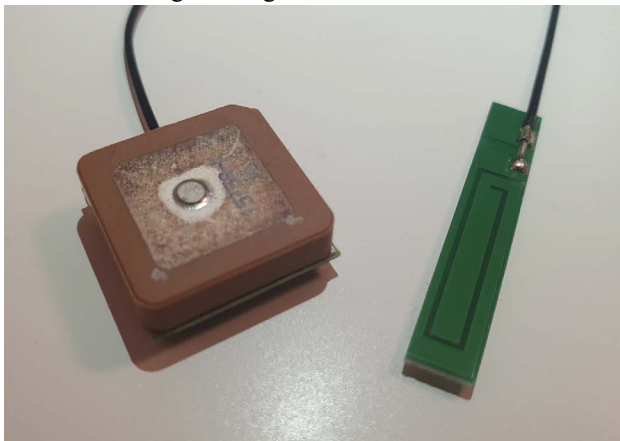


Fig.6 The GPS and GPRS antennas

The GPS antenna has a working frequency of 1575.42 ± 2.0 MHz with a bandwidth of 10 MHz and a gain of 1 dB. The impedance is 50 ohms, and the supply voltage is 3V.

The GPRS antenna is a 3DBI GSM/GPRS/3G PCB Antenna with IPEX13 Connector.

It has an impedance of 50 ohms, a gain of 3dB, and can operate in the frequency range 824M-960MHz 1710M-1990MHz.

IV. SOFTWARE

The software package contains 4 components:

- the software for the microcontroller on the board with the GPS receiver;
- the server's software for the backend part;
- the administrator software for the frontend accessible from the browser,
- the smartphone application for scooter user.

The microcontroller software is responsible for operating the GPS-GPRS module.

It was developed in the C++ language, using the CCS compiler, the transfer to the microcontroller being done with the help of the PicKit3 programmer.

This software follows the diagram in the following image 7. All the code has been structured in reusable

blocks and parameterized for possible future development or improvement.

After initializing the hardware resources of the microcontroller (clocks, digital ports, serial communication), the code runs a series of routines that ensure the connection, maintenance, and interruption of the connection to the GSM network and the mobile data connection, receiving data from satellites, filtering them for elimination altered data, Internet communication with the system server.

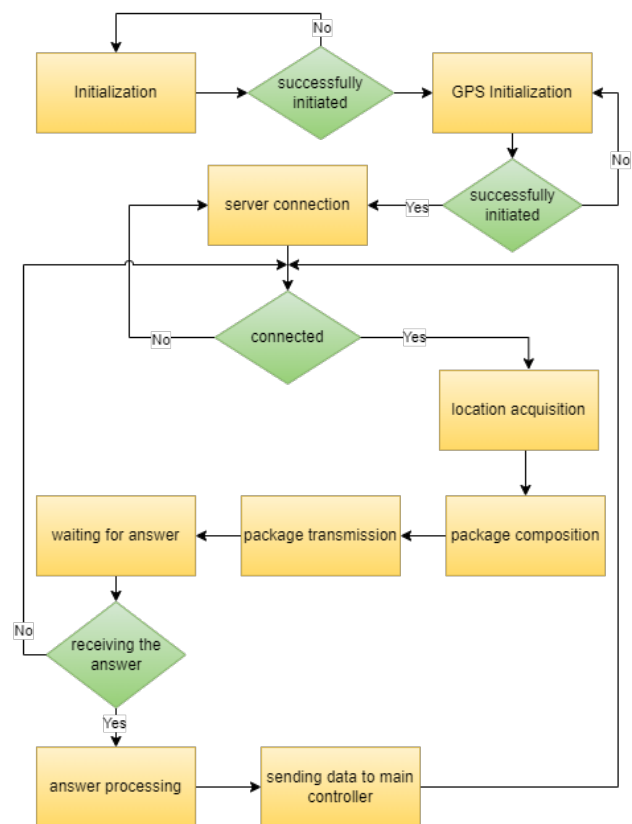


Fig. 7 The microcontroller software diagram

The first part of the program initializes the module, which consists of the following steps(for each step the AT commands used will be specified):

- checking if the module responds to AT commands (AT),
- checking the connectivity of the SIM card and the availability of the GSM network (AT+CGREG?),
- setting the APN (AT+CSTT="APN"),
- configuring the server's IP address and communication port (AT+CIICR, AT+CIFSR, AT+CIPSTART="TCP","server_address","port")
- starting the GPS module (AT +CGNSPWR=1),
- setting the format in which to transmit the positioning data (AT+CGNSSEQ="RMC").

The data provided by the GPS module follows the NMEA GPRMC format and it is obtained by command: AT+CGNSINF.

The GPRMC sentences are the most common sentences transmitted by the Global Positioning System (GPS) devices.

That data contains UTC time, positioning status (effective positioning or invalid positioning), latitude, latitude hemisphere, longitude, longitude hemisphere, ground speed, ground heading, UTC date, magnetic declination, magnetic declination direction, mode indication (autonomous positioning, differential, estimation, invalid data) [4].

The NMEA format for longitude and latitude is (d)ddmm.mmmm. In order to use the data on the Google Maps map, it is necessary to convert these data into decimal degrees.

To get to decimal degrees from degrees and minutes, we can use the following formula:

$$(d)dd + (mm.mmmm/60) (* -1 \text{ for W and S}) \quad (1)$$

Based on these transformations, Haversine's formula [5][6] is used to calculate the ground distance between two coordinate points.

$$a = \sin^2((\Delta lat)/2) + \cos(lat1) \cdot \cos(lat2) \cdot \sin^2((\Delta lon)/2) \quad (2)$$

$$c = 2 \cdot \text{atan2}(\sqrt{a}, \sqrt{1-a}) \quad (3)$$

$$d = R \cdot c \quad (4)$$

where,

$$\Delta lat = lat1 - lat2$$

$$\Delta lon = lon1 - lon2$$

R is radius of earth i.e 6371 KM or 3961 miles and d is the distance computed between two points.

```

distanceInM (lat1, lon1, lat2, lon2) {
  var earthRadiusKm = 6371000;
  var dLat = degreesToRadians(lat2-lat1);
  var dLon = degreesToRadians(lon2-lon1);
  lat1 = degreesToRadians(lat1);
  lat2 = degreesToRadians(lat2);
  var a = Math.sin(dLat/2) * Math.sin(dLat/2) +
    Math.sin(dLon/2) * Math.sin(dLon/2) *
    Math.cos(lat1) * Math.cos(lat2);
  var c = 2 * Math.atan2(Math.sqrt(a), Math.sqrt(1-a));
  return earthRadiusKm * c;
}

degreesToRadians(degrees) {
  return degrees * Math.PI / 180;
}
    
```

Fig.8 The code sequence for calculating the distance based on the GPS coordinates of two points

The API server runs a software package under Linux Debian distribution on a VPS. A virtual private server was created at DigitalOcean in the San Francisco datacenter to test the performance of the system when the communication is over long distances.

This software package is developed in Php and JavaScript using Laravel framework served by Apache2 web server and MySQL database server. All APIs served by this are authenticated with tokens and protected by Laravel Passport module.

It has two components: one responsible for receiving and storing messages from the devices located on the vehicles and providing them with the commands that must

be executed (On, Off, Lock), as well as one that performs the entire authentication part, processing the data stored in MySQL database.

The first component uses web socket technology that makes it possible to open a two-way interactive communication session between the scooter and the server. The way this part works is described in the following image.

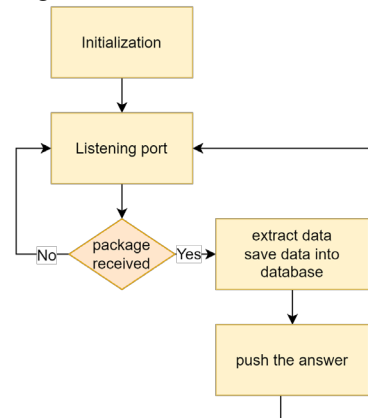


Fig.9 Websocket package

Data processing is done with the aim of providing the user with information about the position, the route traveled, and the condition of the vehicle.

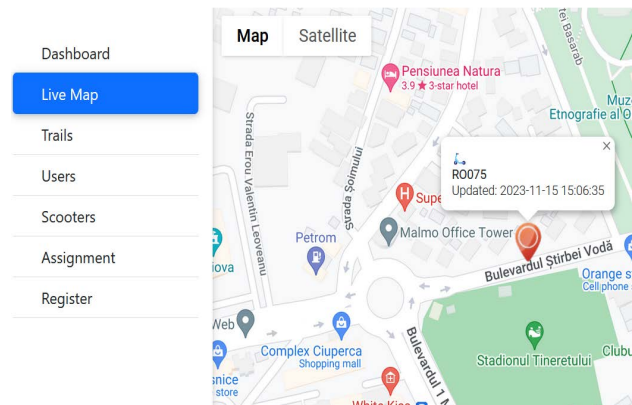


Fig.10 Live Map

Various operations can be performed in the administration interface available in the browser, such as: the positions of the scooters can be viewed in real time, their routes can be viewed in a selected time range, user administration and the allocation of scooters, viewing their status.

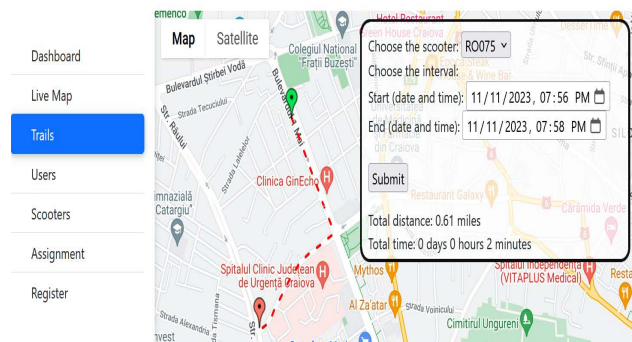


Fig.11 Viewing a route in a selected time interval

The mobile application for smart devices was developed using JavaScript language and React-Native framework, which allowed the creation of a version for Android devices as well as for iOS using the same base code.

To run, the application requires at least iOS 13.0 or Android 8. Its role is to allow the user to interact with the system and implicitly with the equipment[7].

System status

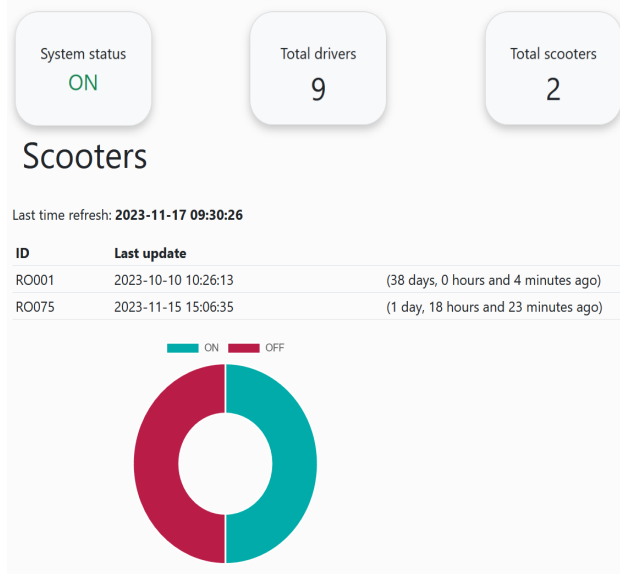


Fig.12 System status dashboard

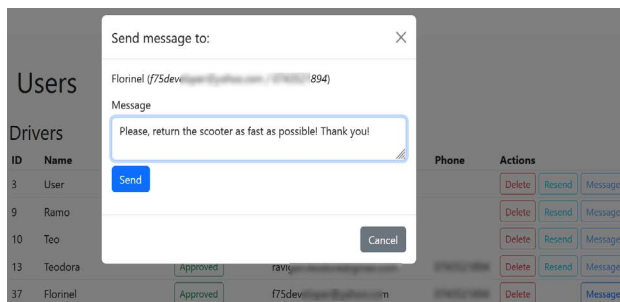


Fig.13 Sending messages from the admin panel via OneSignal

The application needs permission to access the location of the device, as well as to receive notifications. The system has implemented the possibility of sending push notifications using the OneSignal platform.

The application allows the following operations:

- the authentication procedure (Accounts are created by the system administrator in the backend and approved after confirming the email address, but the account creation from the application can be easily implemented),
- viewing the position of the equipment as well as that of the user on the map,
- the state of the vehicle,
- the analysis of the distances covered,
- the time of use,
- the history of trips on the map.

The act of pressing the start button will lead to starting the vehicle, and it can be used. The interface also offers a

button with which the scooter can be locked. Through this blocking, the scooter will not be able to be used by other people because its wheel will be blocked (the BLDC motor will instantly enter dynamic braking mode), and when the wheel is moved the horn will sound an alarm and the brake light will also flash very fast[8].

Also, the interface allows searching and identifying the scooter when it is not visible, by triggering the horn that will emit three short sounds.

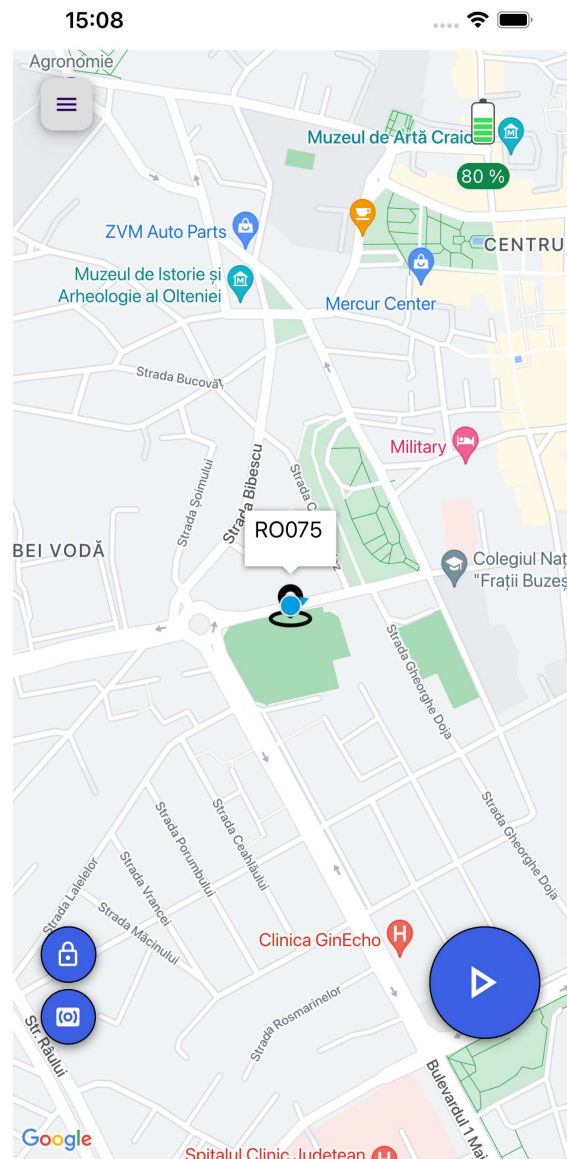


Fig.14 The main user interface of the mobile app

In the upper right part of the mobile application interface, the scooter's battery level can be monitored in real-time.

On the map in the application, you can see both the position of the scooter (black marker) and the position and orientation of the user (blue marker).

Also, in the upper part, there is a button that allows access to a menu through which the online account can be accessed, a history can be viewed as well as statistics related to the duration and distance of trips.

All statistics calculations are done in the backend to reduce the processing effort of the application and to provide a better user experience.

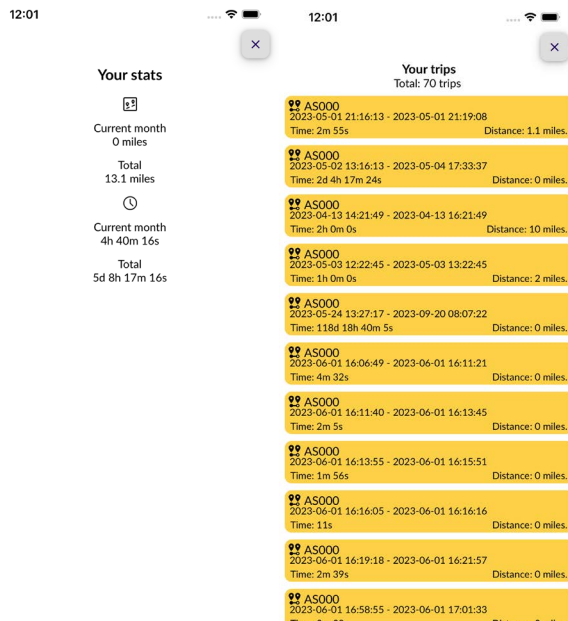


Fig.15 Viewing statistics and travel history

V.CONCLUSIONS

Starting from the described system, it can be developed and used in a variety of applications that require the location management of some devices.

This system can be used to monitor fleets of electric scooters or bicycles, cars, boats, and industrial equipment. During system testing, the designed hardware proved to be very reliable, providing stable connectivity even in conditions with weak GSM signal, as well as location information with small errors.

ACKNOWLEDGMENT

Source of research funding in this article: this work has been fully developed within the Department of Electromechanics, Environment, and Applied Informatics within the Faculty of Electrical Engineering of the University of Craiova.

Contribution of authors:

First author – 60%

First coauthor – 20%

Second coauthor – 20%

Received on July 17, 2023

Editorial Approval on November 15, 2023

REFERENCES

- [1] <https://www.geotab.com/blog/what-is-gps/>
- [2] <https://datasheetspdf.com/datasheet/SIM868.html>
- [3] https://datasheet.lcsc.com/lcsc/1811081614_XLSEMI-XL7005A_C50848.pdf
- [4] https://openrtk.readthedocs.io/en/latest/communication_port/nmea.html
- [5] <https://www.igismap.com/haversine-formula-calculate-geographic-distance-earth/>
- [6] G. M. Djuknic and R. E. Richton, "Geolocation and assisted GPS," in *Computer*, vol. 34, no. 2, pp. 123-125, Feb 2001, doi: 10.1109/2.901174.
- [7] D. Atunggal, N. H. Ausi and C. A. Rohkmana, "Developing Android Application for Precise Geotagging Using RTK GPS Module," *2018 4th International Conference on Science and Technology (ICST)*, Yogyakarta, Indonesia, 2018, pp. 1-5, doi: 10.1109/ICSTC.2018.8528570.
- [8] M.Rakesh, P.V.R.L. Narasimham - Different Braking Techniques Employed to a Brushless DC Motor Drive used in Locomotives. *International Electrical Engineering Journal (IEEJ)* Vol. 3 (2012) No. 2, pp. 784-790 ISSN 2078-2365
- [9] F.Ravigan, Gh.Manolea - The command by GSM for positioning systems of anti-hail ramps. *Analele Universitatii Eftimie Murgu Resita Fascicola De Inginerie, Anul XXI, nr.2, 2014*
- [10] F.Ravigan, N.Boteanu, L.Alboteanu-The Online Temperature Control. *Analele universitatii din craiova: seria Inginerie Electrica, 2015*

Configuration of SCADA System Graphical User Interface for Electrical Station

Cosmin-Ionuț Toma, Mihaela Popescu, Mihăiță Daniel Constatinescu, Gabriel Cosmin Buzatu

*University of Craiova, Faculty of Electrical Engineering, Craiova, Romania, ctoma@em.ucv.ro, mpopescu@em.ucv.ro, mconstatinescu@em.ucv.ro, cosmin.buzatu@incesa.ro

Abstract - In order to efficiently and practically solve the problem of analyzing the performance of the SCADA (Supervisory Control and Data Acquisition) system of the power grid, this paper proposes to reconfigure the graphical user interface (GUI) in the substation, as well as to remap the signals according to the hardware structure used. After replacing the hardware solution with PLC and software for protocol conversion installed on the local HMI with a specialized remote terminal unit for data storage and protocol conversion in the substations, it is important to adapt the graphical user interface of the SCADA system according to the latest hardware configuration. This is necessary for the stability and reliability of the SCADA system. In the last part of the paper, the configuration of the graphical user interface of a SCADA system and the remapping of the signals in the specialized software in an electrical substation in Romania is presented and highlighted through screenshots.

Cuvinte cheie: SCADA, interfață utilizator, automat programabil, stație electrică, flux de date

Keywords: SCADA, Graphical User Interface (GUI), Programmable Logic Controller (PLC), electrical substation, data flow.

I. INTRODUCTION

The fundamental objective of most integrated monitoring and control systems for installations, networks, or power systems is to provide users with adequate information and facilities for monitoring and control. The aim is to enable the safe, secure, and economical operation of the specific power system. These systems are commonly known as Supervisory Control and Data Acquisition (SCADA) systems, as shown in Figure 1.

The most basic SCADA system is a two-tiered master-slave configuration. It involves a primary coordinating master computer with interfaces for user dialogue and data transmission, alongside a subordinate Remote Terminal Unit (RTU) process computer. The RTU is equipped with interfaces for both analogue and digital inputs and outputs, as well as a communications interface. These systems fall into the category of small-scale and are not frequently employed in the monitoring and control of power systems.

In [1], the authors present a brief overview of distribution system automation. Current implementation philosophies and current challenges in distribution system automation are discussed. In [2], a solution for the design of the GUI for a SCADA system on an industrial platform is proposed. The production and use of electricity from classical or renewable energy sources can no longer be conceived without the automation of the technological process.

Several projects of distribution and transmission stations that combine SCADA and Protection & Control (P&C) are reviewed in [3]. There are considerations on the analog input, digital status and control. Aspects of discrete and analog I/O operation within a substation for the SCADA system are also reviewed, considering the flexibility and maintenance benefits offered.

Owing to the intricate nature of processes in power engineering, it becomes imperative to employ multiple process computers distributed across various hierarchical levels. This results in the establishment of a hierarchical monitoring and control system, allowing for distributed control of the process in a hierarchical framework, as outlined in references [4], [5], [6].

II. PROGRAMMABLE LOGIC CONTROLLER

Programmable Logic Controllers (PLCs) are equipment designed for automatic monitoring and control of industrial processes. They are part of distributed monitoring and control systems and are real-time control systems.

PLCs perform two main tasks, concerning the monitoring and automation of a process, as illustrated in Fig. 2:

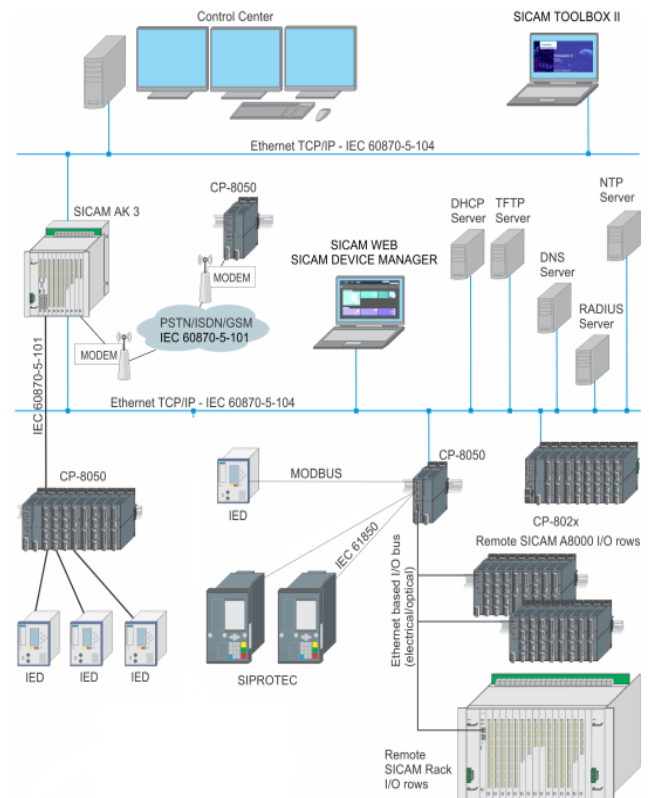


Fig. 1 A typical SCADA system architecture.

- acquisition, which involves monitoring the state of the process by acquiring via sensors, buttons, limit switches, the state variables in the process;
- control, which consists of processing the information received and generating the necessary commands to the execution elements of the automated process according to a specific software.

From a structural point of view, the following can be distinguished:

- PLCs with an open structure in the form of a printed circuit board without a housing - these are very cheap variants, but the number of inputs and outputs is limited and there is no possibility of adding extension modules;
- PLCs with a monobloc structure in a closed housing - these have all the components grouped together in a housing, the dimensions of which depend on the number of input and output terminals, and allow the connection of extension modules, which have a separate housing and are connected by means of connecting cables;
- PLCs with a modular structure with a large number of inputs and output, a multitude of control possibilities and consequently a large number of available extension models, presented in Fig 3.

The hardware of a PLC consists of a microprocessor (or microcontroller) based central processing unit (CPU), a memory, input modules (for signals coming from the transducers and the operator), output modules (through which commands are transmitted to the execution elements and signals to the operator) and serial/parallel interfaces for connecting the PLC with programming devices, PC computers or other PLCs [7], [8], [9], [10].

The operation of the programmable controller is based on the repeated execution of the program written in its memory.

Each program execution cycle consists of 3 steps:

- reading inputs;
- execution of the program instructions;
- updating outputs.

The duration of such a cycle depends both on the speed of the processor with which the PLC is equipped and on the length of the user's program.

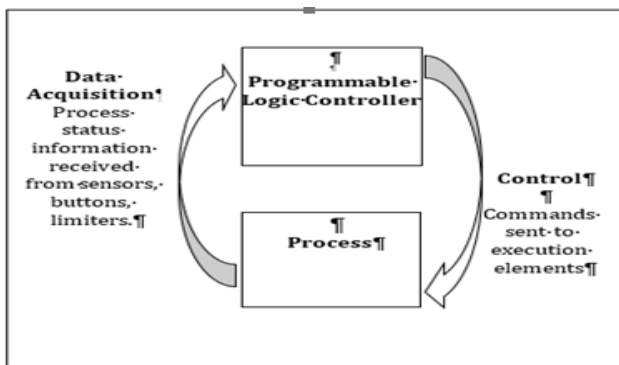


Fig. 2 Block diagram of a monitoring and automation system using a PLC.



Fig. 3. PLC in the SCADA panel.

The PLC executes the program from the first line to the last and then repeats this cycle which is carried out in 3 steps:

- Reading the inputs: the PLC scans each input in order to determine the ON or OFF status of the sensors or switches connected to the inputs, whether they are activated or not; the information collected during this step is stored in the memory to be used in the next step;
- Program execution: the PLC executes the program instructions sequentially (instruction by instruction), and, as a result, one or more outputs may be activated, or information may be stored in specific areas in memory, to be used in the next step;
- Update outputs: the PLC checks the states of the outputs and modifies them if necessary and the changes are based on the states of the inputs read during the first step and the results of the second step program execution.

After the execution of the third step, the programmable logic controller resumes the program cycle.

III. REMOTE TERMINAL UNIT

In order to meet the performance requirements of the system user, the RTU equipment must fulfill several requirements.

A. Remote Terminal Unit Equipment Design

In the control center of each substation, the system contains at least one RTU, which "interrogates" all the terminals in the substation, acting as a data concentrator, a real-time data server, and a communication server to the higher hierarchy level providing the interface to a graphical console for the operator.

The RTU has an open, distributed processing architecture with the following main features:

- low power consumption, able to work in a high voltage electrical installation, having a robust physical construction with immunity to the electrical noise;
- modular construction (Fig. 4 and Fig. 5); the failure of one module shall not affect the operation of the other modules, and the replacement of any module shall be carried out without disturbing the overall operation of the RTU equipment;
- be provided with serial ports for interfacing with electronic meters, digital relays, programmable logic controllers;
- communication with other SCADA-Master Stations using different communication protocols;
- microprocessor-based construction;
- after powering up the unit, it must be designed to operate without manual intervention; in addition, it must restart automatically and be able to communicate with the higher hierarchical level (Master Station) without affecting its operation, and the existence of appropriate indicators, such as LEDs, must provide staff with correct information to easily determine the status of the RTU;
- the Master Unit shall monitor the operation of the RTU with the possibility of diagnosing errors concerning overflow of memory capacity, local software operation, status of communication ports, status of input/output modules;
- to enable fault detection, there will be a separate list of events and each event will be identified with the ID number, event type, time of occurrence;

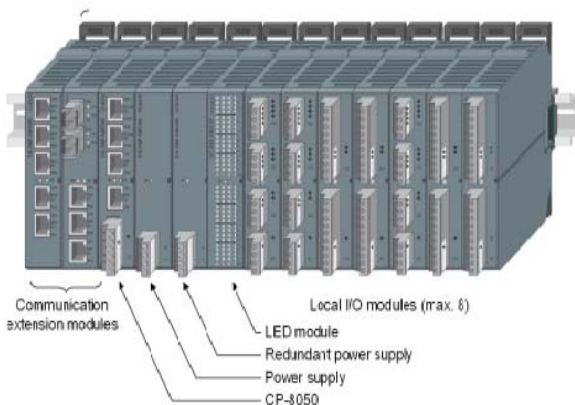


Fig. 4 Remote terminal unit.

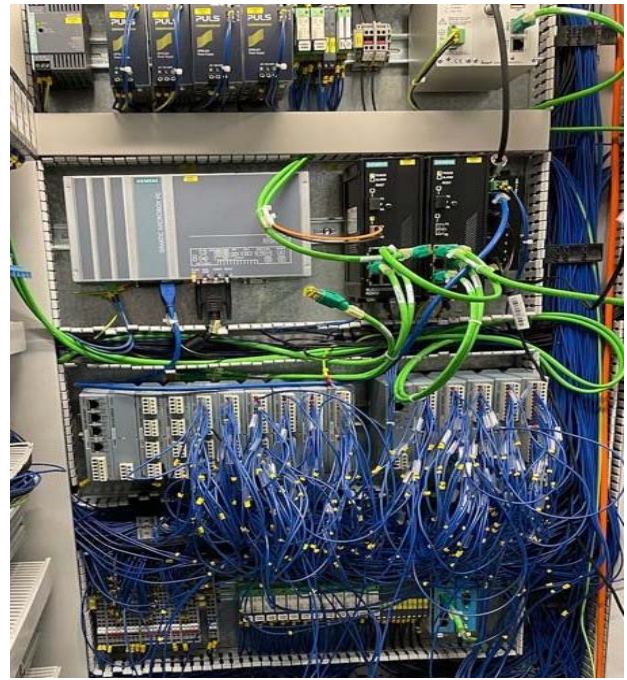


Fig. 5 RTU in the SCADA panel.

- the RTU will allow storage of up to 2000 events;
- the RTU will be equipped with an internal real-time clock, with a resolution of one millisecond, synchronized via communication protocol by the master, for the list of events to be accompanied by the time stamp;
- the data associated with each event will be stored in the RTU for later transmission;
- within the RTU, events will be reported at certain time intervals with a time accuracy of +/- 1ms;
- input/output (I/O) modules;
- I/O modules will be intelligent modules containing microprocessors, and will be configured as slaves to the RTU mainframe module;
- inputs will be scanned at least every millisecond by the digital input module;
- there will be software filtering of parasitic pulses or some other method of reducing false alarms caused by devices that change state fairly quickly and for which it is not necessary to report this change of state every time;
- the RTU will be able to support point change detection of analogue and numerical magnitude high-lights;
- the RTU shall not lose fast status changes, therefore status changes shall be determined by the RTU and stored until they can be transmitted to the next higher level (SCADA-Master Station).

Each RTU will have multiple communication ports (at least 8 communication ports. 7 ports will support communications with other equipment: electronic counters, microprocessor relays, sub-RTUs, and the 8th port will be a dedicated maintenance port: an RS-232 or RS-485 serial port that must provide connection to a local PC for diagnostics and configuration).

Each communication port will be selectable for operation in the (300...19,200) bps range.

RTU shall be able to communicate with another RTU at the same level or higher (SCADA-Master Station); each Master Station may use different communication protocols and transmission rates, which are in agreement with IEC 61850 and IEC 60870-104 standards [11], [12].

B. Internal Data Flow

The basis for remote terminal unit is a modular, open, and thus non-technology-dependent system architecture for processing, communication, and peripherals (single-processor system, firmware).

The adaptation to the specific needs of the application is accomplished by relying on an individual hardware configuration and by loading standard firmware and parameters. Within their defined limits, the parameters thereby not only influence the behavior of the firmware functions, but also that of the hardware functions. As a result, mechanical parameterizations such as the changing of jumpers or loads are no longer necessary on any of the module types. This permits not only online reconfiguration but also the gapless documentation of set parameters by the engineering system, as well as simplified inventory management.

Due to the different requirements in terms of functionality, also different data flow concepts are produced and can be illustrated by means of Fig. 6.

For telecontrol tasks and the distribution of user data in networked plants, the use of spontaneous transmission proves advantageous for optimizing the utilization in many cases limited communication bandwidth. This helps to avoid constant burdening of the data sinks with unnecessary data.

For the implementation of a freely definable open/closed-loop control function, a deterministic guaranteed reaction time is needed. This is achieved by using the consistently periodic concept with regard to data acquisition, execution of functions, and data transfer, regardless of the number of changing signals [13].

IV. GRAPHICAL USER INTERFACE CONFIGURATION

The Zenon Energy Edition software platform is the foundation of the application used in the analysis of an electricity substation in Romania, providing facilities specifically designed to simplify the processes of (GUI) configuration and signal remapping. The objective of this platform is to efficiently configure and diagnose automation systems at the level of an electrical substation.

Figures 7, 8 and 9 show how to configure the signals in the RTU, remapping the signals in the GUI development application according to the list of signals implemented in the RTU. Fig. 10 shows a screenshot of the feeder during real-time tests.

The software platform has two ways of working:

- development - mode of work used when designing an application; the user has the possibility to create or modify files in the project, accessing available resources and configuring them through the specific properties of each type of object;
- runtime - mode used when running the program; the user has the possibility to view the data taken from the process and to enter the commands that were left available in the design phase [14].

The software works around a central core represented by the real-time database containing all the tags needed to run the program, a simple operating interface for the SCADA solution. The Communications Module is used to transfer information to and from the Real-Time Database from all devices connected to the network. To do this, the Communications Module uses a set of communication drivers that allow it to:

- connecting via network to a Client Server.
- connect to PLCs over Modbus;

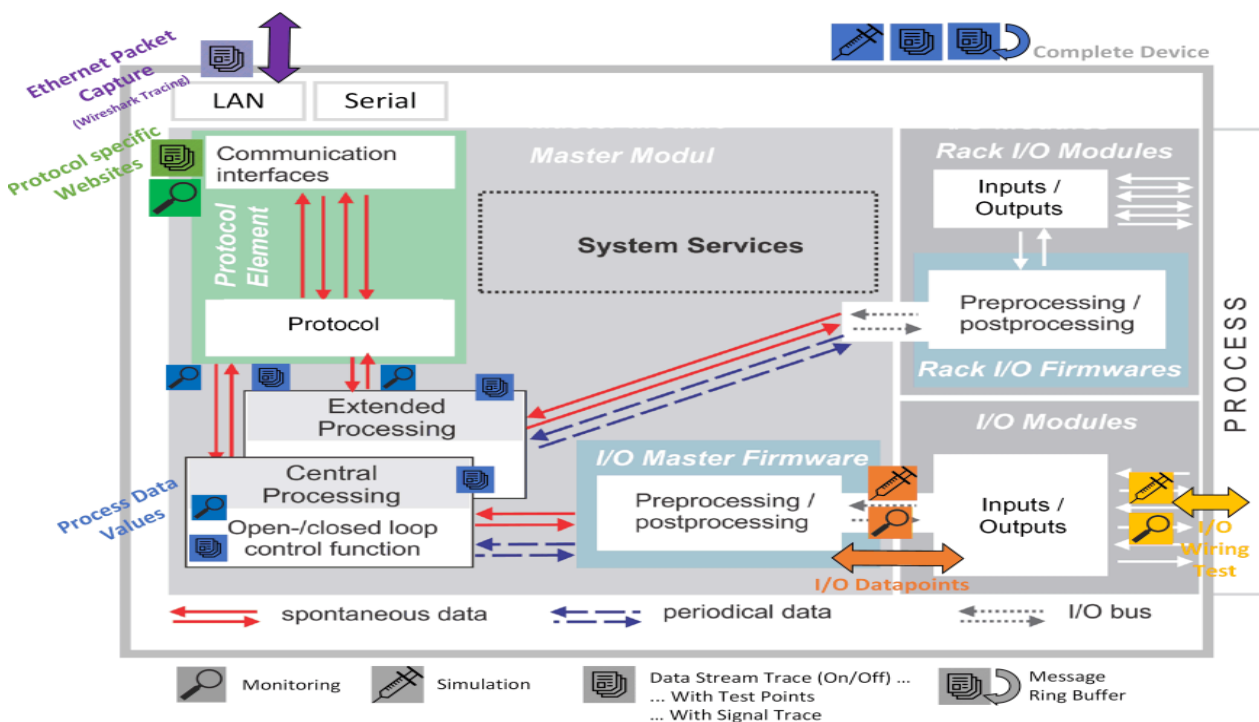


Fig. 6 RTU process diagram.

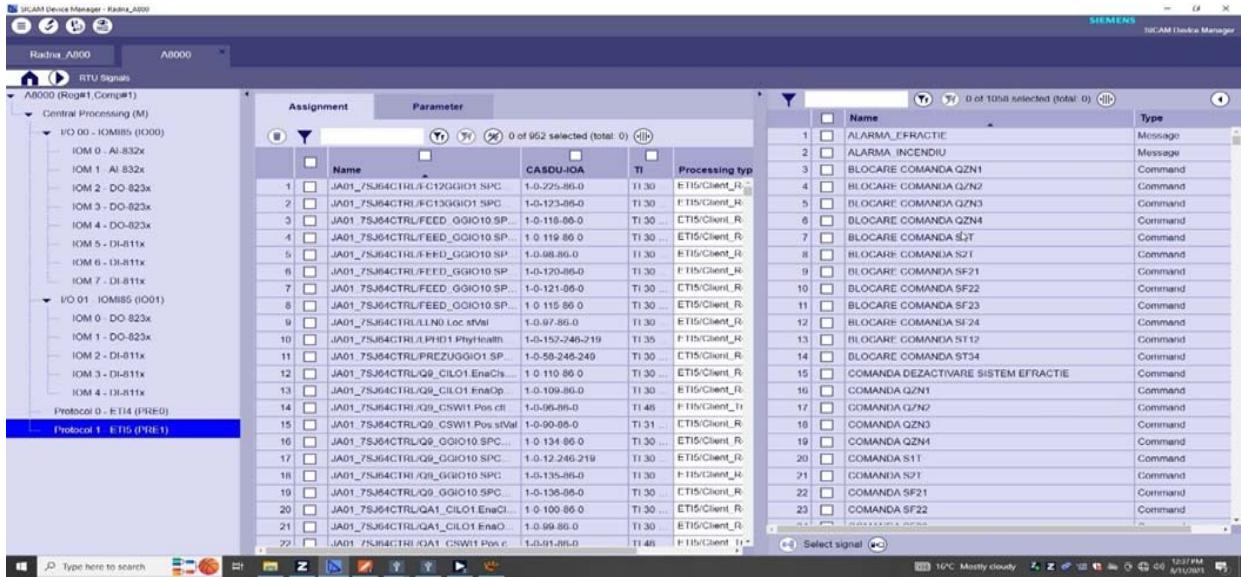


Fig. 7 List of signals implemented in RTU.

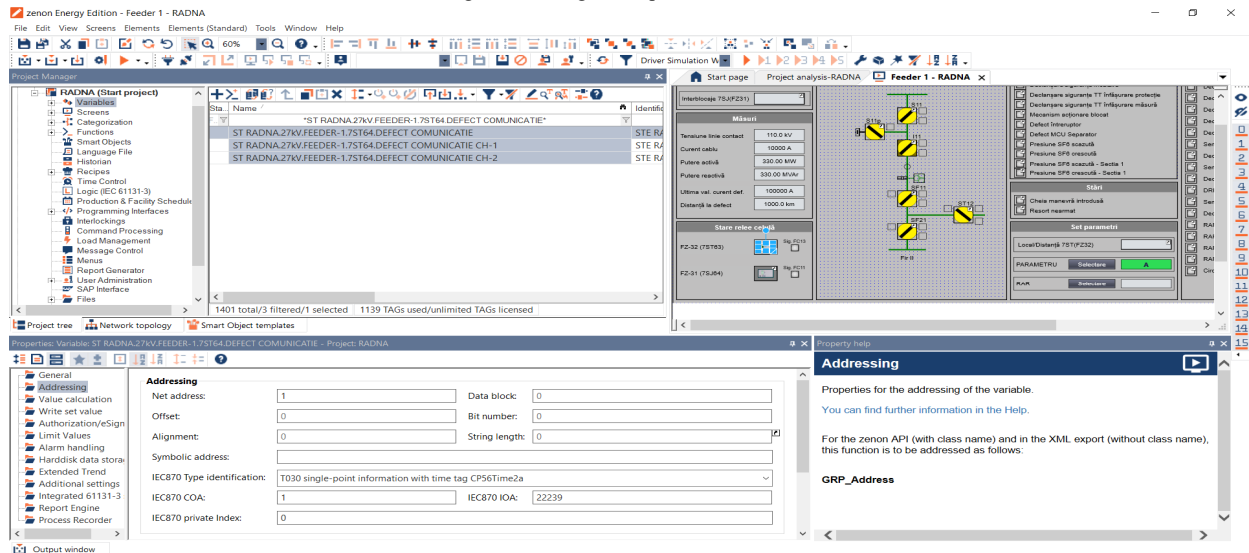


Fig. 8 Signal list configuration in the feeder of the electrical substation.

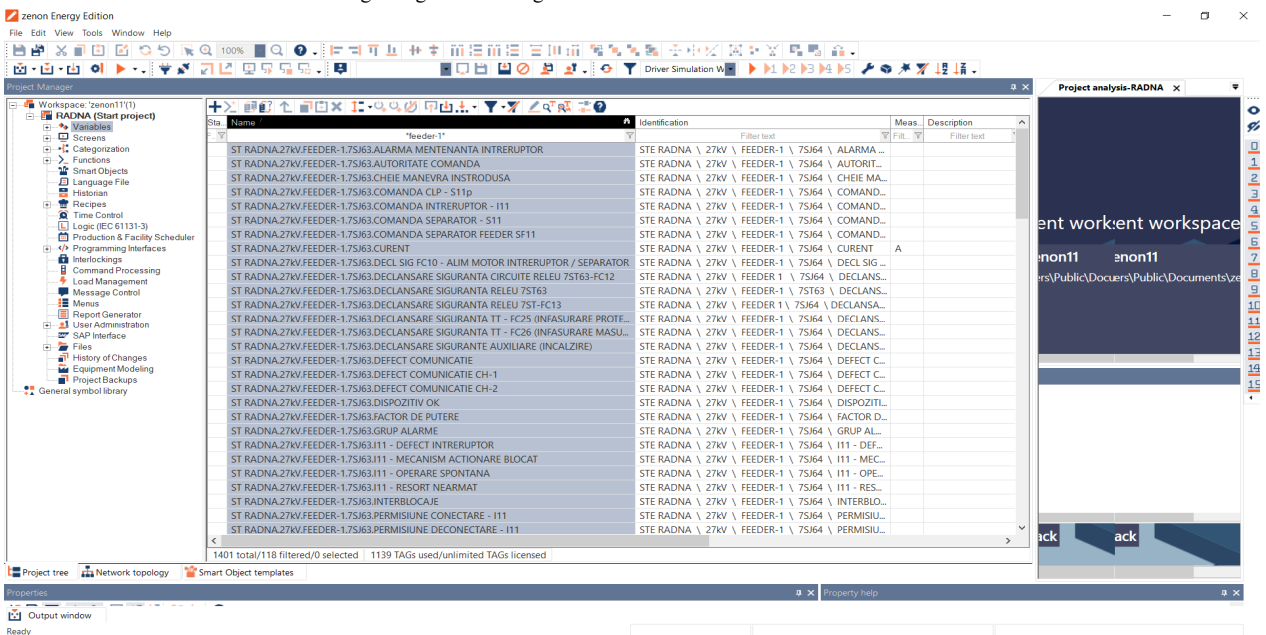


Fig. 9: Signal List of Feeder

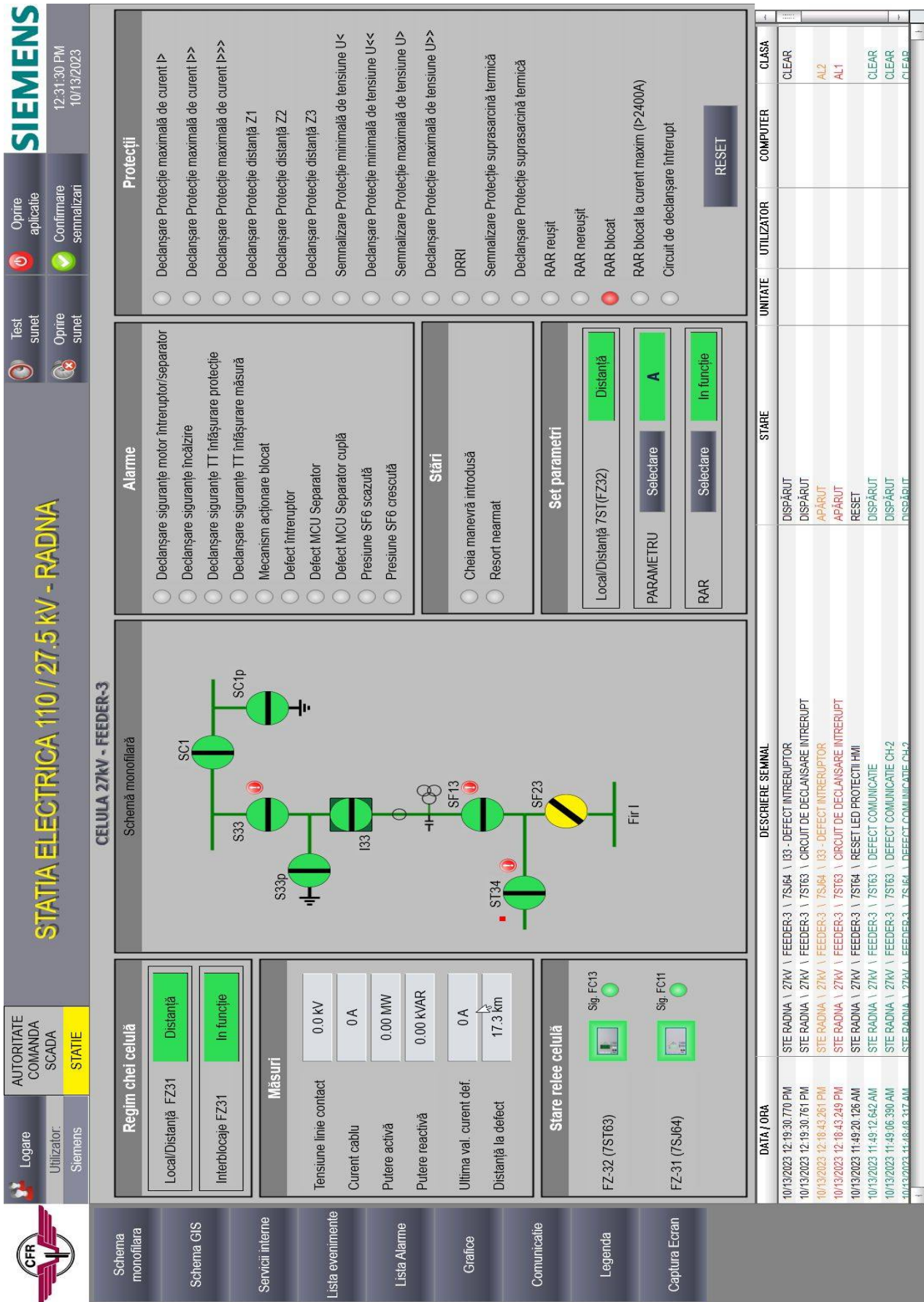


Fig. 10 Real-time test of feeder graphical user interface

The main feature of the program is to provide a number of powerful resources and tools (object libraries, symbol libraries, communication drivers, real-time databases, etc.) that make it easier to design and build an application [15].

The projects realized through the Zenon software platform are made up of a series of component groups (known as Project Resources) such as the Real-Time Data Base (DB Real Data Base), Data Records, Raptors, Alarms, etc. All these component groups are displayed in a tree-like structure in the main "Project Manager" window of the application.

V. CONCLUSIONS

This paper shows that by configuring the GUI and mapping the signals according to the hardware structure of the SCADA system, dedicated to these SCADA applications, there are many advantages.

By means of a case study in an electrical substation in Romania, the configuration of the GUI is illustrated, as well as the correct operation in real time.

The software application at the central monitoring level communicates wirelessly (GSM/GPRS) with the local acquisition and control system as well as with other monitoring systems.

ACKNOWLEDGMENT

Source of research funding in this article: Research program of the Electrical Engineering Faculty financed by the University of Craiova.

Contribution of authors:

First author – 25%

First coauthor – 25%

Second coauthor – 25%

Third coauthor – 25%

Received on July 16, 2023

Editorial Approval on November 22, 2023

REFERENCES

- [1] T. Frauenschlager and J. Mottok, "Security-Gateway for SCADA-Systems in Critical," *2022 International Conference on Applied Electronics (AE)*, 19 October 2022.
- [2] I. C. Hoarcă, N. Bizon, F. M. Enescu, "The design of the graphical interface for the SCADA system on an industrial platform," *2020 12th International Conference on Electronics, Computers and Artificial Intelligence (ECAI)*, 25-27 June 2020.
- [3] C. Wester, N. Engelman, T. Smith, K. Odetunde, B. Anderson, J. Reilly, "The role of the SCADA RTU in today's substation," *68th Annual Conference for Protective Relay Engineers*, March 30 2015-April 2, 2015.
- [4] M. Moga, *Sisteme inteligente pentru conducerea rețelelor de distribuție*, Editura AGIR, București 2000.
- [5] M. Moga, *Introducere în sisteme informatice pentru electroenergetică*, Ed. Politehnica, Timișoara, 2008.
- [6] T. S. Sidhu and Y. Yin, "IED modelling for IEC61850 based substation automation system performance simulation," *2006 IEEE Power Engineering Society General Meeting*, Montreal, QC, Canada, 2006, pp. 7.
- [7] https://mctr.mec.upt.ro/wp-content/uploads/2017/12/Curs_AP_2017.pdf
- [8] <http://web.ulbsibiu.ro/laurean.bogdan/html/PLCprincipii.pdf>
- [9] <http://electrical-engineering-portal.com/what-can-a-plc-do-why-do-we-use-them>
- [10] L. Fang, "Application of PLC technology in electrical engineering and automation," *Proceedings of the 2016 2nd International Conference on Materials Engineering and Information Technology Applications (MEITA 2016)*, February 2017.
- [11] Remote Terminal Units (RTUs) for Substation and Distribution <https://www.kalkitech.com/products/sync-2100/>
- [12] <https://www.transport.nsw.gov.au/.../ep-11-03-00-02-sp.pdf>
- [13] Manual_A8000_CP-8031_CP-8050_ENG_DC8-026-2_18, <https://support.industry.siemens.com/cs/document/109757272/sicam-a8000-series-manual-cp-8031-cp-8050-?dti=0&lc=en-RO>
- [14] A. Ramadhan, M. A. Murti and L. V. Yovita, "Implementation of networked control systems using programmable controller based Ethernet network," *2013 International Conference of Information and Communication Technology (ICoICT)*, Bandung, Indonesia, 2013, pp. 22-27.
- [15] F. Fadhil, "Analysis and design of a modern SCADA system," *Thesis for: MasterAdvisor: Qutaiba Ali*, January 2019.

Small Scale Models of Solar Tracking Systems

Ionel Laurentiu Alboteanu*, Cristian Bratu†, Florin Ravigan*

* University of Craiova / Department of Electromechanical, Environmental and Applied Informatics, Craiova, Romania, e-mail: lalboteanu@em.ucv.ro, ravigan.florin@gmail.com

† University of Craiova / Department of Electrical, Energy and Aerospace Engineering, Craiova, Romania, e-mail: cbratu@elth.ucv.ro

Abstract - Increasing the efficiency of photovoltaic panels using solar tracking systems is a current topic. The use of solar tracking systems is a solution, especially in low power applications. The paper presents two types of solar tracking systems, one based on astronomical data, and the other based on tracking the point of maximum illumination. Both systems are made on small scale for educational purposes. These systems can be used for the analysis of methods, principles and particularities in order to use them in practical applications. For the two experimental models of solar tracking made, the hardware and software structure are presented. To orient the photovoltaic panels in the two directions (East-West, respectively South-North) DC motors or stepper motors are used. One motor is used for each axis of rotation. Both structures have the control part composed of a microcontroller development system. This control method has the advantage that can significantly reduce the number of electronic components as well as the cost of designing and building of equipment. For the solar tracking system based on astronomical data, a remote monitoring and control system has been achieved. It uses a friendly graphic interface made on PC with the help of Visual Basic software. Both models were tested and the experimental results showed correct operation according to the imposed protocol. Finally, an energy efficiency analysis was done and it was found that the PV panel that uses the tracking systems produces 35% more energy compared to a fixed PV panel.

Cuvinte cheie: sistem de orientare solar, panou fotovoltaic, microcontroler, instruire, eficiență energetică.

Keywords: solar tracking system, photovoltaic panel, microcontroller, training, energy efficiency.

I. INTRODUCTION

In recent years, the evolution of photovoltaic systems has registered an increasing trend in the context of the energy crisis and environmental protection considerations. This upward evolution also requires a specialized and qualified human resource in the field.

Since photovoltaic (PV) panels have a rather low yield (max. 30%, in laboratory conditions), their energy optimization is aimed at. An accessible method of optimizing solar energy conversion with real implementation possibilities is the use of orientation systems.

Specialized literature shows that the use of solar tracking systems increases the amount of energy produced by conversion by 20% to 40% [1].

Ideally, a PV panel should follow the Sun so that the incident rays fall perpendicular to its surface, thus maximizing the capture of solar energy and therefore maximum output power [1], [2].

Practically, passive and active solar systems are distinguished [3], [4]. Passive tracking systems follow the Sun in the absence of a drive motor and are frequently used in equatorial areas because they have a single-axis tracking structure that allows maximum efficiency to be achieved only in those [5], [6], [7].

Active solar tracking systems use servo motors to move the PV panels. There are two distinct modes of active tracking of the PV panels [4], [6], [8]: along a single axis of rotation and along two perpendicular axes of rotation (biaxial).

The paper presents two types of biaxial active solar tracking systems made on a small scale for educational purposes, based on different tracking methods. The first solar tracking system uses the astronomical data method, and the second one uses the maximum light point method. Both systems use tracking programs implemented in control structures with microcontrollers.

II. SMALL SCALE MODEL OF SOLAR TRACKING SYSTEM BASED ON ASTRONOMICAL DATA

A. Elements of celestial geometry for the positioning of the PV panel

In order to understand the essence of the calculations, some notions from astronomy are used, in particular, the analytical relationships that describe the apparent motion of the Sun on the sky [9].

It is known that the Earth carries out a complete rotation movement during a year, around the Sun in an elliptical orbit and a complete rotation movement around its own axis during 24 hours. The rotation axis of the Earth has a fixed direction in space and is inclined with the angle $\delta_0=23.4^\circ$ to the perpendicular to the plane of the orbit (Fig. 1). The angle between the direction to the Sun and the equatorial plane, δ , is named declination and varies throughout the year from $+23.4^\circ$ at the time of the summer solstice (June 21) to -23.4° - at the time of the winter solstice (December 21).

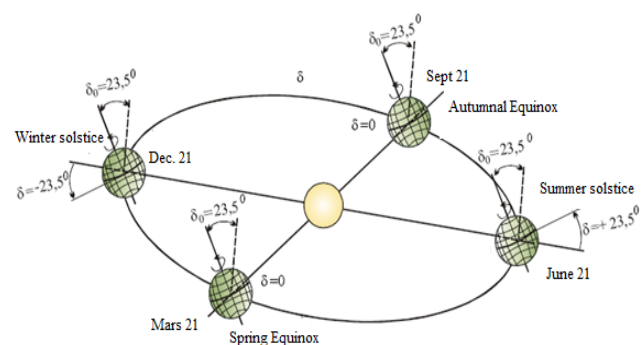


Fig. 1. Earth's orbit and declination angle, δ [7].

On March 21, respectively - September 21, the declination $\delta=0$ and the durations of day and night are equal.

Declination can be calculated with Cooper's formula [1]:

$$\delta = 23,45 \cdot \sin\left(360^\circ \frac{284 + n}{365}\right) \quad (1)$$

where n - is the number of the day of the year, the first day being January 1.

The geometric relations between a plane arbitrarily oriented with respect to the horizontal and the direct solar radiation that falls on this plane at any instant of time, the position of the sun with respect to this plane can be described in terms of several angles [9].

Latitude, φ , - is the angle measured from the equator to the point of interest on the earth's surface, is considered positive for the northern hemisphere and negative - for the southern one.

The angle of inclination of the PV panel β , - is the angle between the plane of the surface in question and the horizontal surface; $0^\circ \leq \beta \leq 180^\circ$ (Fig. 2). For usual solar installations, the maximum value does not exceed 90° .

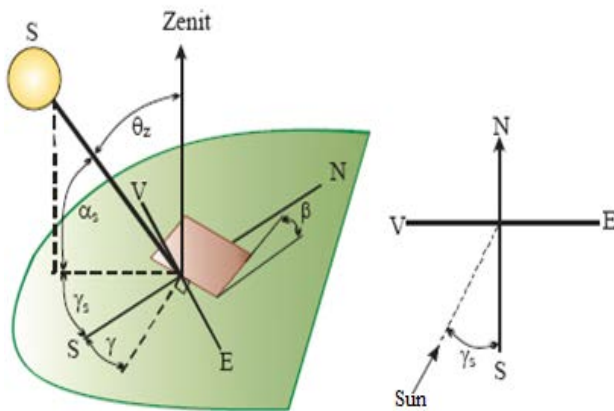


Fig. 2. Explanatory regarding the characteristic angles [9].

The azimuthal angle, γ , - is the angle between the projection on the horizontal plane of the perpendicular on the surface of the plane in question and the local meridian (fig. 3); is equal to zero for the plane in question oriented to the south, negative - to the east, positive - to the west; $-180 \leq \gamma \leq 180$.

The angle of elevation of the sun, α_s , - is the angle between the horizon line and the line connecting the sun to the point of interest, therefore, it is the incident solar ray at the point of interest (Fig. 2).

The zenith angle, θ_z , - is the angle between the vertical and the line connecting the sun to the point of interest, in other words, it is the angle complementary to the angle α_s (Fig. 2).

The hour angle, ω , - determines the position of the sun on the sky at the given moment. It is equal to zero when the sun crosses the local meridian, in other words at noon, positive to the east and negative - to the west (Fig. 3). Respectively, ω_s corresponds to the angle of sunrise, and $(-\omega_s)$, the angle of sunset.

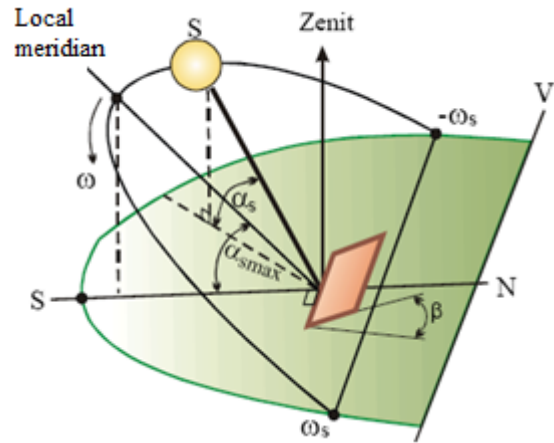


Fig. 3 Explanatory regarding the hourly angle ω , sunrise, ω_s and sunset $(-\omega_s)$ of the sun [9].

It is obvious that in one hour the sun crosses the sky at an angle equal to 15° , and its position at any hour T is determined with the expression:

$$\omega = 15 \cdot (12 - T) \quad (2)$$

If we know the angles δ , φ and ω , then it is easy to determine the position of the sun on the sky at the point of interest for any hour and any day, using the expressions [9]:

$$\sin \alpha_s = \sin \delta \sin \varphi + \cos \delta \cos \varphi \cos \omega = \cos \theta_z \quad (3)$$

$$\cos \gamma_s = \frac{\sin \alpha_s \sin \varphi - \sin \delta}{\cos \alpha_s \cos \varphi} \quad (4)$$

Two 5V stepper motors will be used to orient the photovoltaic panel. The pitch angle is 1.8° . To halve it, mixed control will be adopted. On instance, for a complete rotation, $360/1.8 \cdot 2 = 400$ command sequences (number of steps) will be required.

In the azimuth direction, it is considered that an opening of 220° is sufficient. The corresponding number of steps is $220 \cdot 400 / 360 = 245$. The photovoltaic panel is placed in the south direction at an azimuth command of 123 steps. From this point he can move 110° east or west. The relationship that expresses the dependence between the azimuth angle and the position of the photovoltaic panel in the azimuth direction is:

$$\text{Azimuth number of steps} = 245 / 220 \cdot (110 + \gamma_s) \quad (5)$$

For the direction of elevation, an aperture of 80 degrees is chosen, i.e. $80 \cdot 400 / 360 = 89$ steps. The elevation of the sun and the angle of inclination of the PV panel are complementary. The relationship that defines the connection between the number of impulses and the elevation of the sun is:

$$\text{Elevation number of steps} = (\alpha_s - 10) \cdot 89 / (90^\circ - 10^\circ)$$

that is:

$$\text{Elevation number of steps} = (\alpha_s - 10) \cdot 89 / 80^\circ$$

where

$$10^{\circ} \leq \alpha_s \leq 90^{\circ} \quad (6)$$

We will evaluate a data set for the microcontroller of the PV panel orientation system for each month of the year [10]. The day in the middle of the corresponding month will be chosen as a reference. Positioning of the PV panel will be done every 30 minutes. The PV panel is always initialized at 6:30 a.m. and the first orientation is done at 7:00 a.m. The last orientation takes place at 16:30. The hourly angle will be calculated with relation (2) for the middle of each adjustment interval.

B. Structure of small model of solar tracking system

B1. Hardware structure

The model of solar tracking system using astronomical data [11], [12] is made with a structure developed around an 18F4520 type microcontroller produced by MICROCHIP (Fig. 4). Three functional blocks can be identified: the control module, the amplifier module and the power supply.

The control module, in addition to the PIC18F4520 chip, also contains a keyboard, an alphanumeric display, a real time clock and a TTL/RS232 adapter. The amplifier module ensures the adaptation of the signals to control the two motors step by step. Also, a hardware processing of the position initialization signals for azimuth and elevation (S1 and S2) is done. In the case of the power supply, an industrial model was chosen.

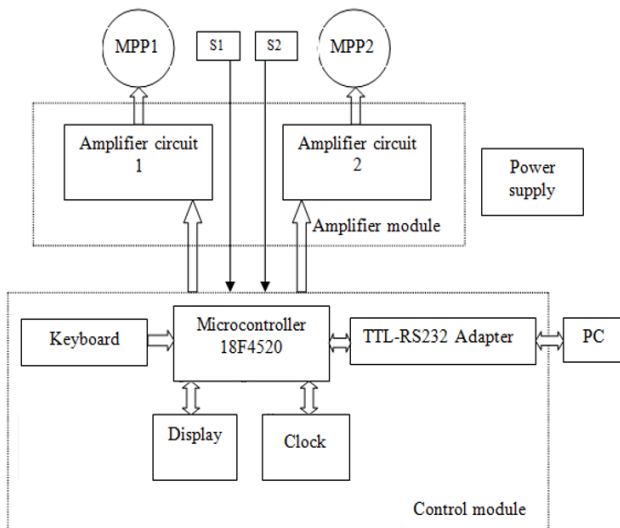


Fig. 4. Block diagram of the automaton for the solar tracking system.

B2. Software structure

Functions of the microcontroller program:

- control of two stepper motors (movement and initialization);
- the acquisition of three analogue inputs;
- setting and saving in the EEPROM memory some values that define the functioning of the microcontroller;
- serial interconnection with an electronic computer through a UART port;
- transmission of data packets to the PC organized according to a pre-established protocol;

- receiving from the PC some data packages organized according to a predetermined protocol;
- adjusting the speed of the two stepper motors;
- the choice of three program menus: testing, tracking by calendar and calendar simulation;
- scanning a keyboard consisting of three push buttons for setting parameters and program configuration;
- displaying some functional messages on a 2x16 character alphanumeric display;
- use and the possibility of configuring your own clock;
- display of error messages when abnormal operating modes are detected.

The C programming language was used for the microcontroller program, because it is easier to understand and maintain. Using such a language closer to the natural way of thinking, the programmer can focus his efforts on the design of the algorithms and less on their individual way of implementation, which leads to obtaining a more understandable code, therefore easier to test and debug.

The program (Fig. 5) starts with the initialization of the microcontroller and the variables used, then enters a loop in which it executes a group of procedures, scans the three human interface keys and calls a new loop, with a similar structure, depending by the value of the „Menu Counter” variable.

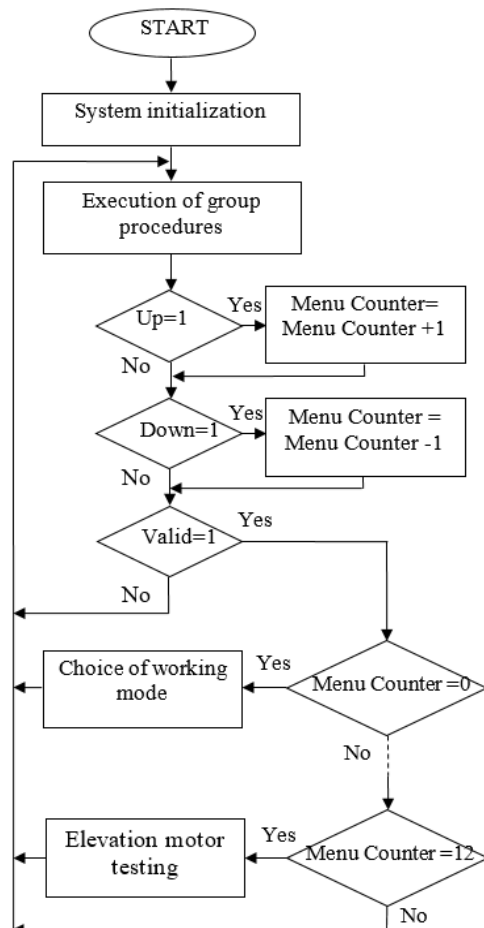


Fig. 5. Microcontroller program flow chart.

Regardless of the loop in which the program is located, the group of procedures will always be executed (fig. 6). Here, the counter system is first decremented, then the three analog inputs are scanned, the three keys are scanned, the motor for azimuth and the motor for elevation are managed. The sequence ends with the processing of the serial communication and with the command of the alphanumeric display.

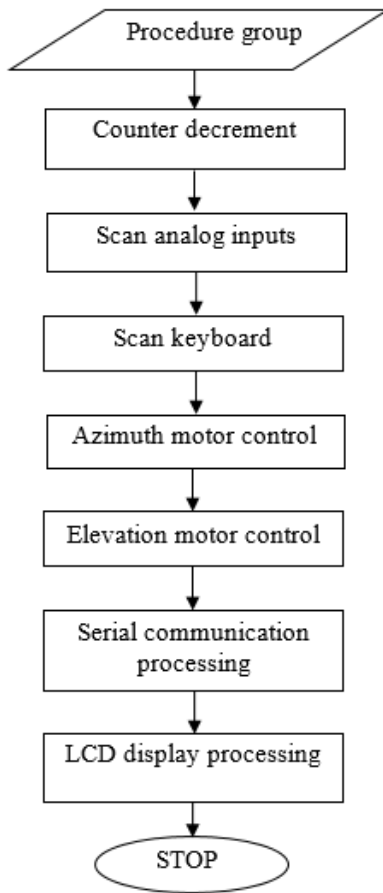


Fig. 6. Flow chart of the "procedure group" sequence.

When the orientation system works according to the calendar, every 30 minutes the required value for azimuth is obtained (Azimuth Prescription - organizational chart from fig. 7) and elevation. For example, for the azimuth direction, the algorithm will test the imposed value (Azimuth Prescribed) with the current one (Azimuth Motor Pulse Index) and depending on the ratio of the two values, the Azimuth Motor Sequence will increase or decrease. It can take only eight values and is the input size in the Azimut Motor procedure. Here, depending on the value, the motor phases are controlled step by step along the azimuth direction by controlling the assigned microcontroller pins (fig. 8).

The data packets D4..D7 in the organizational chart of the program (fig.8) have the following meaning:

- D.4- Index of Azimuth Motor Pulse_H
- D.5- Index of Azimuth Motor Pulse_L
- D.6 – Azimuth prescribed_H
- D7. - Azimuth prescribed_L

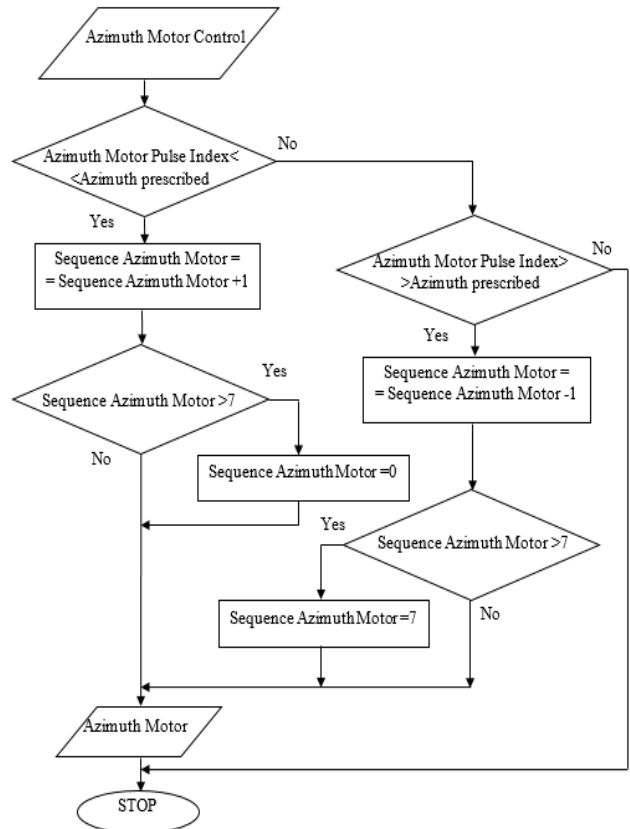


Fig. 7. Flow chart of the motor control in the azimuth direction.

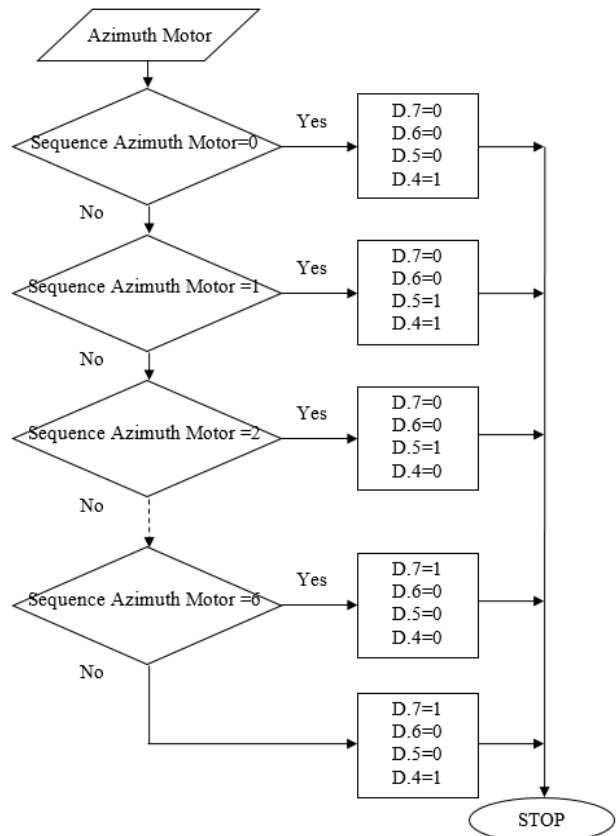


Fig. 8. Flow chart of the actual motor control in the azimuth direction.

C. Solar Tracking system experimentation

Experimentation of the tracking system was done for all work procedures carried out within the tracking program.

The solar tracking system (Fig. 9) contains:

- 1- Power supply
- 2- Mechanical structure of tracking system
- 3- Stepper servomotors
- 4- Development system with microcontroller
- 5- PC

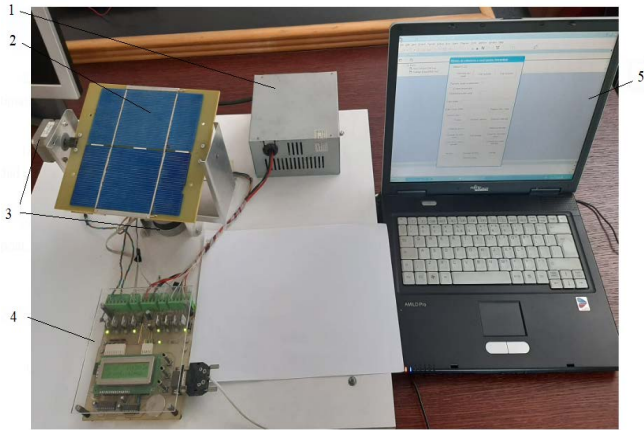


Fig. 9. Solar tracking system achieved.

During a work procedure, information about the date and time as well as the work procedure being executed is displayed on the screen of the development system. As can be seen in figure 10, the date 26.07, time 11:42 and the work procedure "Calendar Orientation" are displayed. For this date and time, the PV panel has the position shown in the figure.



Fig. 10. Solar tracking system working of „Tracking calendar” mode.

The Visual Basic language was used to create the program for PC, [12]. It is frequently found in industrial applications, being easy to use in human-machine interfaces. It should be noted that it contains an object specialized in ensuring the serial connection with other digital equipment, ensuring practically the only convenient way of transferring information between the PC and the targeted equipment.

Figure 11 shows the graphical interface of the created application, named "Tracking system of PV panel"

Then choose the serial port (Fig. 11) by pressing the Serial port selection button. The establishment of the serial link between the two devices is highlighted by the Received serial packets counter. By pressing the Monitor button, the second window of the program will be activated (Fig. 12). Here you can see the content of the received serial packets, the values scanned by the three analogue channels and the numerical values imposed and achieved by the two stepper motors.

The commands from the PC are valid only when the microcontroller is in the first screen (status screen).

In figure 12, it can be seen that the two stepper motors are at rest, after having executed the PV panel positioning sequence according to the two axes (Index motor azimuth=Azimuth motor prescribed; Index motor elevation=Elevation motor prescribed).

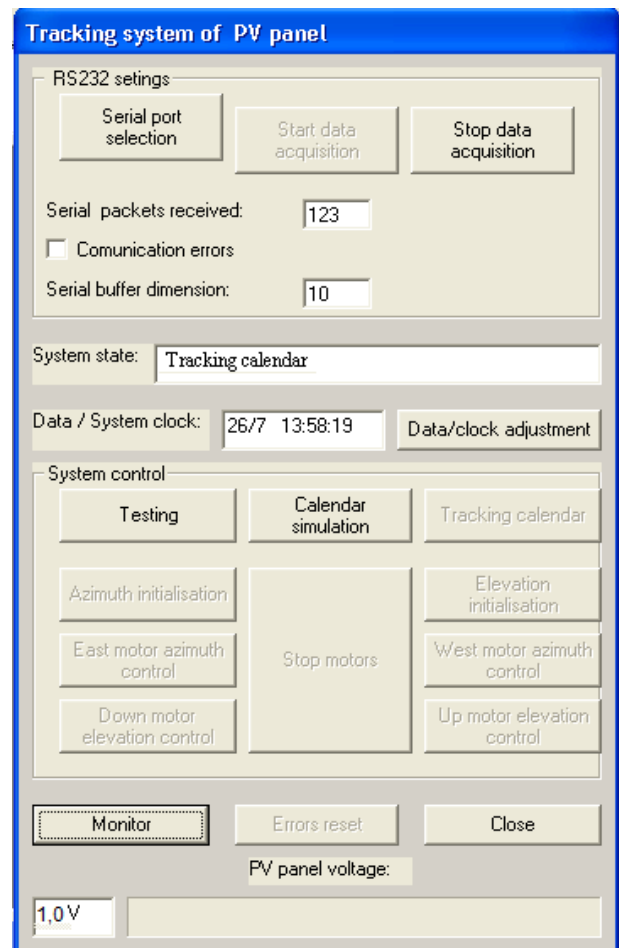


Fig. 11. The main window of the PC program.

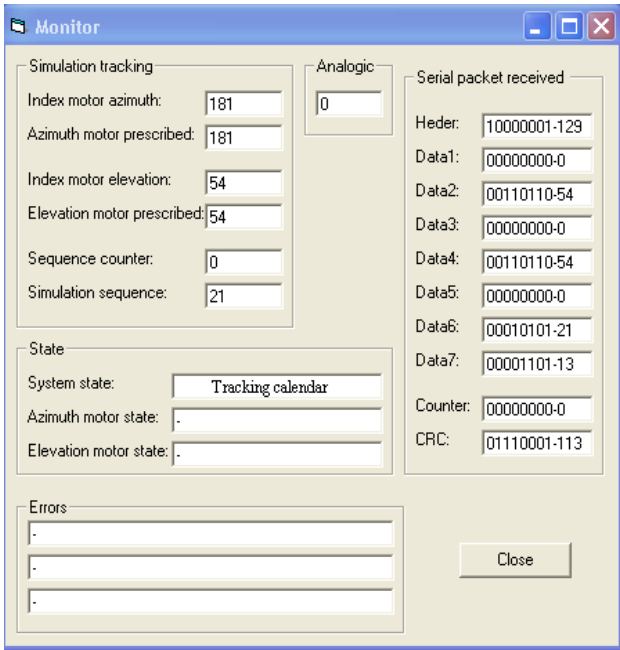


Fig. 12. Additional details window.

In the System Status window, you can see the „Tracking calendar” mode in which the automatic for the orientation of the photovoltaic panels is located

The set serial communication speed is 9600 bits/s. One character is transmitted at this speed in about 1 millisecond (ms) and ten characters in about 10 ms. The recording from figure 13 confirms this – the packet was transmitted in 10.3 ms.

The serial packets are transmitted from the microcontroller to the PC at intervals of 252 ms (verified aspect in the recording from figure 14).

Figures 15 and 16 show the stepper motor control motor at maximum speed, respectively at half of maximum speed. Taking into account the fact that a mixed control is performed, the phase switching interval of 10 ms and 20 ms respectively is checked.

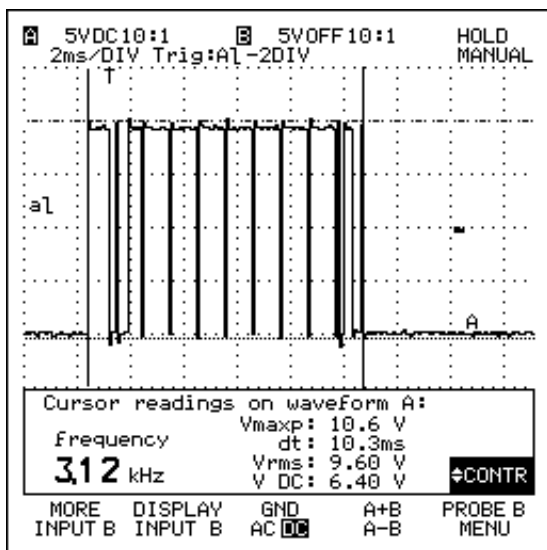


Fig. 13. Data packet transmission to the PC.

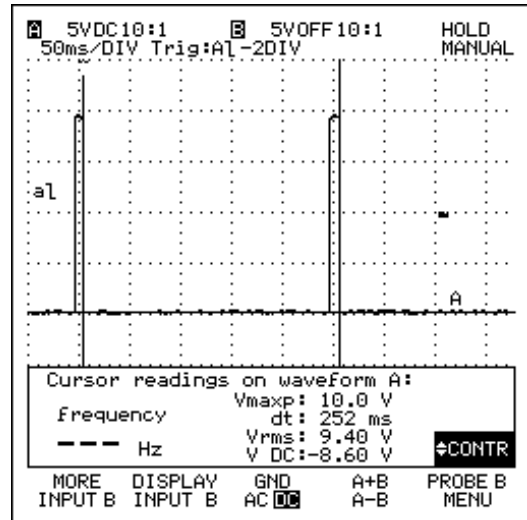


Fig. 14. Illustrative for the rhythmicity of the serial data packets transmitted to the PC.

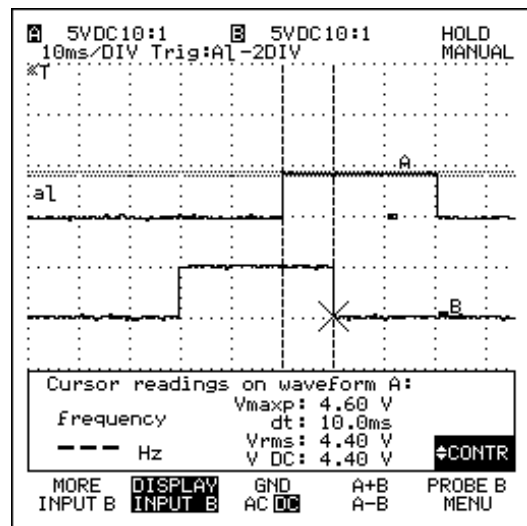


Fig. 15. Illustrative regarding to control of stepper motors at maximum speed

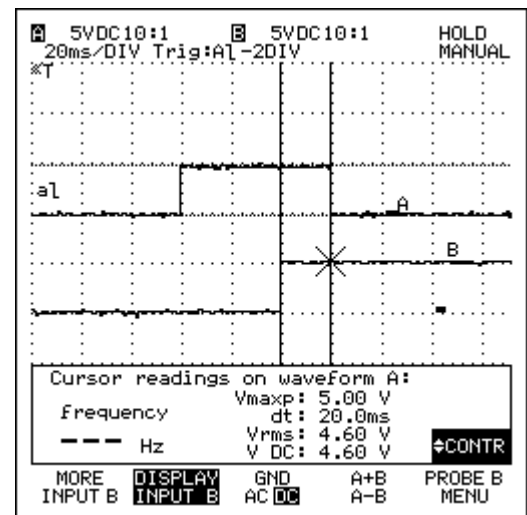


Fig. 16. Illustrative regarding to control of stepper motors at half maximum speed.

The modular nature of the serial communication procedures and the code sequences that identify the received commands, allows their inclusion in the structure of other programs that run on microcontrollers from the same family. The development of a complex serial communication procedure for PC is part of the current trend of PC-equipment interconnection, this duet being almost indispensable especially in the phase of design and verification of programs written for microcontrollers.

The experimental results obtained with the automatic solar tracking system, designed and realized in the work, constitute a convincing method by which the correctness and coherence of the proposed solutions are demonstrated.

III. SMALL MODEL OF SOLAR TRACKING SYSTEM BASED ON MAXIMUM LIGHT INTENSITY

A. Structure of solar tracking system

The structure of the tracking system based on the point of maximum light intensity [14] is presented in figures 17 and 18. The tracking system is composed of the following blocks: photo resistor block (LRD1...LRD4), command platform with Arduino Uno microcontroller [15], servo motors SM1, SM2 for orientation along both axes of the photovoltaic panel, the power supply.

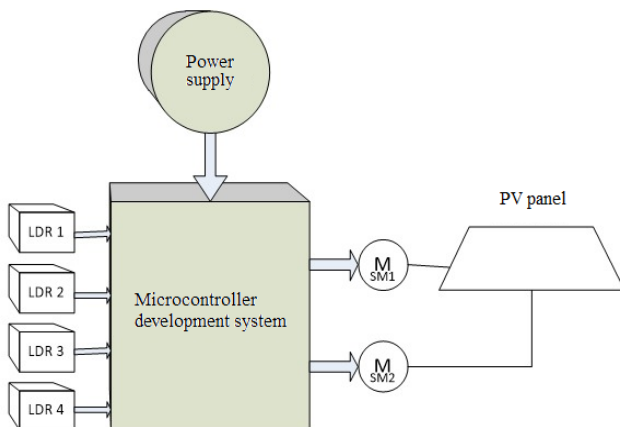


Fig. 17. Structure of Solar tracking system.

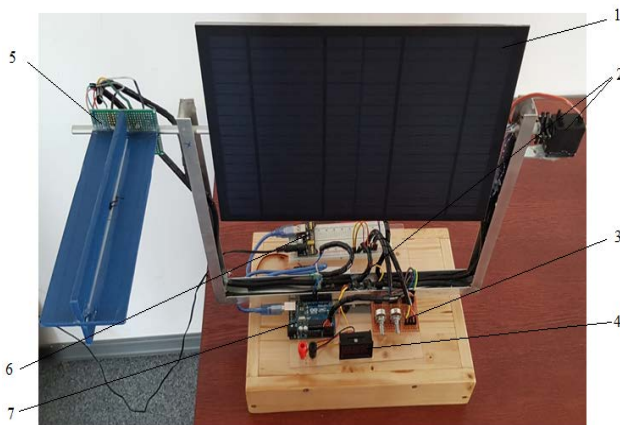


Fig. 18. Solar tracking system achieved: 1-PV panel; 2- servo motors; 3- adjustable resistors; 4- digital voltmeter; 5- photorezistors; 6- power supply; 7- Arduino Uno microcontroller.

Servomotors SM1, SM2 type MG995 that ensure the orientation of the photovoltaic panel according to the two axes have the following technical specifications:

- Operating voltage: 4.8V - 7.2V
- Operating voltage speed at 4.8V: 0.20sec / 60°
- Operating voltage speed at 6.6V: 0.16sec / 60°
- Maximum rotation angle: 180°

Photo resistors type 5528 LDR are passive electronic components that change their electrical resistance depending on the intensity of light radiation.

Technical specifications:

- Maximum voltage: 150 Vdc
- Maximum power consumption: 100 mW
- Operating temperature: - 30°C +70°C
- Spectral value : 540 nm
- Light resistance at 10Lux: 2 KΩ

The Arduino Uno R3 platform is a development board based on the ATmega 328 microcontroller, 14 digital inputs and 6 analogue inputs.

The Arduino IDE (Integrated Development Environment) [15] software was used for the tracking program, which supports C, C++ languages using special code organization rules.

The four photo-resistors are placed on the sides of the photovoltaic panel according to [16], [17], (Fig. 18). Photo resistors change their electrical resistance depending on the intensity of solar radiation [18]. Servomotors connected to the microcontroller board position the PV panel in the direction of the Sun [19].

When the light intensity from the two LDRs on the right is higher, the horizontal servo motor moves the PV panel slowly to the right, and if the intensity on the LDRs on the left is higher, the panel direct slowly to the left.

When the light intensity from the two LDRs, located at the top, is higher, the vertical servo motor rotate the panel to the top, and if the intensity in the LDRs located at the bottom is higher, the panel is oriented to bottom.

The tracking accuracy of the solar tracker system is evaluated by calculating the deviation between the solar panel's actual position and the ideal position based on the sun's movement.

B. Analysis of the operation of the solar tracking system

B1. Calculation of the photovoltaic panel efficiency in standard conditions

The characteristics of the photovoltaic panel measured under standard conditions, solar radiation 1000 W/m², temperature 25°C are the following:

- Power: 10 W
- Open circuit voltage: 21,6 V
- Short circuit current: 630 mA
- Maximum current: 556 mA
- Maximum voltage; 18 V
- PV cell type: polycrystalline Si
- PV panel size (mm.) 220×340×3 mm

The yield of the photovoltaic panel under standard conditions is:

$$\eta = \frac{P_m}{A \cdot E} = \frac{10}{0.22 \cdot 0.34 \cdot 1000} = 0,1336 \rightarrow 13,36\% \quad (7)$$

A- PV panel surface [m²]

E- solar irradiation [W/m²]

B2. Analysis of the efficiency of the solar tracking system

Table 1 presents the results of measuring the voltage and the short-circuit current of the photovoltaic panel for two scenarios: a fixed panel oriented to the South at 40 degrees and a PV panel with tracking system. The measurements were carried out using the same PV panel, under identical irradiation conditions, at regular time intervals during a day for the two analysed cases.

TABLE I. MEASUREMENTS PERFORMED FOR THE TWO SCENARIOS: FIXED PANEL AND ORIENTED PANEL

Stationary PV panel			PV panel with tracking system		
Voltage U [V]	Current I [A]	Power P [W]	Voltage U [V]	Current I [A]	Power P [W]
8,1	0,054	0,44	10	0,113	1,13
10,2	0,151	1,55	11,4	0,242	2,76
11,8	0,270	3,19	11,9	0,409	4,87
12	0,466	5,68	14	0,533	7,47

The achieved solar tracking system is a functional prototype. The use of a system for tracking the movement of the Sun leads to a quantity of captured solar energy (and implicitly a quantity of electricity produced by the photovoltaic panel) up to 35% higher, taking into account the own consumption of electricity tracking system.

IV. CONCLUSIONS

The use of a solar tracking system for PV panels implies an increase in the electrical energy provided by the PV system by up to 30-40%. This was observed from the experimental results.

Implementation of a solar tracking system for PV panels requires complex interdisciplinary knowledge of astronomy, geography and engineering sciences, therefore the presented tracking systems were made on a small scale for educational purposes.

The use of a development system with a microcontroller to control and monitor the solar tracking system is a solution that can significantly reduce the number of electronic components as well as the cost of designing and achieved of equipment.

The sensors, electrical equipment and electronic components used in the two solar tracking systems present a high degree of accessibility and performance using standard software and interfaces.

The hardware and software infrastructure used allows monitoring and control of solar tracking systems in real time.

The models achieved can be used by students in the training process or adapted to a suitable scale can be used in real practical applications.

Starting from these models, some students of the Faculty of Electrical Engineering made similar models for their graduation projects. Other engineering graduates work in the field ensuring the maintenance or installing photovoltaic systems.

ACKNOWLEDGMENT

Source of research funding in this article: Research program of the Electrical Engineering Department financed by the University of Craiova.

Contribution of authors:

First author – 60%

First coauthor – 30%

Second coauthor – 10%

Received on July 01, 2023

Editorial Approval on November 20, 2023

REFERENCES

- [1] R. Messenger, J. Ventre, Photovoltaic System Engineering, CRC Press, 2004, Sec. Edition.
- [2] C. Bratu, "Evaluation of solar irradiance to a flat surface arbitrary oriented", Annals of the University of Craiova, Electrical Engineering series, No. 32, 2008, pp. 310-314
- [3] H. Moradi, A. Abtahi, R. Messenger "Annual performance comparison between tracking and fixed photovoltaic arrays". 43rd IEEE Photovolt Spec Conf, 2016, pp.3179–3183.
- [4] M. Comșit, Tracking mechanisms specific to solar energy conversion systems, Mecanisme de orientare specifice sistemelor de conversie a energiei solare, Teza de doctorat, Universitatea Transilvania din Brașov, 2007.
- [5] A.Z. Hafeza, A.M. Yousefa, N.M. Haraga, "Solar tracking systems: Technologies and trackers drive types – A review", Renewable and Sustainable Energy Reviews, No. 91, 2018, pp. 754–782
- [6] S. Rachala, K. Rajan, "Solar tracking system – a review", International Journal of Sustainable Engineering, Volume 10, 2017 - Issue 2, pp. 72-81.
- [7] S. Degeratu, I.L. Alboteanu., S. Rizescu, D. Coman, N. Bizdoaca, "Active solar panel tracking system actuated by shape memory alloy springs", Proc. of International Conferencon Applied and Theoretical Electricity (ICATE), 2014, pp. 1-5.
- [8] R. Perez, "To Track... or not to Track", Home Power, no 101, june & july, 2003.
- [9] I. Bostan, V. Dulgheru, I. Sobor, V. Bostan, A. Sochirean, Renewable energy conversion systems, Sisteme de conversie a enrgiilor regenerabile, Ed. Tehnica-Info, Chișinău, 2007.
- [10] L. Alboteanu, Gh. Manolea, Fl. Ravigan, "Positioning systems for solar panels placed in isolated areas", Proc. of the International Conference of Applied and Theoretical Electricity, 26-28 oct., Baile Herculane, 2006, Ed. Universitaria 2006, pp.163-168.
- [11] L. Alboteanu, F. Ravigan, "Design of a sun tracking automaton for photovoltaic panels with low concentration of solar radiation", Procc. of International Conference on Applied and Theoretical Electricity (ICATE), 2014, pp. 1-5.
- [12] L. Alboteanu, Gh. Manolea, "Automatic Tracking System for Photovoltaic Panel based on Programmable Logic Controller", Acta Electrotehnica, 2016, Vol. 57, Issue 3/4, pp. 394-398.
- [13] *** Microsoft, MSDN Visual Studio 6.0.
- [14] D. Bawa, CY. Patil, "Fuzzy control based solar tracker using arduino uno", International Journal Engineering Innovation Technology, No. 2, 2013, pp.179–187.
- [15] *** <https://www.arduino.cc/>
- [16] M. Ghassoul, "A dual solar tracking system based on a light to frequency converter using a microcontroller", Fuel Communications 6 (2021), 100007.
- [17] S.S. Kumar, S. Suryanarayana, "Automatic Dual Axis Sun Tracking System using LDR Sensor", International Journal of Engineering Innovation Technology, No. 4, Oct., 2014, pp 3214–3217.
- [18] F.Z. Baouche, B. Abderezzak, A. Ladmi, K. Arbaoui, G. Suciuc, T.C. Mihaltan, M.S. Raboaca, S.V. Hudisteanu, F.E. Turcanu, "Design and Simulation of a Solar Tracking System for PV", Applied Science, No. 12, 2022.
- [19] J. K. Tharamuttam, A. Keong Ng, "Design and Development of an Automatic Solar Tracker", Energy Procedia, 2017, pp. 629-634.

Pentru comenzi și informații, contactați:

Editura Universitaria

Departamentul vânzări

Str. A.I. Cuza, nr. 13, cod poștal 200585

Tel. 0251598054, 0746088836

Email: editurauniversitaria@yahoo.com

marian.manolea@gmail.com

Magazin virtual: www.editurauniversitaria.ro